

# Elementary reactions in the catalytic reduction of NO on rhodium surfaces

**Citation for published version (APA):**

van Hardeveld, R. M. (1997). *Elementary reactions in the catalytic reduction of NO on rhodium surfaces*. [Phd Thesis 1 (Research TU/e / Graduation TU/e), Chemical Engineering and Chemistry]. Technische Universiteit Eindhoven. <https://doi.org/10.6100/IR497380>

**DOI:**

[10.6100/IR497380](https://doi.org/10.6100/IR497380)

**Document status and date:**

Published: 01/01/1997

**Document Version:**

Publisher's PDF, also known as Version of Record (includes final page, issue and volume numbers)

**Please check the document version of this publication:**

- A submitted manuscript is the version of the article upon submission and before peer-review. There can be important differences between the submitted version and the official published version of record. People interested in the research are advised to contact the author for the final version of the publication, or visit the DOI to the publisher's website.
- The final author version and the galley proof are versions of the publication after peer review.
- The final published version features the final layout of the paper including the volume, issue and page numbers.

[Link to publication](#)

**General rights**

Copyright and moral rights for the publications made accessible in the public portal are retained by the authors and/or other copyright owners and it is a condition of accessing publications that users recognise and abide by the legal requirements associated with these rights.

- Users may download and print one copy of any publication from the public portal for the purpose of private study or research.
- You may not further distribute the material or use it for any profit-making activity or commercial gain
- You may freely distribute the URL identifying the publication in the public portal.

If the publication is distributed under the terms of Article 25fa of the Dutch Copyright Act, indicated by the "Taverne" license above, please follow below link for the End User Agreement:

[www.tue.nl/taverne](http://www.tue.nl/taverne)

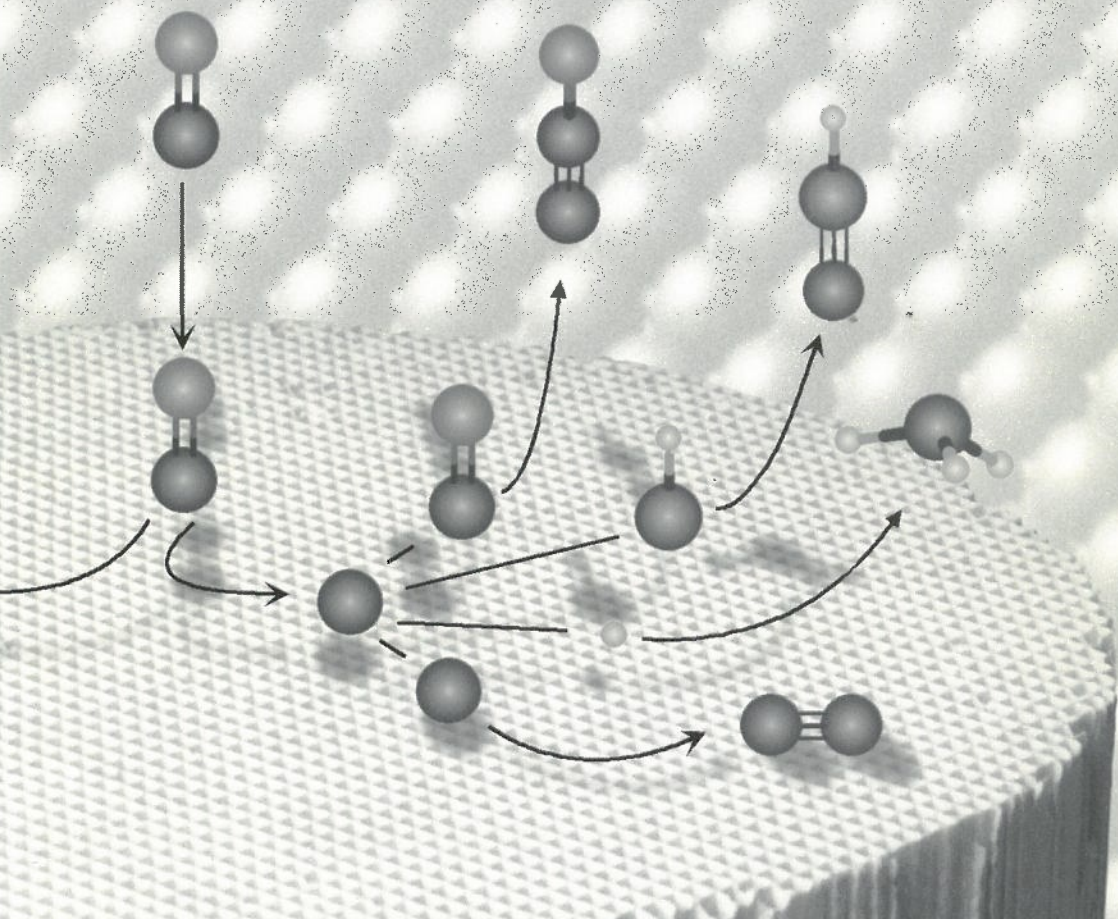
**Take down policy**

If you believe that this document breaches copyright please contact us at:

[openaccess@tue.nl](mailto:openaccess@tue.nl)

providing details and we will investigate your claim.

# Elementary Reactions in the Catalytic Reduction of NO on Rhodium Surfaces



Martijn van Hardeveld

# **Elementary Reactions in the Catalytic Reduction of NO on Rhodium Surfaces**

Proefschrift

ter verkrijging van de graad van doctor aan de  
Technische Universiteit Eindhoven, op gezag van  
de Rector Magnificus, prof.dr. M. Rem, voor een  
commissie aangewezen door het College van  
Dekanen in het openbaar te verdedigen op  
woensdag 17 september 1997 om 16.00 uur

door

**Robert Martijn van Hardeveld**

geboren te Geldrop

Dit proefschrift is goedgekeurd door de promotoren:

prof.dr. R.A. van Santen

en

prof.dr.ir. J.W. Geus

copromotor: dr. J.W. Niemantsverdriet

The work described in this thesis has been carried out at the Schuit Institute of Catalysis, Laboratory of Inorganic Chemistry and Catalysis, Eindhoven University of Technology, the Netherlands. Financial support has been supplied by the Netherlands Foundation for Chemical Research (SON) with aid from the Netherlands Organization for Scientific Research (NWO).

Printed at the *Universiteitsdrukkerij*, Eindhoven University of Technology

CIP-DATA LIBRARY TECHNISCHE UNIVERSITEIT EINDHOVEN

Hardeveld, Robert M. van

Elementary reactions in the catalytic reduction of NO on rhodium surfaces / by Robert M. van Hardeveld. - Eindhoven : Technische Universiteit Eindhoven, 1997.

Proefschrift. -

ISBN 90-386-0858-6

NUGI 813

Trefw: katalyse / stikstofoxiden / chemische reductie / rhodium / reactiemechanismen

Subject headings: catalysis / nitrogen oxide / reduction kinetics / rhodium

# Contents

<b>1</b>	<b>Introduction</b>	<b>7</b>
1.1	The importance of catalysis for society	7
1.2	The principle of catalysis	7
1.3	Chemical kinetics and catalysis	8
1.4	Spectroscopy and catalysis	10
1.5	Automotive exhaust catalysis	12
1.6	Scope of this thesis	14
<b>2</b>	<b>Experimental set-up and techniques</b>	<b>17</b>
2.1	Introduction	17
2.2	Technical description of the UHV systems	17
2.3	Secondary ion mass spectrometry	20
2.3.1	The principle of SIMS	20
2.3.2	Secondary ion yields	21
2.3.3	Application of SIMS in surface science	23
2.4	Other surface analysis tools	24
2.4.1	Temperature programmed reaction spectroscopy	24
2.4.2	Low energy electron diffraction	25
2.4.3	Auger electron spectroscopy	26
<b>3</b>	<b>The adsorption and dissociation of NO on Rh(111)</b>	<b>29</b>
3.1	Introduction	29
3.2	Experimental	30
3.3	Experimental results	30
3.3.1	Low temperature adsorption of NO on Rh(111)	30
3.3.2	Adsorption of NO at various temperatures on Rh(111)	35
3.3.3	Coverage dependence of the NO dissociation reaction	41
3.4	Mathematical modeling of NO adsorption at various temperatures	42
3.4.1	Introduction	42
3.4.2	Model description	43
3.4.3	Modeling molecular NO adsorption between 150 and 225 K	44
3.4.4	Modeling isothermal NO adsorption between 225 and 350 K	47
3.5	Discussion	50
3.5.1	Molecular NO adsorption at low temperatures	50
3.5.2	The role of lateral interactions	51
3.5.3	The NO dissociation mechanism	52
3.6	Conclusions	55
<b>4</b>	<b>Preparation of atomic nitrogen adlayers on Rh(111)</b>	<b>59</b>
4.1	Introduction	59
4.2	Experimental	60

4.3	Results	60
4.3.1	Preparation of atomic nitrogen by reaction between NO and H <sub>2</sub>	60
4.3.2	Preparation of atomic nitrogen layers by NH <sub>3</sub> decomposition	64
4.3.3	Preparation of atomic nitrogen from NO+H <sub>2</sub> mixtures	66
4.4	Discussion	67
4.4.1	Comparison of methods to prepare N <sub>ads</sub> on Rh(111)	67
4.4.2	N <sub>2</sub> desorption from atomic nitrogen layers	68
4.4.3	NH <sub>3</sub> decomposition	71
4.5	Conclusions	72
<b>5</b>	<b>The mechanism of NH<sub>3</sub> formation on Rh(111)</b>	<b>75</b>
5.1	Introduction	75
5.2	Experimental	76
5.3	Results	76
5.3.1	Preparation of atomic nitrogen layers on Rh(111)	76
5.3.2	Hydrogenation of atomic nitrogen at constant temperature and H <sub>2</sub> pressure	77
5.3.3	Dependence of the NH <sub>3</sub> formation rate on the H <sub>2</sub> pressure	78
5.3.4	Identification of NH <sub>x</sub> reaction intermediates by SIMS	79
5.3.5	Evidence for NH <sub>x</sub> intermediates from TPD	82
5.3.6	Dependence of the NH <sub>3</sub> formation rate on the temperature	84
5.4	Discussion	84
5.4.1	Mechanism and kinetic description of NH <sub>3</sub> formation on Rh(111)	84
5.4.2	The H <sub>2</sub> pressure dependence of the NH <sub>3</sub> formation rate	86
5.4.3	Presence of NH <sub>x</sub> intermediates on the surface under reaction conditions	87
5.4.4	Kinetic parameters of the NH <sub>3</sub> formation	88
5.5	Conclusions	89
<b>6</b>	<b>Adsorption and desorption of NH<sub>3</sub> on Rh(111)</b>	<b>91</b>
6.1	Introduction	91
6.2	Experimental	92
6.3	Results	93
6.3.1	Temperature programmed desorption	93
6.3.2	D <sub>2</sub> coadsorption	94
6.3.3	LEED of NH <sub>3</sub> on Rh(111)	95
6.3.4	Coverage calibration and sticking coefficient	96
6.3.5	Work function measurements	97
6.3.6	Secondary Ion Mass Spectrometry	98
6.4	Discussion	101
6.4.1	Adsorption states of NH <sub>3</sub>	101
6.4.2	Effective dipole moment of adsorbed NH <sub>3</sub>	102
6.4.3	Coverage dependent effects	103
6.4.4	SIMS of NH <sub>3</sub> on Rh(111)	104
6.4.5	Adsorption site of NH <sub>3</sub>	106
6.5	Conclusions	106

<b>7 Reduction of NO by ethylene on Rh(111)</b>	<b>109</b>
7.1 Introduction	109
7.2 Experimental	110
7.3 Results	110
7.3.1 NO on Rh(111)	110
7.3.2 C <sub>2</sub> H <sub>4</sub> on Rh(111)	110
7.3.3 Reactions between O and H	112
7.3.4 Reactions between O and C <sub>2</sub> H <sub>4</sub>	113
7.3.5 NO and ethylene at low coverage	115
7.3.6 NO and ethylene at intermediate coverage	116
7.3.7 Coverage dependence	119
7.3.8 NO and ethylene at saturation coverage	124
7.4 Discussion	126
7.5 Conclusions	128
<b>8 C-N coupling in reactions between atomic nitrogen and ethylene on Rh(111)</b>	<b>131</b>
8.1 Introduction	131
8.2 Experimental	131
8.3 Results	132
8.3.1 TPRS of atomic nitrogen and ethylene	132
8.3.2 Static SIMS of surface reactions between atomic nitrogen and ethylene	135
8.3.3 Kinetics of CN formation	136
8.3.4 Kinetics of CN decomposition	139
8.3.5 Work function measurements	141
8.4 Discussion	142
8.5 Conclusions	144
<b>9 Summary and conclusions</b>	<b>147</b>
<b>Samenvatting</b>	<b>151</b>
<b>Publications</b>	<b>155</b>
<b>Dankwoord</b>	<b>157</b>
<b>Curriculum vitae</b>	<b>158</b>

# 1 Introduction

## 1.1 The importance of catalysis for society

Whereas some disciplines of "Arts & Science" might sometimes have difficulties with explaining their relevance to society, catalysis does not or ought not. Since Berzelius introduced the name "Catalysis" around 1836, many examples have appeared which illustrate the importance of catalysis to society. We arbitrarily mention a few examples through history. In the beginning of the nineteenth century the miner's safety lamp was developed by Humphry Davy. It saved many mine worker's lives by preventing explosions caused by mine gas. The synthesis of ammonia for agricultural needs (and sadly also for the production of explosives) was unsuccessful until a catalytic route was developed by Haber in the beginning of the 20<sup>th</sup> century. Midway this century the fluid catalytic cracking (FCC) process was developed which enabled the upgrading of heavy oil fractions to the high quality gasoline necessary for the rapidly increasing fleet of cars. There were also several contributions in the field of polymerization reactions. Best known are Ziegler and Natta who received the Nobel prize in 1963 for the discovery of a Ti-based catalysts for the polymerization of polyethylene and polypropylene, respectively. The last few decades, catalytic processes have significantly contributed to the reduction of environmentally hazardous waste streams. We mention the success of hydrodesulfurization of fuels, which has resulted in a significant reduction of the SO<sub>x</sub> emissions. Also the conversion of NO, CO and C<sub>x</sub>H<sub>y</sub> from automotive exhaust gases to the environmentally harmless gases N<sub>2</sub>, CO<sub>2</sub> and H<sub>2</sub>O by the three-way catalyst is an elegant example of the benefits catalysis brings to society.

At this moment more than 80% of the chemical products is produced by processes that involve at least one catalytic reaction step. In the future, emission control and processes efficiency will become more and more important. This requires adaptation of old and development of new processes, which promises a challenging future for catalysis.

## 1.2 The principle of catalysis

Old textbooks often define a catalyst as a substance that accelerates a certain chemical reaction without being consumed. Although this description as a whole is correct, it may lead to the misconception that a catalyst does not undergo changes during reaction. It is therefore better to think of catalysis in terms of cyclic processes. At the beginning of a cycle, the reactants and the catalyst interact. Due to this interaction the chemical behaviour of the reactants changes and some specific reactions are facilitated. For the completion of the catalytic cycle, it is essential that the product-catalyst interaction is broken so that reactants can interact with the catalyst again and the cycle can be repeated over and over. The interaction between the catalysts and the reactants



often appears to be very critical. For this reason, almost every catalytic process has its own catalyst and the development of these highly specific catalysts requires great research efforts.

Catalysts come in a very wide variety; they can be metals, oxides, sulfides, organometallic complexes, enzymes, *etc.* There are many different ways to categorize catalysts. For instance, this can be done based on the nature of the catalytical material (metals, oxides, sulfides), or on the type of reaction that is catalyzed (oxidation, hydrogenation, isomerization, polymerization). Another commonly used distinction is between homogeneous and heterogeneous catalysts. In heterogeneous catalysis, the reactants and the catalysts are in a different phase: the catalyst typically is a solid, whereas the reactants and products are gases or liquids. This thesis describes reactions of gases catalyzed by a metallic rhodium (model) catalyst and therefore belongs to the discipline of heterogeneous catalysis. In heterogeneous catalysis, three main steps of the catalytic cycle can be distinguished: adsorption, reaction and desorption, as shown schematically for the CO-NO reaction on rhodium in Figure 1.1.

NO-CO reaction on Rhodium

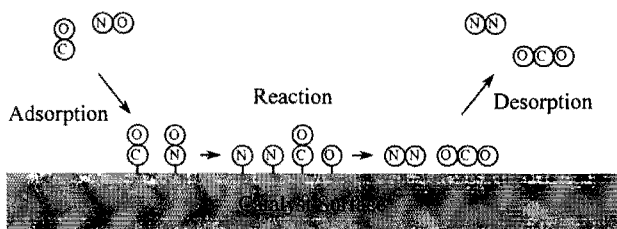


*Figure 1.1 Schematic representation of the rhodium catalyzed NO-CO reaction.*

One of the most important steps in the NO-CO reaction cycle is the dissociation of NO. The energy to break the NO bond in the gas phase is 650 kJ/mol [1], whereas a typical value for the NO dissociation energy on a rhodium surface is 60 kJ/mol [2], which is less than 10% of the gas phase NO bond energy. This nicely illustrates the role of the rhodium catalyst in this particular case. Indeed, we can say that, in general, catalysts assist in breaking and forming chemical bonds.

### 1.3 Chemical kinetics and catalysis

Since catalysis deals with the acceleration of chemical reactions there is a close relation with reaction kinetics. The connection between these disciplines can be made on different levels. On a macroscopic scale, conversions and selectivities can be linked to the activity and performance of the catalyst. However, in order to understand the fundamentals of catalysis, which in truth is a molecular science, a comparison with

reaction kinetics on the molecular scale is desirable.

The theory of rate processes on the molecular level was developed around 1935 by Eyring [3,4], Polanyi [5] and Evans [6], based on a statistical mechanical approach. This theory states that an elementary reaction proceeds via a so-called "activated complex" or "transition state". This transition state corresponds to the reaction complex at the top of the energy barrier, as indicated schematically in Figure 1.2.

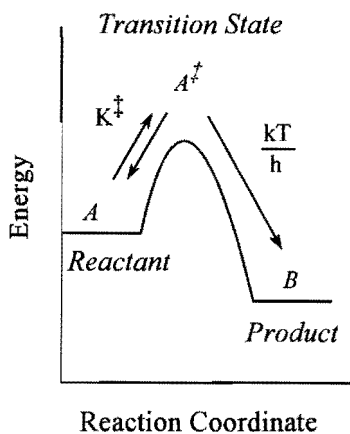


**Figure 1.2** Basic concept of the transition state theory. The reactant  $A$  is in equilibrium with the activated complex at the top of the energy barrier  $A^\ddagger$ , for all degrees of freedom with exception of the one corresponding to the reaction coordinate. The effective rate of crossing the energy barrier equals  $kT/h$ .

The passage of the reacting complex over the barrier is assumed to be a one dimensional, classical event which involves only one degree of freedom, the reaction coordinate. For all other degrees of freedom equilibrium is assumed between the reactant  $A$  and the activated complex  $A^\ddagger$ . The value of the equilibrium constant,  $K^\ddagger$ , can be derived from the partition functions ( $pf$ ) of the reactant in the ground state and the activated state:

$$K^\ddagger = \frac{pf_{A^\ddagger}}{pf_A} \quad (1.1)$$

$$pf = \sum_i e^{-\frac{\epsilon_i}{kT}} = pf_{trans} \cdot pf_{rot} \cdot pf_{vibr} \cdot e^{-\frac{U_0}{kT}}$$

Partition functions,  $pf$ , are defined as the summation over all the energy levels  $\epsilon_i$  of a molecular system as shown in equation 1.1. Partition functions contain contributions from translational, rotational and vibrational energies and are often defined with respect to the ground state energy  $U_0$  of the molecular system.

The partition function of the activated complex,  $pf_{A^\ddagger}$ , does not contain the contribution that corresponds to the reaction coordinate. Furthermore, it can be derived that the effective rate of crossing the energy barrier by the activated complex equals  $kT/h$  [7]. In this way the transition state theory yields the following expression for the rate

constant:

$$k_{TST} = \frac{k T}{h} \cdot \frac{P f_{A^\ddagger}}{P f_A} \cdot e^{-\frac{\Delta E}{kT}} \quad (1.2)$$

In this equation,  $\Delta E$  is the energy difference between the potential energy minimum for A and the energy of the activated complex  $A^\ddagger$  at the top of the barrier, both corrected for the zero point vibration energy. For more details, the interested reader is referred to excellent textbooks on this subject [8,9].

Note that there is a slight difference with the widely used definition of the rate constant as introduced by Arrhenius:

$$k_{Arr} = v_{Arr} \cdot e^{-\frac{E_{act}}{kT}} \quad (1.3)$$

In this case all temperature dependence is in the exponential term and, as a consequence,  $E_{act}$  and  $\Delta E$  from equation 1.2 are not necessarily the same.

Finally, it is important to note that catalysis can *not* beat thermodynamics: a catalyst can accelerate a chemical reaction but has no influence on thermodynamic equilibria.

## 1.4 Spectroscopy and catalysis

The development of (surface) spectroscopy has transformed catalysis from art into science, as is nicely illustrated by a comprehensive overview on the role of spectroscopy in catalysis as given by Niemantsverdriet [10]. Generally speaking, there are two different areas where spectroscopy contributes to catalysis science. The first one is closely related to material science. Commercial catalysts are highly complex systems, consisting of a supporting material and a variety of active components, including promoters, *etc.* Spectroscopy is indispensable to determine the composition and structure of the catalyst, preferentially on a molecular scale. This knowledge is necessary in order to optimize preparation routes and understand phenomena like catalyst deactivation. Secondly, surface spectroscopy can yield essential information about surface reactions by studying the reactivity of adsorbed species and identifying reaction intermediates and products. The ultimate goal would be to relate catalyst composition on the atomic scale to catalytic activity under realistic process conditions. Especially, this last requirement causes severe practical problems for the spectroscopist. Since the majority of the surface spectroscopic techniques uses electrons or ions, either as excitation source or for detection purposes, measurements are restricted to high vacuum conditions ( $p < 10^{-6}$  mbar). Just a limited

number of techniques, *e.g.* EXAFS, Mössbauer Spectroscopy, and RAIRS, which all use photons for excitation and detection, enable monitoring under high pressure conditions. The discrepancy between the experimental and realistic pressure conditions often hinders translation of results from one area to the other, and has led to the introduction of the term "pressure gap".

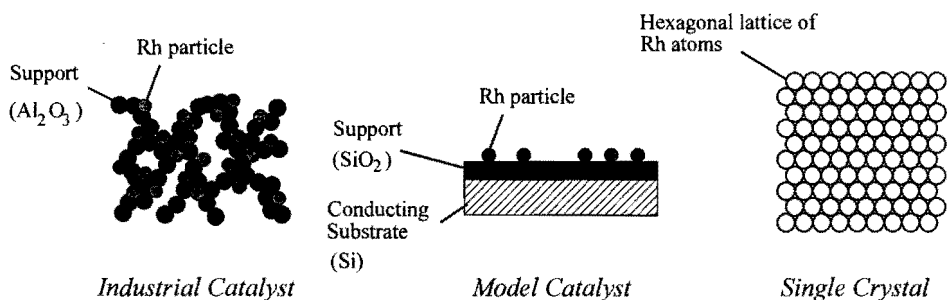


**Figure 1.3** Schematical representation of a porous industrial catalysts (left), a model catalyst on a flat, conducting support (middle), and a single crystal (right) representing a homogeneous active phase.

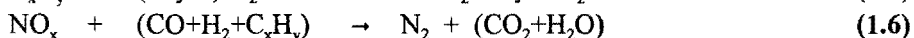
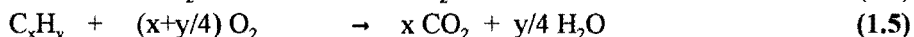
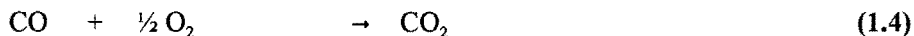
Another practical problem stems from the nature of a practical catalyst. Since catalysis is a surface phenomenon, a high specific surface area of the catalytically active material is required, especially when this is an expensive material, such as rhodium. In practice, this is realized by finely distributing the active material over a porous support which has a high specific surface area and provides mechanical strength, see Figure 1.3. Consequently, most of the active material is hidden and not accessible for analysis by surface sensitive techniques. Furthermore, supports often are insulating materials, which can result in charging problems and accompanied loss of spectroscopic information. One of the possibilities to solve these problems is using model supports, see Figure 1.3. A model support typically consists of a conducting substrate which is topped by a flat, thin layer of the supporting material, *e.g.* a silicon wafer with a 5 nm thick SiO<sub>2</sub> oxide layer. On this model support the active phase can be deposited by evaporation [11] or by wet chemical methods which more closely resemble commercial catalyst preparation routes [12-15]. Applications of model catalysts and supports have recently been reviewed by Gunter *et al.* [16].

Many catalytic reactions have appeared to be structure sensitive [17,18], which requires knowledge of the surface structure on the atomic level. This information can hardly ever be obtained from industrial catalysts. For this reason, single crystals, of which the atomic arrangements at the surface are known, are often used. Spectroscopic data obtained from single crystals can provide information on the molecular level, which enables comparison with theory, like the transition state theory, and theoretical cluster calculations [19]. Although the gap is large, the bridge to realistic catalysts is there, since

reactivity studies on single crystals significantly contribute to the unravelling of highly complex reaction systems, by providing rate parameters for elementary steps.

## 1.5 Automotive exhaust catalysis

By far the most important application of rhodium is as the active component in catalytic converters for automotive exhaust gases. In 1990, 84% of the total Western-world demand for rhodium originated from the production of autocatalysts [20]. The currently used catalytic exhaust gas converter is the "three-way catalyst", which is named this way since it promotes the removal of 3 pollutants; CO, NO<sub>x</sub> and hydrocarbons:



In three-way catalysts, rhodium is important for the selective catalytic reduction of NO<sub>x</sub> to N<sub>2</sub>, while it contributes significantly to CO and C<sub>x</sub>H<sub>y</sub> oxidation as well [20].

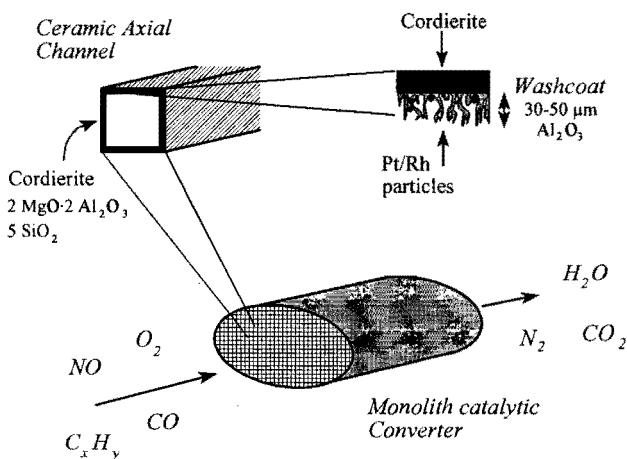


**Figure 1.4** Schematic representation of the three-way exhaust gas converter. The monolith consists of parallel ceramic channels which are covered with an Al<sub>2</sub>O<sub>3</sub> washcoat acting as support for the Pt and Rh particles.

Figure 1.4 shows a schematic representation of the commercial automotive exhaust converter. In order to avoid pressure build up, a monolith consisting of parallel axial channels is used (~60 channels per cm<sup>2</sup>, total volume 1400-1800 cm<sup>3</sup>). The monolith is composed of cordierite (2MgO·2Al<sub>2</sub>O<sub>3</sub>·5SiO<sub>2</sub>) and is covered with an Al<sub>2</sub>O<sub>3</sub> washcoat, which is the actual supporting material. The noble metals Pt and Rh are applied to the support by impregnation (typical loadings 2 g and 0.22 g, respectively). The catalyst contains several additives which improve catalyst performance and durability. Ceria

(CeO<sub>2</sub>) is added in large amounts, 10-30 wt% of the washcoat, whereas also small amounts of lanthanum oxide and alkaline earth oxides are present. Ceria has many functions, for instance, it acts as a reversible oxygen storage component and it stabilizes the alumina support.

The three-way catalyst simultaneously has to execute CO and C<sub>x</sub>H<sub>y</sub> oxidation, on the one, and NO<sub>x</sub> reduction, on the other hand (see equations 1.4, 1.5 and 1.6, respectively). High activity on both oxidation and reduction reactions requires tight control of the air-to-fuel ratio in the combustion mixture for the car engine (A/F = 14.7±0.3). Under fuel-lean conditions (net oxidizing), NO<sub>x</sub> reduction rapidly deteriorates, whereas CO oxidation is hampered in the reverse case. Practically, the oxygen excess in the exhaust gas is measured by an oxygen sensor ( $\lambda$ -sonde) and by means of an electronic module the A/F ratio is adapted so that optimum conditions for catalysis are maintained. The time delay in the feed back is in the order of one second owing to which the A/F ratio in the exhaust oscillates with a frequency of 1 Hz around the stoichiometrically balanced ratio. Interestingly, these oscillations (provided they comprise a rather small window, A/F = 14.7±0.3) have been found to increase the effectiveness of the converter [20].

Future exhaust emission legislations require further development of the catalytic converter. For the reduction of CO and C<sub>x</sub>H<sub>y</sub> emissions, the focus lies on the shortening of the light-off period (this is the time for the catalyst to reach operating conditions 350-650 °C). However, NO<sub>x</sub> emission predominantly occurs with the fully warmed-up engine and further reduction of the emissions requires improvement of the catalyst activity. This explains the contemporary research efforts on NO<sub>x</sub> reduction by rhodium. Other new challenges for emission control are the development of catalysts for NO<sub>x</sub> reduction from diesel and lean burn engines, where A/F ratios are larger than 17:1. Also the influence of fuel composition on the exhaust composition and thereby catalyst performance is a point of interest.

Another future application of rhodium may be in syngas production. Hickman and Schmidt [21] showed that rhodium is capable of converting methane to syngas, by direct oxidation (efficiencies larger than 90%) when reaction times are kept very short, <10<sup>-3</sup> s.

Syngas can be used to produce a variety of products. Methanol can be produced by using a copper/zinc catalyst, while hydrocarbons can be obtained by the Fischer-Tropsch process. Interestingly, rhodium based catalysts can produce oxygenates like ethanol and ethanal from syngas [22-24]. The product selectivity in syngas conversion is determined by elementary reactions, such as CO dissociation, C-C coupling and CH<sub>x</sub> hydrogenation. These reactions have been studied extensively on transition metal surfaces including rhodium.

## 1.6 Scope of this thesis

The purpose of this thesis is to investigate elementary surface reactions that occur during NO reduction on rhodium, with the ultimate ambition to determine the associated kinetic parameters. We will pay special attention to the reactivity of atomic nitrogen atoms, which play a decisive role in the selectivity of NO reduction reactions. Knowledge of kinetic parameters is essential to get a better understanding of the processes that determine the performance of the three-way catalyst, which is an important requirement for further development. Kinetic parameters of elementary NO reduction reactions are also indispensable for the understanding and modelling of the oscillatory reaction behaviour which has been reported for many NO reduction reactions on rhodium [25,26].

A rhodium (111) single crystal surface has been used as a model for the catalyst and all experiments have been carried out in an Ultra High Vacuum (UHV) system. For the determination of kinetic parameters of certain elementary steps, we have employed a combination of two techniques: temperature-programmed desorption or reaction spectroscopy (TPD, TPRS) together with secondary ion mass spectrometry (SIMS). This combination of techniques has been proven very powerful, since, TPD or TPRS provide information about the gaseous products formed and SIMS monitors reactions on the surface and detects intermediates.

In the following we describe the arrangement of this thesis. Chapter 2 depicts the experimental set up and gives a brief description of the physical principles that underlie the surface spectroscopies we have employed. Special attention is paid to the strengths and weaknesses of SIMS. Chapter 3 deals with the adsorption and dissociation of NO where the importance of lateral effects is illustrated. Chapter 4 shows how atomic nitrogen layers can be prepared. The mechanism of ammonia formation, by the stepwise hydrogenation of atomic nitrogen, is the subject of Chapter 5. The adsorption and desorption of ammonia have been studied separately and the results are described in Chapter 6. Chapter 7 deals with the reduction of NO by hydrocarbons, which has been investigated by reactions between NO and ethylene. The formation of cyanides and HCN has been studied in detail in Chapter 8, in which also kinetic parameters for both CN formation and decomposition are presented. Finally, Chapter 9 summarizes the most important results and conclusions of this thesis.

### References:

- [1] A.B. Callear and I.W.M. Smith, *Disc. Faraday Soc.* 37 (1964) 96.
- [2] H.J. Borg, J.F.C.-J.M. Reijerse, R.A. van Santen, and J.W. Niemantsverdriet, *J. Chem. Phys.* 101 (1994) 10052.
- [3] H. Eyring, *J. Chem. Phys.* 3 (1935) 107.
- [4] W.F.K. Wynne-Jones and H. Eyring, *J. Chem. Phys.* 3 (1935) 492.
- [5] M. Polanyi, *J. Chem. Soc.* (1937) 629.
- [6] M.G. Evans and M. Polanyi, *Trans. Faraday Soc.* 31 (1935) 875.
- [7] S. Glasstone, K.J. Laidler, and H. Eyring, *The Theory of Rate Processes*, McGraw-Hill, New York, 1941.

- [8] R.A. van Santen and J.W. Niemantsverdriet, *Chemical Kinetics and Catalysis*, Plenum, New York, 1995.
- [9] O.K. Rice, *Statistical Mechanics, Thermodynamics and Kinetics*, W.H. Freeman, San Francisco, 1967.
- [10] J.W. Niemantsverdriet, *Spectroscopy in catalysis: An introduction*, VCH, Weinheim, 1993.
- [11] F. Rumpf, H. Poppa, and M. Boudart, *Langmuir* 4 (1988) 722.
- [12] J. Nickl, R. Schlögl, A. Baiker, H. Knözinger, and G. Ertl, *Catal. Lett.* 3 (1989) 379.
- [13] E.W. Kuipers, C. Laszlo, and W. Wioldraaijer, *Catal. Lett.* 17 (1993) 71.
- [14] L.M. Eshelman, A.M. de Jong and J.W. Niemantsverdriet, *Catal. Lett.* (1991) 201.
- [15] R.M. van Hardeveld, P.L.J. Gunter, L.J. van IJzendoorn, W. Wioldraaijer, E.W. Kuipers, and J.W. Niemantsverdriet, *Appl. Surf. Sci.* 84 (1995) 339.
- [16] P.L.J. Gunter, J.W. Niemantsverdriet, F.H. Ribeiro, and G.A. Somorjai, *Catal. Rev.-Sci. Eng.* 39 (1997) 77.
- [17] R. van Hardeveld and F. Hartog, *Surf. Sci.* 15 (1969) 189.
- [18] G.A. Somorjai, *Introduction to surface chemistry and catalysis*, Wiley-Interscience, New York, 1994.
- [19] R.A. van Santen, *Theoretical heterogeneous catalysis*, World Scientific, Singapore, 1991.
- [20] K.C. Taylor, *Catal. Rev. -Sci. Eng.* 35 (1993) 457.
- [21] D.A. Hickman and L.D. Schmidt, *Science* 259 (1993) 343.
- [22] M.M. Bhasin and G.L. O' Conner, Belgian Patent 824,822 to Union Carbide Corp., 1975.
- [23] P.C. Ellgen and M.M. Bhasin, U.S. Patent 4,014,913 to Union Carbide Corp., 1977.
- [24] P.C. Ellgen, W.J. Bartley, M.M. Bhasin and T.P. Wilson, *Adv. Chem.* 178 (1979) 147.
- [25] A.G. Makeev, M.M. Slinko, N.M.H. Janssen, P.D. Cobden, and B.E. Nieuwenhuys, *J. Chem. Phys.* 105 (1996) 7210.
- [26] P.D. Cobden, N.M.H. Janssen, Y. van Breugel, and B.E. Nieuwenhuys, *Surf. Sci.* 366 (1996) 3.



## 2 Experimental set-up and techniques

### 2.1 Introduction

Experiments form the backbone of the research in this thesis. In this chapter we give a brief description of the experimental set-ups and techniques we have employed. First we describe the technical set-up of the UHV systems. Next we provide some physical background about the surface spectroscopic techniques we have employed: secondary ion mass spectrometry (SIMS), temperature-programmed desorption or reaction spectroscopy (TPD/TPRS), low energy electron diffraction (LEED), and Auger electron spectroscopy (AES). We most extensively discuss the SIMS technique, which is the major surface analysis tool for the experiments presented in this thesis.

### 2.2 Technical description of the UHV systems

The vast majority of the experiments has been carried out in a stainless steel ultra high vacuum (UHV) system, equipped with facilities for secondary ion and neutral mass spectrometry (SIMS/SNMS), temperature-programmed desorption and reaction spectroscopy (TPD/TPRS), and Auger electron spectroscopy (AES). In principle also ultraviolet photon electron spectroscopy (UPS) and low energy ion scattering (LEIS) can be performed, but these techniques have not been applied in this study.

Figure 2.1 shows a schematic drawing of the UHV system as adapted from my predecessor Borg [1]. The system consists of an analysis chamber for low-pressure reactions and surface analysis, and a preparation chamber for sample cleaning. A high pressure stage (up to 10 atm) is incorporated, but has not been used in any of the experiments. The commercially available spherical analysis chamber (Leybold REZ 12/M) is pumped with a 360  $\ell$ /s turbomolecular pump (Leybold 360 CSV) and a water-cooled 600  $\ell$ /s titanium sublimation pump (Leybold V 150-2). The pressure is measured with an ionization gauge of the extractor type (Leybold IE 514) and is typically around  $1 \times 10^{-10}$  mbar. Gases can be introduced in the analysis chamber by two different leak valves, which allow a precise adjustment of the composition of gas mixtures. Both leak valves are positioned between the analysis chamber and a gas dosing system which can be evacuated up to  $5 \times 10^{-8}$  mbar by a 56  $\ell$ /s turbomolecular drag pump (Baltzers TMH 065).

The analysis chamber is equipped with a Leybold SSM 200 mass spectrometer and a differentially pumped ion gun (Leybold IQE 12/63) for secondary ion and neutral mass spectrometry (SIMS/SNMS). The mass spectrometer is also used for residual gas analysis (RGA) and temperature-programmed desorption and reaction spectroscopy (TPD/TPRS). The SSM 200 module incorporates three functional groups: an ion optics assembly, a Balzers QMG 511 quadrupole mass spectrometer (for the mass range  $m/e=0-511$ ), and ion

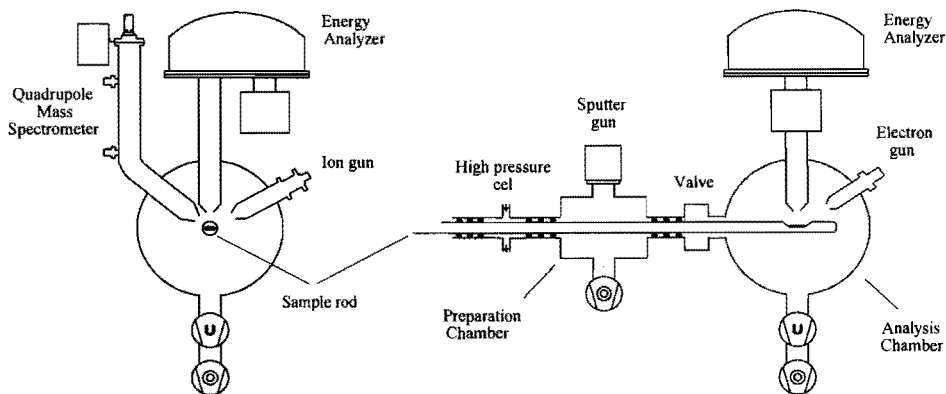


**Figure 2.1** Schematic representation of the UHV system consisting of an analysis chamber, a preparation chamber and a high pressure cell. The analysis chamber is equipped with a quadrupole mass spectrometer, an ion gun, an electron gun, and a hemispherical energy analyzer. The preparation chamber is separated from the main chamber by a valve and is equipped with a sputter gun for sample cleaning.

counting electronics. The ion optics consists of a set of collector lenses, an ionizer (for SNMS, RGA, and TPD), an energy selector comprised of a  $45^\circ$  electrostatic sector, and an exit lens to project the ions onto the aperture of the quadrupole mass spectrometer. In the quadrupole section the actual mass selection takes place: only ions with a certain  $m/e$  ratio are transmitted. These ions are subsequently accelerated and detected by an electron multiplier. The spectral data are acquired with a Leybold data acquisition unit (DAU 865 985); subsequently, they can be sent via an IEEE interface to a PC for analysis and storage. The analysis chamber furthermore contains a Leybold EA 10 hemispherical energy analyzer and a Leybold PS-EQ 22 electron gun, for electron spectroscopy.

The preparation chamber is separated from the analysis chamber by a valve which is closed during sample cleaning and when the preparation chamber is aerated (which is necessary during replacement of the heating wires). Due to this construction excellent pressure conditions can be maintained in the analysis chamber. The preparation chamber was designed and built at the central workshop (CTD) of the TUE. It is pumped with a 150  $\ell/s$  turbomolecular pump (Leybold 150 CSV). The pressure in the preparation chamber is measured with a ionization gauge of the Bayard-Alpert type (Leybold IE 20) and is typically  $10^{-8}$  mbar. This chamber is equipped with a Penning ion gun (Leybold IQP. 10/63) for sputter-cleaning single crystalline samples and a leak valve for gas exposures.

The sample is mounted on a horizontally moveable sample rod, so that it can be transferred rapidly between the two UHV vessels. The sample rod was developed and built at the central workshop (CTD) of the TUE. It consists of a polished stainless steel

tube with an outer diameter of 12 mm, an inner diameter of 8 mm, and a total length of 1250 mm. It enters the UHV system through a gate equipped with a vacuum feedthrough system. The latter is based on a set of differentially pumped Viton™/Teflon™ O-rings, which prevent leakage along the tube and the inner wall of the vacuum chamber, and are kept in place by a set of hollow brass cylinders. The main chamber and the preparation chamber are separated by a similar feedthrough.

The sample is mounted by pressing two tantalum wires of 0.30 mm diameter into small grooves in the edges of the crystal; the tantalum wires are suspended between gold-plated copper contacts at each side of the crystal. The sample can be cooled by flowing liquid nitrogen through copper tubes; sample temperatures of 100 K are routinely obtained; cooling from 1400 to 100 K takes about 6 minutes. The sample is resistively heated by passing currents up to 20 A through the copper tubes and tantalum wires.

The sample temperature is regulated by a thermal control unit which was developed and assembled at the central workshop (CTD). The unit consists of a Eurotherm™ 900 EPC PID controller and a Delta power supply. After tuning of the PID parameters, heating rates up to 10 K/s are constant with deviations smaller than 0.2 K/s while isothermal conditions could be maintained within 0.1 K. We have limited the maximum temperature to 1500 K in order to avoid rapid wearing of the tantalum wires.

Temperatures are measured with a chromel-alumel thermocouple spotwelded to the back of the sample. The thermocouple wires also leave the system through the sample rod, via vacuum feedthroughs of the appropriate thermocouple material. The reference junction is located outside the UHV system. The thermocouple voltage is amplified by an isolation amplifier, digitalized with an analog-to-digital converter, and stored in a personal computer (PC).

The other UHV system comprises a slightly modified version of the RAIRS system as designed and built by De Jong in cooperation with the technical workshop (CTD) [2]. Compared to the old system, which is described in detail in ref. [2], the high-pressure cell (up to 1 bar) has been detached and the sample manipulation system has been changed. Originally, the sample could be detached and transferred from the xyzθ-manipulator in the main chamber to the one in the high-pressure cell, which required breaking/re-establishing both heating and thermocouple contacts. This concept shows limitations when extreme heating and cooling conditions are required (100-1500 K). We have replaced the detachable sample holder by a system with a fixed sample similar to the one described in the previous section. We only used the main chamber of the system which was equipped with a reverse view four grid AES/LEED optics (Spectaleed, Omicron Vakuum physik GmbH) and a Leybold-Heraeus Quadruvac Q100 mass spectrometer for TPD and TPRS. We predominantly used this system for LEED experiments and explorative TPRS studies. The base pressure of the system was typically around  $2 \times 10^{-10}$  mbar.

## 2.3 Secondary ion mass spectrometry

### 2.3.1 The principle of SIMS

The history of SIMS goes back to 1910, when Thomson observed and identified the emission of positive secondary ions when a metal surface was bombarded with high energetic primary ions in a discharge tube [3]. However, it took until the 1960s before SIMS came practically into use. Conceptually, the principle of SIMS seems rather simple. A surface is exposed to a beam of high energetic primary ions (0.5-5 keV). The primary ions penetrate into the substrate and create a number of collision cascades. Part of the collision energy flows back to the surface and stimulates the ejection of atoms and multi-atomic clusters, the majority as neutrals but also as positive and negative ions, see Figure 2.2. Secondary ions can be detected directly with a mass spectrometer, whereas the detection of neutrals requires post-ionization. In the latter case the term SNMS, secondary neutral mass spectrometry is used.

For metallic substrates, the incoming primary ion is neutralized near the surface and when it penetrates into the surface, elastic collisions with nuclei of the substrate form the major source of energy loss. Due to a very efficient process of recombination, the number of lattice defects that remain is limited to  $1 \cdot 10^{-3}$  per incoming primary ion [4]. The ejected atoms and clusters almost exclusively stem from the surface of the substrate and provide information in several ways:

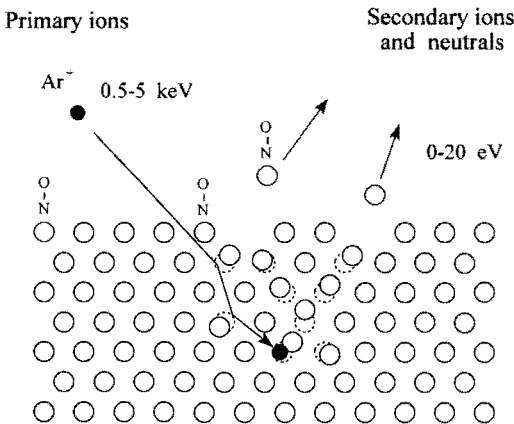


**Figure 2.2** Schematic representation of the SIMS principle. High energetic primary ions penetrate into the surface and cause a collision cascade. Part of the energy flows back to the surface and stimulates the emission neutrals and ions, which are detected with a mass spectrometer.

- *single atoms* give information about the elements that are present at the surface
- *molecular clusters* can indicate the presence of surface compounds
- *characteristic fragmentation patterns* of molecular clusters can sometimes give additional information about the type of compound (e.g.  $\text{MoO}_3$  versus  $\text{MoO}_2$ ).
- in some cases *intensity ratios* between secondary ions can give (semi-) quantitative information about surface coverages.

SIMS can be performed in various modes yielding rather different types of information. In *dynamic* SIMS, a very high flux of primary ions is used which results in the removal of several tens of monolayers per minute. This highly destructive mode is generally used to monitor elemental composition as a function of depth, for instance, to determine the concentration depth profile of a boron implant in a silicon wafer. Thanks to the development of primary ion beams with diameters as small 50 nm [5], SIMS can be used to generate chemical maps of surfaces; this mode is called *imaging* SIMS. In this thesis we apply SIMS in a *static* mode in which very low primary ion fluxes are used (1 nA/cm<sup>2</sup>) and the time to remove a monolayer is in the order of hours. Consequently, the surface structure does not change on the time scale of a measurement (seconds, minutes) and the molecular ion fragments are indicative for the chemical structure of the surface. The surface damage caused by a static SIMS experiment is even smaller than that caused by a standard Auger or XPS measurement. The delicacy of this technique is illustrated by the fact that intact emission of very large molecules, like vitamin B<sub>12</sub> ( $m/e=1356$ ), from metallic substrates has been observed [6].

One of the most complex issues in SIMS is the emission of the secondary ions, which, despite many extensive investigations, is still only partly understood. In the following section we qualitatively discuss the processes that play a decisive role in secondary ion emission.

### 2.3.2 Secondary ion yields

The yield of a positive or negative secondary ion  $I_s(X^\pm)$ , emitted from a matrix  $M$ , is given by [4]:

$$I_s(X^\pm) = I_p \cdot \theta(X) \cdot Y(X, M) \cdot \alpha^\pm(X, M) \cdot \eta(X^\pm) \quad (2.1)$$

with

$I_s(X^\pm)$	measured flux of positive or negative secondary ions $X^\pm$ (in ions/s);
$I_p$	flux of primary ions (in ions/s);
$\theta(X)$	fractional concentration of element $X$ in the surface layer ( $0 < \theta < 1$ );
$Y(X, M)$	sputter yield of element $X$ from matrix $M$ ( <i>i.e.</i> the number of atoms $X$ emitted per incident ion);
$\alpha^\pm(X, M)$	effective (positive or negative) ionization probability of atom $X$ ejected from matrix $M$ ;
$\eta(X^\pm)$	transmission of the mass spectrometer for ion $X^\pm$ , typically $10^{-3}$ for a quadrupole and $10^{-1}$ for a time-of-flight instrument.

In the static mode, the intensity of the secondary ions is linearly proportional to the flux of the primary ions  $I_p$ . However, in order to maintain static conditions the acquisition time has to be significantly smaller than the monolayer life time. For a primary ion flux

of 1 nA/cm<sup>2</sup>, the number of particles that arrive at the surface is  $\sim 6 \times 10^9$  particles/cm<sup>2</sup>. For sensitive adsorbates like polymers, each primary particle can affect an area of 10 nm<sup>2</sup> [4]. In this case it takes about 25 minutes to entirely alter the first surface layer.

The sputter yield,  $Y$ , is defined as the number of secondary atoms that is ejected per incoming primary ion. For pure elements the sputtering of atoms is reasonably well understood [7-9], the sputter yields roughly vary between 1 and 10 across the periodic table. The sputter yield depends on a number of properties of the incident primary ion beam. Generally, the sputter yield increases with increasing *mass of the primary ion*,  $Y_{Xe} > Y_{Ar} > Y_{Ne}$ . The dependence of the sputter yield on the *energy of the primary ion* goes through a maximum. Although the energy that is transferred to the substrate increases with increasing energy of the primary ion, the effectiveness of sputtering decreases at high energies, since the penetration depth increases and fewer collision cascades reach the surface. Also the dependence of the sputter yield on the *angle of incidence of the primary ion* shows an optimum. The penetration depth of the primary ion decreases at more grazing angles; however, also the probability of scattering increases. Consequently, the sputter yield maximizes at around 70° for surfaces where channelling effects do not play a role [10]. Sputtering from multi-element targets is much more complicated and processes like preferential sputtering have been observed [4].

As stated previously, only a small fraction of the secondary particles is ejected in the form of ions. The ionization process which takes place in the near surface region is not well understood and only some general correlations have been determined [4,6]. We discuss some properties of the ionization probability  $\alpha^+$  for positive secondary ions on the basis of the perturbation model of Nørskov and Lundqvist [15] which is illustrated by the following expression:

$$\alpha^+(X, M) \propto e^{\frac{\varphi(M) - I(X)}{v_{\perp}(X)}} \quad (2.2)$$

with

- $\alpha^+(X, M)$  the net positive ionization probability of atom  $X$  emitted from matrix  $M$ ;
- $\varphi(M)$  the work function of matrix  $M$ ;
- $I(X)$  the ionization potential of emitted particle  $X$ ;
- $v_{\perp}(X)$  the velocity component perpendicular to the surface of emitted particle  $X$ .

The ionization probability increases when the ionization potential decreases. Elements, such as, Na, K, Mg are therefore easily detected in positive SIMS in contrast to elements, such as, O, F and Cl. Furthermore, a high work function prevents that secondary ions are neutralized by an electron from the substrate during emission. The probability for neutralization also decreases with shorter residence times of the secondary ion in the surface region. Therefore, a higher normal velocity  $v_{\perp}$  of the secondary ion results in a higher escape probability of the secondary ion. For elements, the ionization

probabilities vary over five orders of magnitude across the periodic table. However, also the chemical environment of the emitted particle plays a decisive role in the ionization process. This so called matrix effect makes the ionization process rather intangible.

A very important issue with respect to the detection efficiency is the energy distribution of the secondary ions. The energy distribution for elemental secondary ions usually has an optimum between 15-30 eV, almost independent of the energy of the primary ions. For cluster ions, the optimum shifts to lower energy and the distribution becomes much narrower. Since quadrupole mass spectrometers also operate with a narrow energy window, typically 10 eV, the setting of the energy window is very critical, especially for the detection of cluster ions. This phenomenon causes serious problems when insulators are analyzed. In this case (inhomogeneous) charging results in shifting and distorting of the energy distribution, which can seriously deteriorate the detection efficiency.

### 2.3.3 Application of SIMS in surface science

For the applications of SIMS in catalysis and surface chemistry we refer the interested reader to an extensive, recently published review by Borg and Niemantsverdriet [11]. We will focus on the use of SIMS in surface science, which can roughly be separated in two different areas: adsorbate characterization and monitoring of surface reactions.

In favourable cases SIMS can give information about; the *coverage*, the *adsorption state* (dissociative or molecular), and the *adsorption site* of an adsorbate. For instance, Zhu and White [12] showed that the  $\text{Ni}_2\text{H}^+/\text{Ni}^+$  intensity ratio varies linearly with the hydrogen coverage on a Ni(100) single crystal surface. Similar correlations have also been observed for CO and NO on various metal surfaces [11]. The adsorption state of molecules, such as, CO and NO can be derived from the nature of the cluster ions appearing in SIMS. Whereas cluster ions like  $\text{PdCO}^+$  and  $\text{Pd}_2\text{CO}^+$  are characteristic for molecularly adsorbed CO,  $\text{PdC}^+$  and  $\text{PdO}^+$  indicate dissociation [13]. Brown and Vickerman [14-16] have shown that the bonding geometry of CO is reflected by the relative intensities of the cluster ions containing one, two or three substrate metal ions,  $\text{MCO}^+$ ,  $\text{M}_2\text{CO}^+$ ,  $\text{M}_3\text{CO}^+$ .

In those cases where quantitative information about surface coverages is obtained, SIMS can be used to determine kinetic parameters for surface reactions. Due to the relatively short sample time scale, typically around 1 s, reactions can be monitored in real time. Borg *et al.* [17] used temperature-programmed SIMS to determine the kinetic parameters for the NO dissociation reaction on Rh(111). Creighton and White [18] showed that SIMS can monitor, in situ, the H-D exchange in ethylidyne ( $=\text{C}-\text{CH}_3$ ) on Pt(111). Furthermore, SIMS can provide information about the intermediates that are present on the surface during reaction which can aid in the elucidation of complex

reaction mechanisms.

Finally, we would like to state that the combination of SIMS and temperature-programmed reaction spectroscopy (TPRS) is extremely powerful for studying complex surface reactions. Whereas (TP)SIMS provides information about reactions that occur on the surface, desorption products are detected in a similar TPRS experiment.

In the following section we briefly discuss the other surface analysis techniques we have employed.

## 2.4 Other surface analysis tools

### 2.4.1 Temperature-programmed reaction spectroscopy

Conceptually, this technique is rather simple. A surface is covered with one or more adsorbates at low temperature, the sample is heated at a constant rate and the desorbing gases are detected with a mass spectrometer. If desorption is the only reaction process that occurs during the temperature ramp, this technique is called temperature-programmed desorption (TPD) or thermal desorption spectroscopy (TDS). TPD has been widely used in order to obtain information on the desorption kinetics of adsorbates from solid surfaces. If the pumping rate of the UHV system is sufficiently high, it can easily be shown that the mass spectrometer signal for a particular desorption product is linearly proportional to the desorption rate of the adsorbate:

$$r_{des} = - \frac{d\theta}{dt} = k_{des} \cdot \theta^n = v_{des}(\theta) \cdot \theta^n \cdot e^{-E_{des}(\theta)/RT} \quad (2.3)$$

with

$r_{des}$	the desorption rate	[1/s]
$\theta$	the fractional adsorbate coverage	[-]
$t$	the time	[s]
$k_{des}$	the rate constant for desorption	[1/s]
$n$	the order of desorption	[-]
$v_{des}$	the pre-exponential factor of desorption	[1/s]
$E_{des}$	the activation energy of desorption	[kJ/mol]
$R$	the gas constant ( $8.314 \times 10^{-3}$ )	[kJ/mol K]
$T$	the temperature	[K]

Various methods have been developed to determine the pre-exponential factor and activation energy for desorption from TPD spectra [19-23]. Some of them just consider the peak maximum temperature [19], others also peak width [23]. Unfortunately, these methods generally only give reliable results in the limit of zero coverage [24].

In temperature-programmed reaction spectroscopy, the desorption rate of a certain



product can also be determined by a preceding surface reaction. In this case the desorption spectrum does not give information about the desorption parameters but about the rate-determining surface reaction. SIMS can often reveal whether the formation of a gaseous product is *desorption* or *reaction limited*.

TPD is also frequently used to determine (relative) surface coverages. The area below a TPD spectrum of a certain product is proportional to the total amount that desorbs. Therefore, only one calibration point is necessary to determine the correlation between TPD area and absolute surface coverage. Once this correlation is known, TPD can be used to determine uptake curves which correlate gas exposure to surface coverage. TPD areas of different products can directly be compared if the mass spectrometer sensitivities are known.

#### 2.4.2 Low-energy electron diffraction

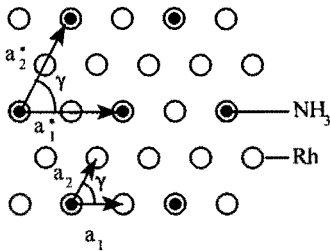
Low-energy electron diffraction (LEED) is a technique which is used to determine the structure of ordered surfaces and adsorbate layers. In principle, it is possible to obtain three-dimensional information and to determine the exact position of adsorbed species [25]. However, in this thesis, we have used LEED only for two purposes; to check the structure of the Rh(111) single crystal surface and to determine ordering of adsorbates. For an extensive description of the technique and all its possibilities, the reader is referred to the textbook of Van Hove and Tong [25].

The LEED technique uses a monochromatic beam of low energetic electrons (50-200 eV), which is aimed at the surface. The electrons, which can be considered as waves, are elastically scattered and will exhibit an interference pattern, which can be visualized by means of a fluorescent screen where places of constructive interference appear as luminous spots. Due to the periodic order of the surface atoms, constructive interference is only observed in directions for which the path length differs by an integral number times the electron wave length. The LEED pattern forms a regular arrangement of spots, representing a two-dimensional lattice with vectors  $\mathbf{b}_1$  and  $\mathbf{b}_2$ . Figure 2.3 shows the correlations that exist between the lattice vectors  $\mathbf{b}_1$  and  $\mathbf{b}_2$ , which construct the LEED pattern, and the vectors  $\mathbf{a}_1$  and  $\mathbf{a}_2$  that represent the two dimensional lattice of surface atoms ( $\mathbf{n}$  represents the surface normal).

In the case that the surface contains an ordered adsorbate layer, the LEED pattern is composed of spots stemming from the substrate and from the adsorbate layer. Figure 2.3 shows the situation where a Rh(111) surface is covered with an ordered  $\text{NH}_3$  adsorbate layer. In many cases, the lattice vectors of the *adsorbate layer* are simply a multiple of the lattice vectors of the substrate.

For the situation sketched in Figure 2.3, the vectors  $\mathbf{a}_1^*$  and  $\mathbf{a}_2^*$  for the  $\text{NH}_3$  adsorbate layer are twice as large as the vectors  $\mathbf{a}_1$  and  $\mathbf{a}_2$  for the Rh(111) surface layer, respectively, which is expressed in the Wood's notation for the adsorbate structure:  $(2 \times 2)\text{-NH}_3$ . Note that there is an inverse correlation between the length of the lattice vectors in

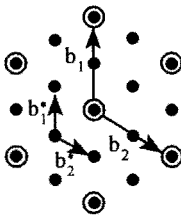
**Lattice:** Rh(111) + (2×2)-NH<sub>3</sub>



$$\vec{b}_1 = \frac{(\vec{a}_1 \times \vec{n})}{(\vec{a}_1 \cdot \vec{a}_2)} \quad \text{with} \quad |\vec{b}_1| = \frac{1}{|\vec{a}_2| \cdot \sin \gamma}$$

and

**LEED:** Rh(111) + (2×2)-NH<sub>3</sub>



$$\vec{b}_2 = \frac{(\vec{a}_2 \times \vec{n})}{(\vec{a}_1 \cdot \vec{a}_2)} \quad \text{with} \quad |\vec{b}_2| = \frac{1}{|\vec{a}_1| \cdot \sin \gamma}$$

**Figure 2.3** Correlation between surface structure of the substrate and adsorbate, and the corresponding LEED pattern illustrated for a Rh(111) surface covered with an ordered NH<sub>3</sub> adsorbate layer.

the adsorbate structure and those in the corresponding LEED pattern. Consequently, the lattice vectors that construct the NH<sub>3</sub> LEED pattern,  $\vec{b}_1^*$  and  $\vec{b}_2^*$ , are half the length of the vectors,  $\vec{b}_1$  and  $\vec{b}_2$ , originating from the Rh(111) substrate.

The LEED pattern only gives information about the periodicities in the adsorbate layer and not about the location of the adsorbates. In Figure 2.3 we have arbitrarily located the NH<sub>3</sub> molecules on top sites.

In some cases, LEED patterns are observed in a rather small coverage window, for which the entire surface is covered with a certain adsorbate structure. If so, the LEED structure can give information about the surface coverage, e.g. a (2×2) structure corresponds to a surface coverage of 0.25 ML (or multiples, in case that the unit cell contains more than one adsorbate).

### 2.4.3 Auger electron spectroscopy

Although Auger electron spectroscopy (AES) provides qualitative and quantitative information about the composition of the surface region of the sample [26,27], we have used AES only in order to check the cleanliness of the rhodium surface. Basis for this

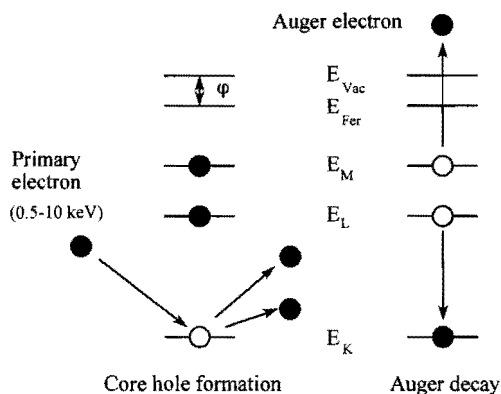


**Figure 2.4** Schematic representation of the Auger process. Irradiation of the surface with primary electrons (or photons) results in the formation of core holes. The core hole is filled by an electron from a higher energy level and the energy released by this transition is used for the emission of the Auger electron.

technique is the Auger process, which is depicted schematically in Figure 2.4.

Irradiation of a sample with primary electrons (0.5-10 keV) or with X-ray photons results in the emission of electrons from the core levels of atoms. The created core hole is filled by an electron from a higher energy level and the energy that is released by this transition is used to emit the Auger electron. The kinetic energy of the Auger electron  $E_{KLM}$  can be approximated by:

$$E_{KLM} = E_K - E_L - E_M - \varepsilon - \varphi \quad (2.4)$$

with

- $E_{KLM}$  the kinetic energy of the Auger electron;
- $E_K$  the binding energy of an electron in the K shell, etc.;
- $\varepsilon$  the energy shift caused by relaxation effects due to the presence of a core hole;
- $\varphi$  the work function of the sample.

Apart from the relaxation effects and the work function of the sample, the kinetic energy of Auger electron is determined solely by the location of the energy levels of the electrons involved in the Auger process (and is thus independent of the energy of the primary electrons or photons). Since the location of the energy levels is element specific, the kinetic energy of the Auger electron provides information about the elements in the surface region. Typical Auger energies are in the range between 0 and 2000 eV. Due to the limited inelastic mean free path of these electrons, the probing depth of Auger is limited to several atom layers only.

**References**

- [1] H.J. Borg, Ph.D. Thesis, Eindhoven University of Technology, 1995.
- [2] A.M. de Jong, Ph.D. Thesis, Eindhoven University of Technology, 1994.
- [3] J.J. Thomson, Phil. Mag. 20 (1910) 252.
- [4] J.C. Vickerman, A. Brown and N.M. Reed, Secondary Ion Mass Spectrometry, Clarendon Press, Oxford, 1989.
- [5] P.D. Prewett and D.K. Jefferies, J. Phys.D: Appl. Phys. 13 (1980) 1747.
- [6] A. Benninghoven, F.G. Rüdener, and H.H. Werner, Secondary Ion Mass Spectrometry, Basic Concepts, Instrumental Aspects, Applications and Trends, Wiley, New York, 1987.
- [7] P. Sigmund, in: *Sputtering by Particle Bombardment I*, ed. R. Behrisch, Topics in Applied Physics, Springer, Berlin, Vol.47, 1981, p.9.
- [8] P. Sigmund, Phys. Rev. 184 (1969) 383.
- [9] N. Matsunami, Y. Yamamura, Y. Itikawa, N. Itoh, Y. Kazumata, S. Miyagawa, K. Morita, R. Shimizu, and H. Tawara, Atomic Data and Nucl. Data Tables 31 (1984) 1.
- [10] H. Oechsner, Z. Physik 261 (1973) 37.
- [11] H.J. Borg and J.W. Niemantsverdriet, in *Catalysis: a Specialist Periodical Report*, Vol 11, Royal Society of Chemistry, Cambridge, 1994, p 1.
- [12] X.-Y. Zhu and J.M. White, J. Phys. Chem. 92 (1988) 3970.
- [13] V. Matolin, M. Rebholz, and N. Kruse, Surf. Sci. 245 (1991) 233.
- [14] A. Brown and J.C. Vickerman, Surf. Sci. 117 (1982) 154.
- [15] A. Brown and J.C. Vickerman, Surf. Sci. 124 (1983) 267.
- [16] A. Brown and J.C. Vickerman, Vacuum 31 (1981) 429.
- [17] H.J. Borg, J.F.C.J.M. Reijerse, R.A. van Santen and J.W. Niemantsverdriet, J.Chem.Phys. 101 (1994) 10052.
- [18] J.R. Creighton and J.M. White, Surf. Sci., 129 (1983) 327.
- [19] P.A. Redhead, Vacuum 12 (1962) 203.
- [20] D.A. King, Surf. Sci. 47 (1975) 384.
- [21] J.L. Falconer and R.J. Madix, J. Catal. 48 (1977) 262.
- [22] E. Habenschaden and J. Küppers, Surf. Sci. 138 (1984) L147.
- [23] C.-M. Chan, R. Aris, and W.H. Weinberg, Appl. Surf. Sci. 1 (1978) 360.
- [24] A.M. de Jong and J.W. Niemantsverdriet, Surf. Sci. 233 (1990) 355.
- [25] M.A. van Hove and S.Y. Tong, *Surface Crystallography by LEED*, Springer, Berlin, 1979.
- [26] G. Ertl and J. Küppers, *Low Energy Electrons and Surface Chemistry*, VCH, Weinheim 1985.
- [27] D. Briggs and M.P. Seah, *Practical Surface Analysis, Vol.1, Auger and Photoelectron Spectroscopy*, Wiley, Chichester, 1990.

## 3 The adsorption and dissociation of NO on Rh(111)

### 3.1 Introduction

For a long time, rhodium has been virtually irreplaceable as constituent in the catalytic automotive exhaust gas converter [1]. Whereas platinum is an excellent catalyst for the oxidation of both CO and hydrocarbons, rhodium is necessary for the selective reduction of NO<sub>x</sub> to N<sub>2</sub>. For this reason, the interaction of NO with both polycrystalline [2] and single crystal rhodium surfaces [3-16] has been studied extensively. It has been well established now that NO adsorbs molecularly on all rhodium surfaces at liquid nitrogen temperatures. Furthermore, the reactivity for NO dissociation strongly depends on the surface structure. This is illustrated, for instance, by the large differences in the temperature at which NO dissociation becomes apparent at the various crystal planes. At low coverages, NO dissociation starts at around 275 K on the close-packed Rh(111) surface [17], at around 200 K on the Rh(110) surface [16], and at around 170 K on the Rh(100) surface [11]. Despite the large number of investigations, the mechanism of NO dissociation is still only partly understood. The dissociation of an NO molecule requires a large ensemble of empty sites which makes the reaction strongly coverage dependent [17]. Another factor which complicates determination of the rate parameters for NO dissociation is the existence of strong lateral interactions between NO and its dissociation products N and O. This has led to detailed studies of the NO and N, and NO and O<sub>2</sub> coadsorption systems on Rh(111) [18,19].

This chapter deals with NO adsorption and dissociation on the Rh(111) surface. The first part of this chapter is devoted to a careful calibration of the NO coverage and the construction of an NO uptake curve. NO coverage calibration is a prerequisite for the quantitative preparation of atomic nitrogen as described in Chapter 4 and the reactivity studies between NO and ethylene as described in Chapter 7. The second part of this chapter describes the results obtained from isothermal NO adsorption experiments between 150 and 600 K. We have employed SIMS and TPD to determine the composition of the adsorption layer obtained after saturating the Rh(111) surface with NO at various constant temperatures. The isothermal NO adsorption process has been modeled using a Monte-Carlo based simulation program. Comparison between the experimental results and the simulations has given detailed information about the important role that surface diffusion and lateral interactions play in processes, such as, surface ordering and dissociation. Usually, kinetic parameters for the NO dissociation reaction are derived from temperature-programmed experiments. The strong temperature dependence of the kinetic parameters for the NO dissociation reaction implies that these parameters change during the experiment. Working isothermally during NO adsorption has the advantage that the temperature dependence of the NO dissociation reaction for a particular experiment is ruled out and that only coverage dependent effects have to be considered.

## 3.2 Experimental

TPD, SIMS and work function experiments were performed in a stainless steel ultra high vacuum (UHV) system, pumped with a 360 l/s turbomolecular pump and a water-cooled titanium sublimation pump. The base pressure was typically around  $5 \cdot 10^{-11}$  mbar, and mass spectra of the residual gas indicated the presence of mainly  $H_2$ , CO and  $CO_2$ . The system is equipped with a Leybold SSM 200 quadrupole mass spectrometer for TPD and SIMS, and a Leybold EA 10 hemispherical energy analyzer for AES and  $\Delta\phi$  measurements. Both analyzers were interfaced with a PC for data storage.

SIMS measurements were performed in the static (low damage) mode. Typically, we used a defocused 5 keV primary  $Ar^+$  beam with a current density of 1-10 nA/cm<sup>2</sup>. To average possible anisotropies in the secondary ion emission process we applied a target bias of +45 V and an extractor voltage of -300 V on the entrance lens of the quadrupole system.

LEED experiments were performed in a different UHV system equipped with a Leybold Quadrupac Q100 mass spectrometer and a reverse view, four grid AES/LEED optics (Spectaleed, Omicron Vakuumphysik GmbH). LEED data were obtained with an electron beam current between 20 and 30  $\mu$ A.

Each UHV system contained a rhodium crystal which was cut in the [111] orientation within  $0.5^\circ$  and polished by standard procedures. The temperature was measured by a chromel-alumel thermocouple spotwelded on the back of the crystal. The standard cleaning procedure consisted of an argon sputter treatment (900 K, 1.5 keV,  $5 \mu$ A/cm<sup>2</sup>) followed by annealing in  $2 \cdot 10^{-8}$  mbar  $O_2$  (900 K-1100 K) and a final annealing treatment in vacuum at 1420 K. NO (Messer Griesheim, 99.5%) was used without further treatment. Exposures are reported in Langmuirs (1L =  $1.33 \times 10^{-6}$  mbar.s) and coverages are expressed with respect to the number of Rh surface atoms (1 ML =  $1.6 \times 10^{15}$  cm<sup>-2</sup>).

## 3.3 Experimental results

### 3.3.1 Low-temperature adsorption of NO on Rh(111)

Figure 3.1 shows temperature-programmed desorption spectra of  $N_2$  (28 amu, left panel) and NO (30 amu, right panel), obtained after exposing the Rh(111) crystal to various amounts of NO at 120 K and heating at 10 K/s. At exposures below  $\sim 0.4$  L all NO dissociates upon heating, as is evidenced by the absence of molecular NO desorption. Only  $N_2$  and  $O_2$  desorption is observed.  $O_2$  desorption spectra are not shown, since the heating rate was not linear over the entire  $O_2$  desorption regime (900-1400 K). We also monitored for  $N_2O$  (44 amu), but this product was not observed in any of the experiments. At NO exposures above 0.4 L an increasing amount of the adsorbed NO desorbs molecularly in a narrow desorption state, denoted  $\alpha_2$ -NO, with a peak maximum at 430 K. Together with the appearance of molecular NO desorption, a second  $N_2$  desorption

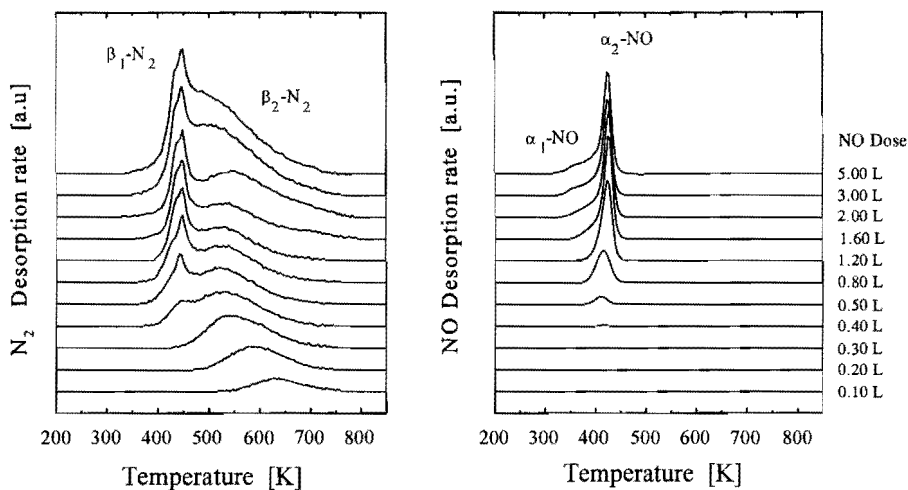


**Figure 3.1** Temperature-programmed desorption spectra for  $N_2$  ( $m/e = 28$ , left panel) and  $NO$  ( $m/e = 30$ , right panel) obtained after exposing a  $Rh(111)$  crystal to various amounts of  $NO$  at 120 K and heating at 10 K/s.

state, denoted  $\beta_1-N_2$ , is observed which shows pseudo first order desorption behaviour. At low coverage, all nitrogen desorbs in a regular second-order  $N_2$  desorption state, denoted  $\beta_2-N_2$ , of which the maximum shifts from 640 K to 525 K with increasing coverage. At  $NO$  exposures above  $\sim 1.6$  L a second  $NO$  desorption state, denoted  $\alpha_1-NO$ , is observed as a broad low temperature shoulder of the  $\alpha_2-NO$  desorption state. In the discussion section we will further dwell on the nature and origin of the various desorption states. For the moment, we will just use the desorption data for the calibration of the  $NO$  surface coverage versus  $NO$  exposure.

The amount of adsorbed  $NO$  is proportional to the weighted sum of the TPD areas of the  $N$  containing products, which are  $N_2$  and  $NO$  in our case. Since one  $N_2$  molecule stems from two dissociated  $NO$  molecules, the  $N_2$  TPD area is multiplied by 2. In order to correct for differences in ionization probability of  $NO$  and  $N_2$  ( $S_{NO}/S_{N_2} = 1.2$ ), the  $NO$  peak area was divided by 1.2. The link between the sum of the TPD areas and the actual  $NO$  coverage requires at least one calibration point, which can be a saturation coverage or a well defined coverage corresponding to an ordered structure observable by LEED. As calibration point, we have used the  $NO$  saturation coverage of 0.68 ML as reported by Root *et al.* [4] for adsorption at 120 K. This was preferred above calibration based on  $NO$  LEED patterns, which were observable in a rather broad coverage regime.

Figure 3.2 shows the  $NO$  coverage as a function of the  $NO$  exposure at 120 K as derived from the  $NO$  and  $N_2$  TPD areas according to the above described procedure. The solid line in Figure 3.2 represents a fit of the  $NO$  uptake curve based on the Langmuir adsorption model. This model assumes that the probability for adsorption on an occupied

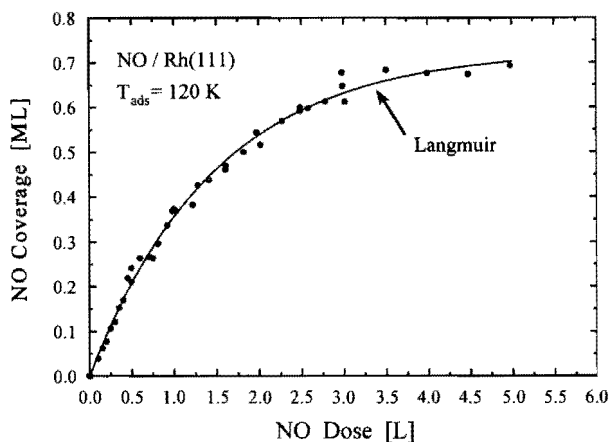


**Figure 3.2** NO coverage (ML) as a function of NO exposure (L) for adsorption at 120 K on a Rh(111) single crystal. The solid line represents a fit based on the Langmuir adsorption model.

site is zero, whereas it is equal to the initial sticking coefficient  $S_0$  (i.e. the sticking probability for a molecule on an empty surface) on an empty site:

$$S(\Theta) = S_0 (1 - \Theta / \Theta_{NO,sat}) \quad (3.1)$$

Figure 3.2 shows that the NO adsorption behaviour can well be described by the Langmuir adsorption model. Contrary to Borg *et al.* [17] we have no evidence for the existence of a mobile precursor state for adsorption. We will tackle this phenomenon in the discussion section.

In the literature two ordered adsorbate structures are reported for NO adsorption on Rh(111) at low temperatures. Kao *et al.* [8] observed a LEED pattern corresponding to a  $c(4 \times 2)$ -2NO structure at a coverage of 0.50 ML at 120 K. The other ordered structure, a  $(2 \times 2)$ -3NO structure, corresponding to an NO coverage of 0.75 ML, could only be obtained if NO was adsorbed at 250 K [8].

Figure 3.3 shows the LEED patterns which we obtained, corresponding to a  $c(4 \times 2)$ -2NO ordered structure (left panel) and a  $(2 \times 2)$ -3NO ordered structure (right panel) obtained by dosing  $\sim 1.8$  L NO at 120 K and 5.00 L NO at 225 K, respectively. The LEED pattern corresponding to the  $c(4 \times 2)$ -NO was observed in a rather broad exposure regime,  $1.8 \pm 0.2$  L, and could therefore not act as a reliable calibration point for the NO uptake curve. The  $(2 \times 2)$  LEED pattern could only be observed when the Rh(111) surface was saturated at more elevated temperatures, viz. at  $\sim 225$  K.

On Ni(111) a similar  $c(4 \times 2)$ -2NO structure has been observed by various authors [20-23]. This structure has thoroughly been studied since it has become clear that former NO adsorption site assignments, based on vibrational frequencies, were erroneous. On Ni(111), Surface Extended X-ray Adsorption Fine-Structure (SEXAFS) [20],



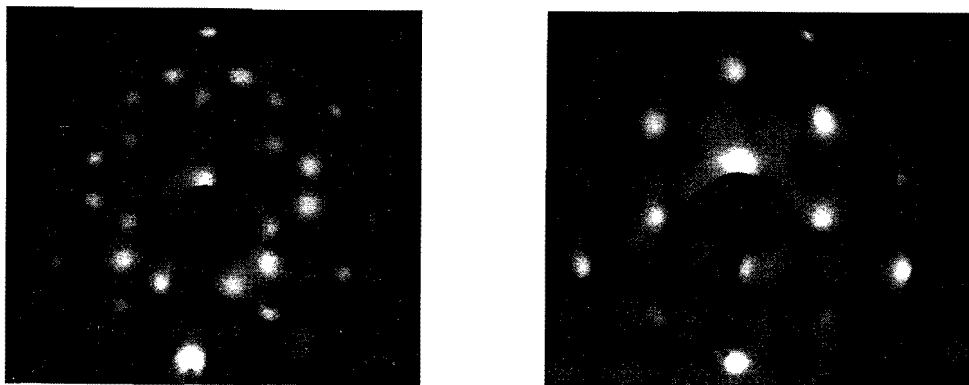


**Figure 3.3** The left panel shows a  $c(4 \times 2)$  LEED pattern observed after dosing  $\sim 1.8$  L NO at 120 K. The right panel shows a  $(2 \times 2)$  LEED pattern observed after dosing 5.00 L NO at 225 K.

Photoelectron Diffraction (PD) [21] and dynamical LEED [22,23] studies all indicate that NO adsorbs at threefold hollow sites over the entire coverage regime. The  $c(4 \times 2)$ -2NO structure has been found to contain two distinct NO molecules, which are distributed over both fcc and hcp threefold sites (an hcp site contains a second layer rhodium atom directly underneath, an fcc site does not).

Figure 3.4 shows a schematic representation of the  $c(4 \times 2)$ -2NO adsorbate structure in which one of the NO molecules occupies an fcc site and the other an hcp site. Both the  $c(4 \times 2)$  unit cell, which contains 4 NO molecules, and the associated primitive unit cell, which contains two NO molecules, are indicated. If both hcp and fcc sites are occupied the ordered structure contains a "pseudo" glide-line which is indicated by the horizontal line in Figure 3.4. The term glide-line refers to a combined symmetry operation which consists of a translation and a reflection. Figure 3.4 shows that an fcc NO adsorption site transforms into an hcp NO adsorption site by translation over one unit vector along the horizontal axis followed by a reflection in the plane through the glide-line and the surface normal. The term "pseudo" glide-line is used, since the symmetry operation transforms an fcc site into an hcp site. On the surface layer, fcc and hcp sites are equal, but when the second layer is considered too, the fcc and hcp sites can be distinguished.

Figure 3.4 also indicates the situation where both NO molecules are adsorbed at the same threefold site (this can either be an fcc site or an hcp site). In this case the second NO molecule in the centre of the primitive unit cell occupies a different position which is indicated by a grey circle. If this were the correct structure, a "real" glide-line would be present as indicated by the vertical dashed line in Figure 3.4.

The existence of symmetry within the unit cell has important implications for the observed LEED patterns, since particular spots may be absent due to extinction.

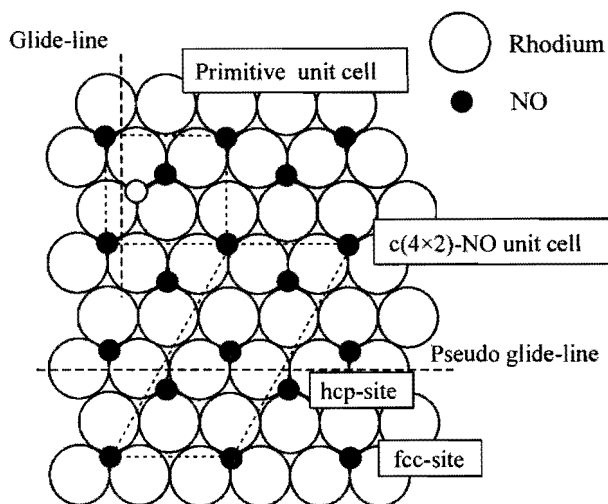


**Figure 3.4** Schematic representation of the  $c(4 \times 2)$ -2NO structure in the case that one of the NO molecules occupies an fcc site and the other an hcp site. The grey solid circle indicates the situation when both NO molecules occupy fcc sites.

Consequently these, so called, "missing spots" can provide valuable information about symmetry within the unit cell.

Figure 3.5 shows the LEED patterns that are calculated for the NO adsorbate structures as indicated in Figure 3.4. Note that ordered structures on the Rh(111) surface are present in three different domains, which transform into each other by rotation over  $120$  or  $240^\circ$ . The unit vectors associated with one domain are indicated with arrows in Figure 3.5. The left panel of Figure 3.5 shows the LEED pattern which is expected for the  $c(4 \times 2)$ -2NO structure, where one NO molecule occupies an fcc site and the other an hcp site. In consequence of the presence of the pseudo glide-line, some of the spots are not observed at low beam energies (these spots are marked by open circles). At higher electron energies, where multiple scattering becomes more important, the fcc and hcp site become distinct, the symmetry disappears, and the spots become visible. The right panel of Figure 3.5 shows the LEED pattern which is expected for the  $c(4 \times 2)$ -2NO structure in which both NO molecules occupy identical threefold sites resulting in a true glide line (the vertical line in Figure 3.4). In this case the family of  $(\frac{1}{2}, \frac{1}{2})$  spots is missing, also at higher beam energies.

The observed  $c(4 \times 2)$ -2NO LEED pattern, see Figure 3.3, is identical to the LEED pattern that is expected for the adsorbate layer shown in Figure 3.4 with one NO molecule at an fcc and the other at an hcp site. Unfortunately, LEED provides no information about the adsorption site itself. However, if we draw the analogy with Pt(111) and Ni(111), NO adsorption in threefold sites seems the most probable hypothesis. We therefore conclude that NO orders into a  $c(4 \times 2)$ -2NO structure in which one half of the NO molecules occupies fcc and the other half hcp sites upon adsorption of 0.50 ML of NO at 120 K.

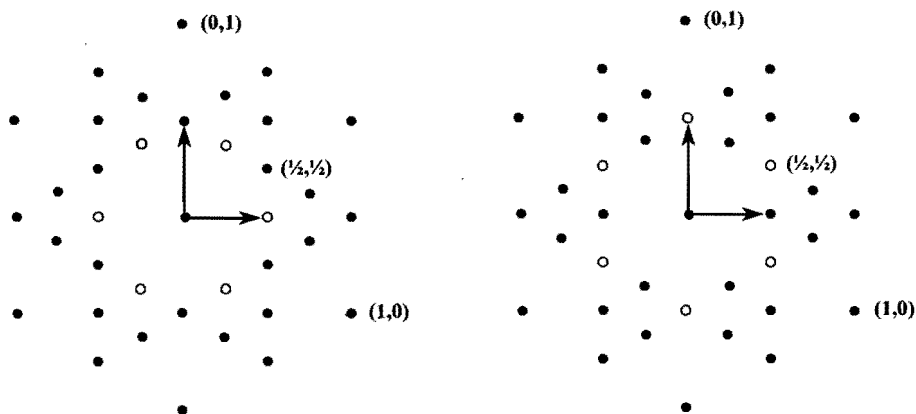


**Figure 3.5** The left panel shows the calculated LEED pattern for the  $c(4 \times 2)$ -2NO adsorbate structure on Rh(111) in the case that one NO molecule occupies an hcp and the other an fcc site (conform the situation sketched in Figure 3.4). The open dots are not observed in single scattering. The right panel shows the calculated LEED pattern for the situation that the two NO molecules occupy the same threefold adsorption site either fcc or hcp. In this case the open circles are missing spots which do not appear at higher energies.

### 3.3.2 Adsorption of NO at various temperatures on Rh(111)

In order to obtain additional information about the NO dissociation process, we have adsorbed NO at various constant temperatures between 150 and 600 K. We have applied identical adsorption conditions in all the experiments; *i.e.* the NO pressure being  $2 \cdot 10^{-8}$  mbar and the NO dose 5.0 L. At 120 K, exposure of 5.0 L NO yields an NO saturated surface. Whereas the NO adsorption rate is expected to be only slightly temperature dependent, the NO dissociation is strongly activated and therefore the rate of dissociation depends very much on the substrate temperature. As long as desorption is not relevant, the composition of the adsorbate layer is mainly determined by the ratio between the rates of adsorption and dissociation. Despite the constant temperature, the NO dissociation rate is not expected to be constant during the entire adsorption experiment. Since NO dissociation requires an ensemble of empty sites, the dissociation rate is expected to be lowered by adsorbed products in the progress of the adsorption experiment. However, at the start of the adsorption all adsorbing molecules experience an empty surface and in this regime the ratio between the adsorption rate and

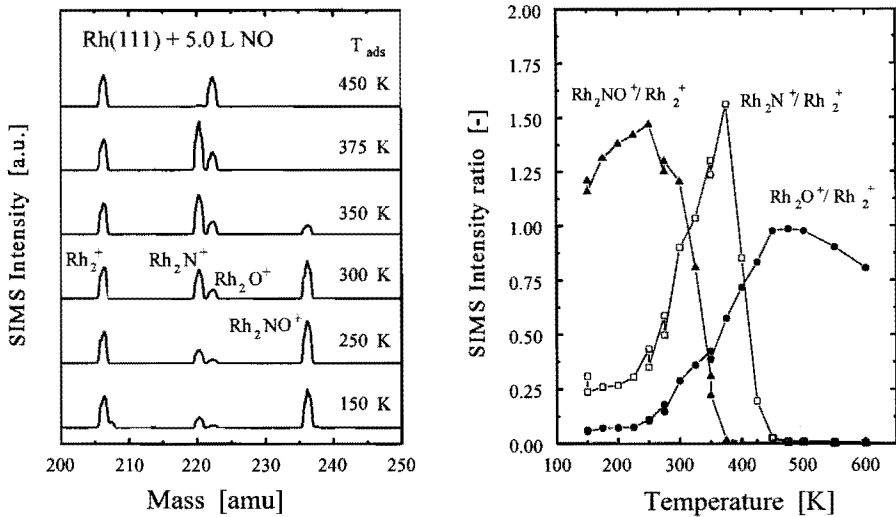


**Figure 3.6** Left panel, SIMS spectra of the Rh(111) surface after dosing 5.0 L NO at the indicated temperatures, the NO pressure was  $2 \cdot 10^{-8}$  mbar. Right panel,  $Rh_2NO^+/Rh_2^+$ ,  $Rh_2N^+/Rh_2^+$ , and  $Rh_2O^+/Rh_2^+$  SIMS intensity ratios as a function of the adsorption temperature.

the dissociation rate is governed merely by the substrate temperature. We have used SIMS to examine the composition of Rh(111) surface after dosing 5.0 L NO at various temperatures.

The left panel of Figure 3.6 shows SIMS spectra of the Rh(111) surface after dosing 5.0 L NO at the indicated temperatures. At 150 K, molecular NO is the only adsorbate, which is evidenced by the  $Rh_2NO^+$  cluster ion ( $m/e = 236$ ) in the SIMS spectra. However, a constant fraction of the  $Rh_2NO^+$  cluster ions fragments into  $Rh_2N^+$  and  $Rh_2O^+$  cluster ions during emission, which explains the small peaks at  $m/e = 220$  and  $222$ , respectively. At 300 K a fraction of the NO has dissociated upon adsorption as is evidenced by the increasing intensity of the  $Rh_2N^+$  and  $Rh_2O^+$  peaks, representative for the presence of atomic nitrogen and oxygen, respectively. At 375 K, the absence of the  $Rh_2NO^+$  cluster ion indicates that molecular NO is no longer present on the surface. Now, atomic nitrogen and oxygen are the only adsorbates. At 450 K, the  $Rh_2N^+$  peak has almost completely disappeared whereas the  $Rh_2O^+$  peak has increased. The translation of SIMS intensities into surface coverages is more precise if appropriate intensity ratios, such as  $Rh_2NO^+/Rh_2^+$ , are used instead of absolute SIMS intensities. In this way, work function effects are ruled out and good correlations with the surface coverage are often obtained [24,25]. The right panel of Figure 3.6 shows the  $Rh_2NO^+/Rh_2^+$ ,  $Rh_2N^+/Rh_2^+$  and  $Rh_2O^+/Rh_2^+$  SIMS intensity ratios as a function of the adsorption temperature. If we take the  $Rh_2NO^+/Rh_2^+$  SIMS intensity ratio as a measure for the NO coverage, Figure 3.6 indicates that the NO coverage increases when the adsorption temperature is increased

from 150 to 225 K.

NO dissociation is negligible at temperatures up to 225 K. However, the fact that the  $\text{Rh}_2\text{N}^+/\text{Rh}_2^+$  and  $\text{Rh}_2\text{O}^+/\text{Rh}_2^+$  SIMS intensity ratios are non zero at this temperature and below is due to fragmentation of the  $\text{Rh}_2\text{NO}^+$  cluster ion. From 250 to 375 K, a parallel increase of the  $\text{Rh}_2\text{N}^+/\text{Rh}_2^+$  and  $\text{Rh}_2\text{O}^+/\text{Rh}_2^+$  SIMS intensity ratios is observed, whereas the  $\text{Rh}_2\text{NO}^+/\text{Rh}_2^+$  SIMS intensity ratio drops to zero. In this temperature range, NO dissociation becomes more and more important and the surface becomes increasingly covered by atomic nitrogen and oxygen at the expense of molecular NO.

From 375 to 450 K, the  $\text{Rh}_2\text{N}^+/\text{Rh}_2^+$  intensity ratio decreases very rapidly indicating a fast decrease of the atomic nitrogen coverage, probably due to  $\text{N}_2$  desorption. In this temperature range, the  $\text{Rh}_2\text{O}^+/\text{Rh}_2^+$  intensity ratio continues to rise. Apparently, the vacancies created by  $\text{N}_2$  desorption are filled up by atomic oxygen. From 450 K to 500 K, the  $\text{Rh}_2\text{O}^+/\text{Rh}_2^+$  intensity ratio remains constant, indicating a constant oxygen coverage. The decrease of the  $\text{Rh}_2\text{O}^+/\text{Rh}_2^+$  intensity ratio might indicate the migration of atomic oxygen into the bulk.

Additional information about the composition of the adsorbate layer that is created by dosing 5.0 L NO at a given temperature can be obtained by carrying out a temperature-programmed desorption experiment. For adsorbate layers which only contain atomic nitrogen and oxygen, the areas of the  $\text{N}_2$  and  $\text{O}_2$  desorption peaks are linearly proportional to the atomic nitrogen and oxygen coverages, respectively. When the adsorbate layer contains molecular NO, the situation is more complex, since NO can dissociate during the TPD experiment and the  $\text{N}_2$  peak area is not unequivocally related to the atomic nitrogen coverage in the adsorbate layer. However, the TPD areas then also provide information about the total amounts of oxygen and nitrogen present in the adsorbate layer.

Figure 3.7 shows temperature-programmed desorption spectra of  $\text{N}_2$  (28 amu, right panel) and NO (30 amu, left panel), obtained after dosing 5.0 L NO to the Rh(111) crystal at the indicated temperatures. The heating rate was 10 K/s.  $\text{O}_2$  desorption spectra are not shown, since the heating rate was not linear over the entire  $\text{O}_2$  desorption range. The NO and  $\text{N}_2$  TPD spectra that are obtained after dosing 5.0 L NO at 150 K are similar to spectra shown in Figure 3.1 for a Rh(111) surface saturated with NO at 120 K. The NO desorption spectrum shows both the  $\alpha_1$ -NO and  $\alpha_2$ -NO desorption states, which have been associated with NO in bridge- and threefold sites, respectively [17]. The  $\text{N}_2$  desorption spectrum shows the  $\beta_1$ - $\text{N}_2$  and  $\beta_2$ - $\text{N}_2$  desorption states, which are associated with the recombination of atomic nitrogen atoms [17,26]. Increasing the adsorption temperature from 150 K to 375 K, see Figure 3.7, results in a significant change of the NO desorption spectra. At increasing temperatures the  $\alpha_1$ -NO desorption state becomes more significant and the  $\alpha_2$ -NO desorption state slightly shifts to lower temperature. Above 250 K the amount of NO that desorbs, starts to decrease and above 375 K no NO desorption is observed, because obviously all NO dissociates. The most conspicuous change in the  $\text{N}_2$  desorption spectra for NO adsorption between 150 and 325 K is the appearance of a small  $\text{N}_2$  desorption state at the low temperature site of the  $\beta_1$ -state, at

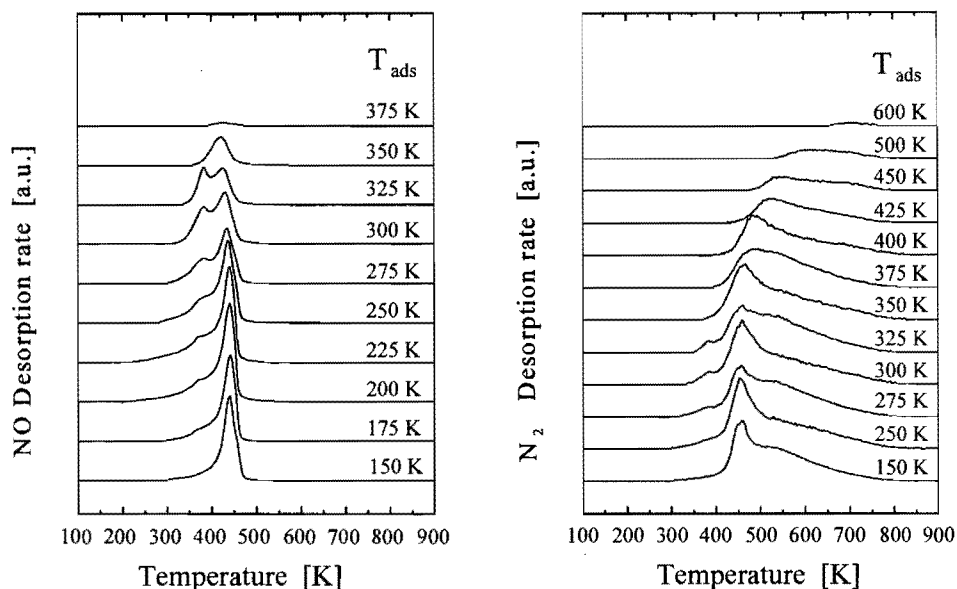


**Figure 3.7** Temperature-programmed desorption spectra of  $N_2$  (28 amu, right panel) and NO (30 amu, left panel) obtained by dosing 5.0 L of NO to Rh(111) at the indicated temperatures. The heating rate was 10 K/s.

about 380 K. For adsorption temperatures above 350 K the amount of  $N_2$  desorbing starts to decrease and for adsorption temperatures above 600 K no  $N_2$  desorption is observed anymore.

Figure 3.8 shows the total  $N_2$ , NO, and  $O_2$  TPD peak areas obtained from experiments after dosing 5.0 L NO at various temperatures. Up to 350 K the  $N_2$  and  $O_2$  TPD peak areas remain constant, which indicates that the amount of NO that dissociates remains constant. For the amount of NO that dissociates it apparently does not matter whether NO dissociation occurs entirely during the TPD experiment, as with adsorption at 150 K, or predominantly during adsorption, as with adsorption at 350 K. The amount of NO that desorbs increases in the temperature range from 150 to 225 K, above which it gradually decreases to zero for adsorption temperatures above 375 K. Since the amount of NO that dissociates remains constant, the increase of the NO desorption area from 150 to 225 K indicates an increase of the NO coverage. The decrease of the NO TPD area between 225 and 375 K shows that the total amount of NO that can be adsorbed decreases. This is due to an increase of NO dissociation. Up to 350 K the ratio between the  $N_2$  and  $O_2$  TPD areas is constant, which indicates that no  $N_2$  desorption occurs during the NO adsorption experiment. Above 350 K the  $N_2$  TPD area decreases, whereas the  $O_2$  TPD area increases. This indicates that part of the atomic nitrogen already desorbs as  $N_2$  during the adsorption experiment. Apparently, the vacancies that are created by desorption of  $N_2$  are used to dissociate some additional NO molecules which results in a

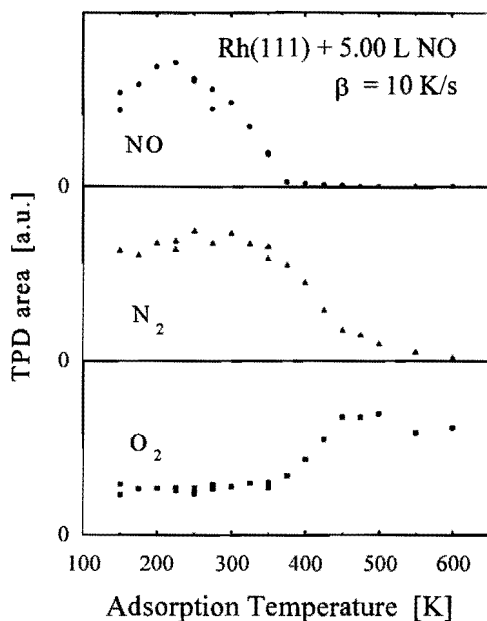


**Figure 3.8** Total N<sub>2</sub>, O<sub>2</sub> and NO TPD peak areas as determined from a TPD experiment after dosing 5.0 L NO at various adsorption temperatures. The heating rate was 10 K/s.

relative increase of the atomic oxygen coverage.

We have combined the information obtained from the SIMS and TPD experiments to determine the composition of the adsorbate layer obtained after NO adsorption at various temperatures. In the temperature regime between 150 and 225 K the SIMS results indicate that molecular NO is the only adsorbate. In this case the NO coverage has been determined from the NO and N<sub>2</sub> TPD areas using the uptake curve shown in Figure 3.2. The SIMS results indicate that at temperatures above 350 K molecular NO is not present anymore. In this case the atomic nitrogen and oxygen coverages have been determined from the N<sub>2</sub> and O<sub>2</sub> TPD areas. Between 225 and 350 K we have determined the atomic oxygen coverage by assuming a linear relation between  $\Theta_{\text{O}}$  and the Rh<sub>2</sub>O<sup>+</sup>/Rh<sub>2</sub><sup>+</sup> SIMS intensity ratio. This linear relation was confirmed for temperatures between 375 and 600 K. Since N<sub>2</sub> desorption is negligible below 350 K, the atomic nitrogen coverage equals the atomic oxygen coverage. The total amount of NO that has been adsorbed can be derived from the NO, N<sub>2</sub> and O<sub>2</sub> TPD areas. The molecular NO coverage is calculated by subtracting the atomic nitrogen coverage from the total amount of adsorbed NO molecules.

Figure 3.9 shows the coverages of N, O, and NO as a function of the NO adsorption temperature obtained by dosing 5.0 L NO at Rh(111). Figure 3.9 also shows the sum of the adsorbate coverages, indicated by  $\Theta_{\text{Total}}$ . Note that for adsorption temperatures between 375 and 550 K the sum of the adsorbate coverages is significantly larger than 1 ML (~1.3 ML), which might indicate the presence of subsurface N and O.

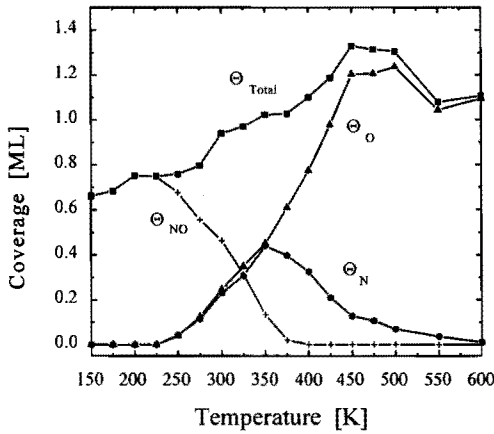


**Figure 3.9** Coverages of N, O, and NO [ML] as a function of the NO adsorption temperature obtained by dosing 5.0 L NO at Rh(111).

In order to get some insight in the development of the surface coverages of N, O and NO during the NO adsorption experiment, we have applied SIMS *in-situ*, *i.e.* during the adsorption process. Figure 3.10 shows the development of the  $\text{Rh}_2\text{NO}^+/\text{Rh}_2^+$ ,  $\text{Rh}_2\text{N}^+/\text{Rh}_2^+$ , and  $\text{Rh}_2\text{O}^+/\text{Rh}_2^+$  SIMS intensity ratios as a function of time when a Rh(111) crystal is exposed to  $2.10^{-8}$  mbar NO at 150, 300 and 450 K, respectively. At 150 K, NO adsorbs exclusively molecularly as is illustrated by the left panel of Figure 3.10. The non-zero intensities of the  $\text{Rh}_2\text{N}^+/\text{Rh}_2^+$  and  $\text{Rh}_2\text{O}^+/\text{Rh}_2^+$  SIMS intensity ratios are due to fragmentation of the  $\text{Rh}_2\text{NO}^+$  cluster ion. At 300 K, the  $\text{Rh}_2\text{N}^+/\text{Rh}_2^+$  and  $\text{Rh}_2\text{O}^+/\text{Rh}_2^+$  SIMS intensity ratios rise before the  $\text{Rh}_2\text{NO}^+/\text{Rh}_2^+$  SIMS intensity ratio increases. This indicates that, initially, NO dissociation is fast as compared to the NO adsorption rate resulting in a small molecular NO coverage. The increasing adsorbate coverage leads to a decrease of the NO dissociation rate, which results in an increase of the molecular NO coverage. After about 50 seconds, the  $\text{Rh}_2\text{N}^+/\text{Rh}_2^+$  and  $\text{Rh}_2\text{O}^+/\text{Rh}_2^+$  SIMS intensity ratios become constant, indicating that the NO dissociation rate has dropped to zero and that the surface is filled up with molecular NO. At 450 K, the NO dissociation is so fast that molecular NO can not be observed on the surface. Initially both atomic nitrogen and oxygen build up on the surface, as indicated by the simultaneous increase of the  $\text{Rh}_2\text{N}^+/\text{Rh}_2^+$  and  $\text{Rh}_2\text{O}^+/\text{Rh}_2^+$  SIMS intensity ratios. However, after some time (at about 65 seconds in Figure 3.10) the  $\text{Rh}_2\text{N}^+/\text{Rh}_2^+$  SIMS intensity ratio starts to drop, indicating that  $\text{N}_2$  desorbs. Being a second-order reaction, the rate of  $\text{N}_2$  desorption increases with coverage proportionally to  $\Theta_{\text{N}}^2$ , while repulsive interactions with atomic oxygen enhance the desorption rate even further. The decrease in the atomic nitrogen coverage is accompanied by an increase of the atomic oxygen coverage. Note that the O-signal continues to rise at the same rate as initially on the bare surface, implying that the NO dissociation rate remains constant. Despite the fact that the N-production rate (equal to the NO dissociation rate) remains constant, the N-coverage decreases. This implies that the  $\text{N}_2$  desorption rate is accelerated with increasing O coverage. After approximately 125 seconds the  $\text{Rh}_2\text{N}^+/\text{Rh}_2^+$  intensity ratio becomes constant, and the dissociation rate decreases,



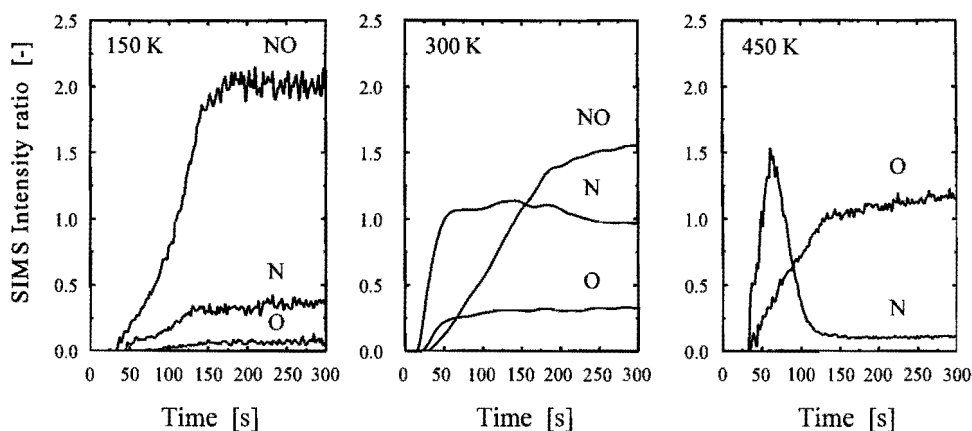


**Figure 3.10** Development of the  $Rh_2NO^+/Rh_2^+$ ,  $Rh_2N^+/Rh_2^+$ , and  $Rh_2O^+/Rh_2^+$  SIMS intensity ratios (indicated by NO, N and O respectively) as a function of time when a Rh(111) crystal is exposed to  $2.10^{-8}$  mbar NO at 150, 300 and 450 K.

indicative of a steady state with respect to N-atoms, which may last until the surface becomes fully saturated.

### 3.3.3 Coverage dependence of the NO dissociation reaction

Previous investigations have shown that the NO dissociation depends very much on the coverage [17]. In this paragraph we describe the coverage dependence of the NO dissociation based on the TPD results measured on the Rh(111) surface covered with various amounts of NO at 120 K.

Figure 3.11 shows the distribution of N between the desorption products  $N_2$  and NO in TPD experiments, as a function of the initial NO coverage at 120 K. Up to an NO coverage of  $\sim 0.20$  ML, all NO molecules dissociate upon heating and  $N_2$  is the only N-containing desorption product. For NO coverages between 0.20 and 0.45 ML, the absolute amount of NO that dissociates remains constant, whereas the amount of NO that desorbs molecularly increases linearly with increasing NO coverage. For NO coverages above 0.45 ML, the amount of NO that dissociates starts to increase again, whereas the amount of NO that desorbs molecularly remains constant. At the NO saturation coverage,  $\Theta_{NO}=0.68$  ML, approximately 1/3 of the initially adsorbed NO desorbs molecularly and 2/3 dissociates and desorbs as  $N_2$ . These numbers are in excellent agreement with those reported by Borg *et al.* [17], but are slightly different from those reported by Root *et al.* [4], who found dissociation percentages of 65% and 55% at saturation, respectively. Borg *et al.* [17] observed that all NO dissociates at coverages below 0.25 ML, after which both the amount of NO desorbing as NO and that desorbing as  $N_2$  rise linearly at increasing

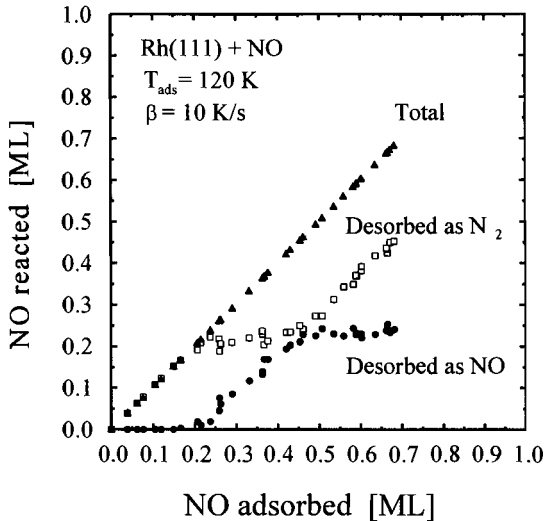


**Figure 3.11** Distribution of N from NO molecules adsorbed at 120 K between the desorption products  $N_2$  and NO in a TPD experiment as a function of the initial NO coverage. The heating rate was 10 K/s.

NO coverage up to saturation. The plateau for the desorbing  $N_2$  between 0.20 and 0.45 ML was not observed by Borg *et al.* [17].

### 3.4 Mathematical modeling of NO adsorption at various temperatures

#### 3.4.1 Introduction

In order to tackle some questions raised by the experimental results described in section 3.3, we have simulated the NO adsorption process at various temperatures, using an advanced Monte Carlo based model.

For adsorption temperatures below 250 K, the experiments indicate that NO adsorbs exclusively molecularly. In this temperature range, both the NO saturation coverage and the degree of ordering of the NO adlayer grow at increasing adsorption temperature. We have simulated the NO adsorption process to investigate whether these experimental results can be explained by surface diffusion of NO.

Furthermore, we have used the model to extract kinetic parameters for NO dissociation from the experimental results. The Monte Carlo model enables us to incorporate the influence of the local environment on the NO dissociation. We will show that incorporation of lateral interactions is necessary to obtain kinetic parameters for NO dissociation which fit within theoretical expectations for rate parameters of an elementary reaction step.

### 3.4.2 Model description

At the Rh(111) surface, rhodium atoms form a hexagonal lattice in which each surface atom has six neighbours. In the Monte Carlo model we have applied a hexagonal lattice with periodic boundary conditions, three types of adsorbed species: NO, N, and O (plus empty sites), and four reactions:



For the rate constants of these four microscopic transitions we have used Arrhenius expressions to describe their temperature dependence. NO and N<sub>2</sub> desorption parameters were taken from Borg *et al.* [17], whereas NO dissociation parameters have been varied to fit the experimental results. The NO adsorption rate at 150 K and 2.10<sup>-8</sup> mbar has been derived from the initial slope of the NO uptake curve, see Figure 3.3, and yields a value of ~7.10<sup>-3</sup> NO molecules/(site.s).

**Table 3.1** Arrhenius parameters of NO adsorption, NO and N<sub>2</sub> desorption as used in the simulations.

Reaction	$\nu$ [s <sup>-1</sup> ]	$E_{\text{act}}$ [kJ/mol]
NO adsorption	0.01	0
NO desorption	3 × 10 <sup>13</sup>	113
N <sub>2</sub> desorption	1 × 10 <sup>10</sup>	118

Unfortunately, we have no information about the adsorption rate at higher temperatures. However, the sticking coefficient for NO adsorption is not expected to vary orders of magnitude with changing substrate temperature. For this reason, we have applied an NO adsorption rate of 10<sup>-2</sup> NO molecules/(site.s) in all simulations. Besides the four reactions, we have included both surface diffusion of NO and of atomic N. Since no experimental data are available on NO surface-diffusion, we have defined its rate with respect to the rate of the fastest other reaction, *e.g.* 100 times faster than the NO adsorption rate at 225 K.

An important issue of the modeling is the selection of the adsorption sites that are involved. Figure 3.12 shows a schematical representation of the Rh(111) surface in which rhodium atoms are located at the corners of the triangles. Four different adsorption sites top, bridge, fcc, and hcp are indicated by circles numbered 1,2,3 and 4, respectively. For both atomic oxygen and nitrogen, it is well established that threefold hollow sites are energetically the most favourable ones [27]. This is also true for NO in the absence of coadsorbates, see section 3.3.1 of this chapter. Each unit cell of the Rh(111) surface

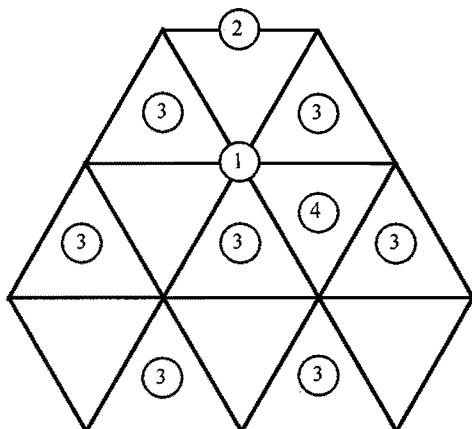


**Figure 3.12** Schematic representation of the Rh(111) surface. Rh atoms are located on the intersections of the lines. Top, bridge, fcc and hcp sites are indicated by the numbers 1, 2, 3, and 4, respectively. Only fcc sites and interactions with the 6 nearest neighbour sites are considered in the model.

contains both one fcc and one hcp site. Consequently, 2 monolayers of threefold sites are present. In the model we have considered only one type of threefold site (so either fcc or hcp, which one is not important in the calculation), which reduces the number of sites available for adsorption to 1 ML. This seems a reasonable assumption, since surface coverages in excess of 1 ML are not observed on Rh(111). If only one type of threefold sites is considered, the sites constitute a hexagonal lattice in which each site is surrounded by 6 neighbouring sites, see Figure 3.12. In the model only the interactions with these 6 nearest neighbouring sites are considered.

### 3.4.3 Modeling molecular NO adsorption between 150 and 225 K

If the Rh(111) surface is saturated with NO at 150 K a disordered layer is obtained with a coverage of 0.68 ML. When the adsorption temperature is increased, the adsorption capacity increases and at 225 K NO orders into a  $(2 \times 2)$ -3NO structure corresponding to a coverage of 0.75 ML. We have incorporated a maximum NO coverage of 0.75 ML in the model by imposing the restriction that only 3 of the 4 corners of a  $(1 \times 1)$  unit cell can be occupied by NO molecules. This restriction is visualized in Figure 3.13, empty



**Figure 3.13** Illustration of the 3 out of 4 restriction for NO adsorption. NO covered sites are colored black, empty sites available for NO adsorption are white, and sites blocked by the restriction are grey.

threefold hollow sites are represented white or grey and sites occupied by NO are black. A site is colored grey if it is the fourth of a  $(1 \times 1)$  unit cell of which three sites are already occupied. NO can only adsorb on white sites thus obeying a global 3 out of 4 restriction.

Incorporation of diffusion in the model is difficult, since it is extremely fast as compared to the other processes. The diffusion rate in the simulation has to be limited because otherwise the simulation consists of diffusion steps only. We have investigated whether the increase of the NO adsorption capacity between 150 and 225 K can be explained by an enhanced NO mobility. Therefore, we have chosen parameters for the surface diffusion such that diffusion is slow as compared to adsorption at 150 K, but about 20 times faster at 200 K. The selection of the absolute values for the diffusion rate is quite arbitrary, unfortunately no experimental data are available. For temperatures above 200 K we took the surface-diffusion to be a hundred times as fast as the fastest other reaction. In the range 200 K-275 K the fastest reaction is adsorption; in the range 300 K-350 K it is dissociation.

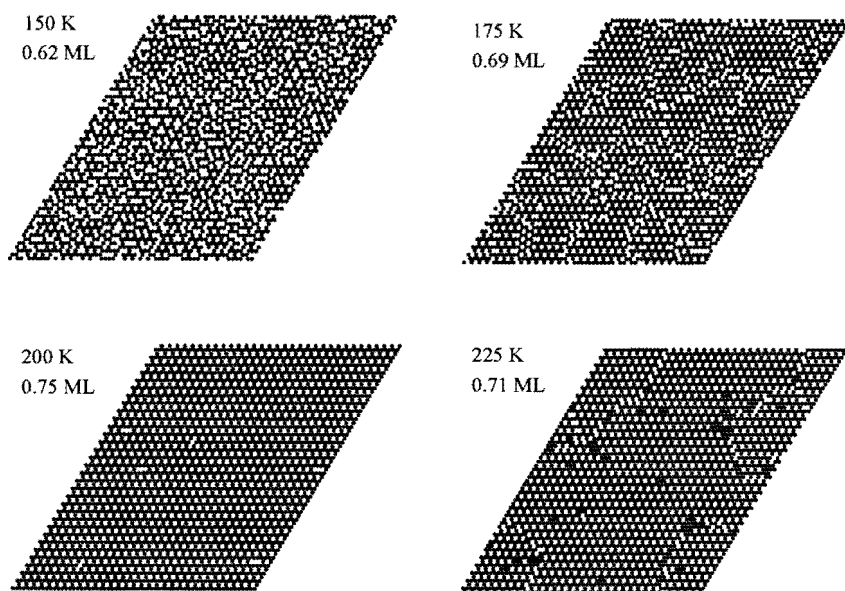


**Figure 3.14** Final configurations of the NO saturated Rh(111) surface for adsorption temperatures of 150, 175, 200 and 225 K. At 150 K the surface is disordered, increase of the adsorption temperature results in almost complete ordering at 200 K. Sites occupied by NO are colored black, sites blocked for NO adsorption are white. At 225 K some dissociation occurs which explains the lower NO coverage of 0.71 ML. Sites occupied by N and O are colored black also, which causes the small black clusters.

Figure 3.14 shows the final configurations of the NO saturated Rh(111) surface for adsorption temperatures of 150, 175, 200 and 225 K. Sites occupied by NO molecules are represented by black spots and sites blocked for NO adsorption due to the 3 out of 4 restriction are colored grey. At 150 K, NO surface-diffusion is 250 times slower than NO adsorption, resulting in a disordered adsorption layer with a coverage of 0.62 ML. Simulations indicate that if diffusion is entirely excluded, the 3 out of 4 restriction yields a saturation coverage of 0.61 ML. With increasing adsorption temperature the mobility of the NO molecules rises, which is reflected by a growing ordering of the adsorbate layer, see Figure 3.14. At 200 K the adsorbate layer is almost fully ordered, although some boundaries remain visible.

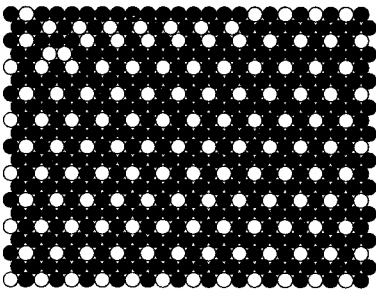


*Figure 3.15* Detail of the Rh(111) surface after saturation with NO at 200 K. The adsorption layer is almost fully ordered. Black sites are occupied by NO, white sites are empty, but blocked due to the 3 out of 4 restriction.

Figure 3.15 shows a magnification of the Rh(111) surface after saturation with NO at 200 K. Sites occupied by NO are black, the white sites are empty, but not available for NO adsorption, since the 3 out of 4 restriction would not be obeyed.

The experimental results indicated that ordering of the adsorbate layer is accompanied by an increase of the adsorption capacity of the Rh(111) surface. Figure

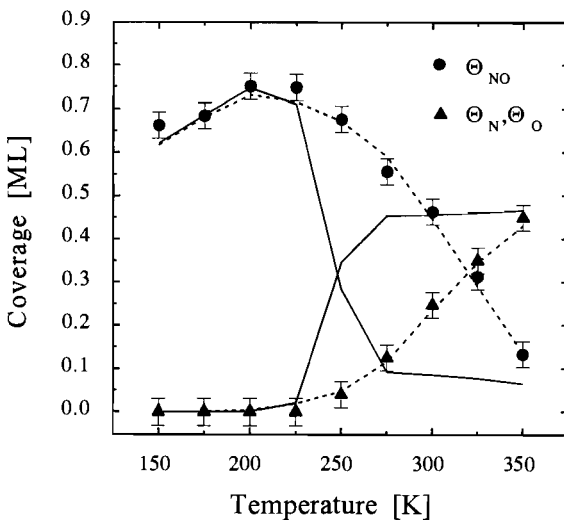


*Figure 3.16* Comparison between experimental and calculated NO (●), and N and O (▲) coverages. Lateral interactions affecting the NO dissociation reaction are not incorporated. Simulation results for NO dissociation parameters of  $\nu=1 \times 10^{11} \text{ s}^{-1}$  and  $E_{act}=65 \text{ kJ/mol}$  are represented by the solid line, and those for  $\nu=30 \text{ s}^{-1}$  and  $E_{act}=23 \text{ kJ/mol}$  by the dashed line.

3.16 shows a comparison between the experimental and the simulated NO, N and O coverages in the temperature range from 150 to 350 K. Below 250 K, where molecular NO is the only adsorbate, very good agreement is observed between the simulated and experimental NO coverage.

The simulations indicate that surface diffusion of NO can explain both the ordering of the adsorbate layer and the increase of the NO saturation coverage with higher adsorption temperature.

#### 3.4.4 Modeling isothermal NO adsorption between 225 and 350 K

For temperatures above 225 K, part of the NO dissociates during the adsorption experiment. By comparing the experimental and the calculated NO, N and O coverages, information can be obtained about the NO dissociation process. For a particular experiment, the adsorption temperature is constant and only coverage-dependent effects influence the NO dissociation rate. By comparison of the adsorption experiments at different temperatures, furthermore, the temperature dependence of the NO dissociation reaction can be investigated.

An important aspect of the modeling is to impose restrictions for the NO dissociation reaction. Obviously, for NO dissociation at least one of the neighbouring sites has to be empty in order to accommodate the resulting atomic oxygen. However, Borg *et al.* [17] showed that for an NO saturated Rh(111) surface dissociation is suppressed up to 430 K, where new vacancies are created by NO desorption. Apparently, the sites which are blocked for NO adsorption by the global 3 out of 4 restriction are also not available for NO dissociation. Another important experimental observation is that at 375 K the sum of the atomic nitrogen and atomic oxygen coverage is approximately 1 ML, see Figure 3.9. This indicates that it should be possible to dissociate 0.5 ML of NO. We have implemented both experimental observations in the model by imposing the global 3 out of 4 restriction only for NO occupied sites. Thus, only if a (1×1) unit cell contains 3 NO molecules the empty site is blocked for both NO adsorption and dissociation. This restriction can explain the NO saturation coverage of 0.75 ML at 200 K. The dissociation is suppressed until NO desorption starts to create new vacancies and allows the total atomic oxygen and nitrogen coverage to rise to 1 ML.

In the first set of simulations we have omitted influences of the local environment on the NO dissociation rate. The only criterion for NO dissociation is the availability of an empty site which obeys the 3 out of 4 restriction. If an empty site is available, the probability for NO dissociation in a certain time interval is determined by the rate of the microscopic transition. We have investigated a number of kinetic parameters for NO dissociation on Rh(111) as reported in the literature. Root *et al.* [6] reported a pre-exponential factor and activation energy of  $10^{14} \text{ s}^{-1}$  and 80 kJ/mol, respectively, while Borg *et al.* [17] found  $10^6 \text{ s}^{-1}$  and 40 kJ/mol. If these latter parameters were used as input for the NO dissociation rate, a large discrepancy between measured and calculated NO,

N and O coverages results. Also adaptation of pre-exponential factor and activation energy in the range reported by these authors could not yield a satisfactory agreement between measured and calculated coverages.

Figure 3.16 shows a comparison between the experimental NO, N and O coverages and the calculated ones (solid line), using a pre-exponential factor and activation energy for NO dissociation of  $1 \times 10^{11} \text{ s}^{-1}$  and 65 kJ/mol, respectively. For temperatures above 225 K, there is a clear discrepancy between the calculated and the experimental NO and O coverages. The simulations predict atomic oxygen coverages that are much too high and NO coverages that are far too low. Apparently, the model overestimates the NO dissociation rate at higher temperatures. If a higher pre-exponential factor and activation energy are used, the discrepancy between the calculated and experimental NO and O coverages becomes even worse.

We found that an excellent agreement between simulation and experiment is obtained for a pre-exponential factor and activation energy for NO dissociation of  $30 \text{ s}^{-1}$  and 23 kJ/mol, respectively. The calculated coverages based on these parameters are indicated by a dashed line in Figure 3.16. However, for an elementary transition these parameters are rather unrealistic, since on theoretical grounds the pre-exponential has to be in the range between  $10^{10}$  and  $10^{16} \text{ s}^{-1}$  [28].

If the NO dissociation rate is influenced by coadsorbates, the above described model is erroneous. Lateral interactions between NO, N and O are known to significantly affect the adsorption energies of the adsorbates. Therefore, it is very well conceivable that also the NO dissociation reaction is influenced by lateral interactions. Introduction of lateral interactions makes the model considerable more complex. Proper implementation of lateral interaction requires knowledge of all the individual interaction parameters between N, O and NO species. Furthermore, it has to be known to what extent several interactions are additive. However, there is very little quantitative experimental information about N, O, and NO interactions, although it is known that all the interactions are repulsive [29]. Qualitatively, the presence of coadsorbates is expected to slow down the NO dissociation.

The NO dissociation is expected to be most rapid in the beginning of the adsorption experiment, where the surface is bare and lateral interactions are insignificant. When the adsorption proceeds the NO dissociation reaction is slowed down by the build up of coadsorbates. Initially these coadsorbates are predominantly atomic nitrogen and oxygen, especially at higher temperatures. For this reason we have introduced a negative influence of both N and O on the NO dissociation rate in the model. If at least one of the six neighbours of an NO molecule is either an N or an O adatom, the activation energy for dissociation is increased by 6 kJ/mol to 47 kJ/mol (when no atomic neighbours are present it is 41 kJ/mol). In both cases a pre-exponential factor of  $1.6 \times 10^5 \text{ s}^{-1}$  is used. Since a neighbourhood containing an N or O adatom is assumed to be less favourable, we have adjusted the surface-diffusion such that NO tends to move away from these spots: the activation energy for diffusion to an empty site with an N or O neighbour is increased by 4.2 kJ/mol.



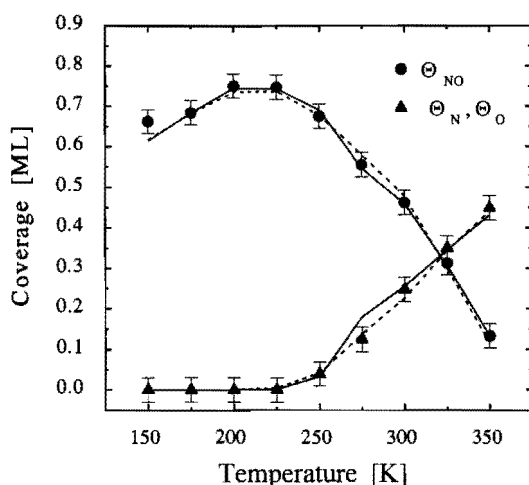


**Figure 3.17** Comparison between experimental and calculated NO ( $\bullet$ ), N and O ( $\blacktriangle$ ). Simulation results for a lateral interactions with one neighbour and dissociation parameters of  $\nu=1.6 \times 10^5 \text{ s}^{-1}$  and  $E_{\text{act}}=40 \text{ kJ/mol}$  are represented by the dashed line, and for lateral interactions with every neighbour and  $\nu=10^{11} \text{ s}^{-1}$  and  $E_{\text{act}}=65 \text{ kJ/mol}$  by the solid line (see text for details).

Figure 3.17 shows a comparison between the measured and the calculated NO, N and O coverages, the calculated data being indicated by the dashed line, using the above described model. Now a very good agreement with the experimental NO and O coverages is obtained over the entire temperature regime.

Although incorporation of a lateral interaction for NO dissociation results in more realistic kinetic parameters, the pre-exponential factor of  $1.6 \times 10^5$  is still too small. We have further expanded the model in order to see whether realistic values for the pre-exponential factor could be obtained. If lateral interactions are additive, NO dissociation is increasingly impeded with increasing occupation of neighbouring sites. We have carried out simulations in which the activation energy for NO dissociation rises with the number of occupied neighbouring sites. The solid line in Figure 3.17 shows the calculated NO, N and O coverages using a pre-exponential factor of  $1 \cdot 10^{11} \text{ s}^{-1}$  and a dependence of the activation energy on the number of neighbours as shown in Table 3.2.

In order to obtain good agreement between calculations and experiment it appeared necessary to use a slightly larger increase in the activation energy going from 0 to 1 occupied neighbouring site, 5.8 kJ/mol, than for the additional neighbours, 4.6 kJ/mol. Figure 3.17 shows a very good agreement between measured and calculated NO, N and O coverages apart from a slight deviation at 275 K.

**Table 3.2** Dependence of the activation energy for NO dissociation on the number of occupied neighbouring sites corresponding to the simulation results shown by the dashed line in Figure 3.17.

Neighbours	0	1	2	3	4	5
$E_{\text{act}}$ [kJ/mol]	65.3	71.1	75.7	80.3	84.9	89.5

These simulation results indicate that incorporation of lateral interactions has a very important impact on the kinetic parameters that are obtained for the NO dissociation rate.

## 3.5 Discussion

### 3.5.1 Molecular NO adsorption at low temperatures

We have investigated the influence of the NO adsorption temperature on both the surface ordering and the saturation coverage. Until now, the increase of the NO saturation coverage at rising adsorption temperatures has never been demonstrated experimentally. Both SIMS and TPD results (see Figures 3.6 and 3.8, respectively) indicate that the NO saturation coverage grows when the adsorption temperature is increased from 150 to 225 K. If, in accordance with Root *et al.* [6], a saturation coverage of 0.68 ML is assumed for adsorption at 150 K, the saturation coverage at 225 K is 0.75 ML. This agrees very well with our LEED results and those of Kao *et al.* [8], which indicate a disordered NO layer for adsorption temperatures below 225 K and a (2×2) ordered structure after saturation at 225 K.

On Ni(111) and Pt(111) it has been well established that NO adsorbs in threefold sites at all coverages [22,30]. On Rh(111), EELS results for NO adsorption at low temperature indicate that only one NO species is present [6]. It seems therefore plausible that, also on Rh(111), NO adsorbs at threefold hollow sites only. However, Kim *et al.* [31] using X-ray Photoelectron Diffraction to determine the NO chemisorption geometry for the (2×2)-3NO structure on Rh(111) found that 2 NO molecules are adsorbed in threefold sites and 1 NO molecule is adsorbed on top.

In the simulations, we are not interested in the actual position of the NO molecules. Therefore we have not attempted to incorporate different types of adsorption sites in the model. In the simulations we have used a hexagonal lattice of threefold hollow sites and imposed a global 3 out of 4 restriction to account for the 0.75 ML saturation coverage. Although the threefold hollow site seems the most favourable one, the actual structure of the NO adsorbate layer will probably be different from the simulated one. However, the simulations of the NO adsorption process qualitatively illustrate that both the ordering of the NO adlayer and the increase of the saturation coverage can be explained by an increase of the NO mobility at higher temperatures.

We found that NO adsorption at 150 K can well be described by the Langmuir adsorption model. This result conflicts with the observations by Borg *et al.* [17], who reported that NO adsorbs via a mobile precursor, resulting in a coverage independent sticking coefficient over a rather broad coverage range. We tentatively give an explanation for this discrepancy. The N<sub>2</sub> TPD spectra of Borg *et al.* [17] show the desorption of small amounts of CO, which probably stems from CO uptake from the background during cooling and NO adsorption at low temperature. Since H<sub>2</sub> is generally

more abundant in the residual gas, it is conceivable that also small amounts of hydrogen are adsorbed. For equal H<sub>2</sub> and CO pressures in the background, moreover, the H<sub>2</sub> adsorption rate is about 6 times faster than that of CO assuming equal sticking coefficients (higher collision frequency of H<sub>2</sub>, two H atoms are formed from one H<sub>2</sub> molecule). However, H atoms are easily displaced from rhodium surfaces by NO, even at low temperature [32]. Consequently, empty sites are created at higher NO coverage, which might explain why the sticking coefficient does not decrease as fast as expected when Langmuir adsorption behaviour is obeyed.

### 3.5.2 The role of lateral interactions

In contrast to what one would expect at first sight, investigation of the reactivity of NO on Rh(111) is an intricate matter. This is mainly caused by the fact that lateral interactions between the adsorbates, *viz.* NO, N and O, strongly influence the rates of all surface reactions, as we will discuss next.

Investigations on the N<sub>2</sub> desorption behaviour from atomic nitrogen layers have shown that repulsive interactions between N atoms have to be considered in order to explain the pronounced shift of the second order  $\beta_2$ -N<sub>2</sub> desorption state to lower temperatures at increasing coverage [33,34]. By modeling of the N<sub>2</sub> desorption spectra Zhdanov [35] calculated a repulsion energy of 7 kJ/mol between two N atoms in neighbouring threefold hollow sites. Several investigations have shown that also the interaction between atomic oxygen and atomic nitrogen is strongly repulsive [17,33] (see also Chapter 4). Makeev and Slinko [29] modeled the N<sub>2</sub> desorption spectrum that is observed during NO decomposition. They attributed the low temperature  $\beta_1$ -N<sub>2</sub> desorption state to the existence of strong repulsive interactions between adsorbed NO and N (10 kJ/mol).

Also the desorption of NO is significantly affected by the presence of coadsorbates. Root *et al.* [19] investigated the NO/O coadsorption system and report an additional low-temperature NO desorption state around 400 K, which can be attributed to repulsive interactions between O and NO. Belton *et al.* [18] investigated the NO/N coadsorption system, and also found a low-temperature NO desorption state (380 K) indicative for repulsive NO-N interactions.

For O<sub>2</sub> desorption the above mentioned interactions are insignificant, since the N and NO coverages are negligible in the temperature range where O desorbs.

Our results also reveal the importance of lateral interactions in surface reactions of NO. Both the NO and N<sub>2</sub> TPD spectra are significantly affected by the composition of the adsorbate layer that is obtained after adsorption of NO at various temperatures. With increasing amounts of N and O in the adsorbate layer, the low-temperature  $\alpha_1$ -NO state, desorbing at 380 K, becomes more significant in good agreement with the results for the NO/O and NO/N coadsorption systems [19,18].

In this respect it is also important to note the small  $N_2$  desorption state around 380 K, which appears upon NO adsorption at temperatures above 250 K. For a saturated adsorbate layer which only contains NO, no atomic nitrogen is present at the surface at temperatures up to 430 K (since NO dissociation is inhibited until NO desorption starts) and therefore this  $N_2$  desorption state at 380 is not observed. It is remarkable that  $N_2$  and NO desorption at 380 K run parallel. This suggests that N-NO interactions are responsible for these low-temperature states.

The importance of lateral effects is also illustrated by the in situ SIMS measurements for NO adsorption at 450 K, see Figure 3.10. In the beginning of the adsorption experiment both atomic nitrogen and oxygen accumulate on the surface. As the coverages increase,  $N_2$  desorption becomes pertinent, which results in a decrease of the atomic nitrogen coverage. Since  $N_2$  desorption is a second-order process, it is not surprising that it becomes more pronounced at higher coverages. However, the atomic nitrogen coverage goes through a maximum and becomes significantly smaller after passing through the maximum. In this region the atomic oxygen coverage continues to increase at a constant rate, which indicates that the decrease of the atomic nitrogen coverage is not a consequence of a decrease of the NO dissociation rate. Therefore, the decrease of the atomic nitrogen coverage has to be attributed to an increase of the  $N_2$  desorption rate by repulsive interactions between N and O. In fact atomic nitrogen is displaced by atomic oxygen.

The rate of the NO dissociation reaction has been found to depend very much on coverage [11,15,17]. This is nicely illustrated by the in situ SIMS experiments for NO adsorption at 300 K, see Figure 3.10. In the beginning of the NO adsorption experiment when the surface is bare, NO dissociation is fast as compared to NO adsorption and no molecular NO can be observed on the surface. As the surface becomes increasingly covered by N and O adatoms, the NO dissociation rate decreases and NO starts to accumulate on the surface. The drop of the NO dissociation rate with increasing adsorbate coverage can be explained by assuming that an ensemble of 3-4 empty sites is necessary for dissociation [17]. However, another explanation could be that lateral interactions between NO and coadsorbates are responsible for the decrease of the NO dissociation rate. We will discuss this matter in the following section.

### 3.5.3 The NO dissociation mechanism

In this section, we will first discuss the information we have obtained about the NO dissociation mechanism from NO TPD experiments for different coverages after low-temperature adsorption. Next, we examine NO dissociation parameters calculated by modeling the NO adsorption experiments at various temperatures.

Summarizing, the most important results from the TPD experiments for various amounts of NO adsorbed at 120 K are:

- 1) All NO dissociates during TPD, for NO coverages below 0.20 ML.
- 2) The temperature of the  $\alpha_2$ -NO desorption state is almost constant, viz. about 430 K.
- 3) The  $\alpha_1$ -NO desorption state is observed in relatively small amounts for NO coverages larger than ~0.50 ML.
- 4) For  $0.20 \text{ ML} < \Theta_{\text{NO}} < 0.45 \text{ ML}$ , the amount of NO that dissociates is constant (~ 0.20 ML), whereas it increases for  $\Theta_{\text{NO}} > 0.45 \text{ ML}$ .
- 5) At the saturation coverage (0.68 ML), about 0.45 ML of the adsorbed NO molecules dissociates.

Both the last two observations are remarkable and cannot be explained by a theory that assumes that the NO dissociation process is governed solely by the availability of empty sites. Note that if 0.45 ML of NO is adsorbed, only 44% dissociates during TPD, while 66% dissociates at the NO saturation coverage of 0.68 ML. Since the NO dissociation is strongly coverage-dependent, the fraction of NO that dissociates is expected to decrease with additionally adsorbed NO. Apparently, other factors play a decisive role in the dissociation process as well.

Additional information about the NO dissociation process is provided by the NO adsorption experiments at various temperatures, and the TPD and SIMS results of the thus obtained adsorbate layer, see Figures 3.6-3.9. The most important results are:

- 1) A total N+O coverage of 1ML can be obtained by adsorption of NO at 375 K.
- 2) For surfaces saturated with NO, the NO dissociation is totally inhibited until NO desorption starts at around 430 K, see also Borg *et al.* [17].
- 3) For NO adsorption below 350 K, the total amount of NO that dissociates in the subsequent TPD experiment is 0.45 ML, irrespective of the composition of the adsorbed layer that is obtained upon NO adsorption.

The first observation indicates that 0.5 ML of NO can be dissociated, in other words, 1 ML of sites is available for dissociation. However, for a surface saturated with NO at low temperature, NO dissociation does not proceed at temperatures up to 430 K, where NO starts to desorb and new sites become available. This indicates that NO dissociation is more significantly blocked by NO than by N or O.

Another important observation is that as long as the Rh(111) surface is saturated with NO, 0.45 ML of NO can be dissociated. Apparently, it makes no difference whether dissociation occurs entirely during the TPD experiment, which is the case for adsorption temperatures below 225 K, or dissociation proceeds already partially during adsorption. This is quite remarkable since, depending on the adsorption temperature, the adsorbate layer differs considerably in composition. A common feature of the saturated adsorbate layers is that NO dissociation in the TPD experiment is suppressed until NO starts to desorb and new vacancies are generated. As a result NO dissociation takes place at relatively high temperatures (around 430 K), which might be a determining feature.

In this respect it is interesting to find an explanation for the fact that NO desorption is already observed in TPD experiments for NO coverages just above 0.20 ML obtained by adsorption at 120 K. Based on the foregoing this is very surprising, since at saturation coverages 0.45 ML NO can be dissociated. The most important difference for the NO dissociation process at low and at high NO coverage is the temperature at which NO dissociation proceeds. During TPD, NO dissociation starts at 275 K and is completed at around 350 K at low coverage, whereas it starts at around 430 K at saturation coverage. At intermediate NO coverages, *e.g.* 0.35 ML, NO dissociation starts at 275 K and continues up to 430 K. Based on the coverage dependence of the NO TPD behaviour we tentatively suggest the following model for the NO dissociation reaction. For NO coverages below 0.20 ML all NO dissociates below the NO desorption temperature and N<sub>2</sub> is the only N-containing product. At intermediate coverages, between 0.20 and 0.45 ML, NO dissociation starts at 275 K, which results in the formation of N and O adatoms and a reduction of the number of empty sites. Since the repulsion between NO and N or O is stronger than that between NO molecules, NO tends to diffuse away from N and O and segregates into islands. We assume that in the N/O islands, at least one site near every N or O adatom remains empty and is therefore not available for dissociation. In the NO islands, NO dissociation is blocked until NO starts to desorb at around 430 K. This interpretation explains why the  $\alpha_1$ -NO desorption state, which is associated with NO near N or O, is absent. The  $\alpha_2$ -NO state does not shift significantly with NO coverage, and the NO desorption already starts just above about 0.20 ML. At high coverages the NO dissociation is inhibited until NO desorbs. At this temperature NO dissociation is very fast and an empty site which is created by desorption of an NO molecule is immediately used for dissociation. In this case NO molecules have no time and no empty space to diffuse away and therefore more sites are available for NO dissociation, which can explain the increase in the fraction of NO molecules that dissociates.

Support for the above described model comes from a recent STM study by Xu and Ng [36], who observed segregation of O, N and NO into separate islands when NO was coadsorbed with O on Rh(111) around 375 K. These authors also report a (1×2)-N reconstruction of the Rh(111) surface. Formation of this phase may also be responsible for enhanced NO dissociation.

By modeling the NO adsorption process at various temperatures we have obtained kinetic parameters for the NO dissociation rate. If lateral interactions on the NO dissociation reaction are omitted and only a free site requirement is imposed, a pre-exponential factor of 30 s<sup>-1</sup> and 23 kJ/mol are calculated. Sellmer *et al.* [37] modeled the NO dissociation reaction on a polycrystalline Rh foil, using first order kinetics and neglecting lateral interactions. These authors calculated a pre-exponential factor and activation energy of 10<sup>-0.2</sup> s<sup>-1</sup> and 8 kJ/mol, respectively. Using the same model, Schmatloch [16] *et al.* reported comparably low values for the pre-exponential factor and activation energy for NO dissociation on Rh(110), *viz.* 10<sup>1.9</sup> s<sup>-1</sup> and 15 kJ/mol, respectively. Interestingly, we have shown that incorporation of lateral interactions for

the NO dissociation reaction in the model results in an entirely different set of kinetic parameters. In this case a theoretically reasonable pre-exponential factor of  $10^{11} \text{ s}^{-1}$  is calculated [28]. This might indicate that neglecting lateral effects when modeling the NO dissociation reaction leads to erroneous (and theoretically unrealistic) kinetic parameters.

Borg *et al.* [17] have studied the kinetics of the NO dissociation reaction for low NO coverage (0.15-0.20 ML) by temperature-programmed SIMS on Rh(111). These authors incorporated an ensemble size requirement for NO dissociation by fitting the experimental results by the following equation:

$$-\frac{d(\theta_{NO}/\theta_{sat})}{dT} = \frac{v_{dis}}{\beta} \cdot \frac{\theta_{NO}}{\theta_{sat}} \cdot \left( \frac{\theta_*}{\theta_{sat}} \right)^n \cdot e^{-E_{dis}/RT} \quad (3.6)$$

In this equation  $\theta_{NO}$  is the absolute NO coverage,  $\theta_*$  is the absolute coverage of empty sites,  $v_{dis}$  is the pre-exponential factor for dissociation,  $E_{dis}$  is the activation barrier for dissociation, and  $\beta$  is the heating rate. These authors normalized the coverages to a saturation value  $\theta_{sat}$  of 0.50 ML, which they assumed to be the concentration of threefold hollow sites available for the adsorption of  $\alpha_2$ -NO, N, and O. The parameter  $n$  has been considered as an effective ensemble size required for the dissociation of NO. For  $n=0$ , these authors found a pre-exponential factor and activation energy of  $10^6 \text{ s}^{-1}$  and 40 kJ/mol, respectively, while for  $n=3-4$  they arrived at  $10^{11} \text{ s}^{-1}$  and 65 kJ/mol, respectively.

For low NO coverage we can easily compare the results of our simulation with the model of Borg *et al.* [17], since  $\theta_* \approx 1$  and most NO molecules have no occupied neighbouring sites. For this situation we have used a pre-exponential factor and activation energy of  $10^{11} \text{ s}^{-1}$  and 65.3 kJ/mol, respectively, see table 3.2, in excellent agreement with the kinetic parameters reported by Borg *et al.* for  $n=3-4$ .

However, we believe that it is more realistic to interpret the decrease in the NO dissociation rate in terms of lateral interactions than by assuming an ensemble of 3-4 empty sites for NO dissociation. In the later case it would not be possible to dissociate more than 0.25 ML NO if the adsorbate species are homogeneously distributed over the surface (which is expected based on the repulsive lateral interactions).

### 3.6 Conclusions

On Rh(111), NO adsorption below 250 K is exclusively molecular and can be described by the Langmuir adsorption model. At 150 K and 0.5 ML coverage, NO orders into a  $c(4 \times 2)$ -2NO structure in which one half of the NO molecules occupies fcc and the other half hcp threefold hollow sites. Saturation of the surface with NO at 150 K results in a disordered layer with a coverage of 0.68 ML. Increasing the NO adsorption temperature to 225 K results in the formation of a well ordered  $(2 \times 2)$ -3NO layer, which is observable by LEED and has a coverage of 0.75 ML. The growth of the NO coverage

with increasing adsorption temperature is evidenced both by TPD and SIMS experiments. Simulations of the NO adsorption process, by means of a Monte Carlo model, indicate that the rise of the NO saturation coverage and the increase of ordering at higher adsorption temperatures can very well be explained by an enhanced surface-mobility of NO.

For temperatures above 250 K a substantial part of the NO dissociates during adsorption. The combination of SIMS and TPD enables us to determine the individual coverages of N, O and NO in the adsorbate layer obtained by saturating the surface with NO at a constant temperature. For adsorption temperatures between 250 and 350 K the adsorbate layer contains both NO, N and O. In this temperature range both N<sub>2</sub> and O<sub>2</sub> desorption are insignificant. Compared to the state at low temperatures, where the NO saturated surface only contains molecular NO, TPD spectra of the NO, N and O containing surface reveal additional desorption states for both NO and N<sub>2</sub>. With increasing N and O content, the low-temperature  $\alpha_1$ -NO desorption state at 380 K becomes more apparent, while an additional N<sub>2</sub> desorption state develops at the same temperature. These observed shifts to lower temperatures can be explained by strong repulsive interactions between NO and O, and NO and N.

With adsorption at temperatures above 350 K, molecular NO is absent in the adsorbate layer; N and O are the only surface species. With increasing NO adsorption temperature the O coverage increases at the expense of the N coverage. At temperatures above 350 K, the sum of the oxygen and nitrogen coverages exceeds 1 ML, which might indicate the formation of subsurface O and N. Support for the formation of subsurface N arises from the observation that, above 425 K N is not observable by SIMS, whereas TPD indicates that significant amounts of sorbed N are still present.

Simulations of the NO adsorption experiment indicate that incorporation of lateral interactions for the NO dissociation reaction is necessary to obtain kinetic parameters that are acceptable from a theoretical point of view. If lateral interactions are omitted and only a free site requirement is imposed, a pre-exponential factor and activation energy for NO dissociation of 30 s<sup>-1</sup> and 23 kJ/mol, respectively, are calculated. If the activation energy for NO dissociation is made dependent on the number of occupied neighbouring sites, the experimental results could satisfactorily be modeled using a more realistic pre-exponential factor of 10<sup>11</sup> s<sup>-1</sup>. In this case we find an activation energy of 65 kJ/mol for NO dissociation in the limit of zero coverage.

## References

- [1] K.C. Taylor, Catal. Rev.-Sci. Eng. 35 (1993) 457.
- [2] C.T. Campbell and J.M. White, Appl. Surf. Sci. 1 (1978) 347.
- [3] D.G. Castner, B.A. Sexton, and G.A. Somorjai, Surf. Sci. 71 (1978) 519.
- [4] T.W. Root, L.D. Schmidt, and G.B. Fisher, Surf. Sci. 134 (1983) 30.
- [5] L.A. DeLouise and N. Winograd, Surf. Sci. 159 (1985) 199.
- [6] T.W. Root, G.B. Fisher, and L.D. Schmidt, J. Chem. Phys. 85 (1986) 4679.
- [7] L. Bugyi and F. Solymosi, Surf. Sci. 188 (1987) 475.
- [8] C.-T. Kao, G.S. Blackman, M.A. Van Hove, G.A. Somorjai, and C.-M. Chan, Surf. Sci. 224



- (1989) 77.
- [9] P. Ho and J.M. White, *Surf. Sci.* 137 (1984) 103.
- [10] R.E. Hendershot and R.S. Hansen, *J. Catal.* 98 (1986) 150.
- [11] J.S. Villarrubia and W. Ho, *J. Chem. Phys.* 87 (1987) 750.
- [12] R.J. Baird, R.C. Ku, and P. Wynblatt, *Surf. Sci.* 97 (1980) 346.
- [13] M. Bowker, Q. Guo, and R.W. Joyner, *Surf. Sci.* 257 (1991) 33.
- [14] G. Cautero, C. Astaldi, P. Rudolf, M. Kiskinova, and R. Rosei, *Surf. Sci.* 258 (1991) 44.
- [15] V. Schmatloch and N. Kruse, *Surf. Sci.* 269/270 (1992) 488.
- [16] V. Schmatloch I. Jirka, and N. Kruse, *Surf. Sci.* 297 (1993) L100; *id.*, *J. Chem. Phys.* 100 (1994) 8471.
- [17] H.J. Borg, J.F.C.-J.M. Reijerse, R.A. van Santen, and J.W. Niemantsverdriet, *J. Chem. Phys.* 101 (1994) 10052.
- [18] D.N. Belton, C.L. DiMaggio, S.J. Schmieg, and K.Y.S. Ng, *J. Catal.* 157 (1995) 559.
- [19] T.W. Root, L.D. Schmidt, and G.B. Fisher, *Surf. Sci.* 134 (1983) 30; *id.*, *J. Chem. Phys.* 85 (1986) 4687.
- [20] S. Aminpirooz, A. Schmalz, L. Becker, and J. Haase, *Phys. Rev.* B45 (1992) 6337.S.
- [21] M.C. Asensio, D.P. Woodruff, A.W. Robinson, K.-M. Schindler, P. Gardner, D. Ricken, A.M. Bradshaw, J.C. Conesa, and A.R. González-Elipe, *Chem. Phys. Lett.* 192 (1992) 259; *id.*, *J. Vac. Sci. Technol.* A10 (1992) 2445.
- [22] L.D. Mapledoram, A. Wander, and D.A. King, *Chem. Phys. Lett.* 208 (1993) 409.
- [23] N. Materer, A. Barbieri, D. Gardin, U. Starke, J.D. Batteas, M.A. Van Hove, and G.A. Somorjai, *Phys. Rev.* B48 (1993) 2859; *id.*, *Surf. Sci.* 303 (1994) 319.
- [24] A. Brown and J.C. Vickerman, *Surf. Sci.* 124 (1983) 267.
- [25] J.C. Vickerman, *Surf. Sci.* 189/190 (1987) 7.
- [26] D.N. Belton, C.L. DiMaggio, and K.Y.S. Ng, *J. Catal.* 144 (1993) 273.
- [27] C.T. Reimann, M. El-Maazawi, K. Walzl, B.J. Garrison, N. Winograd, and D.M. Deaven, *J. Chem. Phys.* 90 (1989) 2027.
- [28] R.A. van Santen and J.W. Niemantsverdriet, *Chemical Kinetics and Catalysis*, Plenum, New York, 1995.
- [29] A.G. Makeev and M.M. Slinko, *Surf. Sci.* 359 (1996) L467.
- [30] J. Abon, J. Billy, and J.C. Bertolini, *Surf. Sci.* 171 (1986) L387.
- [31] Y.J. Kim, S. Thevuthasan, G.S. Herman, C.H.F. Peden, S.A. Chambers, D.N. Belton, and H. Permana, *Surf. Sci.* 359 (1996) 269.
- [32] P. Ho and M. White, *Surf. Sci.* 137 (1984) 117.
- [33] D.N. Belton, C.L. DiMaggio, and K.Y.S. Ng, *J. Catal.* 144 (1993) 273.
- [34] L. Bugyi and F. Solymosi, *Surf. Sci.* 258 (1991) 55.
- [35] V.P. Zhdanov, *Catal. Lett.* 37 (1996) 163.
- [36] H. Xu and K.Y.S. Ng, *Surf. Sci.* 365 (1996) 779.
- [37] C. Sellmer, V. Schmatloch, and N. Kruse, *Catal. Lett.* 35 (1995) 165.

## 4 Preparation of atomic nitrogen adlayers on Rh(111)

### 4.1 Introduction

The reactivity of atomic nitrogen on rhodium surfaces is of great interest for the understanding of the elementary processes in the automotive exhaust gas convertor. Under normal operation conditions,  $\text{NO}_x$  dissociates rapidly on rhodium and thus is a source of both atomic nitrogen and oxygen. Several studies on, for instance, the  $\text{CO}+\text{NO}$  reaction have indicated that significant amounts of  $\text{N}_{\text{ads}}$  can accumulate on the rhodium surface [1-6]. In principle,  $\text{NO}_x$  reduction can yield several N-containing reaction products, of which  $\text{N}_2$ ,  $\text{N}_2\text{O}$  and  $\text{NH}_3$  are the most important (although we will show in the Chapters 7 and 8 that also  $\text{HCN}$  can be formed under certain conditions). In the context of automotive exhaust gas catalysis, reduction of  $\text{NO}$  towards  $\text{N}_2$  clearly is the desired reaction pathway. The reactivity of atomic nitrogen plays an important role in the selectivity issue of  $\text{NO}$  reduction, since it is involved in the formation of all the reaction products:



The presence of coadsorbates can have a significant influence on the reactivity of atomic nitrogen atoms. For instance, the presence of atomic oxygen considerably accelerates the formation of  $\text{N}_2$  [7,8]. In order to simplify the situation and to enable kinetic analysis at the level of elementary steps, preparation of  $\text{N}_{\text{ads}}$  layers can be desirable.

Since  $\text{N}_2$  does not dissociate on  $\text{Rh}(111)$ , an alternative route has to be employed to deposit atomic nitrogen on the surface [9]. The literature reports a number of methods to achieve a layer of nitrogen atoms. Belton *et al.* [10] prepared  $\text{N}_{\text{ads}}$  layers by dissociating  $\text{NO}$  at low temperature with an electron beam and removing  $\text{O}_{\text{ads}}$  by reaction with  $\text{CO}$ . Bugyi *et al.* [11] used a discharge tube to atomize  $\text{N}_2$  before adsorption. Another way to prepare  $\text{N}_{\text{ads}}$  layers is exposing the surface to  $\text{NH}_3$  at temperatures above  $\sim 400$  K [12-14]. All the above mentioned preparation methods have the disadvantage that it is difficult to deposit a controllable amount of atomic nitrogen.

In Chapters 5 and 8 we describe the hydrogenation of atomic nitrogen to  $\text{NH}_3$  and the reactions between atomic nitrogen and ethylene, respectively. For both these studies it is important that a well defined amount of atomic nitrogen can be deposited on the surface in a reproducible way. In the first part of this chapter, we show that the quantity of atomically adsorbed nitrogen can be adjusted by a two-step process in which  $\text{NO}$  is molecularly adsorbed at low temperatures followed by reaction with  $\text{H}_2$  at elevated temperatures to selectively remove the atomic oxygen stemming from the dissociated  $\text{NO}$ .

Oxygen removal by  $H_2$  is preferred above removal by CO, since  $H_2$  desorbs below the  $N_2$  desorption temperature even at high  $N_{ads}$  coverages.

The last part of this chapter describes the preparation of atomic nitrogen layers on Rh(111) by  $NH_3$  decomposition and by exposure of the surface to  $NO+H_2$  mixtures at elevated temperatures. Especially the latter method appears to be suitable for the preparation of high coverages of atomic nitrogen.

## 4.2 Experimental

All experiments were done in a stainless steel ultra-high vacuum (UHV) system, pumped by a 360  $\ell/s$  turbomolecular pump and a water-cooled titanium sublimation pump. The base pressure was typically around  $5 \times 10^{-11}$  mbar, and mass spectra of the residual gas indicated the presence of mainly  $H_2$ , CO and  $CO_2$ . The system is equipped with a Leybold SSM 200 quadrupole mass spectrometer for TPD and SIMS, and a Leybold EA 10 hemispherical energy analyzer for AES and  $\Delta\phi$  measurements. Both instruments were interfaced with a PC for data storage.

SIMS measurements were performed in the static (low damage) mode. Typically, we used a defocused 5 keV primary  $Ar^+$  beam with a current density of 1-10 nA/cm<sup>2</sup>. To average possible anisotropies in the secondary ion emission process we applied a target bias of +45 V and an extractor voltage of -300 V on the entrance lens of the quadrupole system.

The UHV system contained a rhodium crystal which was cut in the [111] orientation within  $0.5^\circ$  and polished by standard procedures. The temperature was measured by a chromel-alumel thermocouple spotwelded on the back of the crystal. The standard cleaning procedure consisted of an argon ion sputter treatment (900 K, 1.5 keV,  $5 \mu A/cm^2$ ) followed by annealing in  $2 \times 10^{-8}$  mbar  $O_2$  (900 K-1100 K) and a final annealing treatment in vacuum at 1420 K. NO (Messer Griesheim, 99.5%),  $H_2$  (Messer Griesheim, 99.995%), and  $NH_3$  (UCAR electronic grade, 99.995%) were used without further treatment. Exposures are reported in Langmuirs ( $1L = 1.33 \times 10^{-6}$  mbar.s) and coverages are expressed with respect to the number of Rh surface atoms ( $1 ML = 1.6 \times 10^{15} cm^{-2}$ ).

## 4.3 Results

### 4.3.1 Preparation of adsorbed atomic nitrogen by reaction between NO and $H_2$

The left panel of Figure 4.1 illustrates the procedure to prepare atomic nitrogen by SIMS spectra of the Rh(111) surface after adsorption of 0.12 ML NO at 120 K, heating to 400 K to dissociate the NO, and after reaction with hydrogen at 400 K to remove the oxygen. The presence of molecularly adsorbed NO at 120 K is indicated in the SIMS spectrum by the appearance of the  $Rh_2NO^+$  cluster ion at  $m/e=236$ . Heating to 400 K

results in complete dissociation of the adsorbed NO molecules. This is evidenced by the appearance of the  $\text{Rh}_2\text{N}^+$  and  $\text{Rh}_2\text{O}^+$  cluster ions (at  $m/e=220$  and  $m/e=222$ ) which are representative for atomic N and O, respectively, and by the disappearance of the  $\text{Rh}_2\text{NO}^+$  cluster ion. The removal of atomic oxygen by reaction with hydrogen is clearly illustrated by the disappearance of the  $\text{Rh}_2\text{O}^+$  peak, the presence of atomic nitrogen remains clearly visible by the  $\text{Rh}_2\text{N}^+$  peak at  $m/e=220$ .

The right panel of Figure 4.1 shows the selective removal of atomic oxygen from a mixed N+O layer,  $\Theta_{\text{N}}=\Theta_{\text{O}}=0.12$  ML, by exposure to hydrogen at 400 K as monitored

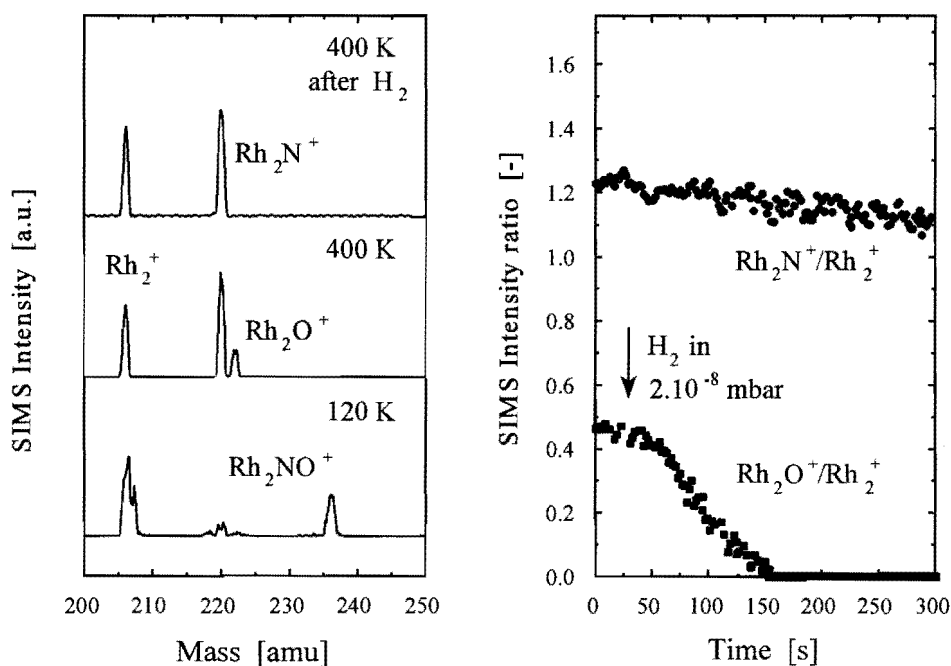


**Figure 4.1** The left panel shows SIMS spectra of the Rh(111) surface after adsorption of 0.12 ML NO at 120 K, after heating to 400 K to dissociate the NO, and after reaction with  $\text{H}_2$  at 400 K to remove the oxygen. The right panel shows the selective removal of oxygen by  $\text{H}_2$  at 400 K followed *in situ* by SIMS.

*in situ* by SIMS. Figure 4.1 clearly shows that the  $\text{Rh}_2\text{O}^+/\text{Rh}_2^+$  SIMS intensity ratio, which is representative for the atomic oxygen coverage, decreases rapidly after  $\text{H}_2$  is introduced. The  $\text{Rh}_2\text{O}^+/\text{Rh}_2^+$  SIMS intensity ratio becomes zero after approximately 150 seconds indicating that all oxygen has been removed. The  $\text{Rh}_2\text{N}^+/\text{Rh}_2^+$  SIMS intensity ratio decreases only slightly indicating that hydrogenation of atomic nitrogen to  $\text{NH}_3$  and  $\text{N}_2$  formation are very slow reactions under these conditions.

In order to prepare pure atomic nitrogen layers by successive reaction between NO and  $\text{H}_2$  it is essential that all NO dissociates. The temperature at which NO dissociates

strongly depends on the initial NO coverage. For NO coverages below 0.15 ML Borg *et al.* [15] showed that dissociation is complete below 350 K, while for the saturation coverage of 0.68 ML dissociation does not start until 430 K. In order to prepare atomic nitrogen layers an optimum temperature has to be found at which all NO is dissociated, the loss of atomic nitrogen due to  $N_2$  desorption is small, the reaction between atomic oxygen and  $H_2$  proceeds rapidly, and  $NH_3$  formation is insignificant.

We have used SIMS to determine to what temperature the Rh(111) surface had to be heated in order to dissociate all adsorbed NO. As could be expected, this temperature depended very much on the initial NO coverage. We found that heating to 400 K was necessary to dissociate all NO when the surface was saturated at 120 K ( $\Theta_{NO}=0.68$  ML).

Figure 4.2 shows the  $Rh_2N^+/Rh_2^+$  and  $Rh_2O^+/Rh_2^+$  SIMS intensity ratios for several mixed N+O adlayers which were obtained by adsorbing various amounts of NO at 120 K and heating to 400 K. For NO coverages below 0.20 ML, no desorption takes place and

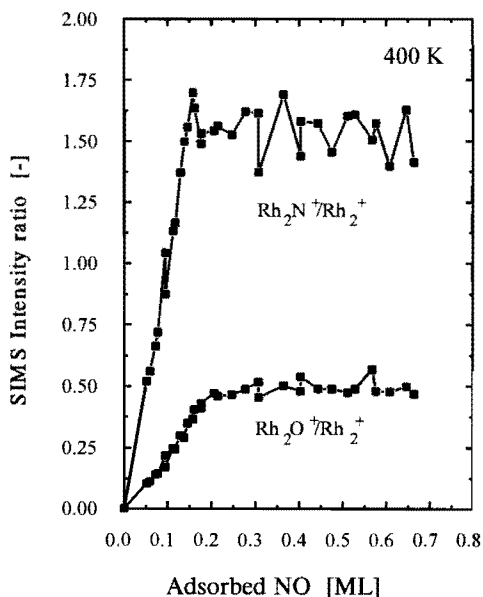


*Figure 4.2*  $Rh_2N^+/Rh_2^+$  and  $Rh_2O^+/Rh_2^+$  SIMS intensity ratios for several mixed N+O adlayers which were obtained by adsorbing various amounts of NO at 120 K and heating to 400 K.

all NO dissociates upon heating (see Chapter 3). In this case, the resulting  $N_{ads}$  and  $O_{ads}$  coverages equal the initial NO coverage ( $\theta_{NO}=\theta_O=\theta_N$ ), provided that no  $O_2$  and  $N_2$  desorption takes place. For oxygen this assumption is certainly valid, since oxygen desorption only becomes significant above 700 K [16]. Figure 4.2 clearly shows a linear relation between the  $Rh_2O^+/Rh_2^+$  SIMS intensity ratio and the initial NO coverage for  $\Theta_{NO}<0.20$  ML, indicating that no NO desorption occurs. The  $Rh_2N^+/Rh_2^+$  SIMS intensity ratio increases linearly with the initial NO coverage below 0.15 ML. Apparently,  $N_2$  desorption becomes important for  $\Theta_{NO}>0.15$  ML. For initial NO coverages above 0.20 ML both the  $Rh_2O^+/Rh_2^+$  and the  $Rh_2N^+/Rh_2^+$  SIMS intensities become constant, although the data exhibit some scatter.

We have used TPD to determine the amount of atomic nitrogen on the Rh(111)

surface both before and after reaction with  $H_2$  at 400 K. In order to relate  $N_2$ -TPD areas to atomic nitrogen coverages we have used the correlation obtained from the NO uptake curve (Figure 3.2). Figure 4.3 shows the  $N_{ads}$  coverage before and after  $H_2$  reaction as a function of the initial NO coverage. For initial NO coverages smaller than 0.15 ML the

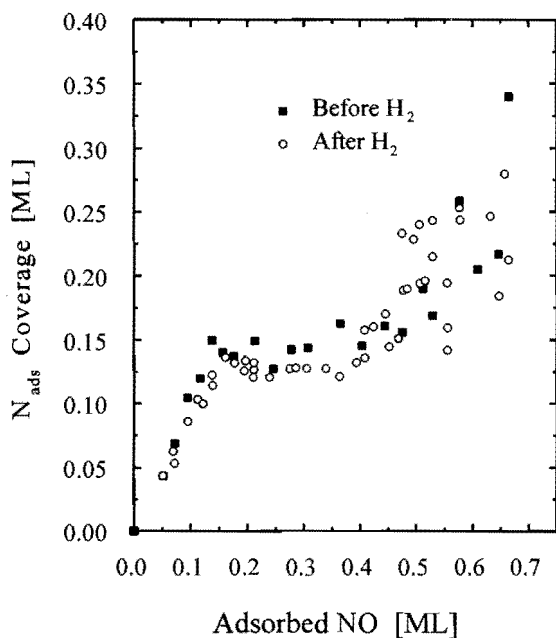


**Figure 4.3** Atomic nitrogen coverages, as determined by TPD, before and after  $H_2$  reaction as a function of the amount NO adsorbed at 120 K.

amount of  $N_{ads}$  that is deposited on the surface equals the amount of initially adsorbed NO. For initial NO coverages between 0.15 and 0.45 ML, the  $N_{ads}$  coverages before and after  $H_2$  reaction are constant. So far these results are fully in line with the SIMS results of Figure 4.2. However, for initial NO coverages larger than 0.45 ML the situation becomes different. Figure 4.3 shows that the  $N_{ads}$  coverage both before and after  $H_2$  reaction increases with the initially adsorbed NO for  $\Theta_{NO} > 0.45$  ML and shows large variations. The increase of the  $N_{ads}$  coverage as determined by TPD conflicts with the SIMS results of Figure 4.2, which indicate a constant  $N_{ads}$  coverage. An increase in the  $N_{ads}$  coverage is surprising anyway, since enhanced NO dissociation results in a higher  $O_{ads}$  coverage and thus further destabilization of  $N_{ads}$  is expected. This would result in an increase of the  $N_2$  desorption and therefore a decrease of the  $N_{ads}$  coverage. We will address this point in the discussion section.

Figure 4.4 shows  $N_2$  TPD spectra,  $m/e=28$ , obtained from adsorbed atomic nitrogen layers with coverages ranging from 0.04 to 0.25 ML. For  $N_{ads}$  coverages from 0.04 to 0.13 ML the desorption tails of the spectra at high temperature overlap very well, as is expected for ordinary second order desorption behaviour. The peak maximum of the

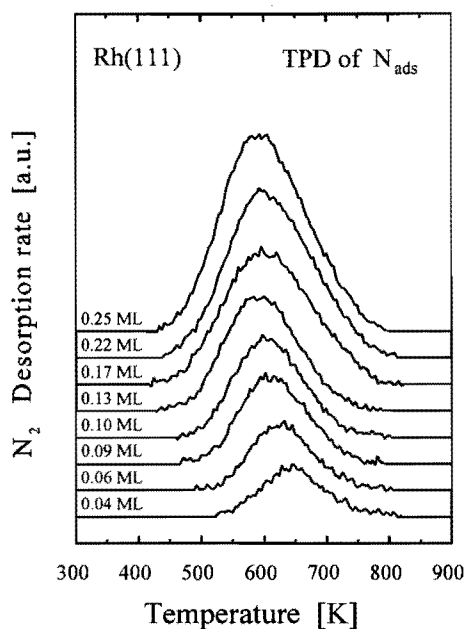


**Figure 4.4**  $N_2$  TPD spectra obtained from  $N_{ads}$  layers of various coverages.  $N_{ads}$  was prepared by adsorbing NO at 120 K, followed by heating to 400 K and reaction with  $H_2$  to remove the oxygen. The heating rate was 10 K/s.

spectra shifts from 645 K at  $\Theta_N=0.04$  ML to 595 K at  $\Theta_N=0.13$  ML. A shift of the peak maximum is inherent to a second order desorption process. However, in this case also repulsive interactions between atomic nitrogen atoms play a role and cause a more pronounced shift of the peak maximum to lower temperature [10,17,18]. If we employ a CAW analysis to these TPD spectra, we find an activation energy and pre-exponential factor of  $120\pm 3$  kJ/mol and  $10^{10.5\pm 1}$  s $^{-1}$ , respectively, for  $N_2$  formation in the zero coverage limit. These parameters are in excellent agreement with those reported by Borg *et al.* [15], who determined the  $N_2$  desorption rate in the presence of O in the limit of zero coverage.

For  $\Theta_N > 0.13$  ML the shape of the desorption spectra becomes remarkably different. Instead of following the desorption trend that was observed for  $\Theta_N < 0.13$  ML, the spectra start to show increased  $N_2$  desorption in the high-temperature range. Remarkable fact is that the deviating  $N_2$  desorption behaviour coincides with the increase of the  $N_{ads}$  coverage for initial NO coverages larger than 0.45 ML, see Figure 4.3.

### 4.3.2 Preparation of atomic nitrogen layers by $NH_3$ decomposition

Atomic nitrogen cannot be obtained by adsorption of  $NH_3$  at low temperature followed by heating, since  $NH_3$  desorption is much faster than  $NH_3$  decomposition on Rh(111), see Chapter 6. For this reason, deposition of atomic nitrogen by  $NH_3$  decomposition is only possible by exposing the Rh(111) crystal to a background pressure of  $NH_3$  at elevated temperatures. We have only briefly investigated this method for the

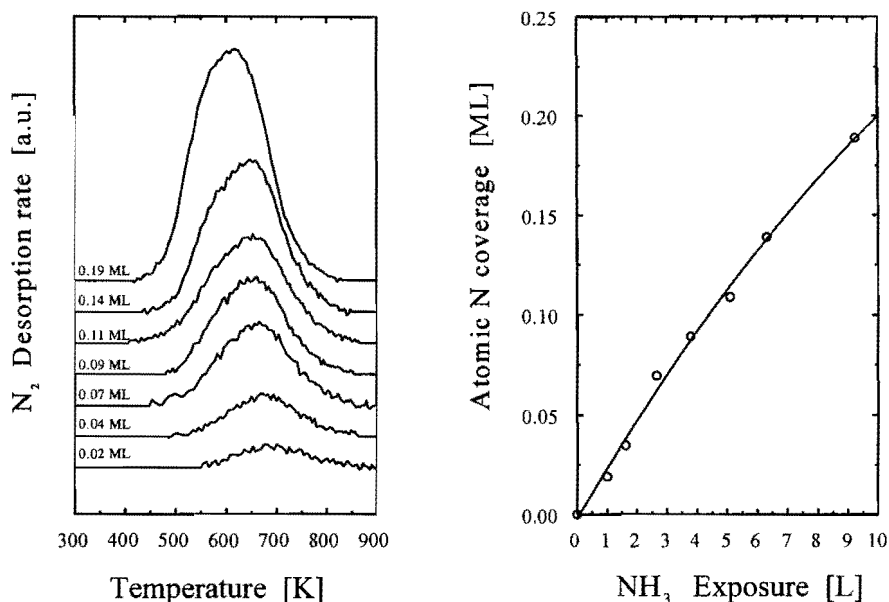


**Figure 4.5** The left panel shows N<sub>2</sub> TPD spectra for various atomic nitrogen coverages obtained by exposing  $1 \times 10^{-8}$  mbar NH<sub>3</sub> at 450 K. The right panel shows the obtained atomic nitrogen coverage as a function of the NH<sub>3</sub> exposure at 450 K.

deposition of atomic nitrogen, since, alike H<sub>2</sub>O, NH<sub>3</sub> has a high tendency to stick to the chamber walls causing a low pumping speed and residual NH<sub>3</sub> in the background and thus strongly deteriorated UHV conditions after NH<sub>3</sub> exposure.

The left panel of Figure 4.5 shows the N<sub>2</sub> desorption spectra ( $m/e=28$ ) obtained from atomic nitrogen layers prepared by exposure of  $1 \times 10^{-8}$  mbar NH<sub>3</sub> at 450 K. H<sub>2</sub> desorption ( $m/e=2$ ) was not observed indicating that no significant amounts of NH<sub>x</sub> are present. We have not applied a CAW analysis to the N<sub>2</sub> desorption spectra, since the heating rate was not perfectly linear over the entire temperature range (approximately 10 K/s on average). Compared to the N<sub>2</sub> TPD spectra of the N<sub>ads</sub> layers prepared by NO+H<sub>2</sub> reaction, see Figure 4.4, the desorption maximum seems to be slightly shifted to higher temperatures. However, a broadening at the high-temperature side is not observed.

The right panel of Figure 4.5 shows the obtained atomic nitrogen coverage as a function of NH<sub>3</sub> exposure. Initially, the atomic nitrogen coverage increases linearly with NH<sub>3</sub> exposure. However, as the atomic nitrogen coverage becomes larger, the growth of the atomic nitrogen coverage with increasing NH<sub>3</sub> exposure (the slope of the solid curve, see Figure 4.5) decreases. Three factors may be responsible for this phenomenon. First, the atomic nitrogen atoms simply block empty sites, which results in a reduction of the number of sites available for NH<sub>3</sub> adsorption. Second, the presence of nitrogen atoms alters the NH<sub>3</sub> adsorption equilibrium resulting in a lower steady state coverage of NH<sub>3</sub>. Third, the NH<sub>3</sub> decomposition rate is decreased by the presence of atomic nitrogen, which



is not inconceivable, since decomposition reactions quite often require ensembles of empty sites.

### 4.3.3 Preparation of atomic nitrogen from NO+H<sub>2</sub> mixtures

We have investigated the deposition of atomic nitrogen by exposing the Rh(111) surface to NO+H<sub>2</sub> mixtures in order to obtain coverages higher than could be obtained by successive NO+H<sub>2</sub> reaction or by NH<sub>3</sub> decomposition. The advantage of using NO+H<sub>2</sub> mixtures above successive reaction between NO and H<sub>2</sub> is that oxygen is removed during the reaction and sites are freed where new NO molecules may dissociate. In order to limit N<sub>2</sub> desorption it is essential to keep the reaction temperature as low as possible. Furthermore it is important to use a low H<sub>2</sub> pressure in order to prevent hydrogenation of atomic nitrogen to NH<sub>3</sub>. On the other hand, the removal of oxygen by H<sub>2</sub> must be fast enough to prevent accumulation on the surface.

We have varied both the reaction temperature and the H<sub>2</sub>:NO pressure ratio to achieve the highest possible atomic nitrogen coverage. Investigation of the surface by SIMS indicates that below 375 K accumulation of NO and O is inevitable when the surface gets covered. For this reason we used a reaction temperature of 400 K and varied the H<sub>2</sub>:NO ratio from 1:1 to 25:1. The NO pressure was  $2 \times 10^{-8}$  mbar in all cases. We found that below a H<sub>2</sub>:NO ratio of about 10:1 atomic oxygen starts to build up when the surface becomes increasingly covered by N<sub>ads</sub>. Apparently, dissociation of H<sub>2</sub> and/or hydrogenation of atomic oxygen to H<sub>2</sub>O is severely hindered at high atomic nitrogen coverages.

Figure 4.6 shows the N<sub>2</sub> desorption spectrum from an atomic nitrogen layer with a coverage of 0.45 ML that was obtained by exposing the Rh(111) crystal to an H<sub>2</sub>:NO mixture of 15:1 at 400 K. Under these conditions, SIMS spectra of the Rh(111) surface after reaction indicated that atomic nitrogen was the only adsorbate. The shape of the N<sub>2</sub> desorption spectrum is significantly different from an ordinary second order desorption spectrum. Not only the steep onset for N<sub>2</sub> desorption at 400 K, but also the broad temperature regime for N<sub>2</sub> desorption (400-750 K) illustrates that other influences, like repulsive lateral interactions, play a significant role. Figure 4.6 also shows the N<sub>2</sub> desorption spectrum resulting from an NO saturated surface of which 0.45 ML of the NO molecules dissociates and 0.23 ML of the NO molecules desorbs. In both cases the amount of N<sub>2</sub> that desorbs is thus similar. However, the N<sub>2</sub> desorption spectra are considerably different. The most striking difference is the less prominent  $\beta_1$ -N<sub>2</sub> desorption state in case of N<sub>2</sub> desorption from a pure atomic nitrogen layer. Apparently, the  $\beta_1$ -N<sub>2</sub> desorption state is favoured by the presence of coadsorbed oxygen and/or NO but is not caused the higher atomic nitrogen coverage. Recently, Makeev and Slinko [19] demonstrated that the appearance of the  $\beta_1$ -N<sub>2</sub> desorption state can be explained by incorporating repulsive NO-N interactions in their mathematical model. This explanation seems more dependable than former theories which attributed the  $\beta_1$ -N<sub>2</sub> desorption state to an NO+N reaction [8,20]. The latter theory was recently invalidated by Belton *et al.* [21] who investigated reactions

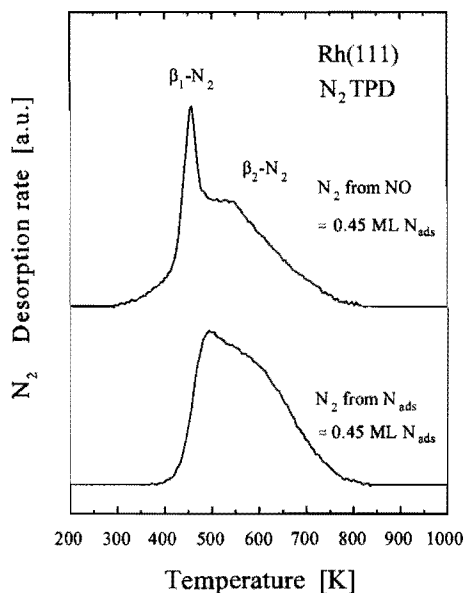


**Figure 4.6** N<sub>2</sub> TPD spectra from an NO saturated surface of which 0.45 ML dissociates (top) and from an atomic nitrogen layer of 0.45 ML (bottom) prepared by reaction of  $2 \times 10^{-8}$  mbar NO +  $2 \times 10^{-7}$  mbar H<sub>2</sub> at 400 K for 5 minutes.

between N and NO on Rh(111). Figure 4.6 also nicely illustrates the influence of repulsive interactions between atomic nitrogen and atomic oxygen. In the presence of atomic oxygen N<sub>2</sub> desorption is more pronounced in the low temperature range.

We did not succeed in preparing atomic nitrogen coverages larger than 0.45 ML by NO+H<sub>2</sub> reaction at 400 K. As Figure 4.6 illustrates, N<sub>2</sub> desorption starts around 400 K, implying that N<sub>2</sub> desorbs also during the NO+H<sub>2</sub> reaction at 400 K. Higher atomic nitrogen coverages might be obtained by applying higher pressures (which is unfortunately not possible in our experimental setup) or by lowering the temperature (which is, however, accompanied by the build up of atomic oxygen and NO).

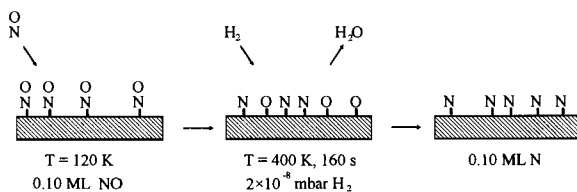
Although we examined many different atomic nitrogen coverages and temperature treatments we did not observe ordering in LEED experiments.

## 4.4 Discussion

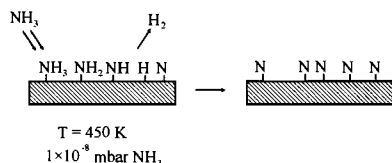
### 4.4.1 Comparison of methods to prepare N<sub>ads</sub> on Rh(111)

Figure 4.7 schematically summarizes the three methods we have explored for deposition of atomic nitrogen on Rh(111): (i) low-temperature NO adsorption followed by H<sub>2</sub> reaction, (ii) NH<sub>3</sub> decomposition, and (iii) exposure to NO+H<sub>2</sub> reaction mixtures. Consecutive reaction between NO and H<sub>2</sub> is the preferred method to deposit controllable amounts of atomic nitrogen. However, this method is only quantitative for NO (N<sub>ads</sub>) coverages below 0.15 ML, where all NO dissociates upon heating and no N<sub>2</sub> desorption

### Consecutive NO + H<sub>2</sub> reaction



### Ammonia decomposition



### In situ NO + H<sub>2</sub> reaction

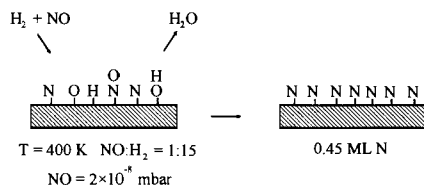


**Figure 4.7** Schematic representation of the three procedures to prepare atomic nitrogen layers on Rh(111).

occurs below 400 K. Deposition of atomic nitrogen by NH<sub>3</sub> decomposition at temperatures above 400 K is very well possible, but undesirable due to deteriorating UHV conditions. Exposure of Rh(111) to NO+H<sub>2</sub> reaction mixtures at 400 K is the obvious way to prepare high coverages of atomic nitrogen. On Rh(110), the experimental method used to deposit atomic nitrogen has a significant influence on the N<sub>2</sub> desorption behaviour [13,14,22]. On Rh(111), this effect on the N<sub>2</sub> desorption is less pronounced. Nevertheless, we will address some peculiarities of the N<sub>2</sub> desorption behaviour in the following section.

#### 4.4.2 N<sub>2</sub> desorption from atomic nitrogen layers

One of the interesting features of N-N recombination is the role of lateral interactions which have been recognized in NO TPD experiments [8, 15]. However, in NO TPD experiments, N<sub>2</sub> desorption is quite complex, since lateral interactions between N, O and NO play a role. The determination of the kinetic parameters for N<sub>2</sub> desorption from atomic nitrogen layers has been an issue of considerable interest [10,11,17,18]. Zhdanov [17] recently simulated N<sub>2</sub> desorption from atomic nitrogen layers on Rh(111) using the data previously reported by Belton *et al.* [10]. A second order desorption

mechanism and an assumed pre-exponential of  $10^{13} \text{ s}^{-1}$  yielded an activation energy of 167 kJ/mol for low coverage and an N-N lateral interaction energy of 7 kJ/mol. These results illustrate that the deviations from ordinary second order desorption can be explained solely by repulsive lateral interactions between nitrogen atoms. This explanation seems more solid than that of Belton *et al.* [10], who used three discrete N adsorption states to simulate  $\text{N}_2$  desorption at high coverages.

$\nu$ [ $\text{s}^{-1}$ ]	$E_{\text{act}}$ [kJ/mol]	$\beta$ [K/s]	Reference	
$10^{13}$	167	10	[17]	<b>Table 4.1</b> Comparison of $\text{N}_2$ desorption parameters from $\text{N}_{\text{ads}}$ layers on Rh(111) in the limit of zero coverage. An asterisk indicates $\text{N}_2$ desorption from NO.
$5.10^{11}$	147	10	[11]	
$10^{10}$	118	10	[15]*	
$3.10^8$	97	8.2	[18]	
$3.10^{10}$	129	10	[9]*	
$3.10^{10}$	120	10	[this work]	

Table 4.1 shows a comparison of the  $\text{N}_2$  desorption parameters in the limit of zero coverage as reported by various authors. The variation in the reported values is quite large, although there is a clear correlation between pre-exponential factor and activation energy, *e.g.* Obuchi *et al.* [18] report both a low pre-exponential factor and a low activation energy. Our values are in between those reported by the other authors and most closely resemble those of Borg *et al.* [15]. All authors describe  $\text{N}_2$  desorption at low coverages by a second order process.

The atomic nitrogen layers prepared by low-temperature NO adsorption followed by reaction with  $\text{H}_2$  show second order desorption behaviour for atomic nitrogen coverages smaller than 0.13 ML, see Figure 4.4. At higher coverages the spectra show broadening at the high-temperature side. In principle, the delayed  $\text{N}_2$  formation can be a consequence of a stronger adsorption site for atomic nitrogen, but can also be a result of another rate-limiting process, like for instance diffusion of atomic nitrogen from the bulk to the surface. In this respect it is interesting to make a comparison with the situation on Rh(110). On this surface N-induced reconstructions have been reported by several authors [13,14,22]. Both  $(2 \times 1)$ -N and  $(3 \times 1)$ -N ordered phases are observed by LEED on the Rh(110) surface. Formation of these ordered structures was accompanied by reconstruction of the Rh(110) surface and resulted in a shift of  $\text{N}_2$  desorption to higher temperatures. Kiskinova *et al.* [14] found that the presence of small amounts of subsurface oxygen resulted in a significant shift of  $\text{N}_2$  desorption to higher temperatures. A discrepancy between TPD deduced coverages and AES nitrogen intensities led several authors [13,22] to conclude that subsurface N is easily formed on Rh(110) at high coverages. Also the formation of 'subsurface oxygen' has been reported by several authors [16,23-25]

On Rh(111) ordering of pure atomic nitrogen layers has never been observed. The

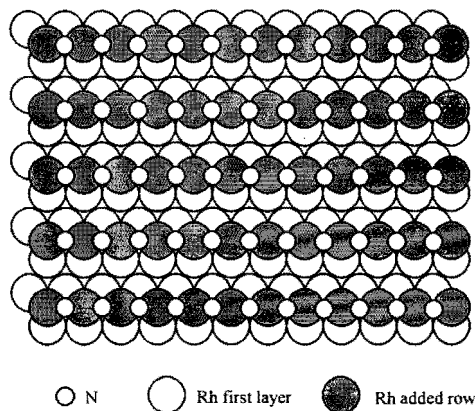


**Figure 4.8** Schematic representation of the  $(2 \times 1)$ -N ordered structure as proposed by Xu and Ng [26]. The Rh(111) surface shows a  $(2 \times 1)$  "added row" reconstruction.

role of oxygen in the formation of ordered structures on Rh(111) has been illustrated by a recent STM study on the adsorption of NO on oxygen precovered surfaces by Xu and Ng [26]. Atomic nitrogen was found to segregate into islands and to order in linear chains forming a  $(1 \times 2)$ -N structure. Figure 4.8 shows a schematic representation of the  $(1 \times 2)$ -N structure as proposed by Xu and Ng [26]. For the formation of this  $(1 \times 2)$ -N phase, a significant surface reconstruction is necessary, since added rows of Rh atoms are formed. This is the first time that a reconstruction of the Rh(111) surface, which as all fcc (111) surfaces is supposed to be very rigid, is reported. Unfortunately, Xu and Ng [26] did not perform TPD experiments of the ordered layers they observed by STM. Hence it remains unclear whether the formation of the ordered  $(2 \times 1)$ -N structure results in an increase of the adsorption energy and consequently a shift of  $N_2$  desorption to higher temperatures.

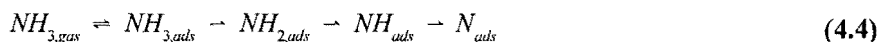
Although we can not rule out that the  $(2 \times 1)$ -N ordered phase is formed in the mixed N+O layers we produce by dissociation of NO at 400 K, we do not believe that ordering of atomic nitrogen is the reason for the delayed  $N_2$  formation for atomic nitrogen coverages above 0.13 ML. Since only a small amount of the nitrogen desorbs at higher temperature this would imply that only a small part of the atomic nitrogen is present in the more stable ordered phase while the majority remains present in the disordered phase. We tentatively attribute the delayed  $N_2$  formation to the existence of a subsurface state of atomic nitrogen. Support for this interpretation comes from a comparison of the SIMS results of Figure 4.2 and the TPD results of Figure 4.3. For initial NO coverages above 0.45 ML, the TPD results of Figure 4.3 indicate that the amount of atomic nitrogen that is deposited by the dissociation of NO increases. However, this increase is not reflected by an increase of the  $Rh_2N^+/Rh_2^+$  SIMS intensity ratio. Although at higher coverages, deviations from linearity between the  $Rh_2N^+/Rh_2^+$  SIMS intensity ratio and the atomic nitrogen coverage can be expected, it is quite unlikely that the dependence changes very abruptly and a very significant increase of the atomic nitrogen coverage cannot be observed by a change in the  $Rh_2N^+/Rh_2^+$  SIMS intensity ratio. It is important to note that the  $Rh_2O^+/Rh_2^+$  SIMS intensity ratio also remains constant, whereas the amount of atomic

nitrogen and, consequently, the amount of atomic oxygen increases. This might indicate that also subsurface atomic oxygen is formed.

There is apparently a threshold for the formation of subsurface N and/or O around an initial NO coverage of 0.45 ML. Interestingly, this is also the coverage regime where the NO dissociation mechanism changes, see also paragraph 3.5.3. Below 0.45 ML, NO dissociates predominantly before NO desorbs. With NO coverages higher than about 0.45 ML NO, dissociation is, however, almost completely inhibited until NO desorption starts around 400 K. Furthermore, the amount of NO that dissociates during a TPD experiment starts to increase at initial NO coverages above about 0.45 ML. Summarizing, with initial NO coverages above 0.45 ML, larger amounts of atomic N and O are formed at temperatures around 400 K, which forces part of the atomic nitrogen and/or oxygen into a 'subsurface' state.

#### 4.4.3 NH<sub>3</sub> decomposition

In this section we discuss the deposition of atomic nitrogen by NH<sub>3</sub> decomposition in order to determine kinetic parameters for the latter process. At 450 K the ammonia desorption rate is much faster than the ammonia decomposition rate (see also Chapter 6). For this reason, the ammonia adsorption can be assumed to be at equilibrium during the experiment. Furthermore, H<sub>2</sub> that is formed by NH<sub>3</sub> decomposition will desorb instantaneously resulting in a very small steady state coverage of hydrogen on the surface. Rehydrogenation of NH<sub>x</sub> fragments seems, therefore, very unlikely. Based on these assumptions we propose the following reaction scheme:



The ammonia adsorption rate can be derived from the collision theory. For an ammonia pressure of  $1 \times 10^{-8}$  mbar and a gas temperature of 300 K the number of NH<sub>3</sub> molecules that collides with the surface is  $\sim 3.7 \times 10^{16}$  [1/m<sup>2</sup>.s]. If we assume that the sticking coefficient is unity, the ammonia adsorption rate at  $1 \times 10^{-8}$  mbar equals 0.0023 [ML/s]. For ammonia desorption from Rh(111) we have determined an activation energy of 81 [kJ/mol] assuming a pre-exponential factor of  $10^{13}$  [s<sup>-1</sup>], see Chapter 6. From these values we can calculate the steady-state NH<sub>3</sub> coverage as follows:

$$\frac{d \Theta_{NH_3}}{d t} = r_{\text{ads}} - v_{\text{des}} \cdot \Theta_{NH_3} \cdot e^{-\frac{E_{\text{des}}}{RT}} - v_{\text{dec}} \cdot \Theta_{NH_3} \cdot e^{-\frac{E_{\text{dec}}}{RT}} = 0$$

$$\Theta_{NH_3} = \frac{r_{\text{ads}}}{v_{\text{des}} \cdot e^{-\frac{E_{\text{des}}}{RT}} + v_{\text{dec}} \cdot e^{-\frac{E_{\text{dec}}}{RT}}} \approx 6 \cdot 10^{-7} \text{ [ML]} \quad (4.5)$$

Since at 450 K  $N_2$  desorption does not proceed at these low coverages, the  $NH_3$  decomposition rate can be calculated from the increase of the atomic nitrogen coverage with time, see Figure 4.5. From the initial slope of the curve, an  $NH_3$  decomposition rate of  $1.9 \times 10^{-4}$  [ML/s] is calculated. Using this value, the  $NH_3$  steady state coverage can be calculated from equation 4.5, yielding a very small value of  $6 \times 10^{-7}$  [ML]

$$\frac{d \Theta_N}{d t} = k_{dis} \cdot \Theta_{NH_3} = \nu \cdot e^{-\frac{E_{act}}{RT}} \cdot \Theta_{NH_3} \quad (4.6)$$

If we assume a pre-exponential factor of  $10^{13}$  [ $s^{-1}$ ], we find an activation energy for  $NH_3$  decomposition of 90 [kJ/mol]. Although this is a rather rough calculation, it very well illustrates that ammonia desorption is much faster than ammonia decomposition. At 450 K the ratio between the rates of ammonia desorption and decomposition is approximately 10.

## 4.5 Conclusions

Adsorption of NO at low temperature followed by heating to 400 K and reaction with  $H_2$  is a suitable method to deposit atomic nitrogen on Rh(111). For coverages below 0.13 ML, atomic nitrogen can be deposited in an adjustable way. In this coverage range, the  $N_2$  TPD spectra show a second order desorption behaviour which is best described by a pre-exponential factor and activation energy of  $10^{10.5 \pm 1}$   $s^{-1}$  and  $120 \pm 3$  kJ/mol, respectively, in the limit of zero coverage. For initial NO coverages higher than 0.45 ML, atomic nitrogen coverages in excess of 0.13 ML can be obtained. However, part of the atomic nitrogen thus applied desorbs at higher temperatures, which is attributed to the formation of 'subsurface' nitrogen.

Atomic nitrogen can be deposited by exposure to  $NH_3$  at elevated temperatures. Initially the amount of deposited atomic nitrogen is proportional to the exposure time. The activation energy for  $NH_3$  decomposition was determined from the increase of the atomic nitrogen coverage with time. Assuming equilibrium adsorption of  $NH_3$  and choosing a pre-exponential factor of  $10^{13}$  [ $s^{-1}$ ] for  $NH_3$  decomposition leads to an activation energy of  $\sim 90$  kJ/mol.

Reaction between NO and  $H_2$  at 400 K temperatures can produce atomic nitrogen coverages as high as 0.45 ML. Reaction at lower temperatures results in the accumulation of atomic oxygen and NO on the surface in the pressure regime investigated ( $P_{tot} < 10^{-6}$  mbar). We have not observed ordering of atomic nitrogen by LEED measurements.

**References**

- [1] C.H.F. Peden, D.N. Belton, and S.J. Schmieg, *J. Catal.* 155 (1995) 204.
- [2] V.P. Zhdanov and B. Kasemo, *Catal. Lett.* 40 (1996) 197.
- [3] H. Permana, K.Y.S. Ng, C.H.F. Peden, S.J. Schmieg, and D.N. Belton, *J. Phys. Chem.* 99 (1995) 16344.
- [4] H. Permana, K.Y.S. Ng, C.H.F. Peden, S.J. Schmieg, D.K. Lambert, and D.N. Belton, *J. Catal.* 164 (1996) 194.
- [5] A.A. Tolia, C.T. Williams, C.G. Takoudis, M.J. Weaver, *J. Phys. Chem.* 99 (1995) 4599.
- [6] S.H. Oh, G.B. Fisher, J.E. Carpenter, and D.W. Goodman, *J. Catal.* 100 (1986) 360.
- [7] R.J. Baird, R.C. Ku, and P. Wynblatt, *Surf. Sci.* 97 (1980) 346.
- [8] T.W. Root, L.D. Schmidt, and G.B. Fisher, *Surf. Sci.* 134 (1983) 30.
- [9] D.O. Hayward, B.M.W. Trapnell, *Chemisorption*, Butterworth: London, 1964.
- [10] D.N. Belton, C.L. DiMaggio, and K.Y.S. Ng, *J. Catal.* 144 (1993) 273.
- [11] L. Bugyi and F. Solymosi, *Surf. Sci.* 258 (1991) 55.
- [12] P.W. Murray, F.M. Leibsle, G. Thornton, M. Bowker, V.R. Dhanak, A. Baraldi, M. Kiskinova, R. Rosei, *Surf. Sci.* 304 (1994) 48.
- [13] S. Lizzit, G. Comelli, Ph. Hofmann, G. Paolucci, M. Kiskinova, and R. Rosei, *Surf. Sci.* 276 (1992) 144.
- [14] M. Kiskinova, S. Lizzit, G. Comelli, G. Paolucci, and R. Rosei, *Appl. Surf. Sci.* 64 (1993) 185.
- [15] H.J. Borg, J.F.C.-J.M. Reijerse, R.A. van Santen, and J.W. Niemantsverdriet, *J. Chem. Phys.* 101 (1994) 10052.
- [16] K.D. Gibson, J.I. Colonell, S.J. Sibener, *Surf. Sci.* 343 (1995) L1151.
- [17] V.P. Zhdanov, *Catal. Lett.* 37 (1996) 163.
- [18] A. Obuchi, S. Naito, T. Onishi, and K. Tamaru, *Surf. Sci.* 130 (1983) 29.
- [19] A.G. Makeev and M.M. Slinko, *Surf. Sci.* 359 (1996) L467.
- [20] S.B. Schwartz, G.B. Fisher, and L.D. Schmidt, *J. Phys. Chem.* 92 (1988) 389.
- [21] D.N. Belton, C.L. DiMaggio, S.J. Schmieg, K.Y.S. Ng, *J. Catal.* 157 (1995) 559.
- [22] G. Comelli, S. Lizzit, Ph. Hoffmann, G. Paolucci, M. Kiskinova, and R. Rosei, *Surf. Sci.* 277 (1992) 31.
- [23] P.A. Thiel, J.T. Yates, and W.H. Weinberg, *Surf. Sci.* 82 (1979) 22.
- [24] P.A. Thiel, J.T. Yates, and W.H. Weinberg, *Surf. Sci.* 90 (1979) 121.
- [25] K.A. Peterlinz and S.J. Sibener, *J. Phys. Chem.* 99 (1995) 2817.
- [26] H. Xu and K.Y.S. Ng, *Surf. Sci.* 365 (1996) 779.



## 5 The mechanism of NH<sub>3</sub> formation on Rh(111)

### 5.1 Introduction

The reduction of NO<sub>x</sub> on rhodium is one of the key reactions that occurs in the automotive exhaust gas convertor. Although the greater part of the NO is reduced by reaction with CO, a substantial part is reduced by hydrogen which is present in exhaust gas and which is, moreover, formed on the surface of the metal particles by decomposition of hydrocarbons and by the water gas shift reaction [1,2]. NO reduction by H<sub>2</sub> may yield three different N-containing products, viz. N<sub>2</sub>, N<sub>2</sub>O and NH<sub>3</sub>, of which the latter two are undesirable from an environmental point of view.

Kinetic studies of the NO+H<sub>2</sub> reaction have been performed on Pt foil [3], Rh foil [4], Pt/Rh single crystals [5,6], Rh/SiO<sub>2</sub> [7], and Rh/Al<sub>2</sub>O<sub>3</sub> [8]. These studies have shown that the reactivity of atomic nitrogen, which is formed by the dissociation of NO, plays a key role in the selectivity issue of the NO+H<sub>2</sub> reaction. Whereas reactions, such as, the NO dissociation [9-11] and the recombination of atomic nitrogen to N<sub>2</sub> [12,13], have been studied extensively, the microscopic mechanisms of N<sub>2</sub>O and NH<sub>3</sub> formation are still unknown. NH<sub>3</sub> formation is commonly described by the stepwise hydrogenation of atomic nitrogen [14]. Indeed, many reports on NH and NH<sub>x</sub> species exist. On Rh(100) [15] and Pt/Rh(100) [6,16] evidence was found by EELS for an NH intermediate which was reversibly formed when a c(2×2)-N adlayer was exposed to H<sub>2</sub>. Zemlyanov *et al.* [17] observed an NH intermediate during the NO+H<sub>2</sub> reaction on Pt(100) by EELS. Prasad and Gland [18] explained the formation of diimide N<sub>2</sub>H<sub>2</sub> during the decomposition of NH<sub>3</sub> and N<sub>2</sub>H<sub>4</sub> on Rh foil by the coupling of NH species on the surface. NH<sub>x</sub> intermediates were also observed in NH<sub>3</sub> and N<sub>2</sub>H<sub>4</sub> decomposition studies on Ni [19,20], Pt [21], Rh [22,23] and Ru [24].

Recently, the NO+H<sub>2</sub> reaction regained interest, in the context of chemical waves and oscillations which develop under specific reaction conditions on Rh single crystal planes [25-30]. Cholach *et al.* [30] concluded that the moving wave front, as observed in FEM, represents the hydrogenation of the atomic nitrogen layer, followed by the decomposition and/or dissociation of NH<sub>x</sub> species into N<sub>2</sub>.

The purpose of this paper is to reveal the mechanism of NH<sub>3</sub> formation on Rh(111). Since the details of the NH<sub>3</sub> formation in the NO+H<sub>2</sub> reaction are concealed by simultaneously running reactions, such as, NO dissociation, N<sub>2</sub> and H<sub>2</sub>O formation, we have chosen to study the NH<sub>3</sub> formation starting from a well defined atomic nitrogen layer. We have prepared atomic nitrogen layers by adsorbing NO at low temperature and removing the O-atoms selectively by reaction with H<sub>2</sub> at temperatures where N-atoms are not yet hydrogenated or desorb as N<sub>2</sub>. Details of the preparation method are described in Chapter 4. Finally, Secondary Ion Mass Spectrometry (SIMS) applied under reaction conditions reveals that NH<sub>2,ads</sub> is the dominant NH<sub>x</sub> species on the surface during the N-hydrogenation.

## 5.2 Experimental

TPD and SIMS experiments were done in a stainless steel ultra-high vacuum (UHV) system, pumped by a 360  $\ell$ /s turbomolecular pump and a water-cooled titanium sublimation pump. The base pressure was typically around  $5 \times 10^{-11}$  mbar, and mass spectra of the residual gas indicated the presence of mainly  $H_2$ , CO and  $CO_2$ . The system is equipped with a Leybold SSM 200 quadrupole mass spectrometer for TPD and SIMS, and a Leybold EA 10 hemispherical energy analyzer, for AES and  $\Delta\phi$  measurements. Both analyzers are interfaced with a PC for data storage.

SIMS measurements were carried out in the static (low damage) mode. Typically, we used a defocused 5 keV primary  $Ar^+$  beam with a current density of 1-10 nA/cm<sup>2</sup>. To average possible anisotropies in the secondary ion emission process we applied a target bias of +45 V and an extractor voltage of -300 V on the entrance lens of the quadrupole system.

The UHV system contained a rhodium crystal which was cut in the [111] orientation within  $0.5^\circ$  and polished according to standard procedures. The temperature was measured by a chromel-alumel thermocouple spotwelded on the back of the crystal. The standard cleaning procedure consisted of an argon sputter treatment (900 K, 1.5 keV, 5  $\mu$ A/cm<sup>2</sup>) followed by annealing in  $2 \times 10^{-8}$  mbar  $O_2$  (900 K-1100 K) and a final annealing treatment in vacuum at 1420 K. The gases, NO (Messer Griesheim, 99.5%) and  $H_2$  (Messer Griesheim, 99.995%), were used without further treatment. Exposures are reported in Langmuirs (1L =  $1.33 \times 10^{-6}$  mbar.s) and coverages are expressed with respect to the number of Rh surface atoms (1 ML =  $1.6 \times 10^{15}$  cm<sup>-2</sup>).

Atomic nitrogen layers with a coverage of 0.10 ML were obtained by adsorbing 0.25 L NO at 120 K and selectively removing the atomic oxygen at 375 K by reaction with  $2 \times 10^{-8}$  mbar hydrogen during 160 s. The atomic nitrogen layers were exposed to  $H_2$  at various pressures and temperatures. The amount of nitrogen remaining after the hydrogenation experiment was determined by TPD. Although the surface also contained  $NH_x$  intermediates,  $N_2$  was the only nitrogen containing desorption product observed. We mention here that the experiments were only possible with an excellent background pressure ( $p < 5 \times 10^{-11}$  mbar), where CO adsorption during the reaction procedure can be prevented.

## 5.3 Results

### 5.3.1 Preparation of atomic nitrogen layers on Rh(111)

For all the experiments we started from an atomic nitrogen layer with a coverage of 0.10 ML ( $\pm 3\%$ ). The atomic nitrogen layer was obtained by adsorption of 0.10 ML NO at 120 K, heating to 375 K to dissociate the NO, and reaction with hydrogen at 375 K to remove the oxygen. Since the initial NO coverage is small, heating to 375 K is sufficient

to dissociate all NO. SIMS indicated that all atomic oxygen could be removed by reaction with  $2 \times 10^{-8}$  mbar  $\text{H}_2$  for 160 seconds at 375 K. We have used a reaction temperature of 375 K in order to entirely exclude  $\text{N}_2$  desorption during the oxygen removal treatment. Further details on the preparation method are described in Chapter 4.

### 5.3.2 Hydrogenation of atomic nitrogen at constant temperature and $\text{H}_2$ pressure

In this section we show how the coverage of an atomic nitrogen layer decreases when it is exposed to a constant  $\text{H}_2$  pressure at a fixed temperature. The decrease of the atomic nitrogen coverage was determined by comparing the  $\text{N}_2$  TPD area after a hydrogenation experiment with the  $\text{N}_2$  TPD area of the initial atomic nitrogen layer.

As we will show in the discussion section, the hydrogen adsorption readily equilibrates under our reaction conditions. We have restricted the upper temperature limit to 400 K in order to prevent that  $\text{N}_2$  formation and desorption takes place during the experiment. We found that up to 400 K the atomic nitrogen coverage remained unchanged when the crystal was kept isothermally in vacuum for several minutes. Under these conditions the rate of ammonia formation equals the decrease of the atomic nitrogen coverage and can be written as:

$$r_{\text{NH}_3} = - \frac{d\theta_{\text{N},\text{tot}}}{dt} = k_{\text{eff}} \cdot \theta_{\text{N},\text{tot}}^n \cdot \theta_{\text{H}}^m = k'_{\text{eff}} \cdot \theta_{\text{N},\text{tot}}^n \quad (5.1)$$

In this equation  $\theta_{\text{N},\text{tot}}$  represents the total of the nitrogen containing products as determined in the TPD experiment (all the  $\text{NH}_x$  intermediates decompose when the hydrogen pressure is removed and desorb as  $\text{N}_2$  in the subsequent desorption experiment). It can be shown that this equation is valid, independent of which hydrogenation step is rate-determining as long as the equilibrium between the  $\text{NH}_x$  intermediates before the rate determining step is maintained. The decrease of the nitrogen coverage with time is determined by the  $n^{\text{th}}$  order dependence of the ammonia formation rate on the nitrogen coverage. Figure 5.1 shows the decrease of the nitrogen coverage with time at  $T=375$  K and  $p_{\text{H}_2}=2 \times 10^{-7}$  mbar, and at  $T=400$  K and  $p_{\text{H}_2}=5 \times 10^{-7}$  mbar. Although the nitrogen coverage continues to decrease below 0.04 ML, the data are not shown in Figure 5.1, since the relative error in the remaining  $\text{N}_{\text{ads}}$  coverage determination by TPD becomes too large.

The decreasing slope of the  $\theta_{\text{N}}$  coverage-versus-time curve indicates a positive order  $n$  of the ammonia formation rate with respect to the nitrogen coverage. If the order  $n$  is assumed to be unity, integration of Equation 5.1 yields:

$$\ln \left( \frac{\theta_{\text{N},\text{tot}}(t)}{\theta_{\text{N},\text{tot}}(0)} \right) = - k'_{\text{eff}} \cdot t \quad (5.2)$$

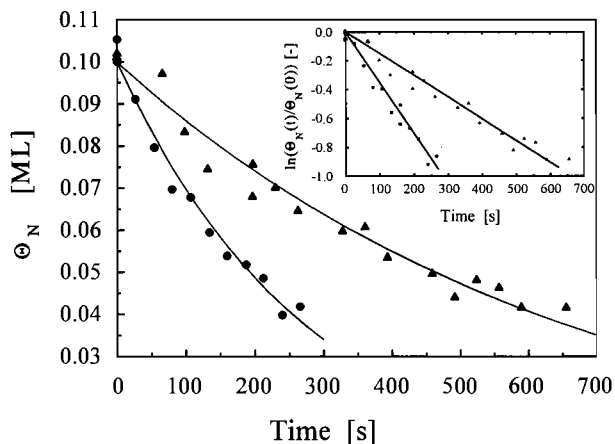


**Figure 5.1** Decrease of the atomic nitrogen coverage with time due to reaction with  $H_2$  at constant temperature and pressure. The inset shows that a linear relation is obtained when the ratio of the initial to the remaining atomic nitrogen coverage is plotted versus the time, indicating that the hydrogenation rate is first order in the atomic nitrogen coverage.

where  $\theta_N(t)$  and  $\theta_N(0)$  are the nitrogen coverages after and before reaction, respectively. The inset of Figure 5.2 confirms that a linear relation is obtained if the logarithm of the coverage ratio is plotted versus the time. This indicates that the ammonia formation rate is proportional to the nitrogen coverage.

### 5.3.3 Dependence of the $NH_3$ formation rate on the $H_2$ pressure

The  $H_2$  pressure dependence of the  $NH_3$  formation rate can give information on the rate-determining step in the consecutive hydrogenation of atomic nitrogen to  $NH_3$ . Under the applied reaction conditions, the hydrogen atom coverage is expected to be small ( $\theta_H \ll 1$ ) and therefore proportional to the square root of the  $H_2$  pressure. In this case the following general dependence is expected:

$$\ln \left( \frac{\theta_{N,tot}(t)}{\theta_{N,tot}(0)} \right) = -k_{eff} \cdot \theta_H^m \cdot t = -k_{eff}'' \cdot p_{H_2}^{m/2} \cdot t \quad (5.3)$$

The pressure dependence of the hydrogenation rate was investigated by keeping the reaction time constant at 160 s and varying the  $H_2$  pressure in the range between  $2 \times 10^{-8}$  and  $1 \times 10^{-6}$  mbar. Figure 5.2 shows a plot of the logarithm of the ratio of the remaining and initial  $N_{ads}$  coverage versus the hydrogen pressure at 375 K. The curve shows that for pressures below  $5 \times 10^{-7}$  mbar, the dependence is close to linear, while the dependence levels off in the pressure range from  $5 \times 10^{-7}$  to  $1 \times 10^{-6}$  mbar. A similar experiment at 400 K showed a similar  $H_2$  pressure dependence.

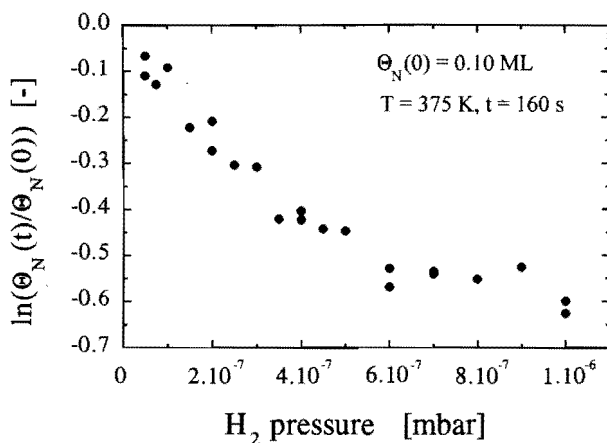


**Figure 5.2** The influence of the  $\text{H}_2$  pressure on the hydrogenation rate indicated by plotting the  $\ln(\theta_{\text{N}}(t)/\theta_{\text{N}}(0))$  after 160 s of reaction versus the  $\text{H}_2$  pressure. Initially the hydrogenation rate is linearly proportional to the  $\text{H}_2$  pressure, but the dependence levels off above  $\approx 5 \times 10^{-7}$  mbar  $\text{H}_2$ .

Based on these results only, assignment of the rate-determining step is not possible. However, we definitely conclude that the first hydrogenation step is not rate-limiting. In that case, the  $\text{H}_2$  pressure dependence would be at most a square root dependence. Figure 5.2, however, shows a linear dependence for  $\text{H}_2$  pressures below  $5 \times 10^{-7}$  mbar.

### 5.3.4 Identification of $\text{NH}_x$ reaction intermediates by SIMS

For elucidating the hydrogenation mechanism of atomic nitrogen to  $\text{NH}_3$ , the identification of surface intermediates is of great significance. In previous studies, SIMS has successfully been applied to identify  $\text{NH}_x$  intermediates on the surface [31,32]. This section presents the SIMS results of the  $\text{Rh}(111)$  surface during N hydrogenation. The collection time for a SIMS spectrum was 15 seconds, which is about 10% of the time scale of a typical hydrogenation experiment. Spectra were taken after 20 s of reaction to be sure that equilibrium was established between the  $\text{NH}_x$  intermediates and to compare different reaction conditions with similar nitrogen coverages.

Figure 5.3 shows two characteristic mass regions of a SIMS spectrum of the  $\text{Rh}(111)$  surface taken after 20 seconds of reaction at  $5 \times 10^{-7}$  mbar  $\text{H}_2$  and 375 K. The presence of  $\text{NH}_3$  on the surface is evidenced by the appearance of the  $\text{Rh}(\text{NH}_3)^+$  cluster ion at  $m/e=120$ . In the high mass range,  $\text{N}_{\text{ads}}$  and  $\text{NH}_{2,\text{ads}}$  are observed as predominant surface species by the appearance of the  $\text{Rh}_2\text{N}^+$  and  $\text{Rh}_2(\text{NH}_2)^+$  cluster ions at  $m/e=220$  and  $m/e=222$ , respectively. From a previous investigation we know that the  $\text{Rh}_2(\text{NH}_2)^+$  cluster ion is not a consequence of the presence of  $\text{NH}_3$  on the surface [32]. The presence of hydrogen on the surface is evidenced by the appearance of the  $\text{Rh}_2\text{H}^+$  peak at  $m/e=207$ , which is not fully resolved from the  $\text{Rh}_2^+$  peak, however. To facilitate the assignment of

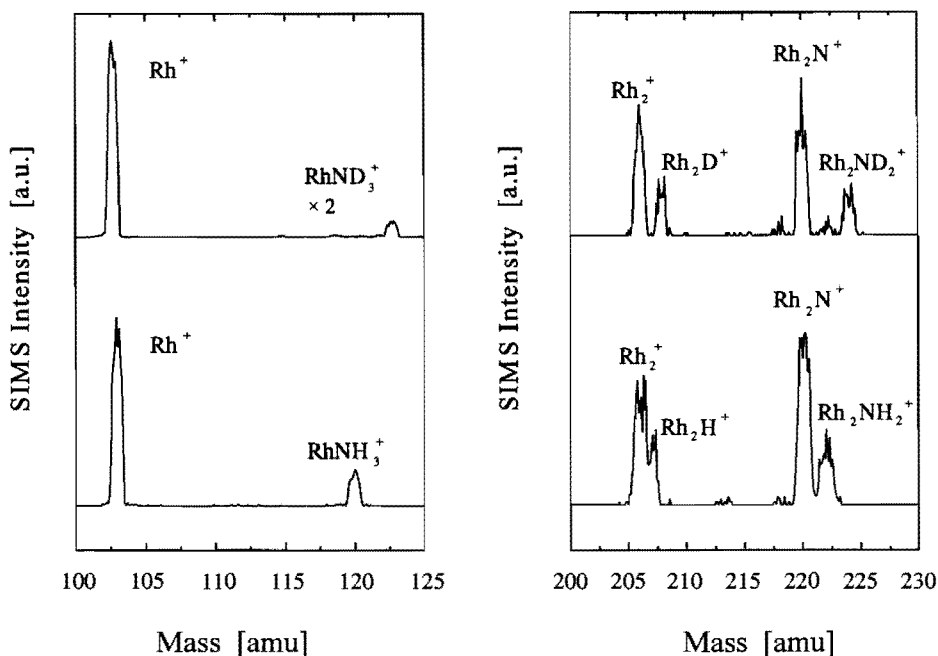


**Figure 5.3** SIMS spectra of the Rh(111) surface during a hydrogenation experiment showing the presence of H ( $\text{Rh}_2\text{H}^+$  207 amu), N ( $\text{Rh}_2\text{N}^+$  220 amu),  $\text{NH}_2$  ( $\text{Rh}_2\text{NH}_2^+$  222 amu) and  $\text{NH}_3$  ( $\text{RhNH}_3^+$  120 amu) as reaction intermediates. Peak assignments were verified by using  $\text{D}_2$  instead of  $\text{H}_2$ . The spectrum was taken after 20 s of reaction, the  $\text{H}_2$  pressure was  $5 \times 10^{-7}$  mbar and  $T=375$  K.

the SIMS peaks,  $\text{H}_2$  was exchanged for  $\text{D}_2$  which resulted in the expected mass shifts, as Figure 5.3 shows. In this case also a small peak at  $m/e=222$  is resolved. Whether this peak stems from the presence of ND on the surface or results from fragmentation of  $\text{ND}_2$  is unknown.

Although the presence of N,  $\text{NH}_2$  and  $\text{NH}_3$  on the surface is clearly established by the spectra in Figure 5.3, interpretation of the peak intensities in terms of surface coverages is rather complicated. Previous studies have shown that SIMS peak intensity ratios can give quantitative information about coverages of adsorbates [32-34]. However, it should be noted that occasionally non-linear correlations between intensity ratios and coverage are observed. Therefore, careful calibration is required in order to obtain quantitative information from SIMS measurements. For  $\text{NH}_3$  we have been able to do such a calibration by studying the adsorption of  $\text{NH}_3$  on Rh(111), see Chapter 6. In the case of  $\text{NH}_x$  intermediates, however, calibration is much more difficult since no methods are at hand to prepare well defined coverages of  $\text{NH}_x$  species on the surface. We have therefore assumed that the  $\text{Rh}_2\text{NH}_2^+/\text{Rh}_2\text{N}^+$  peak ratio reflects at least qualitatively the coverage ratio of  $\text{NH}_2$  and N on the surface. The intensity of the  $\text{Rh}_2^+$  peak was not used

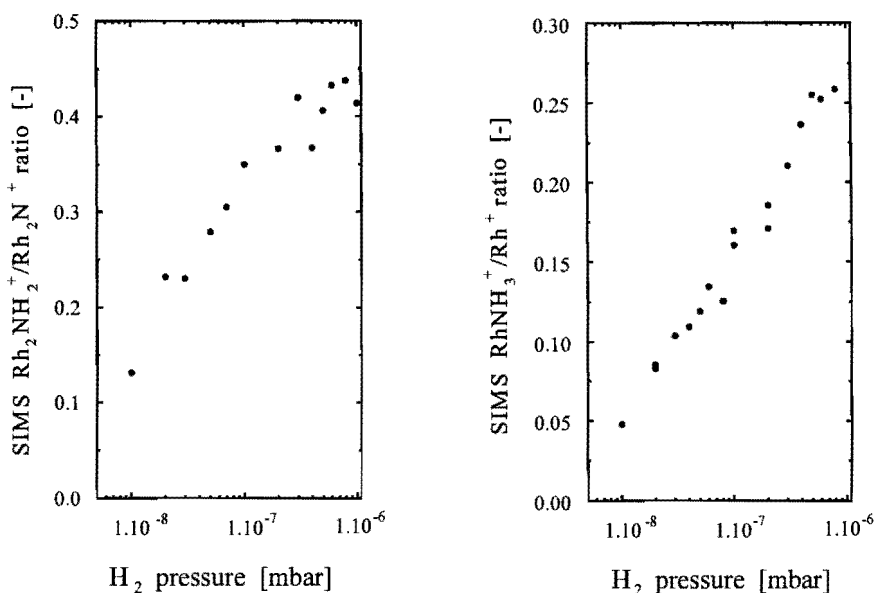


**Figure 5.4** The left panel shows the  $\text{H}_2$  pressure dependence of the SIMS  $\text{Rh}_2\text{NH}_2^+/\text{Rh}_2\text{N}^+$  peak intensity ratio which, initially, increases with  $\text{H}_2$  pressure but reaches a saturation value of  $\approx 0.43$  above  $5 \times 10^{-7}$  mbar. The right panel shows the dependence of the  $\text{RhNH}_3^+/\text{Rh}^+$  peak intensity ratio which monotonically increases with the  $\text{H}_2$  pressure. In both cases the temperature was 375 K and the SIMS spectra were taken after 20 s of reaction.

as a reference, since it was not fully resolved from the  $\text{Rh}_2\text{H}^+$  peak.

Figure 5.4 shows the  $\text{H}_2$  pressure dependence of the  $\text{Rh}(\text{NH}_3)^+/\text{Rh}^+$  and  $\text{Rh}(\text{NH}_2)^+/\text{RhN}^+$  peak intensity ratios at a constant temperature of 375 K. The SIMS spectra were taken after 20 s of reaction. The  $\text{Rh}(\text{NH}_2)^+/\text{RhN}^+$  peak intensity ratio increases in the  $\text{H}_2$  pressure regime between  $1 \times 10^{-8}$  and  $\approx 5 \times 10^{-7}$  mbar, but becomes constant at higher  $\text{H}_2$  pressures. The  $\text{Rh}(\text{NH}_3)^+/\text{Rh}^+$  peak intensity ratio increases over the whole pressure regime. Thus,  $\text{NH}_2$  is the predominant  $\text{NH}_x$  species during the hydrogenation of atomic nitrogen, while small amounts of  $\text{NH}_3$  are present as well. The coverage of both  $\text{NH}_2$  and  $\text{NH}_3$  rises at increasing  $\text{H}_2$  pressure, but for  $\text{NH}_2$  the dependence levels off to a constant value at a pressure of about  $5 \cdot 10^{-7}$  mbar.

We have also investigated the influence of the temperature on the presence of the intermediates on the surface. Figure 5.5 shows the dependence of the  $\text{Rh}(\text{NH}_3)^+/\text{Rh}^+$  and  $\text{Rh}(\text{NH}_2)^+/\text{RhN}^+$  peak intensity ratios on temperature at a constant  $\text{H}_2$  pressure of  $1 \times 10^{-6}$  mbar, also after 20 s of reaction. The  $\text{Rh}(\text{NH}_3)^+/\text{Rh}^+$  peak ratio increases somewhat up to temperatures of 365 K, whereafter it decreases rapidly. Except for the measurement at 325 K, the  $\text{Rh}(\text{NH}_2)^+/\text{RhN}^+$  peak ratio remains more or less constant over the entire temperature range.

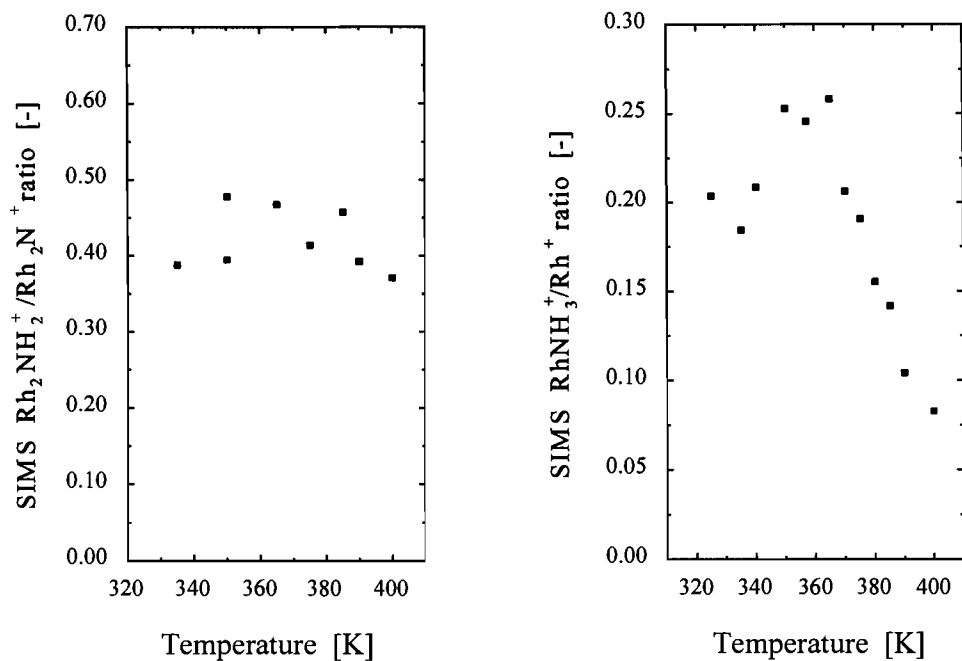


**Figure 5.5** The left panel shows that the SIMS  $\text{Rh}_2\text{NH}_2^+/\text{Rh}_2\text{N}^+$  peak intensity ratio at a  $\text{H}_2$  pressure of  $1 \times 10^{-6}$  mbar is independent of the temperature. The right panel shows that the  $\text{RhNH}_3^+/\text{Rh}^+$  peak intensity ratio first slightly increases with temperature, but decreases rapidly above 360 K. SIMS spectra were taken after 20 s of reaction.

### 5.3.5 Evidence for $\text{NH}_x$ intermediates from TPD

In the literature, much of the evidence for the existence of  $\text{NH}_x$  intermediates is based on the appearance of a reaction limited  $\text{H}_2$  desorption state [23,35,36]. To compare this procedure with our results, we have frozen the intermediates present under reaction conditions by rapid cooling (4 K/s) under  $\text{H}_2$  to 275 K, after which the system was evacuated for 2 minutes and a TPD experiment was performed. Figure 5.6 shows the  $\text{H}_2$  and  $\text{N}_2$  TPD spectra obtained by freezing the reaction at 350 K and  $5 \times 10^{-7}$  mbar  $\text{H}_2$  after 20 seconds. The  $\text{H}_2$  desorption spectrum clearly shows two desorption states. The low-temperature desorption state with a peak maximum at 330 K represents the common second order desorption limited state. The  $\text{H}_2$  desorption state with a peak maximum around 415 K corresponds to a reaction limited state, which is attributed to the decomposition of  $\text{NH}_x$  intermediates.



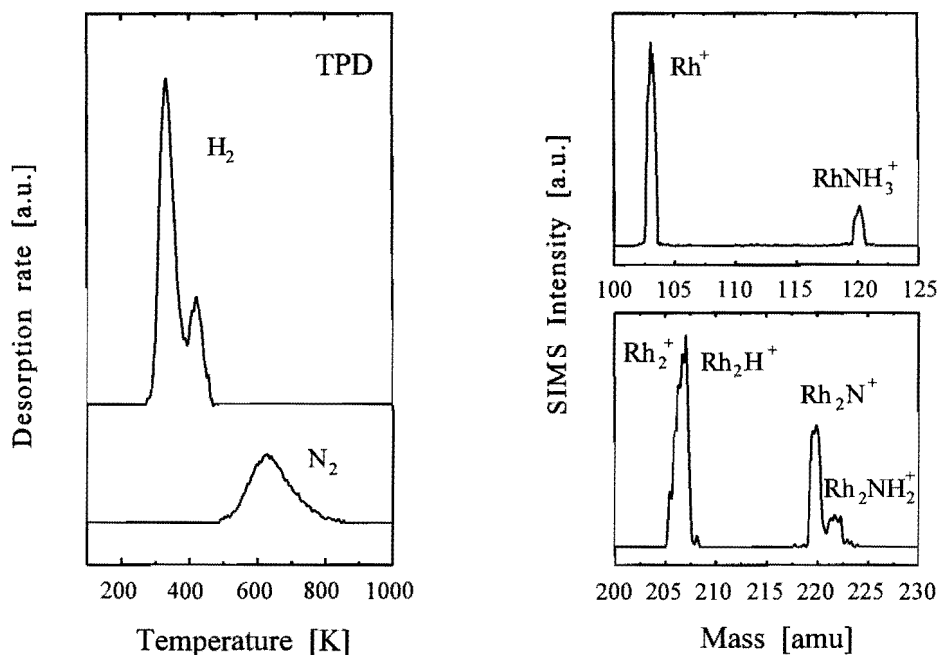


**Figure 5.6** The left panel shows the  $\text{H}_2$  and  $\text{N}_2$  TPD spectra resulting from an  $\text{NH}_x$  covered surface which was obtained by cooling to 270 K after 20 s of reaction at 350 K and  $5 \times 10^{-7}$  mbar  $\text{H}_2$ . The reaction limited  $\text{H}_2$  desorption state at 415 K indicates the presence of  $\text{NH}_x$  intermediates. Comparison of the  $\text{H}_2$  and  $\text{N}_2$  peak areas yields an overall N:H surface ratio in the  $\text{NH}_x$  intermediates of 1:1.1. The right panel shows a SIMS spectrum of the surface before TPD was carried out indicating the presence of H, N,  $\text{NH}_2$  and  $\text{NH}_3$ .

The only nitrogen containing product that was observed during TPD was  $\text{N}_2$ , whereas no  $\text{NH}_3$  and  $\text{N}_2\text{H}_2$  could be detected. Furthermore, it appeared that all  $\text{NH}_x$  had decomposed before  $\text{N}_2$  desorption started at around 500 K. Figure 5.6 also shows a SIMS spectrum of the surface before TPD was performed, which indicates the presence of N,  $\text{NH}_2$  and  $\text{NH}_3$  on the surface.

The ratio between the atomic nitrogen coverage and the amount of hydrogen desorbing in the reaction limited desorption state at 415 K is of interest because it can give additional information about the composition of the  $\text{NH}_x$  intermediate. Comparison of the  $\text{N}_2$  and  $\text{H}_2$  TPD peak areas and correcting for differences in ionization probabilities ( $S_{\text{H}_2}/S_{\text{N}_2}=0.45$ ) yields an overall N:H ratio of 1:1.1 for the  $\text{NH}_x$  intermediates. A different way to determine the N:H ratio is relating the  $\text{N}_2$  and  $\text{H}_2$  TPD areas to the NO and  $\text{H}_2$  uptake curves. In this way, the atomic nitrogen coverage was estimated to be 0.10 ML and the amount of hydrogen desorbing from the reaction limited state was 0.11 ML which results in the same overall N:H ratio of 1:1.1 for the  $\text{NH}_x$  intermediates.

Note that the H:N ratio of 1.1 reflects the overall composition of the surface after 20 s of hydrogenation at 350 K, excluding the atomic hydrogen, and has no bearing on the composition of the  $\text{NH}_x$  species themselves.

### 5.3.6 Dependence of the $\text{NH}_3$ formation rate on temperature

In order to determine the effective Arrhenius parameters, we investigated the rate of  $\text{NH}_3$  formation in the temperature range between 325 and 400 K. In these experiments the  $\text{H}_2$  pressure was kept constant at  $1 \times 10^{-6}$  mbar. Figure 5.7 shows the logarithm of the hydrogenation rate versus the reciprocal temperature. The slope of the curve corresponds to an effective activation energy of 33 kJ/mol while the effective pre-exponential equals  $10^2 \text{ s}^{-1}$ . We use the terms effective activation energy and pre-exponential factor, since several equilibrium and rate constants may be involved depending on the rate-limiting step. At least the hydrogen adsorption equilibrium has to be incorporated, since the  $\text{H}_2$  pressure is kept constant whereas the temperature changes, which results in varying hydrogen coverages.

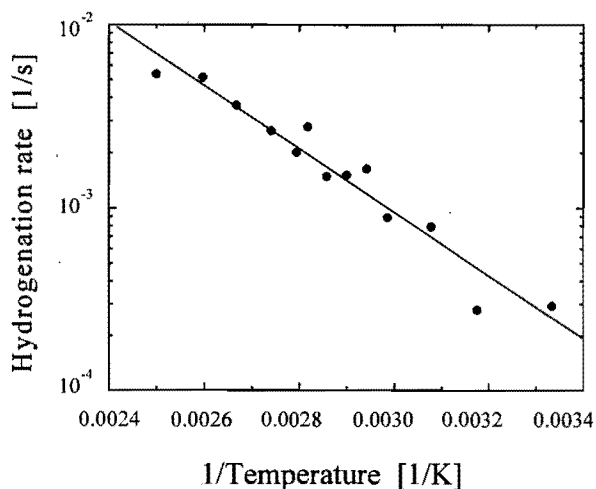


*Figure 5.7* Temperature dependence of the hydrogenation rate determined as  $\ln(\theta_M(0)/\theta_M(t))/t$  after 160 s of reaction at  $1 \times 10^{-6}$  mbar. The effective activation energy was 33 kJ/mol and the effective pre-exponential factor was  $10^2 \text{ s}^{-1}$ .

## 5.4 Discussion

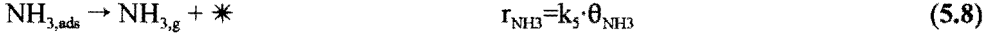
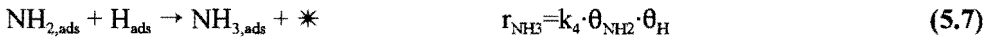
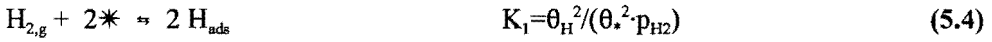
### 5.4.1 Mechanism and kinetic description of $\text{NH}_3$ formation on Rh(111)

With respect to the kinetic mechanism of the step-wise hydrogenation of atomic nitrogen to  $\text{NH}_3$ , the following experimental results are pertinent:

- The rate of ammonia formation is linearly proportional to the hydrogen pressure below  $5 \times 10^{-7}$  mbar  $\text{H}_2$ .

- SIMS spectra indicate that N and NH<sub>2</sub> are the predominant surface species under reaction conditions, whereas NH<sub>3</sub> and possibly NH are present only in very small amounts.
- The reaction-limited H<sub>2</sub> desorption state, emanating from the NH<sub>x</sub> decomposition, indicates the presence of significant amounts of NH<sub>x</sub> on the surface under reaction conditions, the average H:N ratio in the NH<sub>x</sub> intermediates is 1:1.1.

Together, these results point to the hydrogenation of NH<sub>2</sub> as the rate determining step. We therefore propose the following sequence of steps with the associated equilibrium constants:



We will justify and discuss this kinetic mechanism in the following. Under our experimental conditions, *i.e.*  $2 \times 10^{-8} < p_{\text{H}_2} < 1 \times 10^{-6}$  mbar and  $325 < T < 400$  K, the rate of both hydrogen adsorption and desorption are fast compared to the NH<sub>3</sub> formation rate. Furthermore, hydrogen adsorption is sufficiently fast to supply hydrogen for the conversion of atomic nitrogen in NH<sub>x</sub> species. We therefore conclude that H<sub>2</sub> adsorption rapidly reaches equilibrium (within the order of seconds).

While initially all the nitrogen on the surface is present as N<sub>ads</sub>, exposure to hydrogen results in conversion of part of the atomic nitrogen in NH<sub>x</sub> species. It is difficult to determine the exact time scale within which equilibrium between the NH<sub>x</sub> intermediates is established. However, the rapid build up of the NH<sub>x</sub> intermediates and the absence of an induction period in the time-dependent hydrogenation experiments indicate that equilibrium conditions apply for the major part of the time scale of the hydrogenation experiments. In the final step, NH<sub>3</sub> readsorption can be neglected, since the NH<sub>3</sub> production rate is slow as compared to the pumping speed of the vacuum system, resulting in a negligible NH<sub>3</sub> background pressure.

Under the assumption that equilibrium conditions apply for both H<sub>2</sub> adsorption and the NH<sub>x</sub> intermediates up to NH<sub>2</sub>, the following kinetic expression can be derived for the decrease of the nitrogen coverage with time, which is equal to the NH<sub>3</sub> formation rate:

$$\frac{d \theta_{N, \text{tot}}(t)}{dt} = -k_4 \cdot \theta_{\text{NH}_2}(t) \cdot \theta_H$$

$$\frac{d \theta_{N, \text{tot}}(t)}{dt} = -k_4 \cdot \theta_{N, \text{tot}}(t) \cdot \frac{K_2 \cdot K_3 \cdot (K_1 \cdot p_{\text{H}_2})}{1 + K_2 \cdot (K_1 \cdot p_{\text{H}_2})^{1/2} + K_2 \cdot K_3 \cdot (K_1 \cdot p_{\text{H}_2})} \cdot \frac{(K_1 \cdot p_{\text{H}_2})^{1/2}}{1 + (K_1 \cdot p_{\text{H}_2})^{1/2}} \quad (5.9)$$

The number of empty sites available for hydrogen adsorption equals:  $\theta_* = 1 - \theta_H - \sum \theta_{\text{NH}_x}$ . For the derivation of Equation 5.9 we have made the assumption that  $\theta_* \approx 1 - \theta_H$ . This has the advantage that two independent factors are obtained for the  $\text{H}_2$  pressure dependence of the hydrogen adsorption equilibrium and the equilibria of the  $\text{NH}_x$  intermediates (last and forelast factor in Equation 5.9, respectively). The choice of the number of empty sites available for hydrogen adsorption is quite arbitrary anyway, so we have assumed it to be unity in accordance to the situation on the bare surface. In fact the number of empty sites increases during the hydrogenation experiment due to the decrease of the nitrogen coverage. However, the decrease of the atomic nitrogen coverage in a typical hydrogenation experiment was in the order of 0.05 ML, and therefore the increase of the number of empty sites is relatively small. Hence equation 5.9 should be valid under the conditions employed in this work.

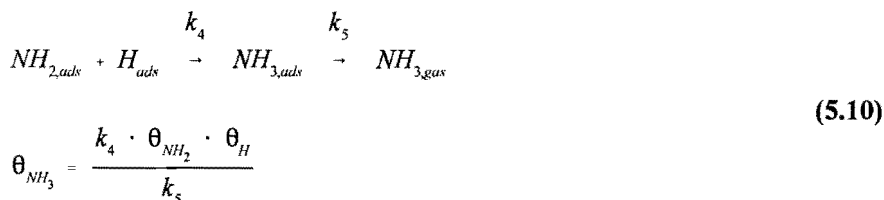
#### 5.4.2 The $\text{H}_2$ pressure dependence of the $\text{NH}_3$ formation rate

As the last but one factor in Equation 5.9 indicates, the order in the  $\text{H}_2$  pressure of the  $\text{NH}_2$  coverage can vary between 0 and 1. As stated previously, the hydrogen atom coverage is small under our reaction conditions and therefore proportional to  $\sqrt{p_{\text{H}_2}}$ . This can easily be seen from the last factor in Equation 5.9, which represents the hydrogen coverage and reduces to  $\sqrt{(K_1 \cdot p_{\text{H}_2})}$ , if  $K_1 \cdot p_{\text{H}_2} \ll 1$ . As a result, the order of the  $\text{NH}_3$  formation rate in the  $\text{H}_2$  pressure can vary between 1/2 and 3/2 as extremes.

Figure 5.4 shows that the  $\text{NH}_2$  coverage grows at increasing  $\text{H}_2$  pressures below  $\approx 5 \times 10^{-7}$  mbar, while the  $\text{NH}_2$  coverage becomes constant at higher  $\text{H}_2$  pressures. From a kinetic point of view, the observed  $\text{H}_2$  dependence of the  $\text{NH}_2$  coverage and the  $\text{NH}_3$  formation rate are consistent. At pressures below  $5 \times 10^{-7}$  mbar both the  $\text{NH}_2$  and the hydrogen coverage depend on the  $\text{H}_2$  pressure resulting in an overall first order dependence of the  $\text{NH}_3$  formation rate on the  $\text{H}_2$  pressure. Above  $5 \times 10^{-7}$  mbar  $\text{H}_2$ , the  $\text{NH}_2$  coverage becomes constant and the  $\text{H}_2$  pressure dependence of the  $\text{NH}_3$  formation rate is determined solely by the pressure dependence of the hydrogen coverage ( $\propto \sqrt{p_{\text{H}_2}}$ ).

### 5.4.3 Presence of NH<sub>x</sub> intermediates on the surface under reaction conditions

The SIMS results of the surface under reaction conditions indicate that N and NH<sub>2</sub> are the predominant nitrogen surface species. Drechsler *et al.* [31], using SIMS, have demonstrated that NH is the main surface species during the NH<sub>3</sub> decomposition on Fe. We may therefore conclude that the absence of NH in our SIMS spectra is not caused by a poor sensitivity, but due to a low surface coverage of NH. NH<sub>3</sub> is also detected, but only in very small amounts. A previous study on the adsorption of NH<sub>3</sub> on Rh(111) [32] indicated that an NH<sub>3</sub> coverage as small as 0.01 ML resulted in a SIMS Rh(NH<sub>3</sub>)<sup>+</sup>/Rh<sup>+</sup> peak intensity ratio as large as ≈7. In the present case the SIMS Rh(NH<sub>3</sub>)<sup>+</sup>/Rh<sup>+</sup> peak intensity ratio does not exceed a value of 0.25, see Figure 5.4, which points to a negligibly low coverage. In fact the NH<sub>3</sub> steady state coverage is determined by the ratio between the NH<sub>3</sub> production and desorption rate:



Under steady state conditions the rate of NH<sub>3</sub> formation is equal to the rate at which the nitrogen coverage decreases. As Figure 5.1 shows, a typical value for the decrease of the nitrogen coverage is 0.0002 ML/s. For the NH<sub>3</sub> desorption rate an activation energy of 81.5 kJ/mol was found if a pre-exponential factor of 10<sup>13</sup> was assumed [32]. Using these values an NH<sub>3</sub> steady state coverage of 4×10<sup>-6</sup> ML is calculated at 375 K. Since this coverage is very small we must, envisage about the role that surface defects might play. If NH<sub>3</sub> is, for instance, adsorbed more strongly to defect sites, the coverage might become significantly higher.

Equation 5.10 predicts that the NH<sub>3</sub> steady state coverage increases if the NH<sub>3</sub> formation rate increases. This is in line with the results in Figure 5.4, which shows that the NH<sub>3</sub> steady state coverage for a given temperature rise at increasing H<sub>2</sub> pressure.

Since no reference is available, it is difficult to give a precise estimate of the NH<sub>2</sub>:N surface coverage ratio on the basis of the SIMS Rh<sub>2</sub>NH<sub>2</sub><sup>+</sup>/Rh<sub>2</sub>N<sup>+</sup> peak intensity ratio. Quantification is complicated, since the relative SIMS sensitivities for N and NH<sub>2</sub>, and the fragmentation of the Rh<sub>2</sub>NH<sub>2</sub><sup>+</sup> cluster ion to Rh<sub>2</sub>N<sup>+</sup> are unknown. Nevertheless, it is remarkable that the SIMS Rh<sub>2</sub>NH<sub>2</sub><sup>+</sup>/Rh<sub>2</sub>N<sup>+</sup> peak intensity ratio becomes independent of the H<sub>2</sub> pressure above 5×10<sup>-7</sup> mbar at 375 K, see Figure 5.4 (note the logarithmic pressure scale), and is also independent of the temperature at a constant H<sub>2</sub> pressure of 1×10<sup>-6</sup> mbar, see Figures 5.5. In all cases the Rh<sub>2</sub>NH<sub>2</sub><sup>+</sup>/Rh<sub>2</sub>N<sup>+</sup> peak intensity ratio saturated at a value of ≈0.43. This might indicate that not all nitrogen is accessible to hydrogen. Yamada *et al.* [15] reported that exposure of a c(2×2)-N adlayer on Rh(100)

to hydrogen only resulted in  $\text{NH}_x$  formation at the edges of nitrogen islands. From our results we have no direct evidence for island formation, but it could explain why the  $\text{NH}_2$  coverage saturates while the  $\text{Rh}_2\text{NH}_2^+/\text{Rh}_2\text{N}^+$  ratio remains small.

In the literature most of the information concerning the stability of  $\text{NH}_x$  intermediates stems from decomposition experiments. Bassignana *et al.* [20] showed that on Ni(110)  $\text{NH}_2$  is the predominant intermediate formed during thermal  $\text{NH}_3$  decomposition at 350 K. An activation energy of 20 kcal/mol was reported for  $\text{NH}_2$  decomposition into N or NH. Rausher *et al.* [24] reported  $\text{NH}_2$  as a stable intermediate also on Ru(001) between 280 and 300 K during  $\text{N}_2\text{H}_4$  decomposition. The  $\text{NH}_2$  intermediate was found to decompose into NH at higher temperatures. On Rh(111), Wagner and Schmidt [22] reported a reaction-limited  $\text{H}_2$  desorption peak at 430 K, when studying the reactions of oxygen with  $\text{NH}_3$  and  $\text{N}_2\text{H}_4$ . This reaction-limited  $\text{H}_2$  desorption peak seems to be identical to the one we observed during TPD of the Rh(111) surface containing the  $\text{NH}_x$  intermediates formed during the hydrogenation of  $\text{N}_{\text{ads}}$ , see Figure 5.6. However, Wagner and Schmidt attributed the  $\text{H}_2$  formation to decomposition of NH rather than to  $\text{NH}_2$ . This latter assignment has been made in a previous investigation by the same authors Wagner and Schmidt [37], in which they investigated the decomposition of  $\text{H}_2\text{NCHO}$ ,  $\text{D}_2\text{NCHO}$ ,  $\text{N}_2\text{H}_4$  and  $\text{NH}_3$  on Rh(111). Decomposition of  $\text{D}_2\text{NCHO}$  showed that the reaction-limited  $\text{H}_2$  ( $\text{D}_2$ ) peak at 430 K stemmed from decomposition of the amino  $\text{NH}_2$  ( $\text{ND}_2$ ) group. Similar to our findings, they determined an overall N:H ratio of 1:1.08, when comparing the  $\text{N}_2$  and reaction limited  $\text{H}_2$  ( $\text{D}_2$ ) desorption peak areas. From this result they concluded that decomposing  $\text{NH}_x$  species was NH. A reaction-limited  $\text{NH}_3$  desorption state was also observed in these experiments, which was explained by hydrogenation of  $\text{NH}_2$ . It should be noted that their results could of course also be explained by assuming that the surface contained N and  $\text{NH}_2$  in a 1:1 ratio.

#### 5.4.4 Kinetic parameters of the $\text{NH}_3$ formation

Figure 5.6 shows that at a  $\text{H}_2$  pressure of  $1 \times 10^{-6}$  mbar the  $\text{Rh}_2\text{NH}_2^+/\text{Rh}_2\text{N}^+$  peak ratio is almost independent of the temperature and equal to the saturation value. If we assume that the  $\text{Rh}_2\text{NH}_2^+/\text{Rh}_2\text{N}^+$  peak ratio is a measure for the  $\text{NH}_2$  coverage, the latter is also temperature independent. This greatly simplifies the interpretation of the measured activation energy, since the temperature dependence of the  $\text{NH}_2$  equilibrium is not incorporated. In this case, the effective rate constant that is measured equals the product of the elementary rate constant for the reaction from  $\text{NH}_2$  to  $\text{NH}_3$  and the square root of the  $\text{H}_2$  adsorption equilibrium constant,  $k_{\text{eff}} = k_4 K_1^{1/2}$ , see equation 5.9. Under these assumptions, the activation energy for the reaction of  $\text{NH}_2$  to  $\text{NH}_3$  equals:

$$E_{\text{act}, \text{NH}_2-\text{NH}_3} = E_{\text{act}, \text{eff}} + \frac{1}{2} E_{\text{des}, \text{H}_2} = 33 + 36 = 69 \quad [\text{kJ/mol}] \quad (5.11)$$

$\text{H}_2$  TPD experiments yielded an activation energy and pre-exponential of 72 kJ/mol and  $10^{11} \text{ s}^{-1}$ , respectively, for desorption in the low coverage limit, in good agreement with the literature [38].

The only activation energy reported in the literature on  $\text{NH}_3$  formation stems from Hirano *et al.* [5]. They found an effective activation energy of 55 kJ/mol for  $\text{NH}_3$  formation by the reaction of  $\text{NO} + \text{H}_2$  on a  $\text{Pt}_{0.25}\text{-Rh}_{0.75}(100)$  single crystal. Comparison with our value is difficult, since it is not clear which reaction constants contribute to the effective activation energy. Shustorovich and Bell [39] have studied the synthesis and decomposition of  $\text{NH}_3$  on transition metal surfaces by a bond-order-conservation-Morse-potential analysis and concluded that the first hydrogenation step, *i.e.* the reaction from N to  $\text{NH}$ , is rate-limiting in  $\text{NH}_3$  formation on Pt. Furthermore, they concluded that both  $\text{NH}_2$  and  $\text{NH}_3$  are more stable surface intermediates than  $\text{NH}$ , and that  $\text{NH}_3$  desorption is favoured above  $\text{NH}_3$  decomposition. Although the calculations are performed for  $\text{Pt}(111)$ , the discrepancies with our findings and those of other authors are striking. First, it contradicts the  $\text{H}_2$  pressure dependence we observed for the  $\text{NH}_3$  formation rate on  $\text{Rh}(111)$  and, secondly, it cannot explain the build up of significant amounts of  $\text{NH}_x$  intermediates, either during  $\text{NH}_3$  decomposition or  $\text{NH}_3$  formation.

## 5.5 Conclusions

Atomic nitrogen layers with well determined surface coverage can be prepared by adsorbing NO at low temperatures, followed by thermal dissociation and selective removal of the atomic oxygen by reaction with hydrogen. When the atomic nitrogen layer is exposed to  $\text{H}_2$  at constant temperature and pressure, the rate at which the atomic nitrogen coverage decreases appears to be first order in the atomic nitrogen coverage. The rate of  $\text{NH}_3$  formation is first order in the  $\text{H}_2$  pressure between  $1 \times 10^{-8}$  and  $5 \times 10^{-7}$  mbar, but the order decreases between  $5 \times 10^{-7}$  and  $1 \times 10^{-6}$  mbar. SIMS spectra of the surface under reaction conditions indicate, by the appearance of  $\text{Rh}_2\text{N}^+$  and  $\text{Rh}_2\text{NH}_2^+$  peaks at  $m/e=220$  and 222, respectively, that N and  $\text{NH}_2$  are the predominant surface intermediates. Small amounts of  $\text{NH}_3$  could be monitored on the surface by the appearance of the  $\text{RhNH}_3^+$  cluster ion in the SIMS spectra. The  $\text{NH}_2$  coverage grows at increasing  $\text{H}_2$  pressure between  $1 \times 10^{-8}$  and  $5 \times 10^{-7}$  mbar at 375 K. In the pressure range between  $5 \times 10^{-7}$  and  $1 \times 10^{-6}$  mbar the  $\text{NH}_2$  coverage became constant. At a pressure of  $1 \times 10^{-6}$  mbar  $\text{H}_2$ , the  $\text{NH}_2$  steady state coverage is independent of the temperature. The presence of  $\text{NH}_x$  species is also evidenced by the appearance of a reaction limited  $\text{H}_2$  desorption state at 415 K, attributed to decomposition of  $\text{NH}_2$ .

From the temperature dependence of the  $\text{NH}_3$  formation rate, an effective pre-exponential and activation energy of  $10^2 \text{ s}^{-1}$  and 33 kJ/mol, respectively, were calculated. The experimental results can best be explained by assuming that the third hydrogenation step, *i.e.* the hydrogenation from  $\text{NH}_2$  to  $\text{NH}_3$ , is rate-limiting. The activation energy of this step is 69 kJ/mol.

**References**

- [1] K.C. Taylor, *Catal. Rev.-Sci. Eng.* 35 (1993) 457.
- [2] T.P. Kobylinski and B.W. Taylor, *J. Catal.* 33 (1974) 376.
- [3] G. Papapolymerou, A.G. Botis, A.D. Papargyris, X.D. Spiliotis, *J. Mol. Catal.* 84 (1993) 267.
- [4] A. Obuchi, S. Naito, T. Onishi, K. Tamaru, *Surf. Sci.* 130 (1983) 29.
- [5] H. Hirano, T. Yamada, K.I. Tanaka, J. Siera, P. Cobden, B.E. Nieuwenhuys, *Surf. Sci.* 262 (1992) 97.
- [6] J. Siera, B.E. Nieuwenhuys, H. Hirano, T. Yamada, K.I. Tanaka, *Catal. Lett.* 3 (1989) 179.
- [7] W.C. Hecker, A.T. Bell, *J. Catal.* 92 (1985) 247.
- [8] H.C. Yao, Y.Y. Yao, K. Otto, *J. Catal.* 56 (1979) 21.
- [9] H.J. Borg, J.F.C.-J.M. Reijerse, R.A. van Santen, J.W. Niemantsverdriet, *J. Chem. Phys.* 101 (1994) 10052.
- [10] J.S. Villarrubia and W. Ho, *J. Chem. Phys.* 87 (1987) 750.
- [11] V. Schmatloch and N. Kruse, *Surf. Sci.* 269/270 (1992) 488.
- [12] L. Bugyi and F. Solymosi, *Surf. Sci.* 258 (1991) 55.
- [13] D.N. Belton, C.L. DiMaggio, K.Y.S. Ng, *J. Catal.* 144 (1993) 273.
- [14] B.J. Savatsky and A.T. Bell, *ACS Symp. Ser.* 178 (1982) 105.
- [15] T. Yamada and K. Tanaka, *J. Am. Chem. Soc.* 113 (1991) 1173.
- [16] T. Yamada, H. Hirano, K. Tanaka, J. Siera, B.E. Nieuwenhuys, *Surf. Sci.* 226 (1990) 1.
- [17] D.Y. Zemlyanov, M.Y. Smirnov, V.V. Gorodetskii, J.H. Block, *Surf. Sci.* 329 (1995) 61.
- [18] J. Prasad and J.L. Gland, *J. Am. Chem. Soc.* 113 (1991) 1577.
- [19] J.L. Gland, G.B. Fisher, and G.E. Mitchell, *Chem. Phys. Lett.* 119 (1985) 89.
- [20] I.C. Bassignana, K. Wagemann, J. Küppers, and G. Ertl, *Surf. Sci.* 175 (1986) 22.
- [21] W.D. Miehler and W. Ho, *Surf. Sci.* 322 (1995) 151.
- [22] M.L. Wagner and L.D. Schmidt, *J. Phys. Chem.* 99, (1995) 805.
- [23] A.R. Cholach and V.A. Sobyenin, *React. Kinet. Catal. Lett.* 26 (1984) 381.
- [24] H. Rausher, K.L. Kostov, and D. Menzel, *J. Chem. Phys.* 177 (1993) 473.
- [25] F. Mertens and R. Imbihl, *Nature* 370 (1994) 124.
- [26] F. Mertens and R. Imbihl, *Surf. Sci.* 347 (1996) 355.
- [27] N.M.H. Janssen, P.D. Cobden, B.E. Nieuwenhuys, M. Ikai, K. Mukai, and K. Tanaka, *Catal. Lett.* 35 (1995) 155.
- [28] N.M.H. Janssen, B.E. Nieuwenhuys, M. Ikai, K. Tanaka, and A.R. Cholach, *Surf. Sci.* 319 (1994) L29.
- [29] M. Gierer, F. Mertens, H. Over, G. Ertl, and R. Imbihl, *Surf. Sci.* 339 (1995) L903.
- [30] A.R. Cholach, M.F.H. van Tol, and B.E. Nieuwenhuys, *Surf. Sci.* 320 (1994) 281.
- [31] M. Drechsler, H. Hoinkes, H. Kaarmann, H. Wilsch, G. Ertl, and M. Weiss, *Appl. Surf. Sci.* 3 (1979) 217.
- [32] R.M. van Hardeveld, R.A. van Santen, and J.W. Niemantsverdriet, *Surf. Sci.* 369 (1996) 23.
- [33] H.J. Borg and J.W. Niemantsverdriet, in: "Catalysis: a Specialist Periodical Report", Vol 11, Royal Society of Chemistry, Cambridge (1994), 1.
- [34] A. Brown and J.C. Vickerman, *Surf. Sci.* 124 (1983) 267.
- [35] J. Prasad and J.L. Gland, *Surf. Sci.* 258 (1991) 67.
- [36] J. Prasad and J.L. Gland, *Langmuir* 7, (1991) 722.
- [37] M.L. Wagner and L.D. Schmidt, *Surf. Sci.* 257 (1991) 113.
- [38] J.T. Yates Jr., P.A. Thiel, and W.H. Weinberg, *Surf. Sci.* 84 (1979) 427.
- [39] E. Shustorovich and A.T. Bell, *Surf. Sci. Lett.* 259 (1991) L791.



## 6 Adsorption and desorption of NH<sub>3</sub> on Rh(111)

### 6.1 Introduction

Understanding the adsorption and the reactivity of NH<sub>3</sub> on rhodium surfaces is of interest for large scale industrial processes. Both the HCN synthesis, according to the Andrussow process [1], and the formation of NO by oxidation of NH<sub>3</sub>, known as the Ostwald process [2], are realized on Pt-Rh catalysts. Furthermore, formation of NH<sub>3</sub> has been considered as a possibility in the reduction of NO by H<sub>2</sub> with automotive exhaust catalysis [3].

Surprisingly little has been reported in the literature about the interaction between NH<sub>3</sub> and rhodium. In contrast to the other transition metals, the attention has been focused mainly on the decomposition of NH<sub>3</sub> in the moderate pressure regime [4,5,6]. Table 1 summarizes what is known about adsorption of NH<sub>3</sub> on rhodium. The results reported thus far suggest that NH<sub>3</sub> decomposes at least partially on defect-rich rhodium surfaces, such as wires and foils, but stays intact on the close-packed (111) surface. Evidence for NH<sub>3</sub> dissociation on the faceted surface of a rhodium field emitter tip was only found when adsorption took place at elevated temperature, as reported by Van Tol *et al.* [7]. Noteworthy is the formation of N<sub>2</sub>H<sub>2</sub>, found by Prasad and Gland [8], and attributed to the recombination of imide (NH<sub>ads</sub>) surface intermediates.

More complete schemes of NH<sub>3</sub> adsorption exist for the transition metals Ni, Pt, Ru, Cu and Ag, for which results have briefly been summarized by Thornburg and Madix [12]. The adsorption behaviour of NH<sub>3</sub> on the various metals shows large similarities. The NH<sub>3</sub>-Ru(0001) system has been studied in greatest detail and will therefore be briefly reviewed here.

TPD experiments indicate four distinct desorption states of NH<sub>3</sub> from Ru(0001) [13,14]. The first two states, denoted  $\alpha_1$ - and  $\alpha_2$ -NH<sub>3</sub>, have peak maxima at 315 and 180 K, respectively. Complete filling of these two states leads to saturation of the first adsorption layer and yields a sharp (2×2) LEED pattern corresponding to a coverage of 0.25 ML. ESDIAD results show that in the  $\alpha_1$ -state, which saturates at ≈ 0.15 ML, NH<sub>3</sub> is adsorbed with its C<sub>3v</sub> symmetry axis perpendicular to the surface; the molecules are either rotating freely around the perpendicular axis or possess a random azimuthal orientation [14]. Filling of the  $\alpha_2$ -state leads to some tilting of the molecules with respect to the surface normal. Further increase of the NH<sub>3</sub> coverage results in the formation of a second adsorption layer, which gives rise to a sharp desorption peak at 130 K, denoted  $\beta$ -NH<sub>3</sub>. During filling of the second adsorption layer a (2√3×2√3)R30° LEED pattern is observed. For this ordered structure a model is proposed in which all first layer molecules, 0.25 ML, occupy threefold sites on which 0.08 ML of 'second layer' or  $\beta$ -NH<sub>3</sub> is adsorbed through hydrogen bonding [14]. The formation of multilayers,  $\gamma$ -NH<sub>3</sub>, commences at coverages in excess of 0.50 ML, and is readily observed by a desorption peak at 115 K.

**Table 6.1** Literature overview on the adsorption of  $\text{NH}_3$  on rhodium

Rhodium substrate	$T_{\text{ads}}$ [K]	Surface species	Evidence	Reference
wire	300-450	N, $\text{NH}_x$ , H	reaction-limited $\text{H}_2$ desorption at 420 K	[9]
foil	80	$\text{NH}_x$ , $\text{NH}_3$ , H	$\text{N}_2$ , $\text{N}_2\text{H}_2$ , and $\text{NH}_3$ desorption	[8]
Rh(111)	100	$\text{NH}_3$	$\text{NH}_3$ desorption only	[10,11]
Rh tip	80-300	$\text{NH}_3$	image clean tip appears at 400 K	[7]
	>400	N, $\text{NH}_x$ , H	tip clean above 650 K due to $\text{N}_2$ desorption	[7]
Rh(111)	120	$\text{NH}_3$	$\text{NH}_3$ desorption only, SIMS	this work

The work function of the  $\text{NH}_3/\text{Ru}(0001)$  surface decreases linearly with coverage during the filling of the  $\alpha_1$ -state. It diminishes further, with a decreasing slope, as the  $\alpha_2$ - and  $\beta$ -states populate, to reach a maximum value of  $\Delta\phi = -2.4$  eV after complete filling of the  $\beta$ -state.

EELS and RAIRS measurements confirm the existence of various adsorption states of  $\text{NH}_3$  on  $\text{Ru}(0001)$  [13,15]. The IR-cross section for the  $\text{NH}_3$  deformation mode appears to behave strongly non-linearly with coverage. During filling of the  $\alpha_1$ - $\text{NH}_3$  state the absorption increases linearly with coverage, but formation of  $\alpha_2$ - $\text{NH}_3$  reduces the cross section and completion of the  $\beta$ - $\text{NH}_3$  state, thought to occur through H-bonding, quenches the deformation mode entirely.

In this chapter we characterize the adsorption of  $\text{NH}_3$  on  $\text{Rh}(111)$  by temperature programmed desorption (TPD), low energy electron diffraction (LEED), work function measurements and static secondary ion mass spectrometry (SIMS). Results of the latter technique serve as a reference for the kinetic study on the hydrogenation of atomic nitrogen on  $\text{Rh}(111)$  [16], as discussed in Chapter 5.

## 6.2 Experimental

TPD, SIMS and work function experiments were performed in a stainless steel ultra high vacuum (UHV) system, pumped with a 360  $\ell/\text{s}$  turbomolecular pump and a water-cooled titanium sublimation pump. The base pressure was typically around  $5 \times 10^{-11}$  mbar, and mass spectra of the residual gas indicated the presence of mainly  $\text{H}_2$ , CO and  $\text{CO}_2$ . The system is equipped with a Leybold SSM 200 quadrupole mass spectrometer for TPD and SIMS, and a Leybold EA 10 hemispherical energy analyzer for AES and  $\Delta\phi$  measurements. Both analyzers were interfaced with a PC for data storage.

SIMS measurements were performed in the static (low damage) mode. Typically, we used a defocused 5 keV primary  $\text{Ar}^+$  beam with a current density of 1-10  $\text{nA}/\text{cm}^2$ . To average possible anisotropies in the secondary ion emission process, we applied a target bias of +45 V and an extractor voltage of -300 V on the entrance lens of the quadrupole system.

Work function changes were determined by measuring the shift of the low kinetic energy onset of the secondary electron emission in AES. In order to minimize damage

effects due to electron irradiation, we used a primary electron beam of 500 eV and 0.02  $\mu\text{A}$ . The sample was biased -10 V with respect to the ground potential. The onset was defined as the energy at which the derivative of the secondary electron distribution maximizes. The shifts are reported with respect to the clean  $\text{Rh}(111)$  surface (5.6 eV) [17].

LEED experiments were performed in a different UHV system equipped with a Leybold Quadruvac Q100 mass spectrometer and a reverse view, four grid AES/LEED optics (Spectaleed, Omicron Vakuumphysik GmbH). LEED data were obtained with an electron beam current between 20 and 30  $\mu\text{A}$ .

Each UHV system contained a rhodium crystal which was cut in the [111] orientation within  $0.5^\circ$  and polished by standard procedures. The temperature was measured by a chromel-alumel thermocouple spotwelded on the back of the crystal. The standard cleaning procedure consisted of an argon sputter treatment (900 K, 1.5 keV, 5  $\mu\text{A}/\text{cm}^2$ ) followed by annealing in  $2 \times 10^{-8}$  mbar  $\text{O}_2$  (900 K-1100 K) and a final annealing treatment in vacuum at 1420 K. The gases,  $\text{NH}_3$  (UCAR electronic grade, 99.995%) and  $\text{D}_2$  (Messer Griesheim, 99.7%) were used without further treatment. Exposures are reported in Langmuirs ( $1\text{L} = 1.33 \times 10^{-6}$  mbar.s) and coverages are expressed with respect to the number of Rh surface atoms ( $1\text{ML} = 1.6 \times 10^{15} \text{cm}^{-2}$ ).

## 6.3 Results

### 6.3.1 Temperature-programmed desorption

After adsorption of  $\text{NH}_3$  at 120 K, temperature-programmed desorption spectra were measured at a heating rate of 5 K/s, by monitoring the mass channels  $m/e=2$  ( $\text{H}_2$ ),  $m/e=17$  ( $\text{NH}_3$ ),  $m/e=28$  ( $\text{N}_2$ ) and  $m/e=30$  ( $\text{N}_2\text{H}_2$ ). In all cases,  $\text{NH}_3$  was the only detectable N-containing desorption product. Some  $\text{H}_2$  desorption was observed, which was attributed to adsorption of small amounts of  $\text{H}_2$  from the background.

The  $\text{NH}_3$  desorption spectra in Figure 6.1 show three distinct desorption states depending on the  $\text{NH}_3$  coverage. The first low coverage state, denoted by  $\alpha_1\text{-NH}_3$ , has a maximum around 320 K which broadens significantly to lower temperature at increasing  $\text{NH}_3$  coverage. Note that the spectra contain a small shoulder at higher temperatures, which grows with increasing exposure. The origin of this signal is not clear; possible explanations will be given in the discussion section.

Application of the Redhead method [18] to the low-coverage peak at 320 K yields a desorption energy of  $81.5 \pm 3$  kJ/mol for  $\alpha_1\text{-NH}_3$ , if a pre-exponential factor of  $10^{13} \text{s}^{-1}$  is assumed. Other analysis methods which in general give more reliable answers [19], appeared to be unsuitable because of the strong dependence of the desorption energy on the coverage.

The transition to the second desorption state  $\alpha_2\text{-NH}_3$ , which maximizes at 155 K, takes place very gradually. Above  $\text{NH}_3$  exposures of  $\approx 0.45$  L, a third desorption state,

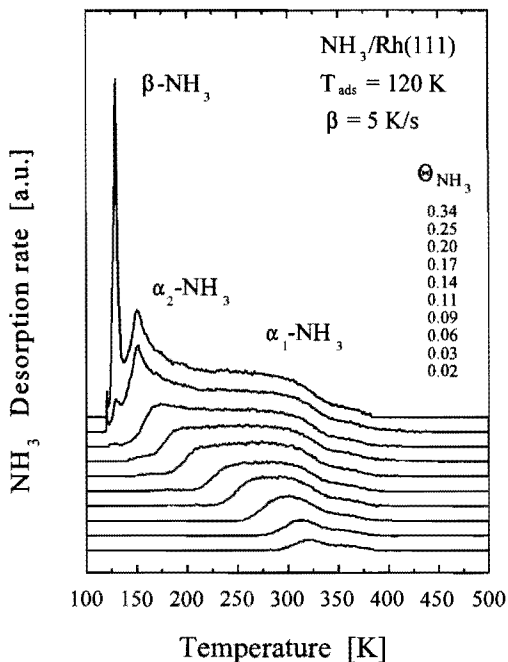


*Figure 6.1* Temperature-programmed desorption spectra of  $\text{NH}_3$  measured after adsorption of various amounts of  $\text{NH}_3$  at 120 K. The heating rate was 5 K/s.

$\beta\text{-NH}_3$ , is observed by a very sharp peak at 130 K. Application of the Redhead method yields a desorption energy of 32 kJ/mol for this  $\beta\text{-NH}_3$ , if a pre-exponential factor of  $10^{13} \text{ s}^{-1}$  is assumed.

### 6.3.2 $\text{D}_2$ coadsorption

The fact that none of the experiments showed any traces of desorbing  $\text{N}_2$  or  $\text{N}_2\text{H}_2$  suggests that  $\text{NH}_3$  adsorbs exclusively intact. In order to confirm this, some TPD experiments were done after coadsorption of  $\text{D}_2$  and  $\text{NH}_3$ . If ammonia decomposes on the surface, and recombines upon desorption,  $\text{NH}_{3-x}\text{D}_x$  would be expected in the gas phase. Deuterated products did not form, however.  $\text{D}_2$ ,  $\text{NH}_3$  and small amounts of HD were the only desorption products observed, see Figure 6.2.

The presence of HD indicates that some hydrogen was present on the surface also. Since the shape of the HD desorption peak is approximately the same as that of  $\text{D}_2$  (see Figure 6.2), it is most likely that this hydrogen stems from background adsorption. The small difference in the peak maximum of HD and  $\text{D}_2$  ( $\approx 10 \text{ K}$ ) is in line with the isotope shift that is observed when comparing  $\text{H}_2$  and  $\text{D}_2$  desorption. Coadsorption of  $\text{D}_2$  appears to destabilize adsorbed ammonia: the  $\text{NH}_3$  peak maximum shifted from  $\approx 300$  to 265 K when 1.0 L  $\text{D}_2$  was post dosed to a surface covered by 0.06 ML of  $\text{NH}_3$ , as Figure 6.2 shows.

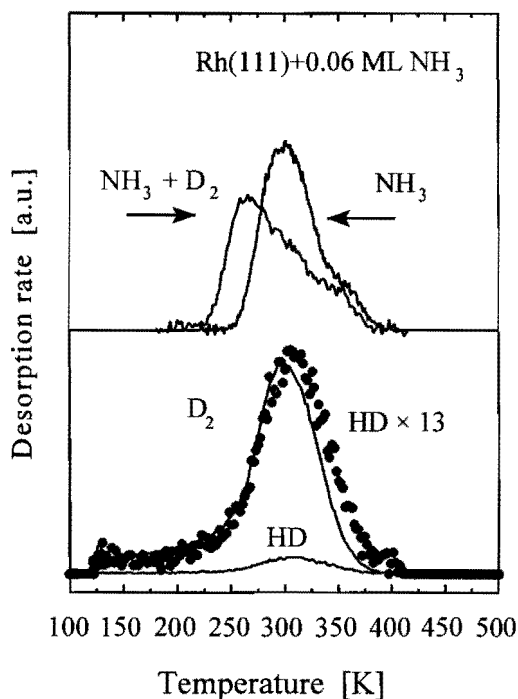


**Figure 6.2** Temperature programmed desorption of 0.06 ML of  $\text{NH}_3$ , in the absence and presence of coadsorbed  $\text{D}_2$  does not indicate deuterated ammonia. HD formation is attributed to  $\text{H}_2$  adsorption from the residual gas. The ammonia desorption shifts to lower temperature by coadsorbed  $\text{D}_2$ .

### 6.3.3 LEED of $\text{NH}_3$ on $\text{Rh}(111)$

LEED experiments have been done to provide a calibration point for the  $\text{NH}_3$  coverages. Figure 6.3 shows the  $(1 \times 1)$  LEED pattern of the clean  $\text{Rh}(111)$  surface and the  $(2 \times 2)$ - $\text{NH}_3$  LEED pattern observed after dosing 0.45 L  $\text{NH}_3$ . The visibility of the  $(2 \times 2)$  pattern depends strongly on the  $\text{NH}_3$  coverage and the  $(2 \times 2)$  pattern arises only at a coverage obtained after a 0.45 L exposure, or after higher exposures followed by heating to 150 K. We therefore conclude that the  $(2 \times 2)$   $\text{NH}_3/\text{Rh}(111)$  structure is uniquely associated with completely filled  $\alpha_2$ - and  $\alpha_1$ -states. The applied beam energy was 58 eV in both cases and the temperature was 120 K. We stress that under our conditions the  $(2 \times 2)$  pattern was observable only for a few seconds.  $\text{NH}_3$  decomposition by electrons is well known [20], but also local heating may contribute to the rapid disappearance of the  $(2 \times 2)$  LEED pattern. We assign the  $(2 \times 2)$  pattern to an  $\text{NH}_3$  surface coverage of 0.25 ML, corresponding to a fully occupied  $\alpha_1$ - and  $\alpha_2$ -state. Similar assignments were made for  $\text{Ru}(0001)$  [14],  $\text{Ni}(111)$  [21] and  $\text{Pt}(111)$  [22].

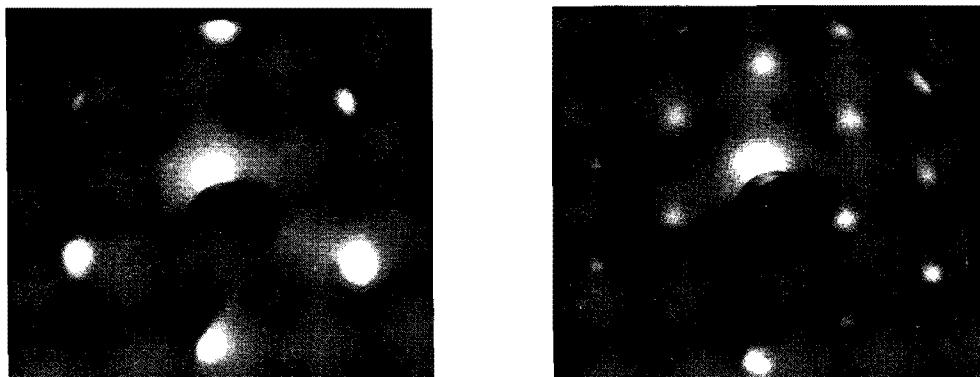


**Figure 6.3** The left picture shows the  $(1\times 1)$  LEED pattern of the clean Rh(111) surface. The right picture shows the  $(2\times 2)$ - $\text{NH}_3$  LEED pattern, corresponding to  $\theta_{\text{NH}_3}=0.25$  ML, obtained after exposure of 0.45 L  $\text{NH}_3$ . The electron energy was  $\sim 58$  eV.

#### 6.3.4 Coverage calibration and sticking coefficient

Figure 6.4 shows the  $\text{NH}_3$  uptake curve which was constructed by integrating the  $\text{NH}_3$  TPD peak areas and using the calibration point that the TPD area obtained after 0.45 L exposure corresponds to 0.25 ML. During the filling of the  $\alpha_1$ - and  $\alpha_2$ - $\text{NH}_3$  states, the  $\text{NH}_3$  coverage increases linearly with  $\text{NH}_3$  exposure, which implies that the sticking coefficient is independent of the coverage. We estimate that the initial sticking coefficient is close to unity. However, uncertainty in the total pressure measurement precludes an accurate assessment.

During the filling of the second adsorption layer above 0.25 ML, the scatter in the data enlarges and the uptake curve starts to deviate from linearity. This is probably due to larger errors that derive from integrating the sharp desorption peak at 130 K. Also desorption of  $\text{NH}_3$  may become important, since the adsorption temperature of 120 K is just below the desorption temperature of  $\text{NH}_3$  in the second layer, 130 K. Multilayers were not observed, as this requires adsorption temperatures below 110 K.

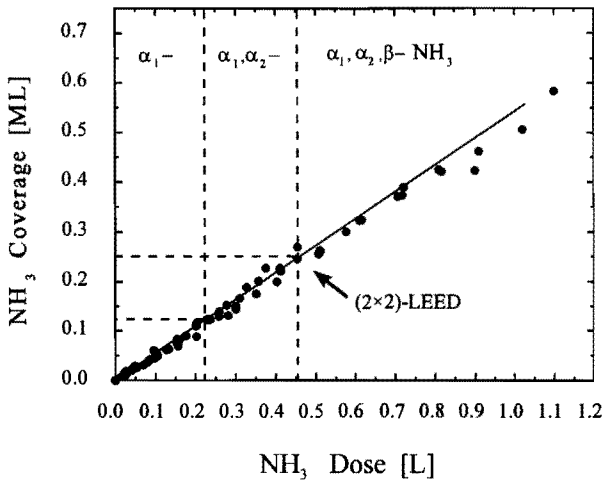


**Figure 6.4** Uptake curve obtained by integration of the  $\text{NH}_3$  TPD peak areas. Exposure of 0.45 L  $\text{NH}_3$  is assumed to correspond to an  $\text{NH}_3$  coverage of 0.25 ML. The sticking coefficient is independent of the coverage and close to unity.

### 6.3.5 Work function measurements

Figure 6.5 shows the change of the work function versus the  $\text{NH}_3$  coverage. Up to an  $\text{NH}_3$  coverage of  $\approx 0.15$  ML, where the  $\alpha_1$ -state prevails, the work function decreases linearly with  $\text{NH}_3$  coverage. The initial slope, indicated by the solid line in Figure 6.5, equals  $-11.5$  eV/ML. For  $\text{NH}_3$  coverages between 0.15 and 0.25 ML, where the  $\alpha_2$ -state becomes occupied, the drop in work function becomes less pronounced. For  $\text{NH}_3$  coverages in excess of 0.25 ML, corresponding to the  $\beta$ -state, the work function becomes constant and reaches a saturation value of  $-2.4$  eV below the value of clean  $\text{Rh}(111)$ .

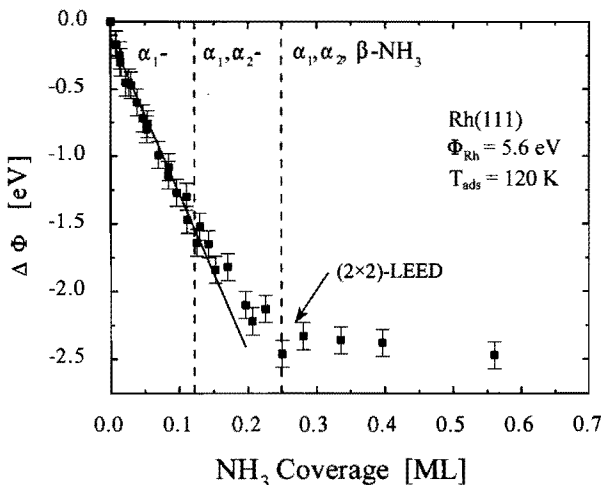


**Figure 6.5** Work function change as a function of the  $\text{NH}_3$  coverage. The solid line indicates the initial work function decrease which equals  $-11.5$  eV/ML. The slope of the curve decreases around an  $\text{NH}_3$  coverage of  $\approx 0.15$  ML, the maximum decrease is  $-2.4$  eV.

### 6.3.6 Secondary Ion Mass Spectrometry

Figure 6.6 shows three characteristic mass regions of a SIMS spectrum of the Rh(111) surface covered with 0.10 ML of  $\text{NH}_3$  at 120 K. The presence of  $\text{NH}_3$  on the surface is best illustrated by the appearance of the  $\text{Rh}(\text{NH}_3)^+$  cluster ion at  $m/e=120$ . In the low-mass region the predominant features are  $\text{H}^+$  and  $\text{NH}_x^+$  stemming from  $\text{NH}_3$  fragmentation during the emission process. Comparable  $\text{NH}_3$  fragmentation was observed in a previous SIMS study on the adsorption of  $\text{NH}_3$  on Fe(110) by Drechsler *et al.* [23]. The appearance of  $\text{NH}_4^+$  is attributed to recombination of  $\text{NH}_3$  and H in the near surface region during emission. The right panel of Figure 6.6 shows the mass region associated

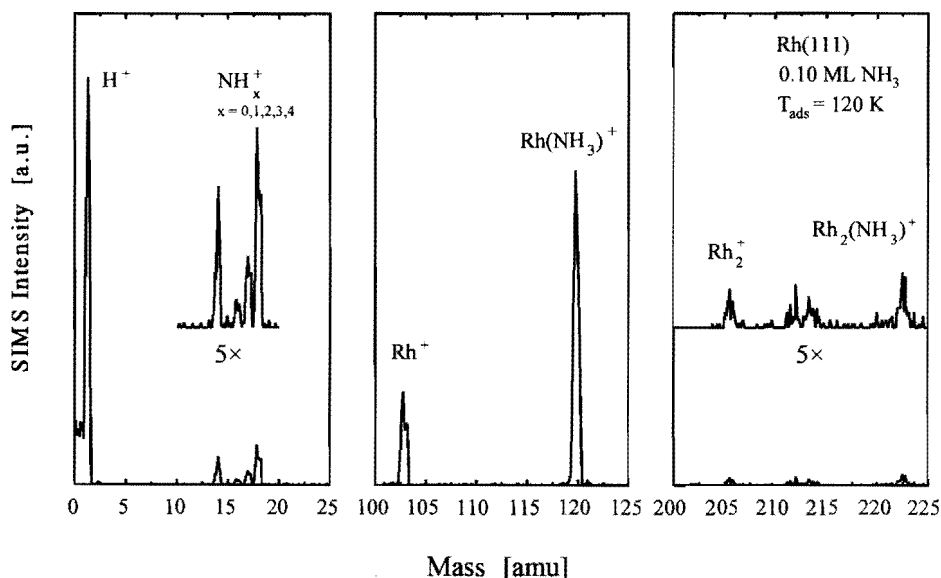


**Figure 6.6** Three characteristic mass regions of a SIMS spectrum of the Rh(111) surface covered with 0.10 ML of  $\text{NH}_3$  at 120 K. The  $\text{Rh}(\text{NH}_3)^+$  peak at  $m/e=120$  is the predominant ammonia-derived cluster.  $\text{NH}_3$  fragmentation products are observed in the low-mass range. Although weak of intensity, the  $\text{Rh}_2(\text{NH}_3)^+$  cluster at  $m/e=223$  can be distinguished.

with the emission of  $\text{Rh}_2$ -related clusters. Although the intensities are close to the noise level, both the  $\text{Rh}_2^+$  and  $\text{Rh}_2(\text{NH}_3)^+$  clusters ions can be recognized at  $m/e=206$  and 223, respectively. The nature of the signals in the region from  $m/e=212$  to 214 is unclear, but the signals might be due to  $\text{Pt}(\text{NH}_4)^+$  cluster ions of the three Pt isotopes, since Pt is a known trace impurity of rhodium.

We note in particular that SIMS gives no evidence for the presence of any dehydrogenated  $\text{NH}_x$  species on the surface. Studies on the hydrogenation of adsorbed N-atoms revealed that such species can be detected in SIMS [16]. The SIMS data thus confirm the intact adsorption of  $\text{NH}_3$  on the Rh(111) surface.



The study of the  $\text{NH}_3$ - $\text{Rh}(111)$  adsorption system by SIMS is somewhat complicated by the fact that the work function of the surface decreases significantly upon increasing the  $\text{NH}_3$  coverage. A work function decrease generally results in a higher neutralization probability of the emitted secondary ions [24,25], which leads to a decrease of the SIMS peak intensities. In practice only the  $\text{Rh}(\text{NH}_3)^+$  cluster ion has enough intensity to give reliable information about  $\text{NH}_3$ - $\text{Rh}(111)$  system in a broad coverage regime.

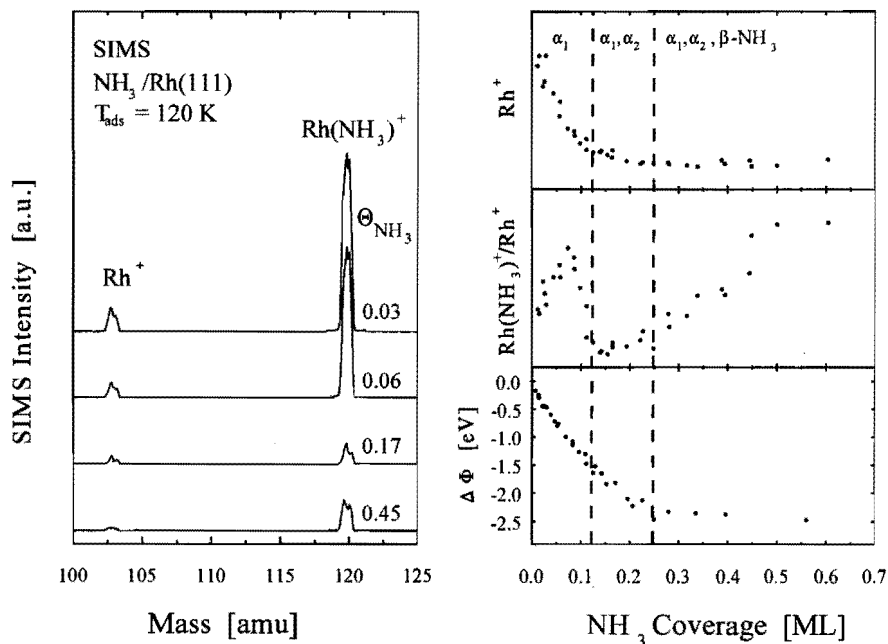


**Figure 6.7** The left panel shows SIMS spectra of the  $\text{Rh}(111)$  surface for some characteristic  $\text{NH}_3$  coverages at 120 K. The right panel shows the decrease of the absolute  $\text{Rh}^+$  peak with increasing  $\text{NH}_3$  coverage. The work function decrease is shown for comparison. The SIMS  $\text{Rh}(\text{NH}_3)^+/\text{Rh}^+$  peak intensity ratio is a strongly non-linear function of the  $\text{NH}_3$  coverage.

The left panel of Figure 6.7 shows some characteristic SIMS spectra in the mass region from  $m/e=100$  to 125 of the  $\text{Rh}(111)$  surface for various  $\text{NH}_3$  coverages at a temperature of 120 K. The spectra clearly show that the absolute intensity of the  $\text{Rh}(\text{NH}_3)^+$  cluster varies non-linearly with the  $\text{NH}_3$  coverage, while also the  $\text{Rh}^+$  peak intensity drops significantly with increasing coverage. The right panel of Figure 6.7 clearly shows the correlation between the decrease of the absolute  $\text{Rh}^+$  SIMS signal and the drop of the work function. During filling of the  $\alpha_1$ -state the  $\text{Rh}^+$  intensity decreases rapidly with increasing  $\text{NH}_3$  coverage, this dependence levels off when the  $\alpha_2$ -state

becomes occupied. Formation of  $\beta$ -NH<sub>3</sub> influences neither the absolute Rh<sup>+</sup> intensity nor the work function.

In order to compensate for work function effects, one has usually considered peak intensity ratios rather than absolute intensities. In studies of adsorbed CO [26,27,28] and NO [29], ratios of the type RhNO<sup>+</sup>/Rh<sup>+</sup> and Rh<sub>2</sub>NO<sup>+</sup>/Rh<sub>2</sub><sup>+</sup> correlated satisfactorily with the actual coverages. The right panel of Figure 6.7 shows the Rh(NH<sub>3</sub>)<sup>+</sup>/Rh<sup>+</sup> ratio as a function of NH<sub>3</sub> coverage. The non-linear behaviour shown by this figure is striking, although certain features are seen to correspond to transitions between the different adsorption states. We discuss the results of Figure 6.7 later on in this chapter.

Temperature-programmed SIMS experiments were carried out to monitor the various NH<sub>3</sub> adsorption states as a function of the temperature and initial coverage. Figure 6.8 shows the Rh(NH<sub>3</sub>)<sup>+</sup>/Rh<sup>+</sup> intensity ratio as a function of the temperature. The upper spectrum is obtained starting from an NH<sub>3</sub> coverage of 0.50 ML, where both  $\alpha_1$ -,  $\alpha_2$ - and  $\beta$ -NH<sub>3</sub> are present. The desorption of NH<sub>3</sub> from the  $\beta$ -state is clearly demonstrated by the decrease of the Rh(NH<sub>3</sub>)<sup>+</sup>/Rh<sup>+</sup> ratio at about 130 K. Both the upper and middle spectrum show that NH<sub>3</sub> desorption in the temperature regime between 150 and 260 K does not result in a significant change of the Rh(NH<sub>3</sub>)<sup>+</sup>/Rh<sup>+</sup> intensity ratio. However, above 260 K the intensity ratio starts to increase again and reaches a maximum at 310 K. The decrease of the Rh(NH<sub>3</sub>)<sup>+</sup>/Rh<sup>+</sup> ratio above 310 K is displayed by all spectra and corresponds to the desorption of  $\alpha_1$ -NH<sub>3</sub> which is present on the surface up to temperatures of 370 K.

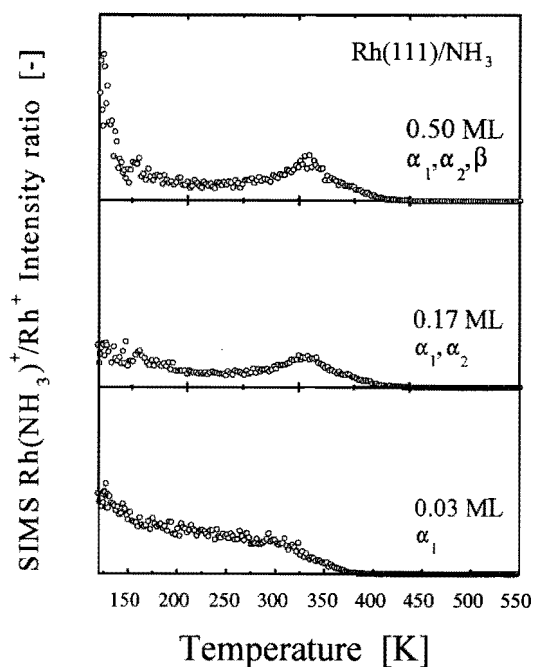


**Figure 6.8** Temperature programmed SIMS spectra showing the Rh(NH<sub>3</sub>)<sup>+</sup>/Rh<sup>+</sup> peak intensity ratio as a function of the temperature for various initial NH<sub>3</sub> coverages. The heating rate was 5 K/s. The desorption of the second adsorption layer at 130 K is clearly illustrated by the upper spectrum. Desorption of  $\alpha_2$ -NH<sub>3</sub> cannot be observed,  $\alpha_1$ -NH<sub>3</sub> desorption above 300 K is exhibited by all spectra.

## 6.4 Discussion

### 6.4.1 Adsorption states of NH<sub>3</sub>

The adsorption of NH<sub>3</sub> on Rh(111) greatly resembles that on the hexagonally close-packed surfaces of other group VIII metals, such as Pt(111), Ru(0001) and Ni(111). This is most prominently shown by the respective temperature-programmed desorption data. Table 6.2 presents an overview of the different desorption states and the corresponding peak maximum temperatures for NH<sub>3</sub> on these metals. Note, however, that different authors used different heating rates, implying that the peak temperatures in Table 6.2 can only serve as a rough guide for comparison.

**Table 6.2:** Comparison of the desorption maxima, maximum work function change  $\Delta\Phi_{\max}$ , and average initial dipole  $\bar{\mu}$  of NH<sub>3</sub> for some group VIII metals.

metal	TPD peak maximum temperature *				$\Delta\Phi_{\max}$ ** [eV]	$\bar{\mu}$ [D]	reference
	$\alpha_1$ -NH <sub>3</sub>	$\alpha_2$ -NH <sub>3</sub>	$\beta$ -NH <sub>3</sub>	$\gamma$ -NH <sub>3</sub>			
Rh(111)	320	155	130	-	-2.4	1.9	this work
Ru(001)	310	180	130	115	-2.4	1.9	[14,15]
Pt(111)	360	-	160	110	-3.0	2.0	[22]
Ni(111)	290	-	145	-	-	-	[21]

\* Note that the heating rates were not the same in the different studies

\*\* The dipole moment of the free NH<sub>3</sub> molecule is 1.47 Debye

The high-temperature desorption state  $\alpha_1$ -NH<sub>3</sub> is observed for all the metals and also the broadening of the  $\alpha_1$ -NH<sub>3</sub> desorption peak towards lower temperature at increasing NH<sub>3</sub> coverage is a common feature. The  $\alpha_2$ -NH<sub>3</sub> desorption state, which occurs on Ru(0001) at about 180 K and on Rh(111) at about 155 K, does not stand out as a separate peak in the desorption of NH<sub>3</sub> from Ni(111) and Pt(111). The separation between the  $\alpha_1$ - and  $\alpha_2$ -NH<sub>3</sub> states is a bit arbitrary anyway, as the transition between the two is rather gradual. Benndorf *et al.* [14] take 0.15 ML of NH<sub>3</sub> on Ru(0001) as the coverage where the  $\alpha_1$ -state saturates and the  $\alpha_2$ -state starts to form. This is in good agreement with what we find for the TPD of NH<sub>3</sub> from Rh(111) in Figure 6.1. In addition, 0.15 ML is also the coverage where the work function changes its slope and the Rh(NH<sub>3</sub>)<sup>+</sup>/Rh<sup>+</sup> intensity ratio shows a sharp decrease. Both observations support the notion of a discontinuity in structure at 0.15 ML of NH<sub>3</sub>.

The  $\beta$ -NH<sub>3</sub> desorption state, associated with desorption from a 'second' adsorption layer, is observed on all metals by the appearance of a sharp desorption peak in the temperature range between 130 and 160 K. We did not observe the formation of the  $\gamma$ -NH<sub>3</sub> state corresponding to multilayers, since the adsorption temperature of 120 K employed here is just above the  $\gamma$ -NH<sub>3</sub> desorption temperature of 100-115 K.

The TPD experiments gave no indication of  $\text{NH}_3$  decomposition. This was evidenced by the complete absence of any decomposition products, and by the  $\text{D}_2$  coadsorption experiments. If any  $\text{NH}_3$  decomposition would take place during heating, this would have been reflected in the HD desorption spectra. However, the HD trace closely follows the  $\text{D}_2$  desorption (Figure 6.2) indicating that the ratio between hydrogen and deuterium on the surface remains constant. This confirms that there is no production of surface hydrogen by decomposition of  $\text{NH}_3$ .

Also the  $\text{NH}_3$  TPD studies on Ru(0001), Pt(111) and Ni(111) show that desorption is highly favoured over dissociation, provided adsorption of  $\text{NH}_3$  is done at low temperatures. Even on Ru(0001), expected to be the most reactive metal, not more than 3% of the adsorbed  $\text{NH}_3$  was found to dissociate [15].

In addition to the three distinct desorption states, the  $\text{NH}_3$  TPD spectra of Figure 6.1 show a small high temperature tail which extends from 340 to 380 K. The TPSIMS spectra reveal that in this temperature range there is still some  $\text{NH}_3$  on the surface. The most obvious explanation for the desorption tail would be limited pumping speed, caused by adsorption of  $\text{NH}_3$  on the UHV chamber walls, resulting in some readsorption on the rhodium surface. In principle the  $\text{NH}_3$  desorption tail might be due to decomposition and rehydrogenation, but this explanation is invalidated by the absence of H-D exchange in  $\text{NH}_3$  in the coadsorption experiments with  $\text{D}_2$ . As the amount of  $\text{NH}_3$  desorbing in this tail accounts for less than 1% of a monolayer, we can also not exclude that defects play a role.

#### 6.4.2 Effective dipole moment of adsorbed $\text{NH}_3$

Adsorption of ammonia results in a significant lowering of the work function. Gas phase  $\text{NH}_3$  has a dipole moment of 1.47 Debye [30]. As  $\text{NH}_3$  is bonded to the substrate via the lone pair of the nitrogen atom, a work function decrease is expected on the basis of the orientation of the dipole on the surface.

The Helmholtz equation [31] translates the initial work function change to an average dipole moment of the adsorbate:

$$\bar{\mu} = \frac{\epsilon_0 \cdot |\Delta\Phi|}{\sigma} \quad (6.1)$$

$\bar{\mu}$	= average dipole moment	[D]
$ \Delta\Phi $	= work function change	[eV]
$\epsilon_0$	= electric permittivity of vacuum	[D.cm <sup>-2</sup> .eV <sup>-1</sup> ]
$\sigma$	= adsorbate concentration	[cm <sup>-2</sup> ]

Inserting the initial work function decrease of -11.5 eV/ML, and using  $\epsilon_0 = 2.66 \times 10^{14}$  D.cm<sup>2</sup>.eV<sup>-1</sup>, and  $\sigma = 1.6 \times 10^{15}$  cm<sup>-2</sup>.ML<sup>-1</sup>, we find an average dipole of 1.9 Debye for the NH<sub>3</sub> molecule adsorbed at low coverage. This value is about equal to the dipole moments calculated in the same way for NH<sub>3</sub> on Ru(0001) [14] and Pt(111) [22], as Table 6.2 shows. It should be noted that the Helmholtz equation attributes the work function change entirely to charge separation in the adsorbate molecule, which is not necessarily true, since also charge transfer between the adsorbate and the substrate has to be considered. However, the fact that the calculated effective dipole of adsorbed NH<sub>3</sub> (1.9 D) is stronger than in the free molecule (1.47 D) indicates that charge transfer from NH<sub>3</sub> to the substrate, or an enhancement of the NH<sub>3</sub> dipole upon adsorption, or a combination of these factors plays a role.

### 6.4.3 Coverage-dependent effects

The outstanding coverage-dependent effect in the adsorption of NH<sub>3</sub> on Rh(111) is the dramatic decrease of the  $\alpha_1$ -NH<sub>3</sub> desorption temperature with increasing NH<sub>3</sub> coverage. Formerly, this broadening has entirely been attributed to a decrease of the desorption energy caused by repulsive lateral interactions between NH<sub>3</sub> molecules [14]. If a constant pre-exponential factor was assumed, the desorption behaviour could be described by assuming the desorption energy  $E_{des}$  to obey the following functional form:

$$E_{des} = E_{des0} - W \cdot \theta^{3/2} \quad (6.2)$$

A problem with the above described explanation is that the dramatic influence of the coverage on the desorption energy is by no means reflected in the coverage-dependent behaviour of the work function. Up to a coverage of  $\approx 0.15$  ML, the work function decreases linearly with the NH<sub>3</sub> coverage, implying that the work function change and, consequently, the average dipole per adsorbed NH<sub>3</sub> molecule is constant. If repulsive lateral interactions are responsible for the large decrease in the desorption energy, the average dipole of the NH<sub>3</sub> molecules is expected to be influenced too. We therefore wonder whether entropy effects could be responsible. In the framework of Eyring's transition state theory, the rate of desorption is written as [32]:

$$r_{des} = \frac{k_B T}{h} \frac{pf^\ddagger}{pf} e^{-E_{des}/RT} \theta_{NH_3} \quad (6.3)$$

$$\begin{aligned} r_{des} &= \text{NH}_3 \text{ desorption rate} && [\text{ML/s}] \\ k_B &= \text{Boltzmann's constant} && [\text{J/K}] \end{aligned}$$

$T$	=	temperature	[K]
$h$	=	Planck's constant	[J.s]
$pf^\ddagger$	=	partition function transition state	[-]
$pf$	=	partition function ground state	[-]
$E_{des}$	=	desorption energy	[J/mol]
$R$	=	gas constant	[J/mol.K]
$\theta_{NH_3}$	=	NH <sub>3</sub> coverage	[ML]

If the adsorption energy and, hence,  $E_{des}$  is constant, as the constant work function decrease seems to suggest, then a coverage-dependence of the desorption rate constant can still be caused by the ratio of the partition functions. For example, suppose that adsorbed ammonia molecules are mobile in the high-temperature / low-coverage regime of the TPD spectra, and that the transition state for desorption is mobile as well, then the ratio of the partition functions  $pf^\ddagger/pf$  is of the order of unity and the molecule desorbs with a pre-exponential factor on the order of  $e \cdot k_B \cdot T/h = 10^{13} \text{ s}^{-1}$ . As the coverage becomes higher, the translational partition function of the ground state decreases, while that of the transition state may remain high. In this respect, it is important to note that the sticking coefficient for adsorption in this coverage regime is constant and of the order of unity, which might point to the existence of a mobile precursor state of ammonia. The result is that the ratio  $pf^\ddagger/pf$  in (6.3) *increases*, causing the pre-exponential to go up with coverage, while the adsorption energy may remain constant until the adsorbate molecules start to interact, in the  $\alpha_2$ -state. Note that, if the above interpretation is correct, the estimate of the low coverage adsorption energy on the basis of the Redhead formula, 81 kJ/mol, should be correct, as the pre-exponential factor would indeed be on the order of  $10^{13} \text{ s}^{-1}$ .

The drop in the work function versus coverage slope at 0.15 ML corresponds to the occupation of the  $\alpha_2$ -NH<sub>3</sub> state, where lateral interactions between adsorbed NH<sub>3</sub> molecules become important. This correlates well with the ESDIAD results on Ru(0001), which indicate that NH<sub>3</sub> tilts above a coverage of 0.15 ML [14]. Although tilting of the NH<sub>3</sub> molecules results in a decrease of the effective dipole moment, mutual depolarization caused by lateral interactions between the NH<sub>3</sub> molecules is expected as well. After adsorption of 0.25 ML of NH<sub>3</sub>, the average dipole per NH<sub>3</sub> molecule is 1.60 D, which is significantly lower than the initial value.

#### 6.4.4 SIMS of NH<sub>3</sub> on Rh(111)

The most striking result from the SIMS experiments is the strongly non-linear behaviour of the  $\text{Rh}(\text{NH}_3)^+/\text{Rh}^+$  ratio as a function of the ammonia coverage. A complete explanation of the SIMS intensities is difficult to present, since the emission process of secondary ions is highly complex and not fully understood. Nevertheless, it is instructive to discuss the intensities in the light of the changing work function (right panel Figure 6.7) on the basis of Nørskov and Lundqvist's perturbation model [33]. The latter

states that the ionization probability, which predominantly determines the positive secondary ion yield, can be written as:

$$R^+ \propto e^{-\frac{\text{const} \cdot (\varphi - I)}{v_{\perp}}} \quad (6.4)$$

$R^+$	=	the ionization probability of R	[-]
$\varphi$	=	work function of the substrate	[eV]
$I$	=	ionization energy of R	[eV]
$v_{\perp}$	=	normal velocity of the sputtered particle	[m/s]

The rationale behind the equation is that the work function affects the neutralization probability of the secondary ion during the emission process.

The decreasing yield of the  $\text{Rh}^+$  ion as shown in the right panel of Figure 6.7 is straightforwardly explained by the decreasing work function when the surface fills with ammonia. It should be realized, however, that the observed correlation can only be qualitative, since the property of interest is not the macroscopic work function of the surface, but the local surface potential or the local work function. Calculations by Janssens *et al.* [34,35] on the electrostatic surface potential of an ordered array of dipoles, chosen to represent the adsorption of potassium on  $\text{Rh}(111)$ , provide at least a qualitative guide for the situation of  $\text{NH}_3$  on  $\text{Rh}(111)$ . In the limit of low  $\text{NH}_3$  coverage, each molecule decreases the work function on the adsorption site and on the nearest neighbour rhodium atoms. The strong local variations in the work function complicate the interpretation of the emission behaviour of the  $\text{Rh}(\text{NH}_3)^+$  cluster ions. In the low coverage regime, however, where mutual interactions between the  $\text{NH}_3$  molecules are of minor importance, the intensity of the  $\text{Rh}(\text{NH}_3)^+$  signal is expected to be proportional to the  $\text{NH}_3$  coverage, which is indeed the case. The question remains why the  $\text{Rh}(\text{NH}_3)^+/\text{Rh}^+$  ratio shows a sharp decrease around an  $\text{NH}_3$  coverage of  $\approx 0.12$  ML. It seems obvious that the decrease is caused by increasing interactions between the  $\text{NH}_3$  molecules. Whether the decrease of the  $\text{Rh}(\text{NH}_3)^+/\text{Rh}^+$  ratio is due to local work function effects, to changes in the adsorption geometry, or to bonding between the  $\text{NH}_3$  molecules cannot be answered from these experiments. However, it should be mentioned that the non-linear behaviour of the SIMS  $\text{Rh}(\text{NH}_3)^+/\text{Rh}^+$  intensity ratio versus the  $\text{NH}_3$  coverage shows some resemblance with the non-linear behaviour of the IR cross section of the  $\text{NH}_3$  umbrella mode with  $\text{NH}_3$  coverage as reported for  $\text{Ru}(0001)$  [13]. The drop in the IR cross section, which was observed at an  $\text{NH}_3$  coverage of  $\approx 0.15$  ML, was attributed to tilting of the  $\text{NH}_3$  molecules and the formation of hydrogen bonds at higher coverages.

SIMS is extremely sensitive towards  $\text{NH}_3$  in the low coverage regime,  $\text{NH}_3$  coverages below 0.01 ML can easily be detected. This makes SIMS very suitable to detect small traces of  $\text{NH}_3$  on the surface under reaction conditions.

### 6.4.5 Adsorption site of $\text{NH}_3$

The adsorption site of  $\alpha_1$ - $\text{NH}_3$  on the transition metals is still under debate. Ab initio calculations on Ni(111) show that the adsorption energies of  $\text{NH}_3$  in the on top site, the fcc threefold site, and the twofold or bridge site are very similar, 79, 75 and 71 kJ/mol, respectively [36]. Tentatively, the fcc site has been suggested for Ni(111) [21] and Pt(111) [22], while on Ru(0001) both the on-top [15] and the fcc site [14] have been proposed. Brown and Vickerman [26] have demonstrated that SIMS intensity ratios yield information on the adsorption site of simple adsorbate molecules such as CO and NO. Unfortunately, it is not possible to determine the distribution of  $\text{NH}_3$  over  $\text{Rh}^+$ ,  $\text{Rh}_2^+$  and  $\text{Rh}_3^+$  clusters because of intensity limitations. Nevertheless, we tend to favour adsorption of  $\text{NH}_3$  in the on top site, since the  $\text{Rh}(\text{NH}_3)^+$  cluster ion is observed very explicitly.

## 6.5 Conclusions

Adsorption of  $\text{NH}_3$  on Rh(111) greatly resembles that on the hexagonally close packed surfaces of Pt, Ru and Ni.  $\text{NH}_3$  adsorbs molecularly on Rh(111) at 120 K and no evidence for any decomposition or H-D exchange is found during heating.

The  $\text{NH}_3$  desorption behaviour shows a very explicit coverage dependence. At low coverage  $\alpha_1$ - $\text{NH}_3$  desorption is observed at 320 K, corresponding to a desorption energy of 81.5 kJ/mol. Gradual broadening of the  $\alpha_1$ - $\text{NH}_3$  desorption state to lower temperatures results in a smooth transition to the second desorption state  $\alpha_2$ - $\text{NH}_3$  at 155 K. Filling of the  $\alpha_1$ - and  $\alpha_2$ - $\text{NH}_3$  states yields a sharp ( $2 \times 2$ ) LEED pattern, which we attribute to completion of the first adsorption layer and an  $\text{NH}_3$  coverage of 0.25 ML. The sticking coefficient of  $\text{NH}_3$  at 120 K is close to unity and independent of the coverage during filling of the first adsorption layer. Desorption of  $\beta$ - $\text{NH}_3$  occurs at 130 K.

During filling of the  $\alpha_1$ -state the work function decreases linearly with coverage, the dependence levels off during filling of the  $\alpha_2$ -state and a maximum decrease of -2.4 eV is found after completion of the first adsorption layer. The enlargement of the average dipole of  $\text{NH}_3$  from 1.47 to 1.9 Debye upon adsorption indicates that either charge transfer from  $\text{NH}_3$  to the substrate or enlargement of the  $\text{NH}_3$  dipole or both has to take place.

The presence of  $\text{NH}_3$  on the surface is clearly evidenced by the appearance of the  $\text{Rh}(\text{NH}_3)^+$  cluster ion in the SIMS spectra. The  $\text{Rh}(\text{NH}_3)^+/\text{Rh}^+$  peak intensity ratio shows non-linear behaviour with the  $\text{NH}_3$  coverage and indicates some structural changes in the adlayer at a coverage of  $\approx 0.12$  ML.

SIMS appears to be very sensitive for  $\text{NH}_3$ . Coverages below 0.01 ML can easily be detected. TPSIMS experiments confirm that desorption of the second adsorption layer occurs at 130 K. Also the desorption of  $\alpha_1$ - $\text{NH}_3$  is observed and it becomes clear that some  $\text{NH}_3$  is present on the surface up to 370 K during TPD.



**References**

- [1] B.Y.K. Pan and R.G. Roth, *Ind. Eng. Chem. Process Des. Dev.* 7 (1968) 53.
- [2] C.N. Satterfield, in: "Heterogeneous Catalysts in Practice", McGraw-Hill, New York, 1980.
- [3] J. Siera, B.E. Nieuwenhuys, H. Hirano, T. Yamada, K.I. Tanaka, *Catal. Lett.* 3 (1989) 179.
- [4] G.A. Papapolymerou and L.D. Schmidt, *Langmuir* 1 (1985) 488.
- [5] A. Vavere and R.S. Hansen, *J. Catal.* 69 (1981) 158.
- [6] T. Pignet and L.D. Schmidt, *J. Catal.* 40 (1975) 212.
- [7] M.F.H. van Tol, Ph.D. Thesis, Leiden, 1993.
- [8] J. Prasad and J.L. Gland, *J. Am. Chem. Soc.* 113 (1991) 1577.
- [9] A.R. Cholach and V.A. Sobyenin, *React. Kinet. Catal. Lett.* 26 (1984) 381.
- [10] M.L. Wagner and L.D. Schmidt, *Surf. Sci.* 257 (1991) 113.
- [11] M.L. Wagner and L.D. Schmidt, *J. Phys. Chem.* 99 (1995) 805.
- [12] D.M. Thornburg and R.J. Madix, *Surf. Sci.* 220 (1989) 268.
- [13] J.A. Rodriguez, W.K. Kuhn, C.M. Truong, and D.W. Goodman, *Surf. Sci.* 271 (1992) 333.
- [14] C. Benndorf and T.E. Madey, *Surf. Sci.* 135 (1983) 164.
- [15] J.E. Parmeter, Y. Wang, C.B. Mullins, and W.H. Weinberg, *J. Chem. Phys.* 88 (1988) 5225.
- [16] R.M. van Hardeveld, J.W. Niemantsverdriet, and R.A. van Santen, *J. Phys. Chem.* 101 (1997) 998.
- [17] G.R. Castro, H. Busse, U. Schneider, T. Janssens, and K. Wandelt, *Phys. Scr.* T41 (1992) 208.
- [18] P.A. Redhead, *Vacuum* 12 (1962) 203.
- [19] A.M. de Jong and J.W. Niemantsverdriet, *Surf. Sci.* 233 (1992) 355.
- [20] C. Klauber, M.D. Alvey and J.T. Yates, Jr., *Surf. Sci.* 154 (1985) 139.
- [21] T.E. Madey, J.E. Houston, C.W. Seabury and T.N. Rhodin, *J. Vac. Sci. Technol.* 18 (1981) 476.
- [22] G.B. Fisher, *Chem. Phys. Lett.* 79 (1981) 452.
- [23] M. Drechsler, H. Hoinkes, H. Kaarmann, H. Wilsch, G. Ertl, and M. Weiss, *Appl. Surf. Sci.* 3 (1979) 217.
- [24] J.C. Vickerman, A. Brown, N.M. Reed, Clarendon Press, Oxford, 1989.
- [25] H.J. Borg and J.W. Niemantsverdriet, in: "Catalysis: a Specialist Periodical Report", Vol 11, Royal Society of Chemistry, Cambridge, 1994, 1.
- [26] A. Brown and J.C. Vickerman, *Surf. Sci.* 124 (1983) 267.
- [27] U. Diebold and P. Varga, *Surf. Sci.* 241 (1991) L6.
- [28] L.L. Lauderback and W.N. Delgass, *J. Catal.* 105 (1987) 55.
- [29] H.J. Borg, J.F.C.-J.M. Reijerse, R.A. van Santen, and J.W. Niemantsverdriet, *J. Chem. Phys.* 101 (1994) 10052.
- [30] K. Jones, "Comprehensive Inorganic Chemistry", Pergamon, Oxford, 1973.
- [31] G.A. Somorjai, "Introduction to Surface Chemistry and Catalysis", John Wiley & Sons Inc., New York (1994) 371.
- [32] R.A. van Santen and J.W. Niemantsverdriet, "Chemical Kinetics and Catalysis", Plenum Press, New York, 1995.
- [33] J.N. Nørskov and B.I. Lundqvist, *Phys. Rev.* B19 (1979) 5661.
- [34] T.V.W. Janssens, G.R. Castro, K. Wandelt, and J.W. Niemantsverdriet, *Phys. Rev.* B49 (1994) 14599.
- [35] T.V.W. Janssens, J.W. Niemantsverdriet, and R.A. van Santen, *J. Chem. Phys.* 101 (1994) 2995.
- [36] A. Chattopadhyay, H. Yang, and J.L. Whitten, *J. Phys. Chem.* 94 (1990) 6379.

## 7 Reduction of NO by ethylene on Rh(111)

### 7.1 Introduction

Although the reaction between NO and CO to CO<sub>2</sub> and N<sub>2</sub> is commonly held responsible for the removal of NO from automotive exhausts in the three-way catalyst, hydrogen and hydrocarbons make a substantial contribution to NO reduction as well [1]. Cracking of gasoline in the engine of a car is the source of H<sub>2</sub> (estimated to account for roughly 30% of the concentration of CO in the exhaust) and a wide range of smaller hydrocarbons, among which methane, acetylene, ethylene, benzene and toluene are the most abundant ones [2]. Unsaturated hydrocarbons, such as ethylene and propylene, readily adsorb on the noble metals of the three-way catalyst and are a source of H- and C-atoms available for reaction with *e.g.* the O-atoms of dissociatively adsorbed NO and O<sub>2</sub>.

Several papers have been published on the reduction of NO by small hydrocarbons in copper-exchanged zeolites [3-5]. However, much less is known about the NO-hydrocarbon interaction on platinum and rhodium [6]. A recent infrared study by Bamwenda *et al.* [7] revealed that the surface of a Rh/Al<sub>2</sub>O<sub>3</sub> catalyst contained NCO and CN species during the selective reduction of NO by propylene. This is illustrative for a rather rich surface chemistry, allowing for several reaction pathways for the formation of undesired products such as HCN, HCNO, NH<sub>3</sub> [8,9] or even NH<sub>4</sub>OCN [10]. DeLouise and Winograd investigated the reactions between NO and carbon on Rh(331) by XPS and SIMS and detected a CN surface species in the temperature range between 400 K and 800 K [11].

In this chapter we use temperature-programmed reaction spectroscopy (TPRS) and secondary ion mass spectrometry (SIMS) to explore the surface reactions between NO and C<sub>2</sub>H<sub>4</sub> on Rh(111). Ethylene has been chosen as model hydrocarbon since it constitutes a substantial part of the hydrocarbon emission in exhaust gas and is characteristic for decomposition (H<sub>2</sub> evolution) of many unsaturated hydrocarbons. Besides, the adsorption and decomposition of ethylene on Rh(111) is well documented in work from several laboratories [12-14].

First we briefly describe the most important characteristics of the separate adsorption and decomposition of ethylene and NO on Rh(111). Next we present the results of two detail studies, *viz.*, H<sub>2</sub>O formation by reaction between atomic oxygen and hydrogen, and reactions between atomic oxygen and ethylene. The results of these studies enables us to present a thorough interpretation of the complex NO-ethylene reaction system. Next follows a qualitative description of the reactions and surface species during heating of coadsorbed NO and ethylene on the basis of TPRS and SIMS measurements. Finally, we discuss the influence of the amount of coadsorbed ethylene on the product distribution on the basis of oxygen and nitrogen mass balances.

## 7.2 Experimental

The experiments were done in a UHV system (base pressure around  $10^{-10}$  mbar) equipped with a Leybold SSM 200 quadrupole mass spectrometer for TPD and SSIMS measurements, as described in detail in Chapter 2. The rhodium crystal, cut in the [111] orientation within  $0.5^\circ$  and polished by standard procedures, was mounted on a moveable stainless steel manipulator with 0.3 mm thick tantalum wires, where it could be cooled to liquid nitrogen temperature and resistively heated up to 1500 K. Temperatures were measured with a chromel-alumel thermocouple spotwelded on the backside of the crystal. Small amounts of bulk impurities, such as sulphur, chlorine, and boron, were removed by cycli of argon sputtering ( $1.5$  keV,  $5 \mu\text{A}/\text{cm}^2$ ) at 900 K and annealing to 1400 K. Carbon was removed by annealing the crystal in  $2 \times 10^{-8}$  mbar  $\text{O}_2$  slowly varying the temperature between 900 and 1100 K. Oxygen was removed from the surface by annealing shortly to 1425 K. Ethylene (Messer Griesheim, 99.95% pure) was used without further purification; gas exposures are reported in Langmuir ( $1\text{L}=1.33 \times 10^{-6}$  mbar.s); coverages are reported in monolayers (ML; number of adsorbate molecules per Rh surface atom).

## 7.3 Results

### 7.3.1 NO on Rh(111)

NO adsorption and decomposition has been described in detail in Chapter 3. Therefore, we just summarize the characteristics of the NO dissociation reaction as far as they are relevant for interpretation of the NO-ethylene reaction system.

If the NO coverage is lower than 0.20 ML, all NO dissociates during a TPD experiment and dissociation starts around 275 K. At higher initial coverages the NO dissociation is shifted to higher temperatures and part of the NO desorbs molecularly around 430 K. NO and  $\text{N}_2$  are the only N-containing desorption products observed.

### 7.3.2 $\text{C}_2\text{H}_4$ on Rh(111)

Decomposition of olefins, such as ethylene and propylene, has extensively been studied on Pt and Rh [12-15]. In brief, ethylene adsorbs molecularly on rhodium at low temperatures, *e.g.* around 120 K, and at around 180 K it reacts to a species called ethylidyne,  $\text{CCH}_3$ , and a H-atom. Around 300 K the ethylidyne decomposes further to acetylide (CCH), CH and carbidic C-atoms [16], see Figure 7.1. The decomposition reaction is impeded at higher coverages.

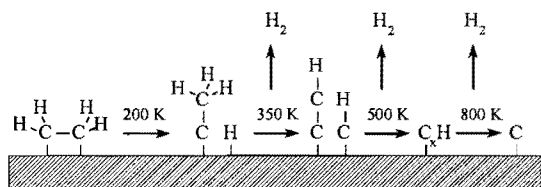


**Figure 7.1** Schematic representation of the  $\text{C}_2\text{H}_4$  decomposition during TPD on Rh(111).

Figure 7.2 shows the evolution of  $\text{H}_2$  during the ethylene decomposition on Rh(111). Up to 0.25 ML, all ethylene decomposes and  $\text{H}_2$  is the only product observed in the gas phase. The spectrum for the smallest ethylene coverage (0.05 ML) shows a sharp  $\text{H}_2$  desorption state at 345 K, representing regular H-H recombination [17]. At

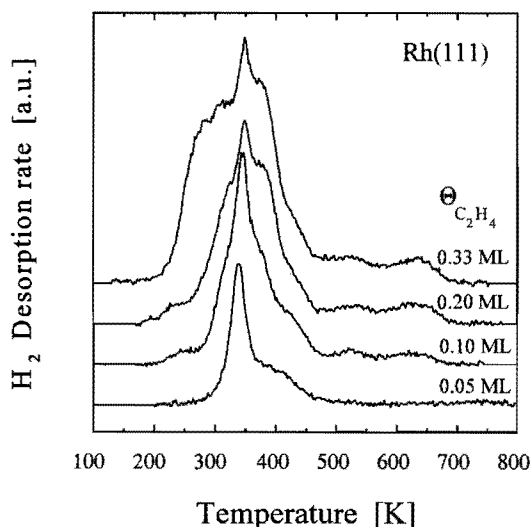


**Figure 7.2** TPD of  $\text{H}_2$  from ethylene on Rh(111). The adsorption temperature was 100 K, and the heating rate 5 K/s.

higher ethylene coverage,  $\text{H}_2$  desorption shifts to lower temperatures. At the highest ethylene coverage,  $\text{H}_2$  desorption starts around 200 K, which is the temperature where surface hydrogen is produced by the ethylene to ethylidyne conversion. For ethylene coverages above 0.25 ML, the excess ethylene desorbs, mainly at 180 K [12]. Note that at the higher coverages, hydrogen continues to desorb up to temperatures as high as 700 K, stemming from the decomposing  $\text{CH}_x$  species, as Figure 7.2 shows.

The conversion of ethylene to ethylidyne on Rh(111) has been followed in situ with static SIMS. For low coverages of ethylene (around 0.05 ML), evidence was found that the reaction proceeds through a vinyl ( $-\text{CH}=\text{CH}_2$ ) intermediate [12]. This in contrast to the situation on Pt(111), where ethylidyne,  $=\text{CH}-\text{CH}_3$ , has been proposed as the intermediate towards ethylidyne [18].

### 7.3.3 Reactions between O and H

During reactions between NO and C<sub>2</sub>H<sub>4</sub>, formation of H<sub>2</sub>O is expected to proceed by stepwise hydrogenation of atomic oxygen [19-21]. We have briefly investigated the reaction between atomic oxygen and hydrogen by TPRS in order to have a reference for the H<sub>2</sub>O formation reaction.

Atomic oxygen was deposited on the Rh(111) surface by adsorbing NO at 120 K followed by heating to 950 K in order to desorb the nitrogen and the excess NO. The resulting oxygen coverage can be determined from the N<sub>2</sub> desorption peak area, since equal amounts of N and O are formed when an NO molecule dissociates. After heating to 950 K, the crystal was cooled down to 120 K at which temperature the surface was saturated with H<sub>2</sub> by an exposure of 1.0 L (on a clean Rh(111) surface this would result in a hydrogen coverage of ~1.0 ML).

Figure 7.3 shows the TPD spectra of H<sub>2</sub>, H<sub>2</sub>O and O<sub>2</sub> obtained after pre-covering a Rh(111) surface with different amounts of O<sub>ads</sub> and subsequent saturation with H<sub>2</sub>. For the lowest oxygen coverage (0.05 ML), the H<sub>2</sub> desorption spectrum is identical to that measured when hydrogen is the only adsorbate. However, with increasing oxygen coverages at least three additional hydrogen desorption states develop. First a desorption state at 260 K appears, followed by desorption states at 210 and 175 K, respectively. The hydrogen desorption is shifted to lower temperatures probably due to repulsive lateral interactions with oxygen atoms. Whether the additional desorption states correspond to hydrogen atoms in different local oxygen surroundings cannot be answered from these experiments. The total amount of hydrogen that desorbs, as either H<sub>2</sub> or H<sub>2</sub>O, is not

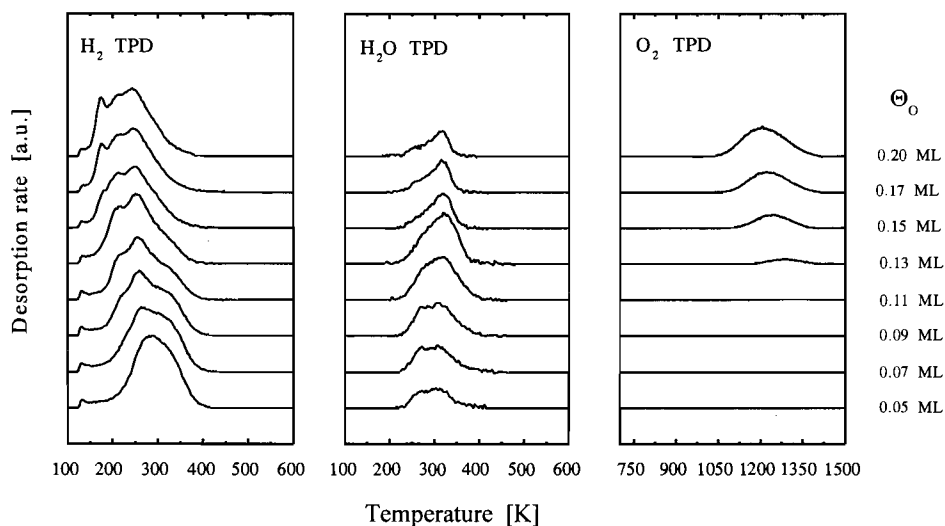


**Figure 7.3** Temperature programmed desorption spectra of H<sub>2</sub>, H<sub>2</sub>O and O<sub>2</sub> obtained after pre-covering a Rh(111) surface with different amounts of O<sub>ads</sub> and saturating with H<sub>2</sub>. The heating rate was 10 K/s below and 7 K/s above 950 K.

strongly affected by the amount of oxygen that is pre-adsorbed, indicating that the  $H_2$  adsorption behaviour is not significantly altered by the presence of  $O_{ads}$ .

Independent of the oxygen coverage, reaction to  $H_2O$  set on at around 225 K and ends at 400 K, the temperature at which all hydrogen has desorbed. The onset temperature for  $H_2O$  formation, 225 K, is in good agreement with the literature [19-21]. Note the irregular shape of the  $H_2O$  desorption spectra from which two desorption states can be discerned. Roughly speaking, the high-temperature state becomes more prominent at higher oxygen coverage.  $H_2O$  desorption starts at 180 K on Rh(111) [19,22], which indicates that the  $H_2O$  desorption observed in these experiments is reaction limited.

Initially, all oxygen can be hydrogenated to  $H_2O$ , but for oxygen coverages above  $\sim 0.11$  ML part of the oxygen desorbs as  $O_2$  between 1050 and 1400 K, see Figure 7.3. The oxygen desorption spectra show second order desorption behaviour and are in good agreement with those reported in the literature [23,24].

Figure 7.4 shows the selectivity of the initially adsorbed oxygen to  $H_2O$  and  $O_2$ . For oxygen coverages below 0.11 ML the selectivity to  $H_2O$  is 100%, but it declines rapidly to  $\sim 20\%$  when the oxygen coverage increases to 0.20 ML. Repulsion between O and H favours  $H_2$  desorption at low temperatures and leaves insufficient H on the surface to hydrogenate all adsorbed oxygen.

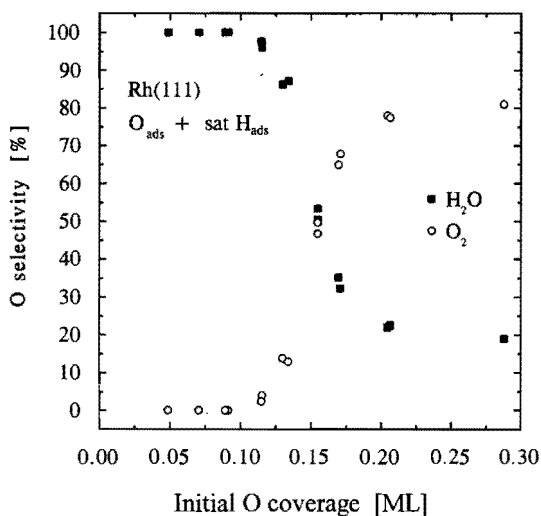


**Figure 7.4** Selectivity of  $O_{ads}$  towards  $H_2O$  and  $O_2$  during TPD after saturating the Rh(111) surface with  $H_2$  at 120 K.

### 7.3.4 Reactions between O and $C_2H_4$

In temperature-programmed reactions between NO and ethylene, besides  $H_2O$  also CO and  $CO_2$  formation is expected, resulting from reaction between atomic oxygen and hydrocarbon fragments. Hence, NO dissociation is an essential prerequisite for oxidation reactions to occur. In order to assess whether CO formation and oxidation reactions are

limited by NO dissociation, we have investigated reactions between atomic oxygen and ethylene. This reaction system is less complex owing to the absence of N-containing products (especially the mass interference between CO and  $N_2$  is eliminated). Atomic oxygen atoms were prepared by dissociating NO and desorbing the nitrogen atoms by heating to 950 K.

Figure 7.5 shows TPD spectra of the various desorbing gases starting from 0.25 ML of adsorbed oxygen atoms coadsorbed with 0.30 ML ethylene. As Figure 7.5 shows, large amounts of  $H_2$  desorb between 250 and 750 K, while only a small fraction of the hydrogen leaves the surface as  $H_2O$  (18 amu) in the range between 250 and 550 K. The mass 28 peak evident at around 260 K reflects the desorption of ethylene, as is confirmed by the simultaneous occurrence of a significant peak at 27 amu, caused by ethylene fragmentation in the spectrometer. Compared to the ethylene only case, the molecular ethylene desorption state has shifted at about 80 K to higher temperatures. The mass 28 peak between 500 and 600 K represents CO. The  $CO_2$  signal (44 amu) is weak, indicating that with an excess of ethylene, CO desorption provides the main channel for oxygen removal from the rhodium surface.

Figure 7.5 shows several interesting points. Firstly, the low-temperature hydrogen peak, which is rate-limited by the recombination of two H-atoms, is much more intense than with a rhodium surface covered entirely by ethylene, and has shifted to lower temperatures (see Figure 7.2 for comparison). Secondly, the ethylene desorption peak is much more intense than in the absence of coadsorbed oxygen. Hence, we conclude

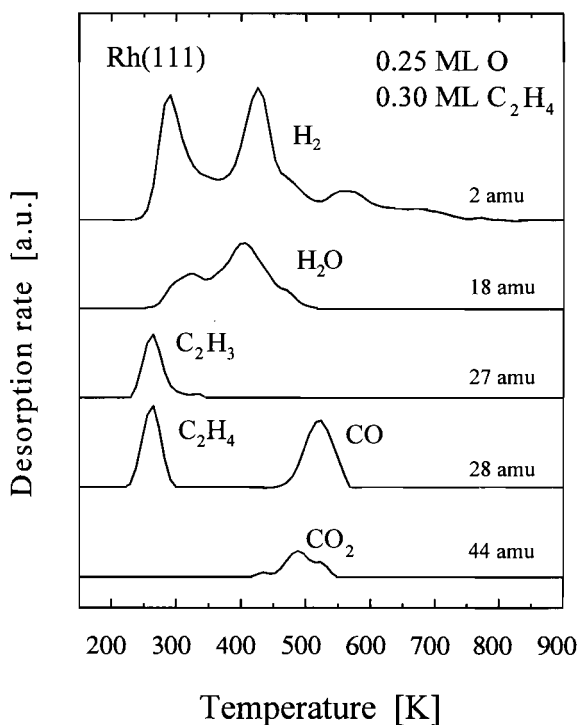


**Figure 7.5** Temperature programmed reactions of 0.30 ML of ethylene coadsorbed with 0.25 ML of oxygen atoms, showing the desorption of the gases  $H_2$ ,  $H_2O$ ,  $C_2H_4$ , CO and  $CO_2$ . The mass 27 signal of  $C_2H_4$  fragmented into  $C_2H_3$  was included to discriminate between the mass 28 signals of  $C_2H_4$  and CO.

that oxygen hinders ethylene decomposition and destabilizes adsorbed hydrogen. The second hydrogen desorption peak at 430 K most probably represents ethylidyne decomposition and/or dehydrogenation of the resulting hydrocarbon fragments. Compared to the ethylene-only case the desorption peak is much more intense and shifted to higher temperatures. This might indicate that, like ethylene, ethylidyne is stabilized by the presence of atomic oxygen. Furthermore, in Figure 7.5 the hydrogen desorption states are much better resolved than in the ethylene-only case, see Figure 7.2. The decreased hydrogen desorption in between the two H<sub>2</sub>-desorption states is most probably the result of H<sub>2</sub>O formation in the 250-450 K temperature range, which provides a competitive channel for H-atoms to leave the surface. However, formation and desorption of H<sub>2</sub> remains the preferred reaction of adsorbed H-atoms.

### 7.3.5 NO and ethylene at low coverage

First we will describe the reaction between adsorbed NO and ethylene at low coverage. Figure 7.6 shows TPD and SIMS spectra obtained during heating of the Rh(111) surface covered with 0.10 ML of NO and 0.03 ML of ethylene. The TPD spectra in the upper half of Figure 7.6 show that H<sub>2</sub>O, CO<sub>2</sub> and N<sub>2</sub> are the main desorption products, along with small amounts of H<sub>2</sub> and some CO. The mass 28 signal consists of two peaks, the one around 500 K, which is characteristic of CO (as appears from checking

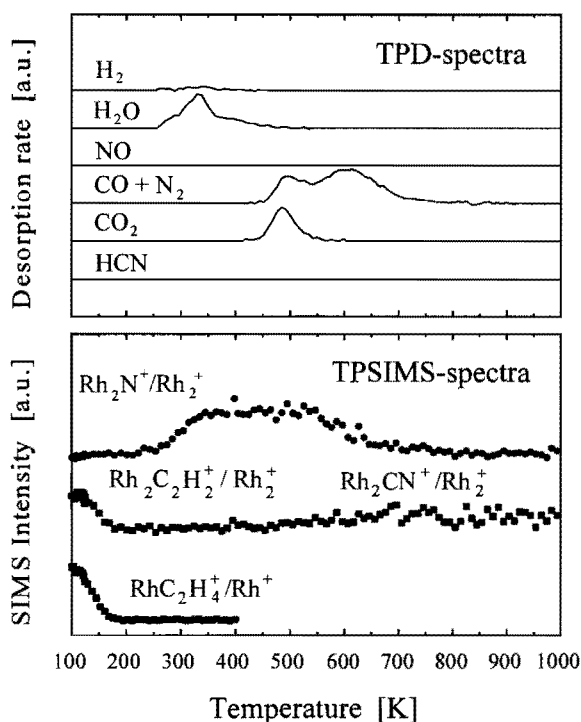


**Figure 7.6** Temperature programmed reactions of 0.03 ML of ethylene coadsorbed with 0.10 ML of NO as observed by TPD and SIMS (see text for explanation). The adsorption was done at 120 K, and the heating rate was 10 K/s.



the masses 12 and 16, see also Figure 7.4 for comparison) and the other with a maximum at 600 K representing  $N_2$  (as appears from checking mass 14). Note that part of the CO signal is a fragment of  $CO_2$  (roughly 10% of  $CO_2$  cracks to CO in the mass spectrometer), and that the actual amount of desorbing CO is small.

The TP-SIMS intensities in the lower half of Figure 7.6 reflect reactions on the surface during heating. In order to compensate at least partially for effects due to changes in work function during decompositions and reactions on the surface, it is customary to consider intensity ratios such as  $RhC_2H_4^+/Rh^+$ , which often quite closely correlate with the adsorbate coverage [25,26]. First, the  $RhC_2H_4^+/Rh^+$  signal ratio in Figure 7.6, which is indicative for adsorbed ethylene, shows that ethylene starts to decompose at about 130 K. From previous work of Borg *et al.* [12] we know that ethylene when present in low coverages on Rh(111), reacts at about 130 K to vinyl,  $-CH=CH_2$ , and a H-atom. The vinyl rearranges at about 180 K to ethynidyne,  $\equiv C-CH_3$ . The latter can in principle be observed by a  $CH_3^+$  signal [27], however, at the coverages employed in Figure 7.6, the intensity is very weak and has therefore not been included.

The  $Rh_2N^+$  ion monitors the dissociation of adsorbed NO, which sets in at about 250 K. N-atoms remain on the surface until desorption of  $N_2$  begins just above 500 K. Note that the onset for  $H_2O$  formation parallels the onset of NO dissociation. The other ion,  $Rh_2CN^+$ , at 232 amu, is included for comparison with experiments to be described later on. The intensity of this mass signal at low temperatures is due to the adsorbed ethylene, which produces a  $Rh_2C_2H_2^+$  fragment of the same mass.

At low coverages, NO and ethylene thus decompose as if they were separately on the Rh(111) surface. The reaction products are mainly the expected  $H_2O$ ,  $CO_2$  and  $N_2$ , while small amounts of  $H_2$  and CO are formed as well.

### 7.3.6 NO and ethylene at intermediate coverages

The results of a TPD/TPSIMS experiment done with 0.20 ML of NO coadsorbed with 0.12 ML of ethylene, shown in Figure 7.7, illustrate the reaction pathways occurring at moderate coverages.

The TPD spectra in the upper half of Figure 7.7 reveal that in addition to  $N_2$ ,  $CO_2$  and  $H_2O$ , significant amounts of  $H_2$ , NO, CO, and HCN are now formed as well. Traces of  $C_2N_2$  (not shown) are observed also. Following the proper fragmentation signals at 12, 14, 16 and 27 amu enables us to interpret the mass 28 signal. It appears that ethylene does not desorb in this particular experiment, that the peaks between 400 and 600 K are due to CO, and that the peak above 700 K is caused by desorption of  $N_2$ .

We discuss the trends of the static SIMS data, represented in the lower half of Figure 7.7, from low to high temperature. The first surface reaction that appears during heating of the adsorbed  $C_2H_4$  and NO is the conversion of ethylene to ethynidyne,  $CCH_3$ , and H-atoms between 190 and 220 K [12]. The SIMS spectra in Figure 7.7 indicate the conversion of ethylene by a decrease of the  $RhC_2H_4^+/Rh^+$  ratio and the accompanied

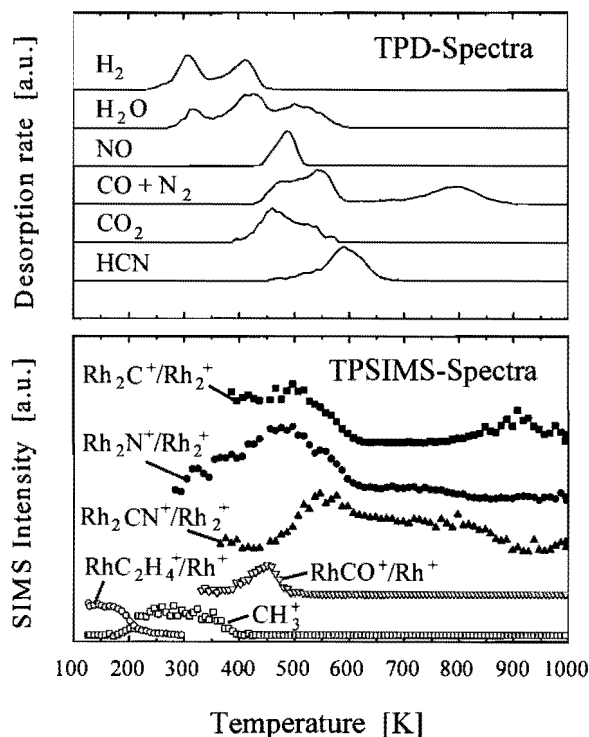


**Figure 7.7** Temperature-programmed reactions of 0.12 ML of ethylene coadsorbed with 0.20 ML of NO as followed by TPD and SIMS. The adsorption was done at 120 K, and the heating rate was 10 K/s.

formation of ethylidyne by the appearance of the methyl secondary ion,  $\text{CH}_3^+$  [27]. The fact that we do not observe the ethylene to vinyl transition at around 130 K by the disappearance of the  $\text{RhC}_2\text{H}_4^+$  signal in Figure 7.6 is consistent with earlier work which showed that this reaction is strongly impeded at higher coverages [12]. From the  $\text{H}_2$  TPD spectra we learn that H-atoms formed in the ethylene  $\rightarrow$  ethylidyne reaction start to desorb around 250 K.

Just below 300 K, NO dissociation sets in, as reflected by the growth of the  $\text{Rh}_2\text{N}^+$  SIMS signal characteristic of N-atoms, and the evolution of  $\text{H}_2\text{O}$ . NO dissociation occurs in two steps, the first between roughly 300 and 350 K, after which the  $\text{Rh}_2\text{N}^+$  intensity reaches a short plateau, and the second above 400 K, as can be inferred from a further rise in the  $\text{Rh}_2\text{N}^+$  intensity and the appearance of additional peaks in the desorption of CO and  $\text{H}_2\text{O}$ , as we will discuss in more detail below.

The decomposition of ethylidyne, evident from the decrease of the  $\text{CH}_3^+$  intensity in SIMS, falls in the temperature range of approximately 300 - 380 K, and is accompanied by the formation of H-atoms, which either desorb as  $\text{H}_2$  or react with O-atoms to  $\text{H}_2\text{O}$ , which desorbs instantaneously.  $\text{H}_2$  desorption terminates at about 450 K. Note, however, that the surface still contains hydrogen - most probably present in the form of carbonaceous species - as  $\text{H}_2\text{O}$  and HCN continue to desorb to almost 600 K and 700 K, respectively.

Oxidation of C-atoms appears to begin at 380 K, as the growth of the  $\text{RhCO}^-/\text{Rh}^-$  ratio in SIMS, and the more or less simultaneous desorption of  $\text{CO}_2$  indicate. Apparently, the reaction between adsorbed CO and O is not sufficiently rapid to prevent accumulation of CO on the surface, which is probably caused by lack of sufficient O-atoms. CO desorption is seen above 450 K both in TPD and in SIMS, in agreement with the literature of CO on Rh(111) [28,29]. Also in this temperature range, 450 - 520 K, the desorption of NO proceeds. Following earlier work [30,31], we propose that the NO desorbs because the surface is to a large extent occupied, implying that the relatively large ensembles of free rhodium atoms necessary for NO dissociation are not available. Hence, NO desorbs as soon as the temperature is high enough to permit thermal desorption. Interestingly, the desorption temperature of NO is significantly (*i.e.* about 70 K) higher than if NO is the only adsorbate [30]. The explanation for this phenomenon is that in the latter case the NO molecules desorb out of a repulsive environment of NO, N- and O-atoms, whereas in the present case the surface contains carbonaceous species as well. The extent to which the shift in NO desorption to higher temperatures is caused by reduced repulsion or by increased attraction by carbonaceous species is not clear, however.

The SIMS data in Figure 7.7 strongly suggest that a large inventory of cyanide groups forms on the surface between 450 and 550 K. First, the  $\text{Rh}_2\text{CN}^+$  intensity increases strongly and second, the intensities of both  $\text{Rh}_2\text{N}^+$  and  $\text{Rh}_2\text{C}^+$ , characteristic of atomic nitrogen and carbon at these temperatures, decrease. Although the  $\text{Rh}_2\text{C}^+$  is observed as a fragment of adsorbed  $\text{C}_2\text{H}_x$  species as well, it is very likely that all C-C bonds have broken at the temperatures where CN groups start to form (*i.e.* 450 K). The  $\text{Rh}_2\text{N}^+$  intensity falls to a low value, most likely reflecting the fragmentation of  $\text{Rh}_2\text{CN}^+$ , while the  $\text{Rh}_2\text{C}^+$  signal drops practically to zero. Note that the appearance of CN on the surface coincides with the onset of the HCN desorption and that CN formation occurs at higher temperatures than CO formation, reflecting that the reaction between carbon and oxygen is preferred above that between carbon and nitrogen atoms.

We do not believe that the cyanide is present as adsorbed HCN, because, first, the SIMS signal of the corresponding  $\text{Rh}_2\text{HCN}^+$  is not observed and second, the irregular leading edge of the HCN desorption trace, starting at 450 K, suggests a reaction-limited desorption process. Indeed, Hwang *et al.* observed a reaction limited HCN desorption state at 430 K starting from methyl amine  $\text{CH}_3\text{NH}_2$  on Rh(111) [32]. We conclude that part of the cyanide inventory is hydrogenated to HCN between 500 and 650 K, as evident from the desorption of HCN and the decrease in the  $\text{Rh}_2\text{CN}^+$  SIMS signal. Apparently, the adsorbate layer is fully dehydrogenated above 650 K. The cyanide species remain stable until about 720 K, where  $\text{N}_2$  desorption starts to occur, as evidenced by the  $\text{N}_2$  signal in TPD (accompanied by a parallel signal at 14 amu), a decrease in the  $\text{Rh}_2\text{CN}^+$  signal in SIMS, and an increase in the  $\text{Rh}_2\text{C}^+$  signal characteristic of adsorbed carbon. The  $\text{Rh}_2\text{N}^+$  ion characteristic of adsorbed N-atoms is not observed, indicating that  $\text{N}_2$  desorbs instantaneously. The decrease of the  $\text{Rh}_2\text{C}^+$  signal above 900 K is attributed to the dissolution of carbon into the rhodium crystal [33].

## 7.3.7 Coverage dependence

Figure 7.8 shows the evolution of the different desorbing gases as a function of increasing ethylene exposure for a fixed coverage of 0.20 ML of NO. Similarly to the ethylene only case, the H<sub>2</sub> TPD patterns start with a desorption-limited state at about 310 K, which at low coverages is largely attributed to the recombinative desorption of H-atoms formed at lower temperature (180 - 220 K) in the ethylene → ethylidyne conversion. However, note that compared to the ethylene only case the H<sub>2</sub> desorption state has shifted

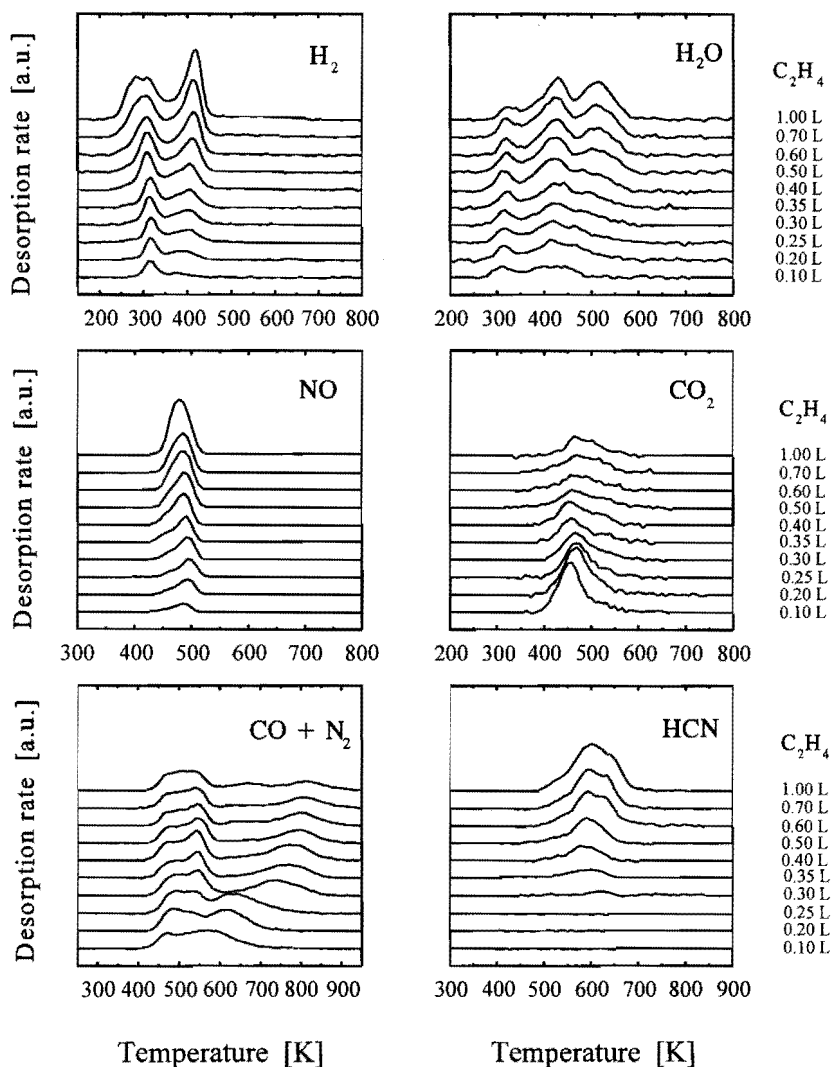


**Figure 7.8** TPD spectra of 0.20 ML of NO, coadsorbed with varying amounts of ethylene on Rh(111), measured at a heating rate of 10 K/s. The adsorption temperature was 120 K.

some 35 K to lower temperature. The second peak growing in the range of 375 - 400 K is entirely attributed to reaction-limited desorption of  $H_2$  originating from the decomposition of hydrocarbon fragments. Whereas  $H_2$  desorption continues up to 700 K with high coverages of ethylene in the absence of coadsorbed NO, it now stops at 450 K.

At all coverages, the  $H_2O$  signal starts to grow at about 275 K, which is the temperature where NO dissociation sets in, see Figure 7.7. The second state, with a peak maximum above 400 K, parallels the second  $H_2$  desorption state and the second NO dissociation step, see Figure 7.8, and is due to recombinative desorption of O-atoms with H-atoms originating from the decomposition of  $C_xH_y$  fragments on the surface. Note that the selectivity of the H-atoms generated in this temperature interval (*i.e.* 350 - 450 K) to form  $H_2O$  is high at initially low ethylene coverages, and decreases when the H-content of the adsorbate layer increases, as expected. Interestingly, a third reaction-limited  $H_2O$  desorption state develops around 500 - 540 K at high initial ethylene coverages. The intensity of this state parallels that of the NO desorption at somewhat lower temperature. We propose that the NO desorption between 450 and 520 K (which is significantly above the dissociation temperature of NO on the Rh(111) surface) together with the desorption of other gases, such as CO and  $CO_2$ , provide surface sites where additional NO can dissociate, thus creating atomic oxygen which is responsible for further  $H_2O$  formation.

The desorption of NO rises strongly with increasing total coverage, reflecting the ensemble requirement of the NO dissociation. The mass 28 TPD spectra in Figure 7.8 are mainly due to CO and  $N_2$ . At high initial ethylene coverages also some  $C_2H_4$  desorbs at around 250 K (not shown in Figure 7.8). For intermediate coverages, one recognizes two CO desorption states with peak maximum temperatures of about 475 and 540-550 K. The first is due to the desorption of adsorbed CO, which formed on the surface between 380 and 475 K (see the  $RhCO^+/Rh^+$  SIMS signal in Figure 7.7). The desorption peaking at higher temperatures occurs almost simultaneously with the third  $H_2O$  desorption state and is attributed to the evolution of O-atoms from NO molecules additionally dissociating at higher temperatures, as discussed previously.

$CO_2$  desorption is seen to commence significantly before CO desorbs, and parallels qualitatively the concentration of adsorbed CO as detected in SIMS (Figure 7.8). Hence we conclude that  $CO_2$  desorption is favoured above desorption of CO, but is limited by the availability of adsorbed O-atoms. This is in agreement with the dependence of the  $CO_2$  TPD intensities on both temperature and initial ethylene coverage.

The maximum of the  $N_2$  desorption shifts from 550-600 K at low to above 800 K at high initial ethylene coverage. We propose that the low-temperature  $N_2$  desorption is due to recombinative desorption of atomic nitrogen, while the states at higher temperature reflect the decomposition of CN species in the range of 750 - 900 K (Figure 7.7), after which N atoms desorb instantaneously in a second order process. The initial shift of the  $N_2$  desorption peak from 550-600 K upward when ethylene is coadsorbed in small amounts may well reflect the relieve of repulsive interactions by oxygen atoms that have been removed as  $H_2O$  and  $CO_2$  or CO [30], see also Chapter 4. The further shift of the  $N_2$  signal to higher temperatures, however, is predominantly the effect of CN formation.

Finally, HCN desorption is observed at higher initial ethylene coverages, *i.e.* above 0.30 L C<sub>2</sub>H<sub>4</sub> exposure.

The product selectivity of the NO-ethylene reaction depends very much on the NO:C<sub>2</sub>H<sub>4</sub> coverage ratio. Trends in the product selectivity can be obtained from TPD peak areas, which are linearly proportional to surface coverages (determination of absolute coverages requires at least one calibration point). We have not been able to deconvolute the mass 28 signal into N<sub>2</sub> and CO contributions. However, the N<sub>2</sub> desorption peak areas have been derived from the mass 14 signal. The CO TPD areas could not be determined from the mass 12 signal due to interference with the CO<sub>2</sub> peak.

Figure 7.9 shows the TPD peak areas for H<sub>2</sub>, H<sub>2</sub>O, CO<sub>2</sub>, N<sub>2</sub>, NO and HCN at two initial NO coverages, *viz.* 0.10 ML and 0.20 ML, as a function of the ethylene exposure. For both low and high coverage of NO, the H<sub>2</sub> TPD areas increase linearly with ethylene exposure up to 1.0 L, after which they become constant. Also the H<sub>2</sub>O production increases with increasing ethylene exposure up to 0.60 L. Note that, initially, the H<sub>2</sub>O production is larger for 0.10 ML NO than for 0.20 ML NO. This is explained by the fact that at lower coverage both NO dissociation and ethylene decomposition occur at a lower temperature; consequently H<sub>2</sub>O formation can proceed at temperatures where H<sub>2</sub> desorption is not competitive yet. At low ethylene exposures the amount of CO<sub>2</sub> that is formed for 0.20 ML NO is roughly twice that observed at 0.10 ML NO, in accordance with the expected O coverages. The amount of CO<sub>2</sub> that is produced decreases rapidly with increasing ethylene exposure.

For low ethylene exposures also the amount of N<sub>2</sub> that is formed for 0.20 ML NO is twice that for 0.10 ML NO, thus resembling the expected atomic nitrogen coverage ratio provided all NO dissociates. However, for both NO coverages the amount of nitrogen that is formed decreases rapidly with increasing ethylene exposure. For 0.10 ML NO, N<sub>2</sub> desorption is not observed for exposures above 0.9 L.

NO desorption is much more significant for 0.20 ML than for 0.10 ML NO. In both cases the amount of NO that desorbs increases linearly with ethylene exposure up to 1.0 L. For both NO coverages, no HCN desorption is observed for ethylene exposures below 0.20 L. For 0.10 ML NO, HCN desorption sets in slightly earlier than for 0.20 ML NO, but in both cases the amount of HCN that is formed increases significantly with ethylene exposures above 0.25 L.

Since the amount of NO that is initially adsorbed is known, it is possible to construct mass balances for N and O provided that the TPD peak areas of *all* the N and O containing desorption products can be determined. The only N-containing products that we observed were N<sub>2</sub>, NO, HCN and small amounts of C<sub>2</sub>N<sub>2</sub>, whereas NH<sub>3</sub>, N<sub>2</sub>O, CH<sub>3</sub>CN were not found.

The saturation coverage of irreversibly adsorbed ethylene was assumed to be 0.25 ML, similar to the coverage on the bare surface [12]. For ethylene exposures above 1.0 L the amount of hydrogen that desorbs (as H<sub>2</sub>, H<sub>2</sub>O and HCN) becomes constant, indicating that the amount of irreversibly adsorbed ethylene becomes constant from there

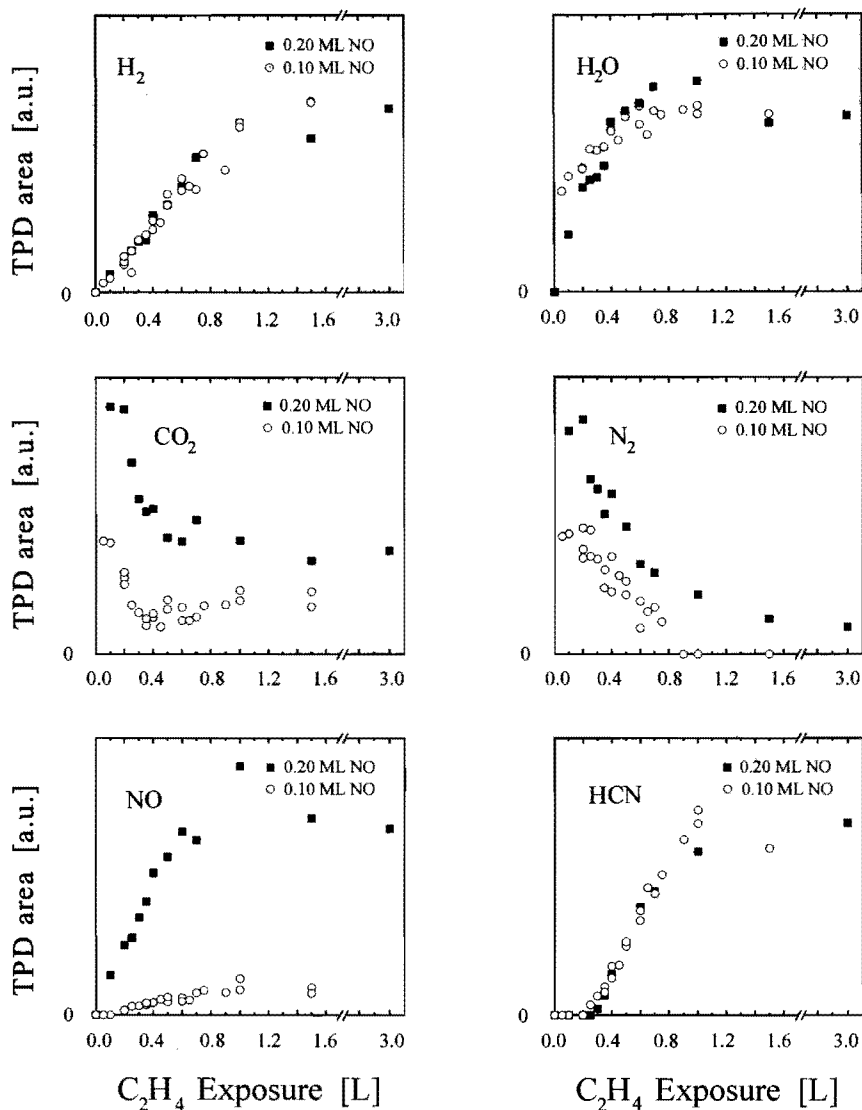
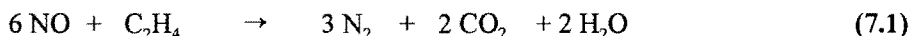


**Figure 7.9** TPD peak areas for  $H_2$ ,  $H_2O$ ,  $CO_2$ ,  $N_2$ ,  $NO$  and  $HCN$  in the reaction of  $NO+C_2H_4$  for two different initial NO coverages, 0.10 ML and 0.20 ML, as a function of the ethylene exposure.

on. Therefore we assumed that the saturation coverage of ethylene, 0.25 ML, is obtained by an exposure of 1.0 L. Furthermore, we assumed a linear dependence between ethylene coverage and exposure below 1.0 L. A coverage independent sticking coefficient for ethylene adsorption is also observed in the ethylene only case [12].

Figure 7.10 shows the N-selectivity for initial NO coverages of 0.10 ML and 0.20 ML as a function of the NO/C<sub>2</sub>H<sub>4</sub> coverage ratio. Note that stoichiometric conditions correspond to an NO/C<sub>2</sub>H<sub>4</sub> coverage ratio of 6:



For both initial NO coverages, the selectivity to N<sub>2</sub> is 100 % under around stoichiometric conditions (NO/C<sub>2</sub>H<sub>4</sub>=6). For 0.20 ML NO the selectivity to N<sub>2</sub> drops faster with decreasing NO/C<sub>2</sub>H<sub>4</sub> ratio than for 0.10 ML NO, which is a consequence of more NO desorption.

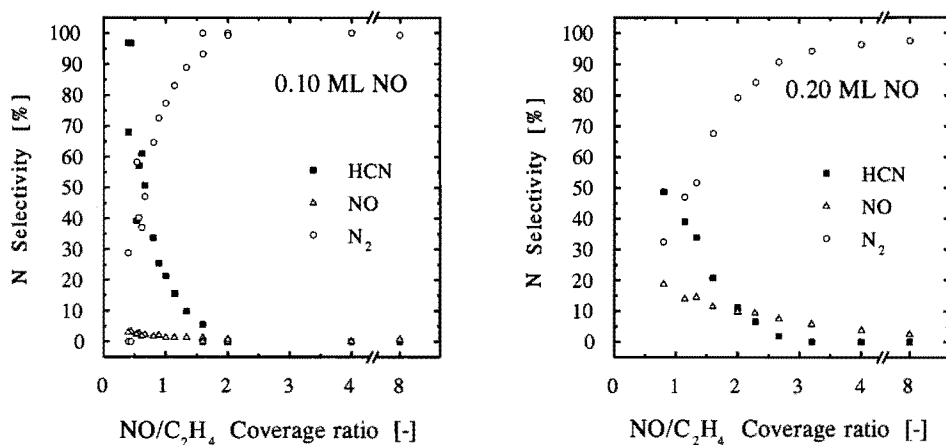


**Figure 7.10** N-selectivity during TPD for two different initial NO coverages, 0.10 and 0.20 ML NO, as a function of the NO/C<sub>2</sub>H<sub>4</sub> coverage ratio.

The onset for HCN formation is at a higher NO/C<sub>2</sub>H<sub>4</sub> ratio for 0.20 ML NO than for 0.10 ML NO. This might be a direct consequence of the enhanced NO desorption through which less oxygen is formed resulting in more reductive surface conditions. For the 0.10 ML NO case, the selectivity to HCN reaches 100% for an NO/C<sub>2</sub>H<sub>4</sub> coverage ratio of 0.4. Since the ethylene coverage is maximal 0.25 ML, the strong reducing conditions cannot be obtained starting from 0.20 ML NO, which explains why the 100% selectivity to HCN cannot be achieved in this case.

We have also constructed an O-mass balance in order to determine the O-selectivity. Unfortunately we have not been able to separate CO from CO<sub>2</sub>. We therefore distinguish only between H<sub>2</sub>O, NO and CO+CO<sub>2</sub>.

Figure 7.11 shows the O-selectivity for initial NO coverages of 0.10 and 0.20 ML as a function of the NO/C<sub>2</sub>H<sub>4</sub> coverage ratio. Of course, the O-selectivity to NO is the same as the N-selectivity to NO as discussed in the previous section. The changes in O-selectivity with changing NO/C<sub>2</sub>H<sub>4</sub> coverage are less spectacular than the changes in the



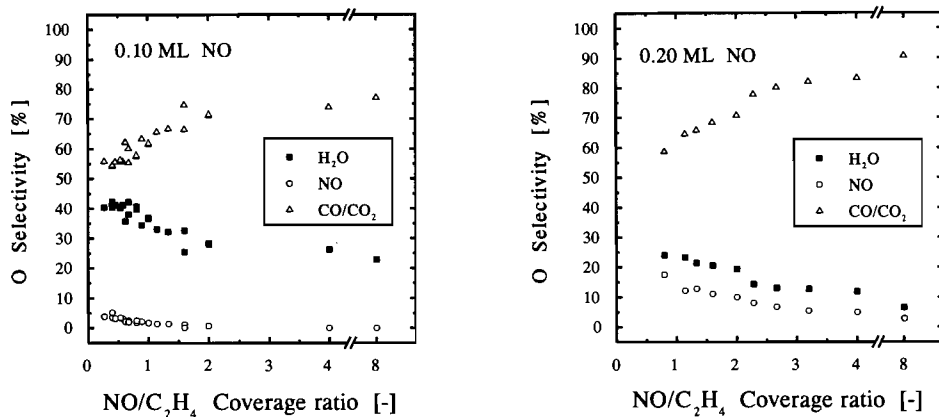


**Figure 7.11** O-selectivity during TPD for two different initial NO coverages, 0.10 and 0.20 ML as a function of the  $\text{NO}/\text{C}_2\text{H}_4$  coverage ratio.

N-selectivity. In both NO cases, the O-selectivity to  $\text{CO}+\text{CO}_2$  decreases and that to  $\text{H}_2\text{O}$  increases with decreasing  $\text{NO}/\text{C}_2\text{H}_4$  ratio, while the selectivity to  $\text{CO}+\text{CO}_2$  is always larger than that to  $\text{H}_2\text{O}$ . For an  $\text{NO}/\text{C}_2\text{H}_4$  coverage ratio of 8, there is an excess of oxygen, which was indeed indicated in TPD by desorption of  $\text{O}_2$  between 1000 and 1400 K. The molecularly desorbing  $\text{O}_2$  has not been considered in the O-mass balance. Qualitative information about the O-selectivity towards CO and  $\text{CO}_2$  can be derived from the  $\text{CO}_2$  TPD areas shown in Figure 7.9. Since the  $\text{CO}_2$  TPD area decreases rapidly for  $\text{C}_2\text{H}_4$  exposures above 0.20 L (~ 0.05 ML ethylene) and the overall selectivity to  $\text{CO}+\text{CO}_2$  remains more or less constant, the O-selectivity to  $\text{CO}_2$  decreases and that to CO increases with decreasing  $\text{NO}/\text{C}_2\text{H}_4$  ratio.

### 7.3.8 NO and ethylene at saturation coverage

For comparison with high pressure conditions, we have investigated the reactions between NO and ethylene at saturation coverages. The coadsorbed layers were prepared by adsorption of a well defined amount of NO at 120 K followed by a saturation exposure of ethylene (1.0 L).

Figure 7.12 shows TPD spectra obtained from the Rh(111) surface saturated with NO and  $\text{C}_2\text{H}_4$  for different coverage ratios. The left panel shows an NO deficient case, in which 0.10 ML NO was adsorbed before the surface was saturated with  $\text{C}_2\text{H}_4$  (in this case the  $\text{C}_2\text{H}_4:\text{NO}$  ratio is expected to be at least 2:1). At this fully covered surface not all ethylene can dissociate, as is evidenced by the molecular ethylene desorption state at 210 K in the TPRS experiments (due to cracking ethylene desorption is also observed at 27 amu, the same mass channel as HCN). In this temperature regime also small amounts

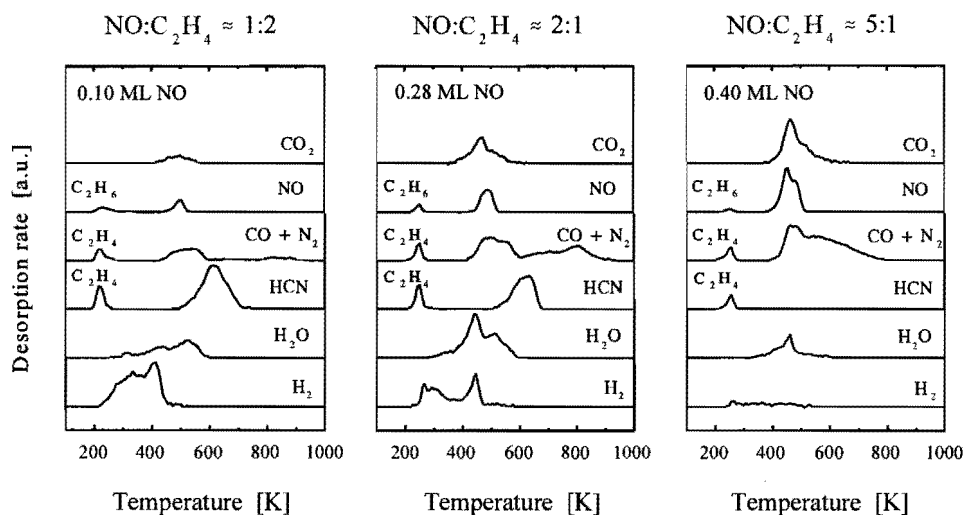


**Figure 7.12** TPD spectra obtained from Rh(111) surfaces saturated with NO and ethylene. The left panel shows an NO-deficient case in which 0.10 ML of NO was adsorbed before the surface was saturated with  $C_2H_4$  at 120 K. The central panel shows the case where 0.28 ML NO was preadsorbed. The right panel shows an NO-enriched case obtained by preadsorption of 0.40 ML NO.

of ethane are formed (see the NO mass channel, 30 amu) just as in the ethylene only case [12]. Little NO desorption is observed (the desorption peak has been multiplied five times) and all nitrogen desorbs as HCN.  $H_2O$  formation starts at 275 K, in good agreement with the onset of the NO dissociation, and extends to 600 K. Furthermore, CO formation is favoured over  $CO_2$  formation, and large amounts of  $H_2$  desorb between 250 and 450 K.

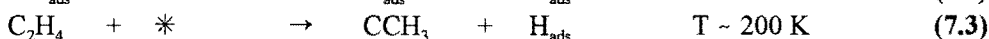
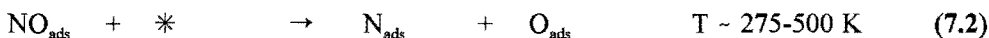
In order to determine the reaction selectivity in excess NO, we have adsorbed 0.40 ML NO and saturated the surface with ethylene by exposure of 1.00 L (in this case the  $NO:C_2H_4$  ratio is expected to be at least 5:1). Higher NO coverages have been found to inhibit ethylene coadsorption almost entirely. Under these conditions no HCN production is observed and excess NO desorbs in two desorption states at 450 and 480 K, respectively. Due to the excess of oxygen, ethylene is predominantly oxidized to  $H_2O$  and  $CO_2$ , and hardly any CO and  $H_2$  desorb. As a consequence of site blocking by NO, part of the ethylene desorbs molecularly at 250 K, which is a significantly higher temperature than in the ethylene-only case and might indicate some stabilization of the ethylene by the presence of the NO.

The central panel of Figure 7.12 shows an intermediate case ( $NO:C_2H_4 \approx 2:1$ ), in which both  $N_2$  and HCN are formed. Note that  $N_2$  desorbs in two distinct states, one around 650 K due to regular N atom recombination, and one at 800 K due to CN

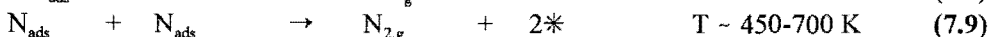
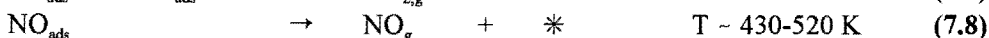
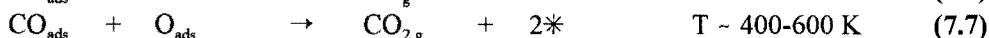
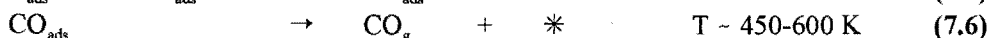
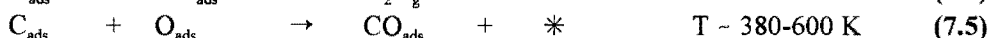
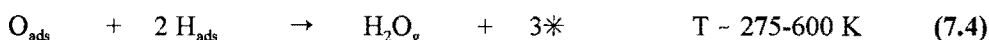
decomposition. Also in this case significant amounts of ethylene and ethane desorb around 250 K.

## 7.4 Discussion

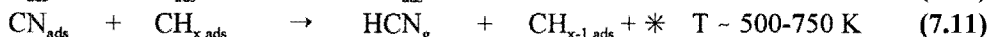
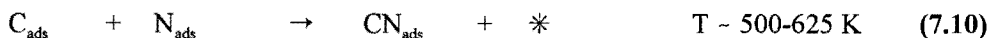
The combination of TPD and TPSIMS results yielded a wealth of information about the reactions that occur between NO and ethylene on Rh(111). No evidence has been found for direct reactions between the molecular species. NO dissociation and ethylene decomposition seem therefore essential prerequisites. These reactions are observed in the following temperature ranges:



Once atomic oxygen, nitrogen, hydrogen and hydrocarbon fragments are present on the surface, many reactions between these species occur. The followed reaction pathways depend strongly on the relative concentrations of the adsorbed species. Varying between oxidizing and slightly reducing conditions ( $\text{NO}/\text{C}_2\text{H}_4$  coverage ratio  $\geq 3$ ) the following reactions are dominant:



However, for strongly reducing conditions ( $\text{NO}/\text{C}_2\text{H}_4$  coverage ratios  $\leq 3$ ) additional reaction pathways become available:



The SIMS results indicate that the conversion of ethylene to ethylidyne and a surface hydrogen is not significantly influenced by coadsorption of NO. Ethylidyne formation starts around 180 K and is finished around 230 K just like with ethylene alone [12]. However, molecular ethylene desorption at high coverages is shifted to higher temperatures (from  $\sim 200$  to  $\sim 260$  K) when either O or NO is coadsorbed, which indicates a stabilization effect. Ethylidyne decomposition proceeds in the same temperature range as in the ethylene only case, 350-400 K. SIMS does not provide detailed information

about the further decomposition of the hydrocarbon fragments. However, TPD indicates that at high coverages of both ethylene and NO/ethylene hydrogen is present on the surface up to 750 K, as indicated by the evolution of H<sub>2</sub> and HCN, respectively.

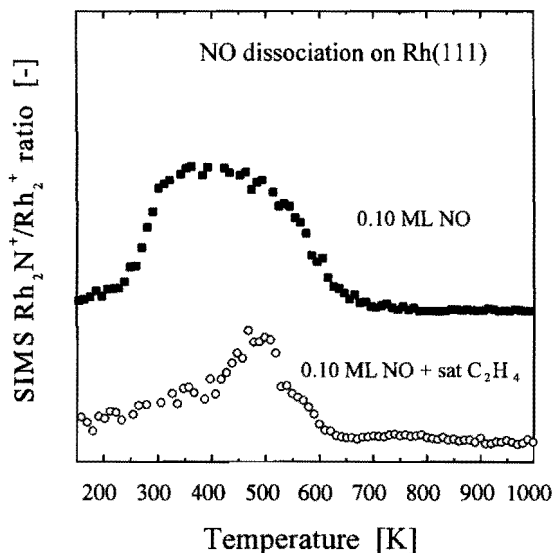


**Figure 7.13** Comparison between NO dissociation (through the  $Rh_2N^+/Rh_2^+$  SIMS intensity ratio) for a Rh(111) surface covered with 0.10 ML NO and covered with 0.10 ML NO and 0.25 ML C<sub>2</sub>H<sub>4</sub>. The heating rate was 10 K/s

NO dissociation is significantly affected by coadsorption of ethylene. Figure 7.13 shows the comparison between NO dissociation (through the  $Rh_2N^+/Rh_2^+$  intensity ratio) on a Rh(111) surface covered with 0.10 NO and covered with 0.10 ML NO and 0.25 ML C<sub>2</sub>H<sub>4</sub>.

Figure 7.13 clearly shows that NO dissociation is impeded by coadsorption of ethylene, which may simply be the consequence of a site blocking effect. When NO dissociation sets in at around 275 K, all ethylene has decomposed to ethylidyne and surface hydrogen. Blackman *et al.* [34] established that NO and ethylidyne form an ordered  $c(4 \times 2)$  structure (containing 0.25 ML NO and 0.25 ML ethylidyne) when NO is exposed to a Rh(111) surface covered with an ordered  $(2 \times 2)$ -ethylidyne structure. This ordering may include the formation of stable NO-ethylidyne complexes on the surface, which could be an alternative explanation for the impeded NO dissociation. NO and ethylidyne are species with opposite work function effects on Rh(111) and therefore attractive dipole-dipole interactions are expected. In this respect it is interesting to note that stable surface complexes also form between NO and NH<sub>3</sub> on Pt(111) [35]. Note that the NO dissociation accelerates at around 400 K, which is also the temperature where ethylidyne decomposes. Attractive interactions between NO and hydrocarbon fragments may also be the reason for the shift of the NO desorption temperature from 430 K for the NO only case to 480 K for high ethylene/NO coverage ratios. However, also the absence of repulsive interactions by atomic oxygen may be responsible for this shift.

The reaction experiments between O<sub>ads</sub> and H<sub>ads</sub> indicate that H<sub>2</sub>O production starts at 250 K and terminates at 400 K due to the absence of surface hydrogen. In NO+ethylene

reactions, H<sub>2</sub>O production is observed up to 600 K, indicating that the hydrocarbon fragments act as efficient hydrogen suppliers for H<sub>2</sub>O formation above 400 K. As neither H-atoms nor OH groups have a sufficiently long residence time on the surface at these temperatures, water formation between 400 and 600 K may involve direct reactions between hydrocarbon fragments and atomic oxygen such as  $O_{\text{ads}} + \text{CH}_{\text{ads}} \rightarrow \text{OH}_{\text{ads}} + \text{C}_{\text{ads}}$ , followed instantaneously by  $\text{OH}_{\text{ads}} + \text{CH}_{\text{ads}} \rightarrow \text{H}_2\text{O} + \text{C}_{\text{ads}}$ .

Also during HCN formation, direct reactions with hydrocarbon fragments may play a role. In principle there are two reaction routes possible for HCN formation. The first one could be a direct coupling according to  $\text{CH}_{\text{ads}} + \text{N}_{\text{ads}} \rightarrow \text{HCN}$ . In the second one, HCN could also be formed by the hydrogenation of CN which has previously been formed by the reaction  $\text{C}_{\text{ads}} + \text{N}_{\text{ads}} \rightarrow \text{CN}_{\text{ads}}$ . In the latter case the hydrogenation of the CN groups can occur by reaction with a surface hydrogen or with a hydrocarbon fragment, such as CH. It should be noted that if HCN formation proceeds according to the hydrogenation of CN by surface hydrogen, this process is highly favoured above H<sub>2</sub> desorption since the latter is not observed. This might be explained by the fact that at high temperature  $\Theta_{\text{H}}$  is small and H<sub>2</sub> formation is a second order process and therefore depends on  $\Theta_{\text{H}}^2$ , whereas the formation of HCN is expected to be first order in  $\Theta_{\text{H}}$ . For details on CN formation and decomposition we refer to Chapter 8 in which they are thoroughly discussed.

The SIMS results indicate that CO formation by reaction between O and hydrocarbon fragments starts around 380 K. Mikhailov *et al.* [36] stated that CO formation by the oxidation of carbidic carbon proceeds by a Langmuir-Hinshelwood mechanism and reported measurable oxidation rates at temperatures above 350 K. Our findings for the onset of CO formation are in good agreement herewith. Also the observation that CO<sub>2</sub> formation (in excess oxygen) is favoured above CO desorption is in good agreement with the literature [37-39].

## 7.5 Conclusions

Temperature-programmed reactions of NO and C<sub>2</sub>H<sub>4</sub> produce a broad spectrum of products. At NO:C<sub>2</sub>H<sub>4</sub> coverage ratios  $\geq 3$ , H<sub>2</sub>O, CO<sub>2</sub> and N<sub>2</sub> are the dominant reaction products, but at NO:C<sub>2</sub>H<sub>4</sub>  $\leq 3$  significant amounts of H<sub>2</sub>, CO, and HCN are formed as well. At low total coverages NO and ethylene decompose as if they are on the Rh(111) surface separately. At higher coverages, NO dissociation becomes hindered and both molecular NO and ethylene desorption are observed at 480 and 260 K, respectively. These desorption temperatures are significantly higher than in the NO-alone (430 K) and ethylene-alone (180 K) case, which indicates a mutual stabilization effect.

CO formation starts around 380 K and is immediately succeeded by CO<sub>2</sub> formation if enough oxygen is present. At decreasing oxygen coverages, CO desorption becomes competitive to CO<sub>2</sub> formation. When oxygen is absent even reactions between C- and N-species occur and surface cyanides are formed at around 500 K. Depending on the

availability of H-atoms which are released from hydrocarbon fragments in the temperature range of 500 - 700 K, CN may be hydrogenated to HCN which readily desorbs. In the absence of hydrogen, the CN species are sufficiently stable towards dissociation and retard the desorption of N<sub>2</sub> by some 200 K to the range of 650-850 K.

H<sub>2</sub>O formation is observed from 275 to 600 K and probably involves reactions between hydrocarbon fragments and O above 400 K.

## References

- [1] K.C. Taylor, *Catal.Rev.-Sci.Eng.* 35 (1993) 457.
- [2] R. Impens, in *Catalysis and Automotive Pollution Control* (A. Crucq and A. Frennet, Eds.), Elsevier Science Publishers, Amsterdam, 1987, p. 11.
- [3] M. Iwamoto and H. Hamada, *Catal. Today* 10 (1991) 57.
- [4] J.N. Armor, *Catal. Today* 26 (1995) 99, and references therein.
- [5] A.P. Walker, *Catal. Today* 26 (1995) 107.
- [6] R. Burch and P.J. Millington, *Catal.Today* 26 (1995) 185.
- [7] G.R. Bamwenda, A. Obuchi, A. Ogata, and K. Mizuno, *Chem. Lett.* (1994) 2109.
- [8] C. Yokoyama and M. Misono, *J. Catal.* 150 (1994) 9.
- [9] F. Radtke, R.A. Köppel and A. Baiker, *Catal. Today* 26 (1995) 159.
- [10] R.J.H. Voorhoeve, C.K.N. Patel, L.E. Trimble and R.J. Kerl, *J. Catal.* 54 (1978) 102.
- [11] L.A. DeLouise and N. Winograd, *Surface Sci.* 154 (1985) 79.
- [12] H.J. Borg, R.M. van Hardeveld, and J.W. Niemantsverdriet, *J.Chem.Soc. Faraday Trans.* 91 (1995) 3679.
- [13] G.A. Somorjai, M.A. Van Hove and B.E. Bent, *J. Phys. Chem.* 92 (1988) 973.
- [14] L.H. Dubois, D.G. Castner and G.A. Somorjai, *J. Chem. Phys.* 72 (1980) 5234.
- [15] F. Zaera, *J. Am. Chem. Soc.* 111 (1989) 8744; *Acc. Chem. Res.* 25 (1992) 260.
- [16] G.A. Somorjai, *Introduction to Surface Chemistry and Catalysis*, Wiley, New York, 1994.
- [17] J.T. Yates, Jr., P.A. Thiel, and W.H. Weinberg, *Surf. Sci.* 84 (1979) 427.
- [18] P. Cremer, C. Stanners, J.W. Niemantsverdriet, Y.R. Shen and G.A. Somorjai, *Surf. Sci.* 328 (1995) 111.
- [19] F.T. Wagner and T.E. Moylan, *Surf. Sci.* 191 (1987) 121.
- [20] M.L. Wagner and L.D. Schmidt, *J. Phys. Chem.* 99 (1995) 805.
- [21] P.A. Thiel, J.T. Yates, Jr., and W.H. Weinberg, *Surf. Sci.* 90 (1997) 121.
- [22] B.E. Nieuwenhuys, *Surf. Sci.* 126 (1983) 307.
- [23] A.N. Salanov and V.I. Savchenko, *Surf. Sci.* 296 (1993) 393.
- [24] P.A. Thiel, J.T. Yates, Jr., and W.H. Weinberg, *Surf. Sci.* 82 (1979) 22.
- [25] J.W. Niemantsverdriet, *Spectroscopy in Catalysis*, VCH, Weinheim, 1993.
- [26] H.J. Borg and J.W. Niemantsverdriet, in *Catalysis: Specialist Periodical Report*, Vol. 11 (ed. J.J. Spivey and A.K. Agarwal), The Royal Society of Chemistry, Cambridge, 1994, p. 1.
- [27] J.R. Creighton and J.M. White, *Surf. Sci.*, 129 (1983) 327.
- [28] P.A. Thiel, J.T. Yates and W.H. Weinberg, *Surf. Sci.* 84 (1979) 54.
- [29] L.H. Dubois and G.A. Somorjai, *Surf. Sci.* 91 (1980) 514.
- [30] H.J. Borg, J.F.C.J.M. Reijerse, R.A. van Santen and J.W. Niemantsverdriet, *J. Chem. Phys.* 101 (1994) 10052.
- [31] R.A. van Santen and J.W. Niemantsverdriet, *Chemical Kinetics and Catalysis*, Plenum, New York, 1995.
- [32] S.Y. Hwang, A.C.F. Kong, and L.D. Schmidt, *J. Phys. Chem.* 93 (1989) 8327.
- [33] D.G. Castner and G.A. Somorjai, *Surf. Sci.* 83 (1979) 60.

- [34] G.S. Blackman, C.T. Kao, B.E. Bent, C.M. Mate, M.A. van Hove, and G.A. Somorjai, *Surf. Sci.* 207 (1988) 66.
- [35] D. Burgess, Jr., R.R. Cavanagh, and D.S. King, *Surf. Sci.* 214 (1989) 358.
- [36] S.N. Mikhailov, L.C.A. van den Oetelaar, H.H. Brongersma, and R.A. van Santen, *Catal. Lett.* 27 (1994) 79.
- [37] C.W.J. Bol and C.M. Friend, *J. Am. Chem. Soc.* 117 (1995) 8053.
- [38] F. Solymosi and G. Klivenyi, *J. Phys. Chem.* 99 (1995) 8950.
- [39] D.A. Hickman and L.D. Schmidt, *Science* 259 (1993) 343.

## 8 C-N coupling in reactions between atomic nitrogen and ethylene on Rh(111)

### 8.1 Introduction

The reactivity of CN bonds on platinum metals is of interest for large scale industrial processes, such as *e.g.* the Andrussov process for the production of HCN by reaction of CH<sub>4</sub>, NH<sub>3</sub> and O<sub>2</sub> over Pt/Rh gauzes at 1050° C [1]. Formation of CN bonds has been observed in the reduction of NO by hydrocarbons on supported Rh catalysts [2,3]. Reduction of NO by hydrocarbons is of interest with the NO<sub>x</sub> reduction from lean-burn car exhausts [4,5]. Hasenberg *et al.* [6] have reported HCN synthesis by reaction between CH<sub>4</sub> and NH<sub>3</sub> with selectivities up to 90 % in a moderate pressure regime on Rh-foil.

CN surface chemistry shows large variations among the group VIII metals. Whereas CN bond fission proceeds rapidly on the Ni(111) surface [7], the Pt(111) surface does not dissociate the surface cyanide bond at all [8]. In between these two extremes is the reactivity of the surfaces of Pd(111) [9], Ru(001) [10] and Rh(111) [11].

Up to now, most information concerning CN surface chemistry has been gathered from adsorption and decomposition experiments with CN-containing molecules, such as C<sub>2</sub>N<sub>2</sub> [11,12], CH<sub>3</sub>NH<sub>2</sub> [12], CH<sub>3</sub>NO<sub>2</sub> [13], and H<sub>2</sub>NCHO [14]. However, literature dealing with the formation of CN on the surface is scarce. DeLouise and Winograd [15] reported formation of surface CN upon reaction of NO with carbidic carbon on Rh(331) using SIMS and XPS. In Chapter 7 we have described the reactions between NO and ethylene on Rh(111) in which the production of HCN and the formation of surface cyanides was observed among many other reactions [16]. Although almost all reaction steps could be identified, the situation was too complex to warrant kinetic analysis.

In this chapter we report upon the selectivity of the reaction between atomic nitrogen and ethylene, and we present kinetic parameters for the formation and the decomposition of CN on the Rh(111) surface. In order to reduce the number of surface reactions we used atomic nitrogen instead of NO. Temperature-programmed reaction spectroscopy (TPRS) is used to monitor the desorbing products, while temperature programmed secondary ion mass spectrometry (TPSIMS) monitors reactions on the surface, especially CN formation and decomposition.

### 8.2 Experimental

The experiments were done in a UHV system (base pressure around 10<sup>-10</sup> mbar) equipped with a Leybold SSM 200 quadrupole mass spectrometer for TPD and (static) SIMS measurements, as described in detail in Chapter 2. Work function changes were determined by measuring the shift of the low kinetic energy onset of the secondary



electron emission in AES. In order to minimize damage effects due to electron irradiation, we used a primary electron beam of 500 eV and 0.02  $\mu\text{A}$ . The sample was biased -10.0 V with respect to the ground potential. The onset was defined as the energy at which the derivative of the secondary electron distribution maximizes.

The rhodium crystal, cut in the [111] orientation within  $0.5^\circ$  and polished by standard procedures, was mounted on a moveable stainless steel manipulator with 0.3 mm thick tantalum wires, where it could be cooled to liquid nitrogen temperature and resistively heated up to 1500 K. Temperatures were measured with a chromel-alumel thermocouple spotwelded on the backside of the crystal. Small amounts of bulk impurities, such as sulphur, chlorine, and boron, were removed by cycles of argon sputtering (1.5 keV, 5  $\mu\text{A}\cdot\text{cm}^{-2}$ ) at 900 K and annealing to 1400 K. Carbon was removed by annealing the crystal in  $2\times 10^{-8}$  mbar  $\text{O}_2$ , by slowly varying the temperature between 900 and 1100 K. Oxygen was removed from the surface by annealing shortly to 1425 K. Ethylene, NO and  $\text{H}_2$  (Messer Griesheim, 99.95%, 99.5% and 99.999% pure, respectively) were used without further purification; gas exposures are reported in Langmuirs (1 L= $1.33\times 10^{-6}$  mbar.s); coverages are reported in monolayers (ML, fractional number of adsorbates per Rh surface atom).

## 8.3 Results

### 8.3.1 TPRS of atomic nitrogen and ethylene

Atomic nitrogen was deposited on the Rh(111) surface by reaction between NO and  $\text{H}_2$ . NO was molecularly adsorbed at 120 K, after which it was thermally dissociated by heating to 375 K. Atomic oxygen was selectively removed by exposing the surface to  $2\times 10^{-8}$  mbar  $\text{H}_2$  during 160 s at 375 K. SIMS spectra of the surface after reaction indicated that atomic nitrogen was the only surface species. Assuming a value of 0.68 ML for the NO saturated surface [17], calibration towards the NO uptake curve indicated that an atomic nitrogen coverage of 0.10 ML was obtained starting from an NO exposure of 0.25 L. The procedure has been described in detail in Chapter 5.

Figure 8.1 shows the TPRS spectra of  $\text{H}_2$  (2 amu), HCN (27 amu),  $\text{N}_2$  (28 amu) and  $\text{C}_2\text{N}_2$  (52 amu) obtained from a Rh(111) surface covered with 0.10 ML of  $\text{N}_{\text{ads}}$  and various amounts of ethylene coadsorbed at 120 K. We also monitored for  $\text{CH}_3\text{CN}$  (51 amu) and  $\text{NH}_3$  (17 amu), but these products were not detected. For comparison, we have added the  $\text{N}_2$  desorption spectrum obtained from a surface solely covered with 0.10 ML of atomic nitrogen. Figure 8.1 shows that, if atomic nitrogen is the only adsorbate,  $\text{N}_2$  desorption is complete at 750 K, which is in good agreement with the literature [19].

For the lowest  $\text{C}_2\text{H}_4$  exposure, 0.05 L, the only observed desorption products are  $\text{N}_2$  and  $\text{H}_2$ . However, the  $\text{N}_2$  desorption has significantly shifted to higher temperatures. With increasing ethylene exposure the  $\text{N}_2$  desorption maximum shifts to 800 K and the amount of  $\text{N}_{\text{ads}}$  desorbing as  $\text{N}_2$  decreases. The latter decrease in  $\text{N}_2$  desorption runs

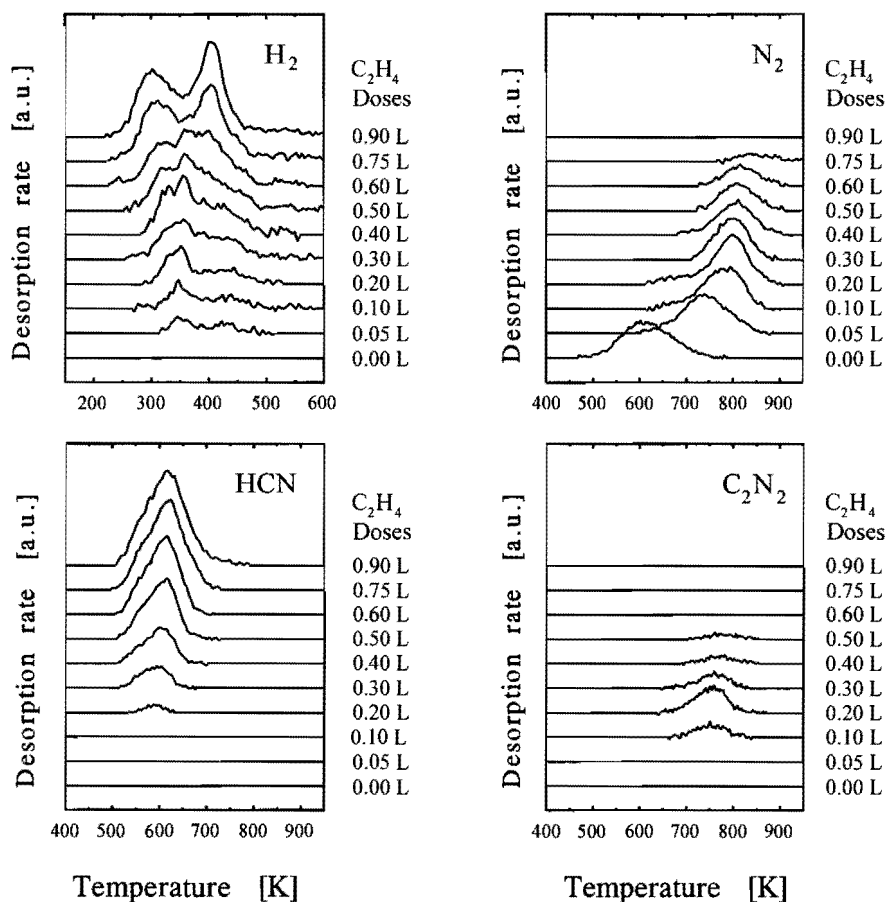


**Figure 8.1** TPRS spectra of  $H_2$ ,  $N_2$ ,  $HCN$ ,  $C_2N_2$  obtained from a  $Rh(111)$  surface covered with 0.10 ML of atomic nitrogen and various amounts of ethylene. The ethylene adsorption temperature was 120 K and the heating rate was 10 K/s.

parallel with an increase of the HCN desorption, which is observed in a broad state around 600 K for ethylene exposures above 0.20 L. Small traces of cyanogen ( $C_2N_2$ ) desorb at 750 K at intermediate ethylene exposures. The  $H_2$  desorption behaviour is quite similar to that observed for  $C_2H_4$  decomposition on the clean  $Rh(111)$  surface [20], with the exception that no  $H_2$  desorption is observed above 500 K. In the absence of nitrogen, significant desorption of  $H_2$  occurs up to  $\sim 700$  K for high coverages of ethylene on  $Rh(111)$  [20]. The  $H_2$  desorption state with a peak maximum at 400 K is associated with ethynidyne decomposition.

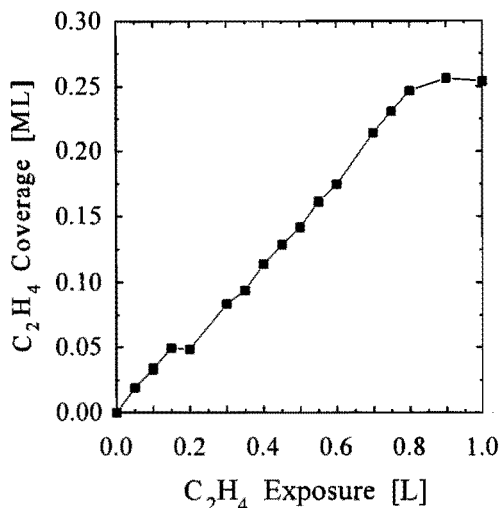


**Figure 8.2** Uptake curve for irreversibly adsorbed  $C_2H_4$ , determined by adding the  $H_2$  and HCN-TPD peak areas and assuming a  $C_2H_4$  saturation coverage of 0.25 ML.

Figure 8.2 shows the uptake curve for irreversibly adsorbed ethylene, which was constructed by adding up the  $H_2$  and HCN-TPD areas and assuming a saturation coverage of 0.25 ML, in conformity with the extent of adsorption on the bare surface [20]. Up to exposures of 0.80 L, the amount of irreversibly adsorbed  $C_2H_4$  increases linearly with the  $C_2H_4$  exposure. This indicates a constant sticking coefficient for  $C_2H_4$  adsorption at 120 K and a mobile precursor state for adsorption, in accordance with the measurements on the clean Rh(111) surface [20]. For ethylene exposures above 0.80 L, molecular ethylene desorption is observed and the amount of  $C_2H_4$  that decomposes becomes constant as reflected by the constant value for the sum of the  $H_2$  and HCN desorption areas.

Figure 8.3 shows the distribution of atomic nitrogen over the reaction products HCN,  $N_2$ ,  $C_2N_2$  as a function of the ethylene exposure. Up to ethylene exposures of 0.20 L, the vast majority of the atomic nitrogen desorbs as  $N_2$ , while also small amounts

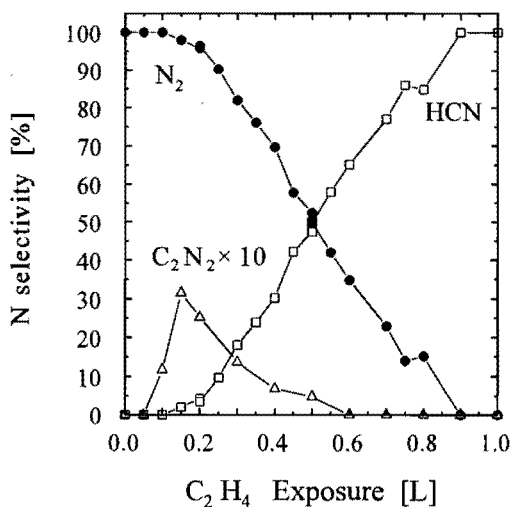


**Figure 8.3** Distribution of atomic nitrogen over the desorption products  $N_2$ ,  $C_2N_2$ , HCN for various amounts of coadsorbed ethylene.

of  $C_2N_2$  are observed. The selectivity towards  $C_2N_2$  maximizes at an  $C_2H_4$  exposure of  $\approx 0.15$  L, where approximately 3% of the atomic nitrogen leaves the surface as  $C_2N_2$ . For ethylene exposures above 0.20 L, the amount of atomic nitrogen desorbing as HCN increases at the expense of  $N_2$  desorption, the selectivity to HCN reaches 100% for the highest ethylene exposures.

### 8.3.2 Static SIMS of surface reactions between atomic nitrogen and ethylene

Figure 8.4 shows three relevant mass regions of SSIMS spectra of the Rh(111) surface, covered with 0.10 ML of  $N_{ads}$  and 0.15 ML of ethylene, after heating to the indicated temperatures and cooling down to 200 K. At 120 K the presence of molecular ethylene is indicated by the appearance of the  $RhC_2H_4^+$  cluster ion (131 amu), while also  $C_2H_4$  fragmentation products are observed, e.g.  $H^+$  (1 amu),  $RhC^+$  (115 amu),  $Rh_2C^+$  (218 amu) and  $Rh_2C_2H_2^+$  (232 amu). Atomic nitrogen is indicated by the presence of the  $Rh_2N^+$  cluster ion (220 amu). Heating to 275 K results in the conversion of ethylene to ethynidyne ( $CCH_3$ ). This is illustrated in the spectra by the disappearance of the  $RhC_2H_4^+$

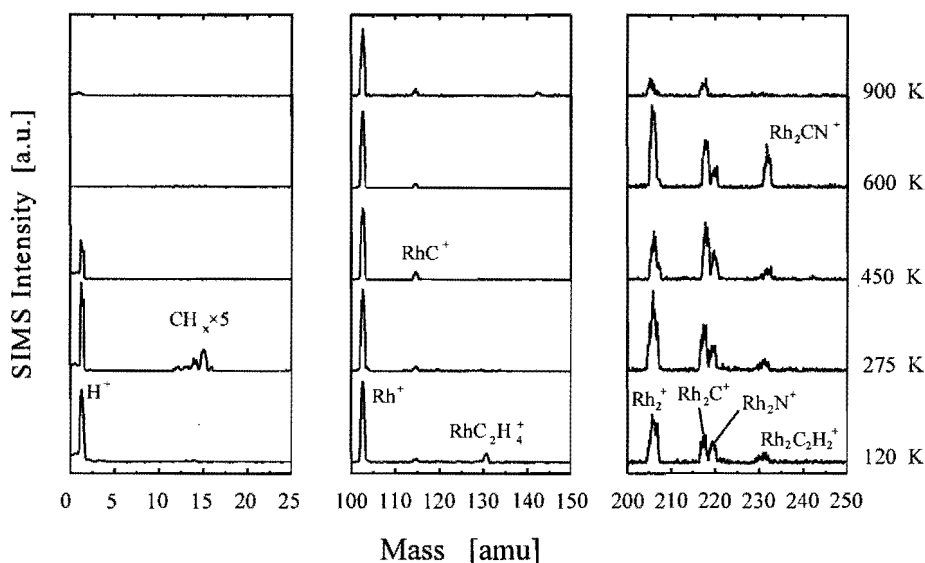


**Figure 8.4** Static SIMS spectra of the Rh(111) surface covered with 0.10 ML of  $N_{ads}$  and 0.15 ML of  $C_2H_4$  after heating to the indicated temperature and cooling back to 200 K. Atomic nitrogen is observed by the  $Rh_2N^+$  cluster ion (220 amu) and molecular ethylene by the  $RhC_2H_4^+$  cluster ion (131 amu) and several fragmentation products. Ethynidyne is observed by the  $CH_3^+$  cluster ion (and its fragmentation products), surface CN is detected exclusively by the  $Rh_2CN^+$  cluster ion.

cluster ion and the appearance of the  $\text{CH}_3^+$  ion (15 amu) and its cracking products (14, 13, 12 amu), which are representative for the methyl group in ethylidyne [21]. The spectrum of the surface at 450 K shows that all the ethylidyne has decomposed and that the surface still contains some hydrogen, reflected by the  $\text{H}^+$  signal (1 amu), most probable as  $\text{CH}_x$  species. Formation of surface CN is evident from the appearance of the  $\text{Rh}_2\text{CN}^+$  cluster ion (232 amu) when the surface is heated to 600 K. Note that the surface CN appears only in the  $\text{Rh}_2\text{CN}^+$  cluster ion and that the  $\text{RhCN}^+$  cluster ion is not observed. The spectrum of the surface heated to 900 K indicates that all CN has disappeared, either by decomposition or by desorption as HCN and that the only surface species remaining is (carbide) carbon, as indicated by the  $\text{Rh}_2\text{C}^+$  and  $\text{RhC}^+$  signals.

### 8.3.3 Kinetics of CN formation

Temperature-programmed Secondary Ion Mass Spectrometry (TPSIMS) has been used to study the kinetics of CN formation on the Rh(111) surface. In contrast to many other surface spectroscopic techniques, SIMS is very powerful in monitoring both the concentrations of atomic and molecular surface species in real time. Usually, linear relations are obtained between adsorbate concentration and appropriate secondary ion intensity ratios [22,23]. We have used the  $\text{Rh}_2\text{C}^+/\text{Rh}_2^+$ ,  $\text{Rh}_2\text{N}^+/\text{Rh}_2^+$  and  $\text{Rh}_2\text{CN}^+/\text{Rh}_2^+$  intensity ratios to monitor the surface coverages of C, N and CN, respectively. Figure 8.5 shows the TPSIMS results obtained from a Rh(111) surface covered with 0.10 ML of  $\text{N}_{\text{ads}}$  and both a small (0.10 L) and a large (1.00 L) amount of coadsorbed ethylene. The heating rate was 4 K/s in both cases.

For the low ethylene coverage case, no HCN desorption is observed and the CN species formed remain stable on the surface up to approximately 700 K where they start to decompose, as is evidenced by the delayed desorption of  $\text{N}_2$ , see Figure 8.1. The formation of CN species starts around 480 K, as is illustrated in the left panel of Figure 8.5 by both the increase in the  $\text{Rh}_2\text{CN}^+/\text{Rh}_2^+$  intensity ratio and the concomitant decrease in the  $\text{Rh}_2\text{C}^+/\text{Rh}_2^+$  and  $\text{Rh}_2\text{N}^+/\text{Rh}_2^+$  intensity ratios. CN formation is completed around 625 K where the  $\text{Rh}_2\text{C}^+/\text{Rh}_2^+$  intensity ratio becomes zero, indicating that all atomic carbon has been consumed in CN formation. The finite  $\text{Rh}_2\text{N}^+/\text{Rh}_2^+$  signal shows the small excess of atomic nitrogen, although partial fragmentation of the  $\text{Rh}_2\text{CN}^+$  cluster ion also contributes to the 220 amu signal. The slight decrease of the  $\text{Rh}_2\text{CN}^+/\text{Rh}_2^+$  intensity ratio between 550 and 600 K might be a consequence of partial CN dimerization since small amounts of  $\text{C}_2\text{N}_2$  desorb under these conditions, see Figure 8.1. Decomposition of the CN groups around 800 K is apparent from the decrease of the  $\text{Rh}_2\text{CN}^+/\text{Rh}_2^+$  signal and an accompanied increase of the  $\text{Rh}_2\text{C}^+/\text{Rh}_2^+$  intensity. An increase of the  $\text{Rh}_2\text{N}^+/\text{Rh}_2^+$  intensity ratio is not observed, indicating that the atomic nitrogen resulting from decomposition of CN groups desorbs immediately as  $\text{N}_2$ , in agreement with Figure 8.1.

With the high ethylene coverage, shown in the right panel of Figure 8.5, the

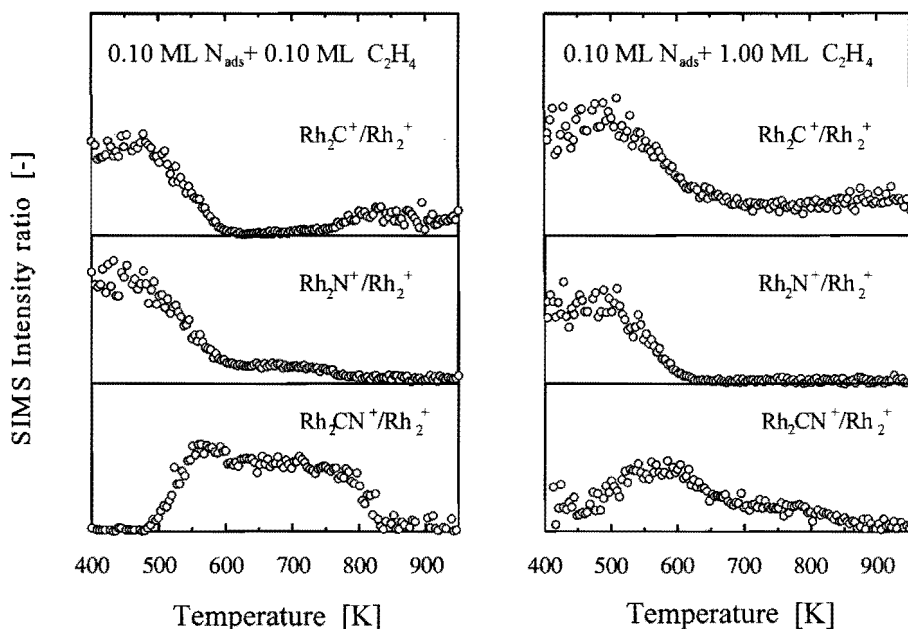


**Figure 8.5** Variation of the  $Rh_2C^+/Rh_2^+$ ,  $Rh_2N^+/Rh_2^+$  and  $Rh_2CN^+/Rh_2^+$  SIMS intensity ratios obtained by heating a Rh(111) surface covered with (a) 0.10 ML  $N_{ads}$  followed by exposure of 0.10 L of  $C_2H_4$  and (b) 0.10 ML  $N_{ads}$  followed by exposure of 1.00 L  $C_2H_4$ . The heating rate was 4 K/s in both cases.

situation is more complex, since CN formation and HCN desorption proceed at the same time. The decrease of the atomic nitrogen and carbon coverages due to CN and HCN formation is still evident from the decrease of the  $Rh_2N^+/Rh_2^+$  and  $Rh_2C^+/Rh_2^+$  intensity ratios. However, the  $Rh_2C^+/Rh_2^+$  intensity does not drop to zero, indicative for an excess of atomic carbon. Interpretation of the  $Rh_2CN^+/Rh_2^+$  signal is complicated, since it may contain a contribution of the  $Rh_2C_2H_2^+$  cluster ion. Ethylidyne decomposition has been found to be a strong coverage-dependent process [20], therefore retention of CC bonds up to 500 K is conceivable with high coverages. This explains the non zero intensity of the 232 amu signal at 400 K. The decrease of the  $Rh_2CN^+/Rh_2^+$  intensity above 600 K indicates a decrease of the CN coverage, most probable by hydrogenation to HCN, which desorbs consecutively.

Evidently, low coverages of  $N_{ads}$  and  $C_{2H_{4,ads}}$ , enabling the hydrocarbon to decompose into elementary carbon at temperatures below the onset of CN formation, give the simplest reaction situation, and hence we have chosen these conditions to determine the kinetic parameters for CN formation. To this end, we have coadsorbed 0.05 ML of atomic nitrogen and 0.025 ML of ethylene, so that, after ethylene decomposition,

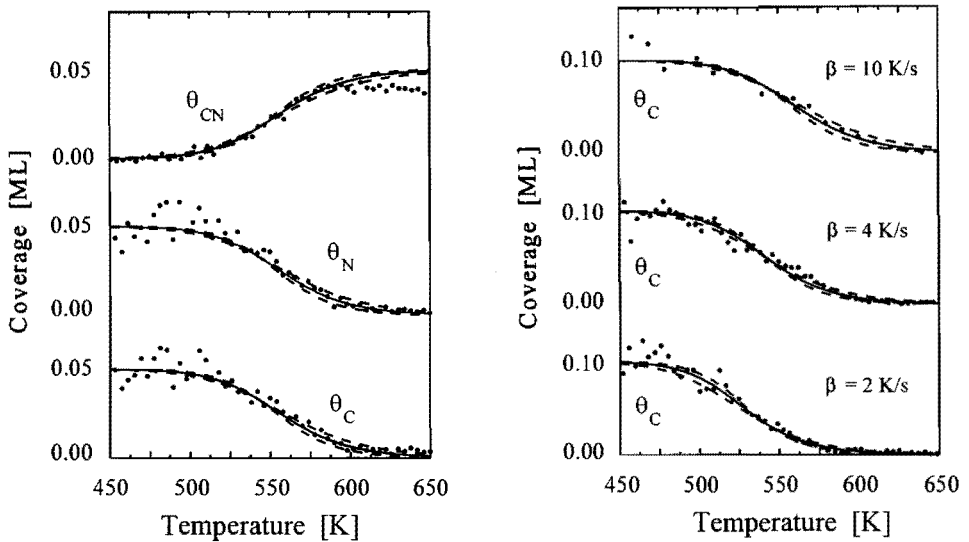


**Figure 8.6** (a) Surface coverages of C, N and CN as a function of the temperature as derived from the SIMS  $Rh_2C^+/Rh_2^+$ ,  $Rh_2N^+/Rh_2^+$  and  $Rh_2CN^+/Rh_2^+$  intensity ratios, respectively. The initial N and C coverages were 0.05 ML and the heating rate was 4 K/s. (b) Change of the atomic carbon surface coverage for various heating rates. In both figures the solid lines represent fits using  $v=10^{11} s^{-1}$  and  $E_{act}=111 kJ/mol$ , while the dashed lines represent fits for  $v=10^9 s^{-1}$  and  $E_{act}=91 kJ/mol$ , and  $v=10^{13} s^{-1}$  and  $E_{act}=131 kJ/mol$ .

atomic nitrogen and carbon are present in equal amounts. The low coverage ensures that ethylene has fully decomposed to carbon before CN formation starts [20]. If we furthermore assume that  $\theta_C$  and  $\theta_N$  are proportional to the  $Rh_2C^+/Rh_2^+$  and  $Rh_2N^+/Rh_2^+$  SIMS intensity ratios, respectively, which is a reasonable assumption at low coverages [17,20,22], we can determine the CN formation rate from the decrease of the atomic nitrogen and carbon coverages during a temperature-programmed SIMS experiment.

In principle, the CN formation rate can also be derived from the increase of the  $Rh_2CN^+/Rh_2^+$  SIMS intensity ratio. If it is assumed that all atomic nitrogen and carbon react to cyanide, the ultimate CN coverage equals 0.05 ML, which could be used to calibrate the  $Rh_2CN^+/Rh_2^+$  SIMS intensity ratio. However, it is not clear if the correlation between the CN coverage and the  $Rh_2CN^+/Rh_2^+$  SIMS intensity ratio is linear over the entire coverage range. Another complicating factor is that CN may dimerize on the surface, which also hinders the interpretation. For this reason we have primarily used the decrease of the atomic carbon and nitrogen coverages to determine the CN formation rate.

Figure 8.6 (a) shows the variation of the atomic nitrogen, atomic carbon and cyanide coverage with the temperature when a surface containing 0.05 ML of atomic nitrogen and 0.05 ML of carbon is heated at 4 K/s. Assuming a homogeneous distribution of C and N on the surface, the rate of reaction can be written as:

$$-\frac{d\theta_C}{dt} = -\frac{d\theta_N}{dt} = \frac{d\theta_{CN}}{dt} = \nu \cdot e^{-E_{act}/RT} \cdot \theta_C \cdot \theta_N \quad (8.1)$$

We find that the experimental results are well described by a pre-exponential factor and activation energy of  $10^{11} \text{ s}^{-1}$  and 111 kJ/mol, respectively, as shown by the solid lines in Figure 8.6 (a). However, reasonable fits could also be obtained by assuming a pre-exponential factor of  $10^9 \text{ s}^{-1}$  and an activation energy of 91 kJ/mol or a pre-exponential factor of  $10^{13} \text{ s}^{-1}$  and an activation energy of 131 kJ/mol, see dashed lines in Figure 8.6 (a).

The upper part of Figure 8.6 (a) shows a comparison between the CN coverage as calculated from Equation 8.1 (lines) and the CN coverage as determined from the  $\text{Rh}_2\text{CN}^+/\text{Rh}_2^+$  SIMS intensity ratio (small circles). We have assumed a linear correlation between  $\theta_{CN}$  and the  $\text{Rh}_2\text{CN}^+/\text{Rh}_2^+$  SIMS intensity ratio, by which good agreement between measured and calculated CN coverages could be obtained for small CN coverages. However, for higher CN coverages the amount of surface cyanide as determined from the  $\text{Rh}_2\text{CN}^+/\text{Rh}_2^+$  SIMS intensity ratio is underestimated, which might be a consequence of a non-linear relation between the CN coverage and the  $\text{Rh}_2\text{CN}^+/\text{Rh}_2^+$  SIMS intensity ratio, but might also be caused by dimerization of CN groups.

In an attempt to determine the pre-exponential factor and the activation energy, we have varied the heating rate. Figure 8.6 (b) shows the decrease of the atomic carbon coverage for heating rates of 2, 4 and 10 K/s, starting from a surface covered with 0.10 ML of atomic nitrogen and carbon. The atomic nitrogen coverage showed the same behaviour as the atomic carbon coverage and is therefore not shown. The best fit results are obtained for a pre-exponential factor and activation energy of  $10^{11} \text{ s}^{-1}$  and 111 kJ/mol, respectively, represented by the solid lines in Figure 8.6 (b). The dashed lines show the results for parameter sets of  $10^9 \text{ s}^{-1}$  and 91 kJ/mol, and  $10^{13} \text{ s}^{-1}$  and 131 kJ/mol. Thus, we take  $\nu=10^{11\pm1} \text{ s}^{-1}$  and  $E_{act}=111\pm10 \text{ kJ/mol}$  as the most probable kinetic parameters for CN formation.

### 8.3.4 Kinetics of CN decomposition

The kinetic parameters for the cyanide decomposition have been determined in two independent ways. First, the CN decomposition rate was determined indirectly from the  $\text{N}_2$  desorption rate, which is possible since desorption of  $\text{N}_2$  is rate-limited by the cyanide decomposition. Second, the CN decomposition rate was derived from the decrease of the cyanide surface coverage as measured during a temperature-programmed SIMS experiment.

Figure 8.7 shows a comparison between the  $\text{N}_2$  desorption rate and the



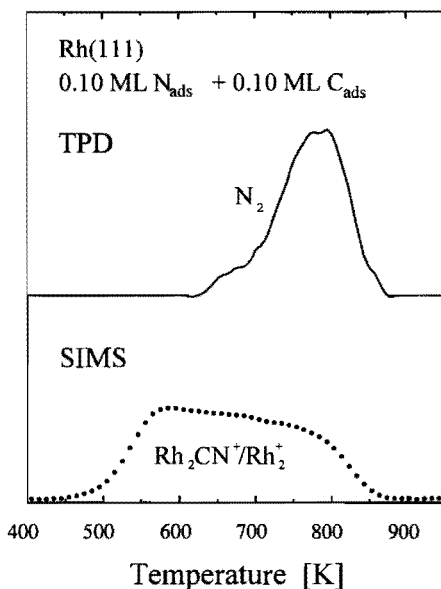


**Figure 8.7** Comparison between the  $N_2$  desorption rate and the  $Rh_2CN^+/Rh_2^+$  SIMS intensity ratio as measured for a Rh(111) surface covered with 0.10 ML of  $N_{\text{ads}}$  and 0.05 ML of  $C_2H_4$  when heated at 10 K/s.

$Rh_2CN^+/Rh_2^+$  SIMS intensity ratio obtained from a Rh(111) surface covered with 0.10 ML of  $N_{\text{ads}}$  and 0.05 ML of  $C_2H_4$  when heated at 10 K/s.  $N_2$  desorption between 630 and 750 K is accompanied only by a slight decrease in the  $Rh_2CN^+/Rh_2^+$  SIMS intensity ratio. Part of the  $N_2$  desorption in this temperature range might be associated with recombination of atomic nitrogen which has not reacted to CN. However, the increase of the  $N_2$  desorption rate around 700 K cannot be explained by the recombination of atomic nitrogen and is attributed to CN decomposition. The absence of a significant decrease of the  $Rh_2CN^+/Rh_2^+$  SIMS intensity ratio due to a decrease of the CN coverage is probably the result of the non-linearity of the  $Rh_2CN^+/Rh_2^+$  SIMS intensity ratio versus the CN coverage. On the high temperature side of the  $N_2$  desorption peak, where the CN coverage is low, the  $Rh_2CN^+/Rh_2^+$  SIMS intensity decreases rapidly with proceeding  $N_2$  desorption. Note that the  $N_2$  desorption finishes when the  $Rh_2CN^+/Rh_2^+$  SIMS intensity ratio becomes zero, *viz.* at around 870 K. Application of the Redhead equation [24] to the reaction-limited  $N_2$  desorption state with a peak maximum at 792 K, see Figure 8.7, yields an activation energy for CN decomposition of 203 kJ/mol, when a pre-exponential factor of  $10^{13} \text{ s}^{-1}$  is assumed.

Figure 8.8 shows the formation and decomposition of surface cyanide as determined from a temperature-programmed SIMS experiment, starting from a surface covered with 0.05 ML of atomic nitrogen and carbon. The heating rate was 4 K/s. The cyanide formation which sets in at around 500 K has already been discussed with Figure 8.6. The solid line shows the fit with a pre-exponential factor and activation energy of  $10^{11} \text{ s}^{-1}$  and 111 kJ/mol, respectively. For these low coverages the decrease of the  $Rh_2CN^+/Rh_2^+$  SIMS intensity ratio between 600 and 750 K is more pronounced than in Figure 8.7. In order to determine the CN decomposition rate from the decrease of the CN

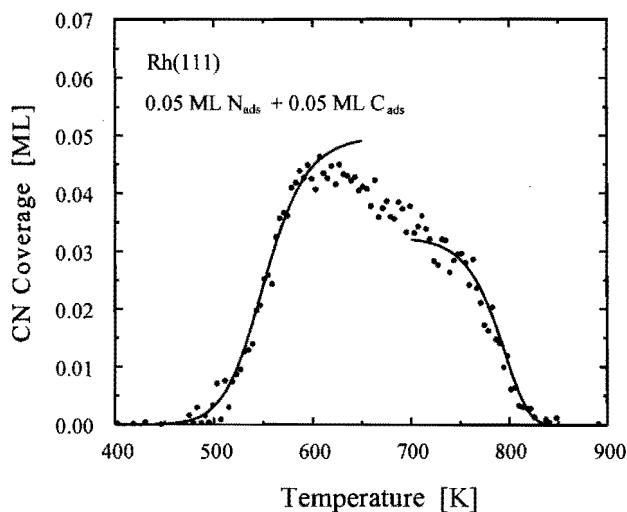


**Figure 8.8** Determination of the CN decomposition rate from the decrease of the CN surface coverage. The solid line represents a fit based on a pre-exponential factor and activation energy of  $10^{13} \text{ s}^{-1}$  and  $210 \text{ kJ/mol}$ , respectively.

coverage we have only considered the temperature range between 700 and 850 K, where a linear correlation between the CN coverage and the  $\text{Rh}_2\text{CN}^+/\text{Rh}_2^+$  SIMS intensity ratio is most probable. The solid line shows a fit for the CN decomposition based on:

$$-\frac{d\theta_{\text{CN}}}{dt} = \nu \cdot e^{-E_{\text{act}}/RT} \cdot \theta_{\text{CN}} \quad (8.2)$$

and a pre-exponential factor and activation energy of  $10^{13} \text{ s}^{-1}$  and  $210 \text{ kJ/mol}$ , respectively. These kinetic parameters are in good agreement with those determined by Redhead's method for the  $\text{N}_2$  desorption maximum and therefore we take  $\nu=10^{13\pm 1} \text{ s}^{-1}$  and  $E_{\text{act}}=210\pm 15 \text{ kJ/mol}$  as the most probable parameters for CN decomposition.

### 8.3.5 Work function measurements

Surface reactions can also be followed in a more indirect way by measuring changes in the work function, which is  $5.60 \text{ eV}$  for the clean Rh(111) surface [25]. Figure 8.9 shows the work function change with respect to the clean surface after deposition of  $0.10 \text{ ML}$  of  $\text{N}_{\text{ads}}$ , coadsorption of  $0.05 \text{ ML}$  of  $\text{C}_2\text{H}_4$  at  $120 \text{ K}$ , and heating to the indicated temperatures. Except for the adsorbed layer at  $120 \text{ K}$ , all work function measurements were done at  $200 \text{ K}$ . Deposition of  $0.10 \text{ ML}$  of atomic nitrogen results in a slight work function increase of approximately  $+0.03 \text{ eV}$ , coadsorption of  $\text{C}_2\text{H}_4$  causes a work function drop of  $-0.16 \text{ eV}$  to a level of  $-0.13 \text{ eV}$  with respect to the clean surface. Formation of ethylidyne by heating to  $200 \text{ K}$  and further heating to  $300 \text{ K}$  does not result in a measurable work function change. At  $400 \text{ K}$ , where all ethylidyne has decomposed,

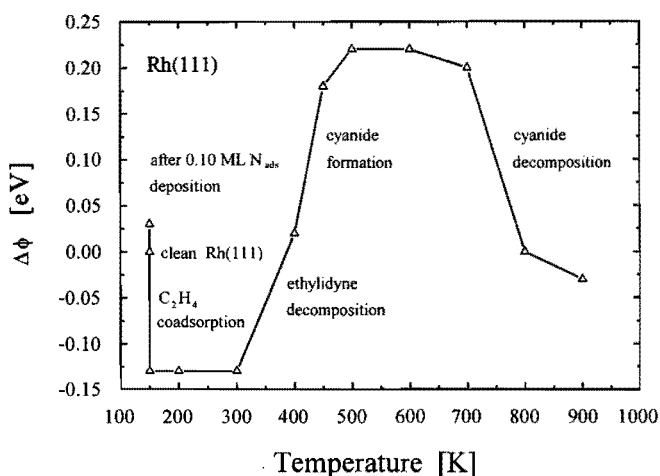


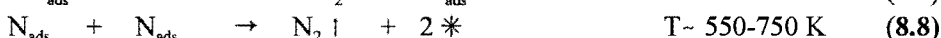
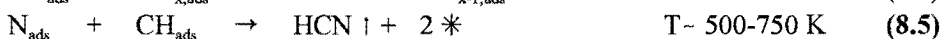
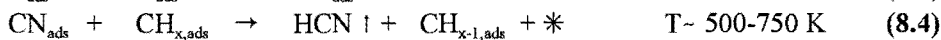
**Figure 8.9** Change of the work function with respect to the clean Rh(111) surface resulting from  $N_{ads}$  and  $C_2H_4$  adsorption and heating to the indicated temperatures. All measurements were done at 200 K.

the work function has increased to +0.02 eV. Formation of CN on the surface is accompanied by a work function increase between 400 and 500 K. Between 500 and 700 K where CN is a stable surface species, a work function increase of +0.22 eV is measured. Heating to 800 K results in the decomposition of the CN species and the work function change drops to zero again, characteristic of the clean Rh(111) surface.

## 8.4 Discussion

Reduction of NO by hydrocarbons, of interest in automotive exhaust catalysis, gives rise to a large number of surface reactions which lead to the desorption of many products, e.g.  $H_2$ ,  $H_2O$ ,  $N_2$ ,  $CO$ ,  $CO_2$ ,  $HCN$  and  $C_2N_2$  [16]. The complexity of this reaction precludes a meaningful kinetic analysis. The aim of the present work is therefore to simplify the situation by highlighting the reaction pathways of atomic nitrogen and ethylene in the absence of oxygen. The results presented here demonstrate the feasibility of the approach, as kinetic parameters could be derived for the formation and decomposition of adsorbed CN species.

Excluding the decomposition of ethylene, which has been extensively discussed [20], the following reactions have been found to be relevant in this study:



The reactions (8.3), (8.6), (8.7) and (8.8) are thought to be elementary, and the reactions (8.4) and (8.5) may be composite in nature. The reaction between atomic carbon and nitrogen to CN, (8.3), could conveniently be studied in the low coverage regime, where ethylene decomposes to fully dehydrogenated carbon below the temperature where CN starts to form. The rate of (8.3) is straightforwardly described by an expression of the form  $r_{\text{CN}} = k \cdot \theta_{\text{N}} \cdot \theta_{\text{C}}$  with an activation energy of  $111 \pm 10$  kJ/mol and a pre-exponential factor of  $10^{11 \pm 1} \text{ s}^{-1}$ . Such parameters are fully consistent with the notion of (8.3) being an elementary step [29]. The onset temperature for cyanide formation, 480 K, is similar to the temperature of 450 K reported by DeLouise and Winograd [15] for the onset of CN formation on Rh(331) by reaction between NO and carbon.

Formation of HCN almost certainly involves  $\text{CH}_x$  species, as single H-atoms have desorbed at 500 K. As known from previous work from several laboratories [20], hydrocarbon fragments may still contain hydrogen, especially at increasing coverages, where the decomposition of ethylene and other alkenes is progressively impeded. Hence, we propose two possibilities for HCN formation, (8.4) and (8.5), which may, but do not have to be, elementary reactions. For example, we cannot exclude that reaction (8.4) proceeds by  $\text{CH}_x$  decomposition, immediately followed by a reaction of the H-atom with a previously formed CN group. Although desorption of  $\text{H}_2$  is not observed, one could argue that if the rate-determining step in the overall reaction (8.4) is  $\text{CH}_x$  decomposition, the surface concentration of H-atoms is so low in comparison to that of CN that  $\text{H}_2$  formation is insignificant. Clear evidence for the occurrence of reaction (8.4) is provided by Figure 8.5 (b), which shows that the surface coverage of CN species decreases while HCN evolves in the gas phase. Unfortunately, we have no such definite proof for reaction (8.5), neither any evidence to discard it, the major problem being that SIMS does not readily distinguish between adsorbed CH and C species.

Interestingly, Schmidt and coworkers [12] reported that the decomposition of  $\text{CH}_3\text{NH}_2$  on Rh(111) results in HCN desorption at around 430 K, *i.e.* some 70 K below the temperatures where HCN forms in this study. This confirms that HCN desorption is limited by the formation of HCN through either of the reactions (8.4) and (8.5).

Cyanogen desorption, around 750 K, has also been observed in  $\text{C}_2\text{N}_2$  adsorption studies [11,12] and has been attributed to recombination of CN groups. Since we start from atomic nitrogen and ethylene we can be certain that  $\text{C}_2\text{N}_2$  formation has to precede desorption. We observe an optimum in the  $\text{C}_2\text{N}_2$  selectivity for an ethylene exposure where the surface concentration of cyanide maximizes. The observation of an optimum can be understood from the fact that, for the lowest ethylene coverage, surface carbon is deficient and CN decomposition is favourable, whereas at high ethylene coverages HCN formation and desorption becomes competitive to  $\text{C}_2\text{N}_2$  formation. The correlation of the  $\text{C}_2\text{N}_2$  selectivity with the cyanide coverage sustains the assignment that the  $\text{C}_2\text{N}_2$  desorption state at 750 K is reaction-limited by dimerization of surface cyanide groups.

CN species start to decompose around 700 K. The reaction could be followed by SIMS, see Figure 8.7, and the kinetics is adequately described by a first-order rate equation with an activation energy of  $210 \pm 15$  kJ/mol and a pre-exponential of  $10^{13 \pm 1} \text{ s}^{-1}$ .

N-atoms released in this reaction recombine and desorb instantaneously. The reaction-limited  $N_2$  desorption state with a maximum at 800 K has also been observed in  $C_2N_2$  and  $CH_3NH_2$  decomposition experiments [11,12].

The increase in the work function as a result of the formation of CN indicates that the cyanide is present as a negatively charged species, which is a common feature for cyanides adsorbed on group VIII metals. Although we have no direct information about the bonding type of the cyanide, the SIMS results suggest that the cyanide species is most probably adsorbed on a site involving more than one Rh atom. Brown and Vickerman [23] have shown that the binding site of CO is reflected by the relative intensities of one, two and three-fold metal-CO clusters in SIMS experiments. Linear CO adsorption displays itself by a dominance of the single metal-CO clusters, while bridge-bonded CO manifests itself by larger intensities of the twofold and threefold metal-CO clusters. If we draw the analogy between CO and CN, it is noteworthy that  $Rh(CN)^+$  cluster ions are entirely absent and only  $Rh_2CN^+$  cluster ions are observed (for sensitivity reasons  $Rh_3CN^+$  cluster ions could not be detected). HREELS and NEXAFS measurements give clear evidence that CN is adsorbed parallel to the surface on Pd(111) [9,26]. Flat-lying CN is neither observable by EELS in the dipole scattering mode nor by IR spectroscopy. This might be the reason why this species was overlooked in adsorption and decomposition studies of  $CH_3NC$  on both alumina-supported Rh and Rh(111) [27,28]. The absence of the  $Rh(CN)^+$  cluster ion in the SIMS spectra could be the consequence of a flat-lying species. However, the exact bonding nature of the CN species needs further investigation.

## 8.5 Conclusions

The selectivity of the reaction between atomic nitrogen and ethylene depends strongly on the ethylene coverage. For small ethylene coverages, ethylene fully decomposes to carbon, which subsequently reacts with atomic nitrogen to a surface cyanide species. The kinetics of CN formation from atomic carbon and nitrogen could best be described by a pre-exponential and an activation energy of  $10^{11\pm1} s^{-1}$  and  $111\pm10$  kJ/mol, respectively. In the absence of surface hydrogen, CN groups are stable up to  $\sim 700$  K. CN decomposition results in a reaction-limited  $N_2$  desorption state with a maximum at 792 K, and can best be described by a pre-exponential factor and activation energy of  $10^{13\pm1} s^{-1}$  and  $210\pm15$  kJ/mol, respectively. For high ethylene coverages, ethylene decomposition is impeded and HCN formation in the temperature range between 500 and 650 K by reaction between atomic nitrogen and  $CH_x$  becomes the preferential reaction pathway. The optimum in the cyanogen selectivity ( $\approx 3\%$ ) corresponds to a maximum in the cyanide surface coverage, and the desorption at 750 K is reaction-limited by, most probably, dimerization of CN groups. Surface cyanide is present as negatively charged, presumably flat-lying, species.

## References

- [1] J.J. McKetta, *Encyclopedia of chemical processing and design*, M. Dekker, New York, 1988.
- [2] G.R. Bamwenda, A. Obuchi, A. Ogata, and K. Mizuno, *Chem. Lett.* (1994) 2109.
- [3] A. Obuchi, A. Ohi, M. Nakamura, A. Ogata, K. Mizuno, and H. Ohuchi, *Appl. Catal. B: Environmental* 2 (1993) 71.
- [4] R. Burch and P.J. Millington, *Catal. Today* 26 (1995) 185.
- [5] R. Burch and T.C. Watling, *Catal. Lett.* 37 (1996) 51.
- [6] D. Hasenberg and L.D. Schmidt, *J. Catal.* 91 (1985) 116.
- [7] J.C. Hemminger, E.L. Muetterties, and G.A. Somorjai, *J. Am. Chem. Soc.* 101 (1979) 62.
- [8] J.R. Kingsley, D. Dahlgren, and J.C. Hemminger, *Surf. Sci.* 139 (1984) 417.
- [9] M.E. Kordesch, W. Stenzel, and H. Conrad, *Surf. Sci.* 186 (1987) 601.
- [10] N.J. Gudde and R.M. Lambert, *Surf. Sci.* 124 (1983) 372.
- [11] F. Solymosi and L. Bugyi, *Surf. Sci.* 147 (1984) 685.
- [12] S.Y. Hwang, A.C.F. Kong, and L.D. Schmidt, *J. Phys. Chem.* 93 (1989) 8327.
- [13] S.Y. Hwang, A.C.F. Kong, and L.D. Schmidt, *J. Phys. Chem.* 93 (1989) 8334.
- [14] W.L. Wagner and L.D. Schmidt, *Surf. Sci.* 257 (1991) 113.
- [15] L.A. DeLouise and N. Winograd, *Surf. Sci.* 154 (1985) 79.
- [16] R.M. van Hardeveld, A.J.G.W. Schmidt, and J.W. Niemantsverdriet, *Catal. Lett.* 41 (1996) 125.
- [17] H.J. Borg, J.F.C.-J.M. Reijerse, R.A. van Santen, and J.W. Niemantsverdriet, *J. Chem. Phys.* 101 (1994) 10052.
- [18] R.M. van Hardeveld, R.A. van Santen, and J.W. Niemantsverdriet, *J. Phys. Chem.* 101(1997) 998.
- [19] D.N. Belton, C.L. DiMaggio, and K.Y.S. Ng, *J. Catal.* 144 (1993) 273.
- [20] H.J. Borg, R.M. van Hardeveld, and J.W. Niemantsverdriet, *J. Chem. Soc. Faraday Trans.* 91 (1995) 3679; and references therein.
- [21] J.R. Creighton and J.M. White, *Surf. Sci.* 129 (1983) 327.
- [22] H.J. Borg and J.W. Niemantsverdriet, in *Catalysis: a Specialist Periodical Report*, Vol 11, Royal Society of Chemistry, Cambridge, 1994, p 1.
- [23] A. Brown and J.C. Vickerman, *Surf. Sci.* 124 (1983) 267.
- [24] P.A. Redhead, *Vacuum* 12 (1962) 203.
- [25] G.R. Castro, H. Busse, U. Schneider, T. Janssens, and K. Wandelt, *Phys. Scr.* T41 (1992) 208.
- [26] A. Wirgin and T. Lopez-Rios, *Opt. Commun.* 48 (1984) 416.
- [27] R.R. Cavanagh and J.T. Yates, Jr., *J. Chem. Phys.* 75 (1981) 1551.
- [28] S. Semancik, G.L. Haller, and J.T. Yates, Jr., *J. Chem. Phys.* 78 (1983) 6970.
- [29] R.A. van Santen and J.W. Niemantsverdriet, *Chemical Kinetics and Catalysis*, Plenum Press, New York, 1995.

## 9 Summary and conclusions

The purpose of this thesis is to investigate elementary surface reactions that occur during NO reduction on rhodium, with the aim ambition to determine the associated kinetic parameters. This research is most relevant to automotive exhaust gas catalysis, since, in the recent three-way catalyst, rhodium catalyzes the conversion of  $\text{NO}_x$  into the environmentally harmless  $\text{N}_2$ . More stringent  $\text{NO}_x$  emission standards in the future and rapidly decreasing rhodium reserves necessitate further improvement of the catalyst system and replacement or more economical use of Rh. In this respect, knowledge of kinetic parameters is essential in order to get a better understanding of the processes that determine the performance of the three-way catalyst in terms of both activity and selectivity.

Since many catalytic reactions are surface sensitive, unambiguous determination of kinetic parameters requires a well defined surface structure. For this reason, a rhodium (111) single crystal, in which the rhodium surface atoms form a close-packed layer, has been used as a model for the catalyst. For the determination of kinetic parameters of certain surface reactions, we have employed a combination of two techniques: temperature programmed desorption or reaction spectroscopy (TPD, TPRS) together with secondary ion mass spectrometry (SIMS). This combination of techniques has been proven very powerful, since, TPD or TPRS gives information about the gaseous products that are formed and SIMS monitors reactions on the surface and detects intermediates. Pressure conditions are restricted to the (ultra) high vacuum regime ( $p < 10^{-6}$  mbar) in order to maintain a reasonable mean free path for the secondary ions detected in SIMS, and to avoid surface contamination.

On the rhodium surface, dissociation of NO into atomic oxygen and nitrogen is the first and most essential reaction step in the NO reduction sequence. Determination of kinetic parameters for the NO dissociation reaction is complicated, since the NO dissociation rate depends strongly on both temperature and coverage. In Chapter 3, we investigate the reactivity of NO on Rh(111) at various temperatures by performing a number of isothermal adsorption experiments. SIMS and TPD have been used to determine the composition of the adsorbate layer, *i.e.* the NO, N and O coverages, that is obtained after saturating the Rh(111) surface with NO at a given temperature. In order to extract kinetic parameters from these experiments, we have simulated the experiment by means of a Monte-Carlo based model, which enables incorporation of surface diffusion and lateral interactions. For adsorption temperatures below 250 K, NO adsorption is exclusively molecular. At 150 K and a coverage of 0.50 ML, NO orders into a  $c(4 \times 2)$ -2NO structure, in which half of the NO molecules occupies fcc and the other half hcp three-fold sites. A disordered adsorption layer is obtained at the saturation coverage of 0.68 ML. However, at 225 K, saturation of the Rh(111) surface with NO results in the formation of a  $(2 \times 2)$ -3NO ordered structure with a coverage of 0.75 ML. The increase of the NO coverage with increasing adsorption temperature is indicated both by SIMS and

TPD results. Simulation of the adsorption process in this temperature range indicates that both the increase in adsorbate ordering and the increase in the NO saturation coverage with higher adsorption temperature can be explained by enhanced mobility of NO.

For NO adsorption between 250 and 350 K, part of the NO dissociates during adsorption, whereas desorption processes are not relevant yet. Modeling of the NO adsorption process illustrates the important effect of lateral interactions on the NO dissociation rate. If such interactions are omitted, a pre-exponential factor and activation energy for NO dissociation of  $30 \text{ s}^{-1}$  and  $23 \text{ kJ/mol}$  are found, respectively, which are not acceptable for an elementary step. Incorporation of lateral interactions of neighbouring NO, N and O on the activation energy for NO dissociation results in theoretically more realistic parameters,  $10^{11} \text{ s}^{-1}$  and  $65 \text{ kJ/mol}$ .

For adsorption above 350 K, molecular NO is absent in the adsorbate layer; N and O are the only surface species. With increasing NO adsorption temperature the O coverage increases at the expense of the N coverage. In this temperature range the sum of the oxygen and nitrogen coverages exceeds 1 ML, which suggests the formation of subsurface O and N. Support for the formation of subsurface N arises from the observation that, above 425 K, N is not observable by SIMS whereas TPD indicates that significant amounts of N are still present.

Chapter 4 illustrates different ways to prepare pure atomic nitrogen layers on Rh(111). The reactivity of atomic nitrogen on rhodium is of considerable interest since it plays a key role in the selectivity issue of NO reduction; two N atoms can react to  $\text{N}_2$ , N can be hydrogenated to  $\text{NH}_3$ , N can react with NO to  $\text{N}_2\text{O}$ , and with hydrocarbon fragments to HCN.

Molecular NO adsorption at 150 K, followed by reaction with  $\text{H}_2$  at 400 K is a suitable method to deposit controllable amounts of N for coverages below 0.13 ML. The  $\text{N}_2$  TPD spectra of these atomic nitrogen layers show second order desorption behaviour and are best described by a pre-exponential factor and activation energy of  $10^{10.5 \pm 1} \text{ s}^{-1}$  and  $120 \pm 3 \text{ kJ/mol}$ , respectively. For initial NO coverages in excess of 0.45 ML, evidence for the formation of subsurface-N or an additional N-phase is provided by a high temperature tail in the  $\text{N}_2$  desorption spectra.

Atomic nitrogen coverages above 0.25 ML can be obtained by exposing  $\text{NO} + \text{H}_2$  mixtures to the Rh(111) surface. The highest atomic nitrogen coverage that can be obtained in this way is 0.45 ML.

Atomic nitrogen can also be deposited by decomposition of ammonia at temperatures above 400 K. The activation energy for  $\text{NH}_3$  decomposition is  $\sim 90 \text{ kJ/mol}$  assuming a pre-exponential factor of  $10^{13} \text{ s}^{-1}$ .

Apart from  $\text{N}_2$  formation, another possible reaction path for atomic nitrogen is hydrogenation to  $\text{NH}_3$ . We have investigated the mechanism of  $\text{NH}_3$  formation by exposing atomic nitrogen layers to  $\text{H}_2$ , at various pressures and temperatures, the results are presented in Chapter 5. SIMS experiments under reaction conditions revealed that



$\text{NH}_2$  is the predominant reaction intermediate. The hydrogenation of  $\text{NH}_2$  to  $\text{NH}_3$  appeared the rate determining step in  $\text{NH}_3$  formation. For this reaction step, an effective pre-exponential factor and activation energy of  $10^2 \text{ s}^{-1}$  and 33 kJ/mol have been determined, respectively.

The interaction of  $\text{NH}_3$  with Rh(111) has been investigated in a separate study and is the subject of Chapter 6. At 120 K,  $\text{NH}_3$  exclusively adsorbs molecularly on Rh(111) and no dissociation is observed during TPD. At low coverage,  $\text{NH}_3$  desorbs in a single state at 320 K, for which an activation energy of 81.5 kJ/mol is calculated if a pre-exponential factor of  $10^{13} \text{ s}^{-1}$  is assumed. The  $\text{NH}_3$  desorption temperature significantly shifts to lower temperatures with increasing  $\text{NH}_3$  coverage and an additional desorption state is observed at 155 K. At 0.25 ML coverage, the first adsorption layer is completed and  $\text{NH}_3$  orders into a  $(2 \times 2)$  structure. Adsorption of  $\text{NH}_3$  results in a large decrease of the work function, -2.4 eV with respect to the clean Rh(111) surface after completion of the first adsorption layer. SIMS appears very sensitive for the detection of  $\text{NH}_3$  and indicates that adsorption occurs preferentially on top sites. Formation of a second  $\text{NH}_3$  adsorption layer is indicated by a sharp  $\text{NH}_3$  desorption state at 130 K.

In the three-way catalytic convertor, NO is reduced by different reductants;  $\text{CO}$ ,  $\text{H}_2$  and hydrocarbons. Whereas the NO/ $\text{CO}$  and NO/ $\text{H}_2$  reaction systems have been studied extensively, the reactions between NO and hydrocarbons have not. This is probably caused by the complexity of the reaction system since many surface reactions proceed simultaneously and large variety of reaction products is formed.

Chapter 7 nicely illustrates how powerful of the combination of TPRS and TPSIMS is in unravelling complex reaction systems, such as those occurring during heating of mixed NO-ethylene layers, prepared by molecular adsorption at 120 K. SIMS monitors reactions on the surface, like *e.g.* NO dissociation and the decomposition of ethylene to ethylidyne and surface hydrogen, whereas TPRS monitors the desorption of products. For stoichiometric conditions on the surface (NO: $\text{C}_2\text{H}_4$  coverage ratio = 6:1),  $\text{H}_2\text{O}$ ,  $\text{CO}_2$  and  $\text{N}_2$  are the main reaction products. However, for strongly reducing conditions (NO: $\text{C}_2\text{H}_4 < 3$ ), significant amounts of  $\text{H}_2$ ,  $\text{CO}$  and even HCN form as well. At low total coverage coverages, NO and ethylene decompose as if they are on the Rh(111) surface separately. At higher coverages, NO and ethylene dissociation become hindered and also molecular desorption states are observed. Apart from CO formation by the recombination of atomic C and O, SIMS also monitors the coupling of C and N to cyanides. These surface cyanides can yield several gaseous products; they can be hydrogenated to HCN, they can dimerize to cyanogen ( $\text{C}_2\text{N}_2$ ) or they can decompose to form  $\text{N}_2$  and surface carbon.

In Chapter 8, we have investigated the formation and decomposition of cyanides by studying reactions between atomic nitrogen and ethylene. The absence of atomic oxygen simplifies the reaction system greatly and enables the determination of kinetic

parameters. For CN formation we find a pre-exponential factor and activation energy of  $10^{11} \text{ s}^{-1}$  and 111 kJ/mol, respectively, for CN decomposition  $10^{13} \text{ s}^{-1}$  and 210 kJ/mol. CN species are stable in the temperature range where regular  $\text{N}_2$  desorption takes place, and therefore cyanides can act as a storage for atomic nitrogen at higher temperatures. Formation of cyanides is accompanied by a work function increase. This indicates that cyanides are present as negatively charged surface species.

In this thesis we have determined kinetic parameters for a number of elementary surface reactions on Rh(111), *i.e.* for NO dissociation,  $\text{N}_2$  formation,  $\text{NH}_3$  formation, decomposition and desorption, and CN formation and decomposition, the values are given in the table below. These results give a rather good picture of the reactivity of atomic nitrogen on Rh(111). In order to investigate the influence of the Rh-N bond strength on the reactivity of N, it would be very interesting to investigate similar reactions on the Rh(100) surface, where atomic nitrogen is bonded more strongly.

Mathematical modeling of experimental results has proven very helpful in confirming or rejecting detailed mechanistical hypotheses. Therefore, we greatly encourage close collaboration between experimentalist and theorists in the future.

*Kinetic parameters for NO reduction related reactions on Rh(111)*

Reaction	$E_{\text{act}}$ [kJ/mol]	$\nu$ [ $\text{s}^{-1}$ ]	Elementary
$\text{NO}_{\text{ads}} + * \rightarrow \text{N}_{\text{ads}} + \text{O}_{\text{ads}}$	65	$10^{11}$	yes
$\text{N}_{\text{ads}} + \text{N}_{\text{ads}} \rightarrow \text{N}_{2,\text{g}} + 2 *$	120	$10^{10.5}$	yes
$\text{N}_{\text{ads}} + 3 \text{H}_{\text{ads}} \rightarrow \text{NH}_{3,\text{g}} + 4 *$	33	$10^2$	no
$\text{NH}_{2,\text{ads}} + \text{H}_{\text{ads}} \rightarrow \text{NH}_{3,\text{g}} + 2 *$	69	-	yes
$\text{NH}_{3,\text{ads}} \rightarrow \text{NH}_{3,\text{g}} + *$	81	$10^{13}$	yes
$\text{NH}_{3,\text{ads}} \rightarrow \text{N}_{\text{ads}} + 3/2 \text{H}_{2,\text{g}}$	90	$10^{13}$	yes
$\text{N}_{\text{ads}} + \text{C}_{\text{ads}} \rightarrow \text{CN}_{\text{ads}} + *$	111	$10^{11}$	yes
$\text{CN}_{\text{ads}} \rightarrow \text{C}_{\text{ads}} + 1/2 \text{N}_{2,\text{g}}$	205	$10^{13}$	yes

## Samenvatting

Dit proefschrift beschrijft een onderzoek naar de katalytische reductie van NO over rhodium, waarbij de bestudering van elementaire oppervlaktereacties en de bepaling van kinetische parameters centraal staan. Het onderzoek speelt een essentiële rol in het kader van de autouitlaatgaskatalyse, aangezien in de huidige drie-weg-katalysator NO<sub>x</sub> met behulp van rhodium wordt omgezet in het milieu-vriendelijke N<sub>2</sub>. Strengere toekomstige regelgeving op het gebied van de NO<sub>x</sub> emissie en de snel afnemende rhodium reserves nopen tot verbetering van de katalysator en vervanging of economischer gebruik van rhodium. Voor een beter begrip van de processen die de activiteit en selectiviteit van de drie-weg-katalysator bepalen, is kennis van de cruciale elementaire oppervlaktereacties en hun kinetische parameters essentieel.

Aangezien vele katalytische reacties oppervlaktespecifiek zijn, is een goed gedefinieerde oppervlaktestructuur noodzakelijk voor het bepalen van eenduidige kinetische parameters. Om deze reden is een rhodium (111) éénkristal gebruikt, waarbij de oppervlakteatomen een dichtstgepakte laag vormen. Voor het vaststellen van de kinetische parameters van bepaalde oppervlaktereacties is een combinatie van twee technieken gebruikt: temperatuurgeprogrammeerde desorptie- of reactiespectroscopie (TPD,TPRS) samen met secundaire ionen massa spectrometrie (SIMS). De combinatie van deze technieken is zeer effectief, aangezien TPRS informatie oplevert over de gasvormige producten die worden gevormd en SIMS bestudering van reacties op het oppervlak en identificatie van intermediären mogelijk maakt. Een nadeel van dit type onderzoek is dat experimentele drukken beperkt zijn tot (ultra-)hoog vacuüm ( $p < 10^{-6}$  mbar). Dit is noodzakelijk om een redelijke vrije weglengte voor de secundaire ionen te behouden en oppervlakteverontreiniging te voorkomen.

De dissociatie van NO in atomaire stikstof en zuurstof, is de eerste en belangrijkste reactiestap in de NO reductie cyclus op het rhodium oppervlak. Bepaling van de kinetische parameters voor de NO dissociatiereactie is gecompliceerd, aangezien de dissociatiesnelheid afhangt van zowel de bedekkingsgraad als de temperatuur. In Hoofdstuk 3 is de reactiviteit van NO op Rh(111) onderzocht door het uitvoeren van een aantal isotherme adsorptie-experimenten. SIMS en TPD zijn gebruikt ter bepaling van de NO, N en O bedekkingsgraden in de adsorbaatlaag die is verkregen door verzadiging van het Rh(111) oppervlak met NO bij een gegeven temperatuur. Om kinetische parameters te bepalen voor de NO dissociatie reactie zijn de experimenten gesimuleerd met een Monte-Carlo model, waarbij de rol van diffusie en laterale interacties zijn onderzocht. Voor temperaturen beneden 250 K, adsorbeert alle NO molecuair. Bij 150 K en een bedekking van 0.50 ML, ordent NO zich in een  $c(4 \times 2)$ -2NO structuur, waarbij de helft van de NO moleculen in fcc en de andere helft in hcp drie-voudige sites adsorbeert. Bij de verzadigingsbedekking van 0.68 ML is de NO structuur wanordelijk. Echter, bij 225 K leidt verzadiging van het Rh(111) oppervlak tot de vorming van een geordende

(2×2)-3NO structuur met een bedekking van 0.75 ML. Deze toename van de NO bedekkingsgraad wordt door de uitkomst van zowel SIMS als TPD experimenten bevestigd. Simulatie van het adsorptieproces in dit temperatuurgebied laat zien dat zowel de toename van de NO bedekkingsgraad als de toenemende ordening met toenemende adsorptietemperatuur kunnen worden verklaard door toenemende mobiliteit van NO.

Tussen 250 en 350 K dissocieert een deel van de NO gedurende het adsorptie experiment, maar desorptiereacties treden nog niet op. Modelleren van het adsorptie experiment laat zien hoe belangrijk de invloed van laterale interacties is op de NO dissociatiesnelheid. Als dergelijke interacties worden verwaarloosd, worden voor NO dissociatie een pre-exponentiële factor en een activeringsenergie van respectievelijk  $30 \text{ s}^{-1}$  en  $23 \text{ kJ/mol}$  gevonden, hetgeen vanuit theoretisch oogpunt niet acceptabel is voor een elementaire reactiestap. Als laterale interacties van NO, N en O uren op de NO dissociatiesnelheid wel worden meegenomen, worden veel realistischer parameters gevonden,  $10^{11} \text{ s}^{-1}$  en  $65 \text{ kJ/mol}$ .

Voor adsorptietemperaturen boven 350 K is NO afwezig in de adsorbaatlaag; alleen N en O worden waargenomen. Met toenemende adsorptietemperatuur neemt de N bedekking af en de O bedekking toe. In dit temperatuurgebied wordt de som van de O en N bedekking groter dan 1 ML, hetgeen de vorming van 'subsurface' N en O kan aangeven. Deze bewering wordt ondersteund door het feit dat er boven 425 K geen stikstofatomen meer waarneembaar zijn in SIMS terwijl TPD aangeeft dat er nog significante hoeveelheden N aanwezig zijn.

Hoofdstuk 4 laat zien hoe adsorbaatlagen van atomaire stikstof kunnen worden bereid op Rh(111). De reactiviteit van atomaire stikstof speelt een belangrijke rol in het selectiviteitsvraagstuk van de NO reductie; twee N atomen kunnen reageren tot  $\text{N}_2$ , N kan gehydrogeneerd worden tot  $\text{NH}_3$ , N kan met NO reageren tot  $\text{N}_2\text{O}$  en met koolwaterstof fragmenten tot HCN.

Moleculaire NO adsorptie bij 150 K gevolgd door reactie met  $\text{H}_2$  bij 400 K, is een geschikte methode om gecontroleerde hoeveelheden N af te zetten voor bedekkingen beneden 0.13 ML. De TPD spectra verkregen van deze atomaire stikstoflagen vertonen tweede-orde desorptiekinetiek, bij lage bedekkingsgraad worden een pre-exponentiële factor en activeringsenergie van  $10^{10.5} \text{ s}^{-1}$  en  $120 \text{ kJ/mol}$  gevonden. Voor initiële NO bedekkingen groter dan 0.45 ML vertonen de  $\text{N}_2$  desorptiespectra verbreding aan de hoge temperatuurzijde, hetgeen kan duiden op de vorming van subsurface-N of een nieuwe N-fase.

Atomaire stikstof bedekkingen boven 0.25 ML kunnen worden verkregen door het doseren van  $\text{NO} + \text{H}_2$  reactiemengsels. Op deze manier kunnen stikstofbedekkingen van maximaal 0.45 ML worden verkregen.

Atomaire stikstof kan ook worden afgezet door dissociatieve adsorptie van ammonia boven temperaturen van 400 K. Voor de  $\text{NH}_3$  ontledingsreactie wordt een activeringsenergie van  $\sim 90 \text{ kJ/mol}$  gevonden als een pre-exponentiële factor van  $10^{13} \text{ s}^{-1}$  wordt aangenomen.

Voor atomaire stikstof is behalve recombinatie tot  $N_2$ , hydrogenering naar  $NH_3$  een mogelijk reactiepad. Het  $NH_3$  vormingsmechanisme is bestudeerd door atomaire stikstof te laten reageren met  $H_2$  bij verschillende drukken en temperaturen, de resultaten zijn beschreven in Hoofdstuk 5. SIMS experimenten tijdens de hydrogeneringsreactie hebben aangetoond dat N en  $NH_2$  de belangrijkste  $NH_x$  adsorbaten zijn. Verder bleek de hydrogenering van  $NH_2$  naar  $NH_3$  de snelheidsbepalende stap. Voor deze reactie zijn een effectieve pre-exponentiële factor en activeringsenergie van  $10^2 \text{ s}^{-1}$  en 33 kJ/mol bepaald.

De interactie van  $NH_3$  met Rh(111) is in detail onderzocht en vormt het onderwerp van Hoofdstuk 6. Bij 120 K adsorbeert alle  $NH_3$  moleculair op Rh(111) en tijdens TPD treedt geen dissociatie op. Bij lage bedekking desorbeert  $NH_3$  in een enkele toestand met een maximum bij 320 K, waarvoor een desorptie energie van 81.5 kJ/mol wordt bepaald als een pre-exponentiële factor van  $10^{13} \text{ s}^{-1}$  wordt aangenomen. Met toenemende bedekkingsgraad verschuift de  $NH_3$  desorptie naar lagere temperatuur resulterend in een extra desorptie toestand bij 155 K. Bij een bedekking van 0.25 ML ordent  $NH_3$  in een  $(2 \times 2)$  structuur en is de eerste adsorbaatlaag volledig gevuld. Adsorptie van  $NH_3$  resulteert in een sterke verlaging van de uittree-arbeid, -2.4 eV ten opzichte van het schone Rh(111) oppervlak bij een  $NH_3$  bedekking van 0.25 ML. De vorming van de tweede adsorbaatlaag wordt aangegeven door een smalle  $NH_3$  desorptie toestand bij 130 K.

In de drie-weg-katalysator reageert NO met verschillende reductanten: CO,  $H_2$  en koolwaterstoffen. In tegenstelling tot de NO/CO en NO/ $H_2$  reactiesystemen, die vrij goed bestudeerd zijn, is er weinig bekend over reacties tussen NO en koolwaterstoffen. Dit komt waarschijnlijk door de complexiteit van het laatstgenoemde reactiesysteem, waarbij verschillende oppervlaktereacties simultaan plaatsvinden en een grote verscheidenheid aan producten gevormd wordt.

Hoofdstuk 7 laat zien dat de combinatie van TPRS en TPSIMS zeer geschikt is voor het ontrafelen van complexe reactiesystemen, zoals die zich voordoen bij het verwarmen van gemengde NO-ethen adsorbaatlagen, bereid door moleculaire adsorptie bij 120 K. SIMS volgt reacties op het oppervlak, zoals bijvoorbeeld de NO dissociatie en de ontleding van etheen naar ethylidyne en oppervlakte waterstof, terwijl TPRS de desorptieproducten detecteert. Voor stoichiometrische condities op het oppervlak ( $NO:C_2H_4 = 6:1$ ), zijn  $H_2O$ ,  $CO_2$  en  $N_2$  de voornaamste reactieproducten. Echter, bij sterk reducerende condities ( $NO:C_2H_4 < 3$ ), worden er ook significante hoeveelheden  $H_2$ , CO en zelfs HCN gevormd. Bij lage totale bedekkingsgraad ontleden NO en etheen op vergelijkbare manier als de individuele systemen op Rh(111). Bij hoge bedekkingsgraad worden zowel de NO als de etheen ontleding geremd en wordt ook moleculaire desorptie waargenomen. Behalve de vorming van CO door de recombinatie van C en O kan ook de recombinatie van C en N tot cyanides met SIMS gevolgd worden. Deze cyanides kunnen verschillende gasvormige producten opleveren; ze kunnen gehydrogeneerd worden naar HCN, ze kunnen dimeriseren naar cyanogeen ( $C_2N_2$ ) en ze kunnen ontleden naar  $N_2$  en

oppervlakte koolstof.

In Hoofdstuk 8, is de vorming en ontleding van cyanides bestudeerd aan de hand van reacties tussen atomaire stikstof en etheen. De afwezigheid van zuurstof leidt tot een aanzienlijke vereenvoudiging van het reactiesysteem waardoor bepaling van kinetische parameters mogelijk wordt. Voor de CN vorming zijn een pre-exponentiële factor en activeringsenergie van respectievelijk  $10^{11} \text{ s}^{-1}$  en  $111 \text{ kJ/mol}$  gevonden, voor CN ontleding  $10^{13} \text{ s}^{-1}$  en  $210 \text{ kJ/mol}$ . In de afwezigheid van coadsorbaten zijn cyanides stabiel in het temperatuurgebied waar normaal gesproken  $\text{N}_2$  desorptie plaatsvindt en daarom kunnen zij fungeren als reservoir voor stikstof bij hogere temperaturen. De vorming van cyanides leidt tot een toename van de uittree-arbeid. Hieruit blijkt dat cyanides als negatief geladen adsorbaat aanwezig zijn.

In dit proefschrift zijn de kinetische parameters van een aantal elementaire oppervlaktereacties op Rh(111) bepaald, te weten: NO dissociatie,  $\text{N}_2$  vorming,  $\text{NH}_3$  vorming, ontleding en desorptie, en CN vorming en ontleding (zie onderstaande tabel). Deze resultaten geven een goed beeld van de reactiviteit van N atomen op Rh(111). Om de invloed van de Rh-N bindingsterkte op de reactiviteit van N te onderzoeken zou het interessant zijn om vergelijkbare reacties te onderzoeken op bijvoorbeeld Rh(100) waar N sterker gebonden is.

Het simuleren van experimenten met een mathematisch model is zeer succesvol gebleken bij het bevestigen of verwerpen van gedetailleerde mechanistische hypothesen. Om deze reden wordt verdere intensivering van de contacten tussen de experimentator en theoreticus ten sterkste aangemoedigd.

#### *Kinetische parameters voor NO reductie gerelateerde reacties op Rh(111)*

Reactie	$E_{\text{act}}$ [kJ/mol]	$\nu$ [s <sup>-1</sup> ]	Elementair
$\text{NO}_{\text{ads}} + * \rightarrow \text{N}_{\text{ads}} + \text{O}_{\text{ads}}$	65	$10^{11}$	ja
$\text{N}_{\text{ads}} + \text{N}_{\text{ads}} \rightarrow \text{N}_{2,\text{g}} + 2 *$	120	$10^{10.5}$	ja
$\text{N}_{\text{ads}} + 3 \text{H}_{\text{ads}} \rightarrow \text{NH}_{3,\text{g}} + 4 *$	33	$10^2$	nee
$\text{NH}_{2,\text{ads}} + \text{H}_{\text{ads}} \rightarrow \text{NH}_{3,\text{g}} + 2 *$	69	-	ja
$\text{NH}_{3,\text{ads}} \rightarrow \text{NH}_{3,\text{g}} + *$	81	$10^{13}$	ja
$\text{NH}_{3,\text{ads}} \rightarrow \text{N}_{\text{ads}} + 3/2 \text{H}_{2,\text{g}}$	90	$10^{13}$	ja
$\text{N}_{\text{ads}} + \text{C}_{\text{ads}} \rightarrow \text{CN}_{\text{ads}} + *$	111	$10^{11}$	ja
$\text{CN}_{\text{ads}} \rightarrow \text{C}_{\text{ads}} + 1/2 \text{N}_{2,\text{g}}$	205	$10^{13}$	ja

## Publications

R.M. van Hardeveld, P.L.J. Gunter, L.J. van IJzendoorn, W. Wieldraaijer, E.W. Kuipers, J.W. Niemantsverdriet, "Deposition of inorganic salts from solution on flat substrates by spin-coating: theory, quantification and application to model catalysts", *Applied Surface Science* 84 (1995) 339-346.

J.C. Muijsers, Th. Weber, R.M. van Hardeveld, H.W. Zandbergen, and J.W. Niemantsverdriet, "Sulfidation study of molybdenum oxide using  $\text{MoO}_3/\text{SiO}_2/\text{Si}(100)$  model catalysts and  $\text{Mo}_3^{\text{VI}}$ -sulfur cluster compounds", *Journal of Catalysis* 157 (1995) 698-705.

H.J. Borg, R.M. van Hardeveld, and J.W. Niemantsverdriet, "Mechanism of the conversion of ethylene to ethylidyne on Rhodium(111): Evidence for a vinylic Intermediate", *Journal of the Chemical Society Faraday Transactions* 91 (1995) 3679-3684.

R.M. van Hardeveld, A.J.G.W. Schmidt, J.W. Niemantsverdriet, "Surface reactions of nitrogen oxide and ethylene on rhodium(111)", *Catalysis Letters* 41 (1996) 125-131.

J.W. Niemantsverdriet, H.J. Borg, R.M. van Hardeveld, and R.A. van Santen, "Surface reactions of ethylene with deuterium, oxygen and nitrogen oxide on rhodium: Kinetics and mechanism", *Recueil des Travaux Chimiques des Pays-Bas* 115 (1996) 486-491.

J.F.E. Gootzen, R.M. van Hardeveld, W. Visscher, R.A. van Santen, and J.A.R. van Veen, "The study of NO adsorbate layers on platinumized platinum in the liquid phase with cyclic voltammetry, DEMS and FTIRS", *Recueil des Travaux Chimiques des Pays-Bas* 115 (1996) 480-485.

R.M. van Hardeveld, R.A. van Santen, and J.W. Niemantsverdriet, "The adsorption of  $\text{NH}_3$  on Rh(111)", *Surface Science* 369 (1996) 23-35.

R.M. van Hardeveld, R.A. van Santen, J.W. Niemantsverdriet, "Kinetics and mechanism of  $\text{NH}_3$  formation by the hydrogenation of atomic nitrogen", *Journal of Physical Chemistry* 101 (1997) 998-1005.

R.M. van Hardeveld, A.J.G.W. Schmidt, R.A. van Santen, and J.W. Niemantsverdriet, "Cyanide intermediates in catalytic reduction of NO by  $\text{C}_2\text{H}_4$  on rhodium(111)", *Journal of Vacuum Science and Technology A*(3) 15 (1997) 1642-1646.

R.M. van Hardeveld, R.A. van Santen, J.W. Niemantsverdriet, "Formation of  $\text{NH}_3$  and  $\text{N}_2$  from atomic nitrogen, and hydrogen on rhodium(111)", *Journal of Vacuum Science and Technology A* 15 (1997) 1558-1562.

R.M. van Hardeveld, H.J. Borg, and J.W. Niemantsverdriet, "Kinetics of Elementary Surface Reactions Studied by Static Secondary Ion Mass Spectrometry and Temperature Programmed Reaction Spectroscopy", accepted for publication in the Journal of Molecular Catalysis.

R.M. van Hardeveld, R.A. van Santen, and J.W. Niemantsverdriet, "C-N coupling in reactions between atomic nitrogen and ethylene on Rh(111)", accepted for publication in the Journal of Physical Chemistry.

R.M. van Hardeveld, J.J. Lukkien, P.A.J. Hilbers, A.P.J. Jansen, J.W. Niemantsverdriet, and R.A. van Santen, "Monte-Carlo modeling of isothermal NO adsorption experiments on Rh(111)", to be published.

A. Siokou, R.M. van Hardeveld, and J.W. Niemantsverdriet, "Surface reactions of nitrogen oxide on rhodium (100), adsorption, dissociation and desorption", submitted to Surface Science.



# Dankwoord

Nu het allemaal op papier staat, realiseer ik me pas goed dat de afgelopen vier jaar omgevlógen zijn. Dit gebrek aan tijdsbesef is zonder enige twijfel het gevolg van het feit dat ik het bijzonder goed naar mijn zin gehad heb. Op deze plaats wil ik graag iedereen bedanken die mijn promotie-periode tot een onvergetelijke tijd heeft gemaakt.

In het bijzonder wil ik mijn promotor, Rutger van Santen, bedanken voor de uiterst stimulerende en leerzame werkbesprekingen die het doen van onderzoek tot een ware hobby hebben verheven. Op dit vlak ben ik ook veel dank verschuldigd aan mijn copromotor, Hans Niemantsverdriet, waarbij ik deze ook nog wil bedanken voor het overbrengen van zijn schrijverskwaliteiten. Mijn tweede promotor, John Geus, en de overige kerncommissieleden, Ben Nieuwenhuys en Rob van Veen, ben ik zeer erkentelijk voor het lezen en corrigeren van het concept-proefschrift. In dit opzicht ben ik ook zeer veel dank verschuldigd aan collega, vriend en vader, Ruud van Hardeveld.

Verder ben ik mij er ten volle van bewust dat onderzoek met behulp van geavanceerde ultrahog vacuüm systemen alleen mogelijk is met vakkundige technische ondersteuning. In dit opzicht wil ik de Centrale Technische Dienst, in het algemeen, en Peer Brinkgreve, Theo Maas, Piet van den Hoogen, Rob van den Berg en Jos de Laat, in het bijzonder, bedanken voor hun professionele ondersteuning en de plezierige samenwerking. Voor de vele overige technische problemen kon ik altijd terecht bij Wout van Herpen en Tiny Verhoeven, ook jullie ben ik veel dank verschuldigd.

De studenten Alex Schmidt, Bart Lebbink, Arno Sanders, Joost Heijnen en Jeroen Kluytmans, wil ik bedanken voor het verrichten van de nodige metingen en de zorgvuldige omgang met de UHV systemen.

De elektrokatalyse groep, onder leiding van Rob van Veen en Wil Visser, wil ik bedanken voor de mogelijkheid om 'nat-chemisch' onderzoek te kunnen doen ten tijde van algehele malaise met de UHV apparatuur. Johan Lukkien wil ik bedanken voor de vele simulaties van de NO adsorptie-experimenten en de prettige samenwerking.

Mijn directe (ex-)collega's, Herman Borg, André Engelen, Albert Gootzen, Pieter Gunter, Marco Hopstaken, Ton Janssens, Arthur de Jong, Hannie Muijsers, Elina Siokou, Peter Thüne, Cees Verhagen, Tiny Verhoeven en Thomas Weber, wil ik bedanken voor alle onvergetelijke ervaringen die we de afgelopen jaren hebben opgebouwd. Het is een prettige gedachte dat sommige collega's niet enkel ex-collega's zullen worden, maar goede vrienden zullen blijven.

Tenslotte wil ik mijn vader en moeder bedanken voor de onvoorwaardelijke steun die ik al die jaren van jullie genoten heb. Verder wil ik alle familie, vrienden en kennissen bedanken voor hun welgemeende interesse in het voortschrijden van dit proefschrift. Ik kan nu zeggen: 'het is af.'

## Curriculum Vitae

Martijn van Hardeveld werd op 21 februari 1970 geboren te Geldrop. In 1982 startte hij zijn middelbare school periode aan de scholengemeenschap Sint Michiel te Geleen, waar hij in 1988 zijn VWO diploma behaalde. Aansluitend begon hij met de studie Scheikundige Technologie aan de Technische Universiteit Eindhoven. In september 1989 werd het propaedeutisch examen afgelegd. In 1992 liep hij voor Shell International stage in Brazilië. In datzelfde jaar werd begonnen aan de afstudeeropdracht in de vakgroep Anorganische Chemie & Katalyse, waar de bereiding en inzwaveling van een  $\text{MoO}_3/\text{SiO}_2$  modelkatalysator werd onderzocht met behulp van X-ray Photoelectron Spectroscopy. Op 21 oktober 1993 werd het ingenieursdiploma met lof behaald. Op 1 november 1993 trad hij als Onderzoeker in Opleiding in dienst van SON en startte zijn promotie-onderzoek aan de Technische Universiteit in de vakgroep Anorganische Chemie & Katalyse. Onder leiding van prof.dr. R.A. van Santen en dr. J.W. Niemantsverdriet werd, in het kader van de autouitlaatgaskatalyse, onderzoek verricht aan elementaire reacties in de katalytische reductie van NO op rhodium oppervlakken. De belangrijkste resultaten van het onderzoek zijn beschreven in dit proefschrift. Vanaf 1 oktober 1997 zal hij werkzaam zijn bij het Shell Research en Technology Centre in Amsterdam.

# **Stellingen**

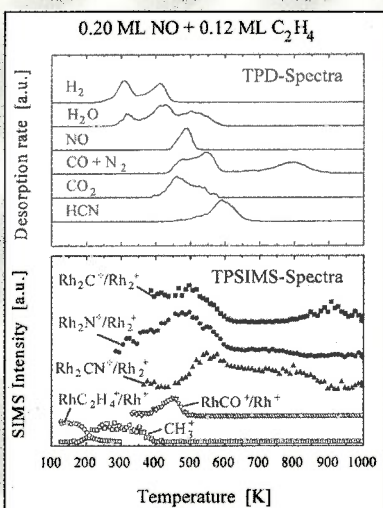
behorende bij het proefschrift

## **Elementary Reactions in the Catalytic Reduction of NO on Rhodium Surfaces**

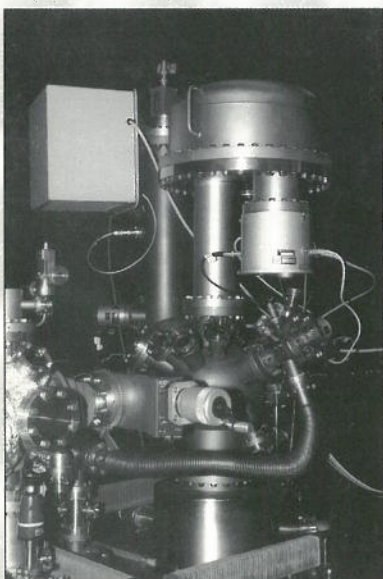
R.M. van Hardeveld

1. De lage pre-exponentiële factoren en activeringsenergieën die gerapporteerd zijn voor de NO dissociatiereactie op rhodium, zijn het gevolg van het verwaarlozen van laterale interacties tussen de adsorbaten bij het modelleren van de experimentele resultaten.  
*V. Schmatloch, I. Jirka and N. Kruse, Surf. Sci. 297 (1993) L100.*  
*C. Sellmer, V. Schmatloch and N. Kruse, Catal. Lett. 35 (1995) 165.*
2. Onder extreme condities kan de produktie van blauwzuur (HCN) in de auto-uitlaatgaskatalysator niet uitgesloten worden.  
*Hoofdstukken 7 en 8 van dit proefschrift.*
3. Het experimentele bewijs voor het in de elektrochemische literatuur voorgestelde mechanisme voor de vorming van N<sub>2</sub>O (lachgas) aan platina elektrodes, door dimerisatie van NOH gevolgd door ontleding van N<sub>2</sub>O<sub>2</sub>H<sub>2</sub> in H<sub>2</sub>O en N<sub>2</sub>O, heeft in ieder geval een stimulerend effect op de lachspieren.  
*I. Paseka and J. Vořková, Electrochim. Acta 25 (1980) 1251.*  
*N.N. Savodnik, V.A. Shepelin and Ts.I. Zalkin, Élektrokimiya 7 (1970) 424.*
4. De afwezigheid van absorpties door CN-vibraties in EELS- en IR-spectra verkregen na adsorptie van methyl-isocyanide (CH<sub>3</sub>NC) bij lage temperatuur op rhodium en verwarming tot 600 K, zegt meer over de adsorptiegeometrie van cyanides op rhodium dan over de afwezigheid van dit adsorbaat.  
*R.R. Cavanagh and J.T. Yates, Jr., J. Chem. Phys. 75 (1981) 1551.*  
*S. Semancik, G.L. Haller and J.T. Yates, Jr., J. Chem. Phys. 78 (1983) 6970.*
5. Bij de modellering van de oxidatie van zowel C als CO op rhodium wordt soms ten onrechte evenwicht aangenomen voor de zuurstof adsorptiereactie.  
*S.N. Mikhailov, L.C.A. van den Oetelaar, H.H. Brongersma and R.A. van Santen, Catal. Lett. 27 (1994) 79.*  
*S.B. Schwartz, L.D. Schmidt and G.B. Fisher, J.Phys.Chem. 90 (1986) 6194.*

6. De stabiliteit van de verschillende  $\text{NH}_x$  intermediairen op rhodium, in zowel  $\text{NH}_3$  vormings- als ontledingsreacties, is in hoge mate vlakkenspecifiek.  
*T. Yamada and K. Tanaka, J. Am. Chem. Soc. 113 (1991) 1173.*  
*Hoofdstuk 5 van dit proefschrift*
7. Veel onbegrip voor abstracte moderne kunst ontstaat pas bij het bestuderen van het prijskaartje.
8. Het is triest te moeten constateren dat de mystieke rol van paddestoelen in sprookjes vervangen lijkt te worden door een louter consumptieve rol voor het opwekken van hallucinaties bij fantasieloze geesten.
9. Uit de populariteit van vermageringsdiëten in de huidige westerse samenleving blijkt dat het menselijk lichaam de enige chemische fabriek is waarvan menigeen de energie-efficiëntie betreurt.
10. Ook in de huidige drinkwaterproblematiek lijkt te gelden dat de laatste loodjes het zwaarst wegen.



TPD and TPSIMS spectra obtained from a rhodium (111) single crystal surface covered with 0.20 ML NO and 0.12 ML ethylene at 120 K. The TPD spectra give information about the products that are formed during heating, while the TPSIMS spectra illustrate the reactions that occur on the surface.



Picture of the analysis chamber of the Ultra High Vacuum (UHV) system that has been used in this thesis. The base pressure in the system is around  $10^{-13}$  atmospheres. Surface reactions can be studied by means of temperature programmed desorption or reaction spectroscopy (TPD/TPRS) and secondary ion mass spectrometry (SIMS).

